

# **Two-dimensional crack growth in FRP laminates and sandwich panels**

**Thèse N° 9421**

Présentée le 3 mai 2019

à la Faculté de l'environnement naturel, architectural et construit  
Laboratoire de construction en composites  
Programme doctoral en génie civil et environnement

pour l'obtention du grade de Docteur ès Sciences

par

**Aida CAMESELLE MOLARES**

Acceptée sur proposition du jury

Prof. E. Brühwiler, président du jury  
Prof. T. Keller, Dr. A. Vassilopoulos, directeurs de thèse  
Prof. L. A. Carlsson, rapporteur  
Prof. J. P. Ramôa Ribeiro Correia, rapporteur  
Dr A. Brunner, rapporteur

2019





*Para mis padres*



# Preface

Fiber-reinforced polymer (FRP) composite materials can offer significant advantages over traditional materials in bridge and building construction and are therefore being increasingly used. Delamination of laminates or debonding of face sheets from the core in sandwich structures represent some of the most critical failure modes, which may affect structural integrity and safety. Delamination and debonding normally originate from small defects or imperfections and then propagate in a two-dimensional (2D) plane in all directions. However, delamination and debonding are currently investigated and characterized by standardized one-dimensional (1D) fracture mechanics tests, which do not capture potential 2D effects. For instance, 1D crack propagation, with the crack width remaining constant, does not represent the increasing crack area and the stiffness conditions as they occur in real 2D cases. The aim of this thesis is thus to investigate, characterize and quantify, experimentally and numerically, potential 2D effects on the 2D delamination in laminates and 2D debonding in face sheet/core interfaces of sandwich structures that are not captured by 1D fracture mechanics tests. The thesis develops the scientific bases for a better understanding of delamination and debonding in real 2D cases.

I would like to acknowledge the support for this research project provided by the Swiss National Science Foundation.

Lausanne, April 2019

Prof. Dr. Thomas Keller  
EPFL-CCLab



# Acknowledgments

Nobody said it would be easy but the truth is that nothing worthwhile is. This doctoral thesis represents the conclusion of four years of intense and gratifying work through which I have achieved extremely valuable professional and personal development. I had the immeasurable luck of sharing this life-changing journey with many kind-hearted and extraordinary people whose constant encouragement, support and goodwill led me here today. I would thus like to express my honest and deep appreciation to all of them.

First I would like to address my sincere gratitude to my thesis director Prof. Thomas Keller for granting me this precious opportunity and for the trust you placed in me. I will always be obliged to you. Thank you for your excellent and wise guidance and your tireless support. Throughout all these years you have helped me not only to largely improve my analytical thinking and technical communication skills but you have also been an example of professionalism and integrity. Thank you also to my co-supervisor Dr. Vassilopoulos for the fruitful discussions, revision of the papers and kind support.

I wish to express my appreciation to my thesis defense committee for the time and effort they devoted to carefully examining my thesis and for their valuable comments: Prof. João Ramôa Correia (Técnico de Lisboa, Portugal), Dr. Andreas Brunner (EMPA, Switzerland), Prof. Leif Carlsson (Florida Atlantic University, United States) and Prof. Eugen Brühwiler (president of the jury, MCS-EPFL). I am deeply honored by your participation in my thesis defense.

Also thanks to Dr. Jordi Renart for granting me the opportunity of spending three months in AMADE Group (Girona, Spain) where I had the chance to learn many numerical tools that widely contributed to the advance of my thesis. Thanks also to Dr. Albert Turon for the “cohesive thinking”. I will always be grateful.

The experimental work presented here was conducted in EPFL’s Structural Engineering Laboratory and could not have been completed without the strong support, patience and hard work of the technicians. I would like to acknowledge Serge, for your incredibly meticulous, precise and high-quality work regarding the preparation of my specimens and the fabrication of the fixtures. Thank you also for being always proactive and respectful regarding my sometimes tight deadlines and for always keeping a kind smile in your face. You made things easier and I will always be obliged to you. Also huge thanks to Gilles, for your valuable and essential assistance in installing the experimental set-ups and performing and monitoring the experiments. I will always remember your commitment during all the many hours we spent working together in the laboratory. A

special mention also to Sylvain, Armin and Gérald for the always interesting conversations and the smiles you elicited.

One of the greatest gifts that performing this research in the EPFL environment has offered me is the possibility of meeting smart, talented and warm people from very different spots on the planet, allowing me to learn both professionally and personally from each one of them. I feel tremendously fortunate for having shared this PhD experience with one of the craziest and smartest people I have ever met, my project colleague and friend Vahid. Thank you for your tireless support, always wise scientific advice, open and crazy mind and true friendship. You made CCLab feel like home and that is something that I will treasure forever. I wish also to thank Julia for her unstinting support, encouragement and friendship. Thank you for always being there to comfort and guide me and also for all the laughter we have shared. Thank you to my longest-standing officemate and friend Myrsini, for your always kind and happy attitude and your constant help since my arrival here. Thank you for introducing me to everyone and for unselfishly opening the doors of your life to me. Also thank you to my office-neighbor Sonia, for our long conversations about life and science and your support; and to Ghazaleh, who arrived late but became a really important part of the team. I am grateful for your friendship and generosity and of course your amazing cooking skills. Thank you also to my current and extraordinary officemate Niloufar for our funny and also important talks and your kindness and support (and also for sharing with me some pieces of your wonderful parallel universe!). I would like to extend my gratitude to all the other “CCLabians” for their support and transfer of experience: Haifeng, Mário, João, Chao, Wei, Xin, Kyriaki, Zhengwen, Luca and Lulu. Special thanks also to Saira, for her administrative coordination and nice conversations and to Mrs. Howett for the thorough correction of the English text of my thesis and papers.

Thank you also to the generous, brilliant and amazing friends that have been there for me in one way or another: Angelica and Francesco, Martina and Manuel, Ioannis, Maria, Francesco Vanin and Danelys. Thank you for the laughter, the intelligent conversation and the friendship. We have created a second family here that I hope stays forever, no matter how far apart we may be.

A special thank you to Goyo and Ana - we met on a boat sailing the Atlantic and today you are still cruising along with me.

I would also like to thank my colleagues at GCons and GME of University of A Coruña (Spain) where I got started: I cherish fond and good memories. Special thanks to Dr. Manuel Herrador who introduced me to research and to Francisco Bermúdez, a kind and brilliant computer engineer who has been always available to solve all my IT problems when I was about to panic. Thank you.

Fran, I cannot find enough words to express how much you mean to me. Thank you for your unconditional love, for staying calm when I am not able to, for comforting me when the fatigue beats me, for believing when I lose hope, for casting light on what seems unachievable, for your optimism, kindness, joy and for loving life. Thank you for making

me laugh, always. You have taught me that happiness lies in the small things and to value every second. Thank you for being reckless with me, for launching yourself in this adventure that has been both complicated and wonderful. Thank you for following me into the great unknown. This work is ours, you know it. Choosing you as partner in life has been my best decision and my greatest pride.

Thank you to my brother, your example has always helped me and served as guide and your support has given me the strength to continue and improve myself. Having you close all these years has been a source of serenity and family comfort.

Dad, Mom, thank you. Thank you for being my eternal and endless support, my shelter, my lighthouse, my mainland. Thank you for having built a wonderful home full of love and respect. With your example you have taught me the value of effort, honesty and family, being a constant inspiration in every aspect of my life. Thank you for believing and encouraging me to always fight for my dreams no matter how unreachable they seemed. Your endorsement and unconditional love at every milestone of my life have brought me here. This work also belongs to you.





# Agradecimientos

Nadie dijo que fuera fácil, pero lo cierto es que nada que merezca la pena lo es. Esta tesis doctoral representa el cierre a cuatro años de intenso y gratificante trabajo gracias al cual he crecido y madurado tanto profesional como personalmente. He tenido la inmensa suerte de compartir este viaje vital con personas extraordinarias y de buen corazón cuyo apoyo constante me ha guiado hasta aquí. Me gustaría por tanto expresar mi profundo y sincero reconocimiento a todas ellas.

Primero desearía manifestar mi más sincera gratitud hacia mi director de tesis Prof. Thomas Keller por concederme esta valiosa oportunidad y por la confianza que depositó en mí. Siempre estaré en deuda con usted. Gracias por su excelente y sabia dirección y por su incansable apoyo. A lo largo de estos años me ha ayudado no sólo a mejorar ampliamente mi pensamiento analítico y mis competencias de comunicación técnica sino que a su vez ha sido ejemplo de profesionalismo e integridad. Gracias también a mi co-supervisor, Dr. Vassilopoulos, por las fructíferas discusiones, la revisión de los artículos y su amable apoyo.

Desearía expresar mi aprecio al jurado de tesis por el tiempo y esfuerzo dedicado a la lectura minuciosa de la misma y por sus valiosos comentarios: Prof. João Ramôa Correia (Técnico de Lisboa, Portugal), Dr. Andreas Brunner (EMPA, Suiza), Prof. Leif Carlsson (Florida Atlantic University, Estados Unidos) and Prof. Eugen Brühwiler (presidente del jurado, MCS-EPFL). Me siento profundamente honrada por su participación.

Gracias también a Jordi Renart por concederme la oportunidad de compartir tres meses con el grupo de investigación AMADE (Girona, España) donde tuve la suerte de aprender herramientas numéricas que contribuyeron en gran medida al avance de mi tesis. Y gracias a Albert Turon, por tu “pensamiento cohesivo”. Siempre os estaré agradecida.

El trabajo experimental que aquí se presenta fue llevado a cabo en el laboratorio de ingeniería estructural de la EPFL y no podría haber sido completado sin el sólido apoyo, paciencia y trabajo duro de los técnicos. Serge, me gustaría agradecerte tu trabajo meticuloso, preciso y de alta calidad preparando mis probetas y fabricando las fijaciones. Gracias también por ser siempre proactivo y respetuoso con mis a veces ajustadas fechas límite y por mantener siempre una sonrisa en la cara. Un gran gracias también a Gilles, por tu valiosa y esencial asistencia en la instalación de los sistemas de ensayo y en la ejecución y monitoreo de los mismos. Siempre recordaré tu compromiso durante las muchas horas que compartimos trabajando juntos en el laboratorio. Mención especial también a Sylvain, Armin y Gérald por vuestra siempre interesante conversación y por la sonrisas sonsacadas.

Uno de los mayores regalos que investigar en la EPFL me ha ofrecido es la posibilidad de conocer personas inteligentes, talentosas y cercanas provenientes de lugares muy diferentes del planeta, permitiéndome aprender de cada uno de ellos. Me siendo tremendamente afortunada de haber podido compartir esta experiencia con una de las personas más locas e inteligentes que jamás he conocido, mi compañero de proyecto y amigo Vahid. Gracias por tu apoyo incombustible, por tus siempre sabios consejos científicos, por tu mente abierta y tu amistad sincera. Convertiste el CCLab en un segundo hogar y eso es algo que nunca olvidaré. Gracias también a Julia, por tu apoyo constante y tu amistad. Gracias por estar siempre ahí para confortarme y guiarme y gracias también por todas las risas compartidas. Gracias a mi compañera de despacho durante los primeros años de tesis, Myrsini, por tu actitud siempre amable y alegre y por tu apoyo incansable desde que llegué. Gracias por presentarme a todo el mundo y por abrirme las puertas de tu vida sin pedir nada a cambio. Gracias a mi vecina de despacho Sonia, por nuestras largas conversaciones sobre la vida y la ingeniería y por tu apoyo; y a Ghazaleh, que aunque llegó más tarde se ha convertido en indispensable. Te agradezco tu amistad, generosidad y por su puesto, gracias por tu increíbles dotes de cocina. Gracias a mi compañera de despacho actual, Niloufar, por nuestras divertidas aunque también trascendentes charlas y por tu amabilidad y apoyo (y también por dejarme entrar de vez en cuando en tu universo paralelo!). Me gustaría extender mi gratitud al resto de “CCLabians” por vuestro apoyo y por compartir vuestra experiencia: Haifeng, Mário, João, Chao, Wei, Xin, Kyriaki, Zhengwen y Luca. Gracias también a Saira por el trabajo administrativo y por las agradables charlas y a Margaret Howett por la rigurosa corrección del inglés tanto en la tesis como en los artículos.

Gracias a mis generosos, brillantes e increíbles amigos que siempre han estado ahí, de una forma u otra: Angelica y Francesco, Martina y Manuel, Ioannis, Maria, Francesco Vanin y Danelys. Gracias por las risas, por vuestra inteligente conversación y por vuestra amistad. Hemos creado una segunda familia que espero perdure siempre independientemente de lo lejos que podamos llegar a estar.

Gracias especialmente también a Goyo y Ana, porque nos conocimos en un barco surcando el Atlántico y todavía hoy navegáis conmigo.

También me gustaría agradecer a mi compañeros del GCons y del GME en la Universidad da Coruña (España), donde empecé. Guardo buenos y agradables recuerdos. Gracias especialmente a Manuel Herrador por iniciarme en el mundo de la investigación en ingeniería y a Francisco Bermúdez, un atento y brillante ingeniero informático que siempre ha estado disponible para resolver problemas técnicos cuando yo entraba en pánico. Gracias.

Fran, no encuentro palabras suficientes para expresar lo mucho significas para mí. Gracias por tu apoyo siempre incondicional, por mantener la calma cuando yo la pierdo, por confortarme cuando el cansancio me gana, por creer cuando yo pierdo la esperanza, por proyectar luz sobre aquello que parece inalcanzable, por tu optimismo, tu bondad, tu alegría, tu amor por la vida. Gracias por hacerme reír, siempre. Me has enseñado que la felicidad está en las pequeñas cosas y a valorar cada segundo. Gracias por atreverte

conmigo, por lanzarte a esta aventura que ha sido tan complicada como maravillosa. Gracias por seguirme a lo desconocido y por creer ciegamente en mí. Este trabajo es de ambos, lo sabes bien. Elegirte como compañero de vida ha sido mi mejor decisión y mi mayor orgullo.

Gracias a mi hermano, tu ejemplo me ha ayudado y servido de guía siempre y tu apoyo me ha dado fuerzas para avanzar y superarme. Tenerte cerca estos años ha sido siempre fuente de tranquilidad y confort familiar.

Papá, Mamá, gracias. Gracias por ser mi eterno e infinito apoyo, mi refugio, mi faro, tierra firme. Gracias por haber construido un hogar maravilloso lleno de amor y respeto. Con vuestro ejemplo me habéis enseñado el valor del esfuerzo, la honestidad y la familia, siendo inspiración constante en todos los aspectos de mi vida. Gracias por mostrarme el inmenso poder de una sonrisa y por enseñarme a ser fuerte y a luchar por mis sueños para nunca ser prisionera de mis miedos. Gracias por creer siempre en mí. Vuestro respaldo y amor incondicional me han ayudado a superar cada obstáculo y a alcanzar cada meta. Este trabajo también os pertenece.



# Abstract

Fiber-reinforced polymer (FRP) composite materials are currently being selected for the design of lightweight and efficient structural members in a wide number of engineering applications. Sandwich panels with glass fiber-reinforced polymer (GFRP) face sheets and low-density cores are notably one of the most common applications of FRP materials in the civil engineering field. The load-bearing capacity of FRP structures can be significantly reduced by delamination and debonding damage which, in actual structural members, may extend all around its perimeter, thus constantly changing the size of the crack front. However, most research efforts concerning the fracture characterization of delamination and debonding damage have focused on one-dimensional (1D) fracture specimens where cracks propagate longitudinally with an approximately constant crack width, thus resulting in fracture properties that may lead to inaccurate predictions of fracture behavior in real structures. With the aim of establishing a more realistic fracture approach to delamination and debonding damage in FRP structures and thus improving their fracture characterization, the two-dimensional (2D) crack growth in GFRP laminates and GFRP/balsa sandwich panels is investigated in this research.

The 2D quasi-static delamination behavior in GFRP plates with embedded defects subjected to out-of-plane tensile loads was experimentally investigated. Increasing loads were obtained due to the disproportionate increase of the crack area throughout the propagation of the 2D crack. Analysis of the load-bearing and compliance responses indicated that a stiffening of the opened part of the plates occurred as a result of in-plane stretching stresses that developed due to the boundary conditions associated with an embedded 2D crack.

To investigate the effect of the stress stiffening and associated fracture mechanisms, the 2D delamination behavior was numerically studied. Results confirmed a 50% increase, compared to 1D fracture, in the total strain energy release rate (SERR) required to propagate the crack. This was correlated to the increase of the fiber-bridging

area as a result of the increase in the flexural stiffness (from beam to plate) and the stress-stiffening effect.

A numerically-based method, suitable for determining the mean total SERR involved in the Mode I-dominated 2D delamination of FRP laminates was further developed and validated. This method permits a reduction of experimental and computational efforts.

The 2D fracture investigation was extended to GFRP/balsa sandwich panels whose 2D debonding behavior was experimentally studied under quasi-static and fatigue out-of-plane tensile loads. Circular embedded disbonds were introduced at the face sheet/core interface. Stretching strains again developed, thereby activating shear fracture modes which, depending on the face sheet layup, triggered different crack propagation behaviors. The fatigue load-displacement hysteresis loops exhibited an increase in the cyclic stiffness due to the stiffening caused by the stretching stresses. The introduction of plies prone to develop fiber-bridging at the face sheet/core interface resulted in enhanced quasi-static debonding resistance, while under fatigue their fracture efficiency was highly dependent on the fatigue amplitude. High  $R$ -ratios improved fatigue performance due to a reduction in fiber-bridging crushing.

### **Keywords**

Two-dimensional crack propagation, delamination, debonding, fiber-bridging, strain energy release rate, finite element analysis, fatigue, laminate, sandwich panel, glass fiber-reinforced polymer.

# Résumé

Les matériaux composites à matrice polymère renforcée de fibres (FRP) sont actuellement sélectionnés pour la conception d'éléments porteurs légers et efficaces dans des structures d'ingénierie. En particulier, les panneaux sandwich avec noyaux à faible densité et peaux en polymère renforcé de fibres de verre (GFRP) sont une des plus habituelles applications des matériaux FRP dans le domaine du génie civil. La résistance des structures en FRP peut être considérablement réduite à cause de fissures entre les différentes couches d'un stratifié (délamination) ou entre le noyau et la peau d'un panneau sandwich (décollement). Dans les structures réelles, ces fissures peuvent s'étendre en toutes directions, changeant ainsi constamment la taille du front de fissuration. Cependant, la plupart des travaux de recherche concernant la caractérisation de ce type de fracture se sont concentrés sur des échantillons de fracture unidirectionnelle (1D) où les fissures se propagent longitudinalement en maintenant une largeur de fissure approximativement constante. Ainsi, les propriétés de fracture obtenues avec ces échantillons peuvent mener à une prédiction incorrecte du comportement à rupture des structures réelles. Cette recherche étudie la propagation bidimensionnelle (2D) de fissures dans des stratifiés en GFRP et des panneaux sandwichs en GFRP/balsa afin d'établir une approche plus réaliste du dommage par délamination et décollement dans les structures en FRP et ainsi obtenir une meilleure caractérisation de son comportement à la fracture.

La délamination en 2D dans des stratifiés en GFRP avec fissures internes soumises à des sollicitations de traction hors plan a été investiguée expérimentalement. Des charges croissantes ont été obtenues en raison de l'augmentation non proportionnelle de l'aire de la fissure 2D durant sa propagation. L'analyse des différentes réponses structurelles a révélé le raidissement de la partie ouverte des stratifiés dû aux tensions d'étirement développées suite aux conditions aux limites existantes.

Afin d'investiguer l'effet de ce raidissement par les tensions d'étirement ainsi que l'ensemble des mécanismes de fracture associés, une étude numérique a été effectuée.

Les résultats ont confirmé une augmentation de 50% du taux de restitution d'énergie (SERR, i.e. ténacité) requise pour la propagation de la fissure en comparaison avec les cas unidirectionnels. Ce résultat a été corrélé avec l'augmentation de la quantité de fibres qui relient les faces de la fissure — en formant un pontage de fibres à grande échelle (FB, «fiber-bridging») — laquelle a été entraînée par une augmentation globale de la rigidité à flexion et par le raidissement par les tensions d'étirement.

Une méthode numérique appropriée pour la détermination du SERR moyen impliqué dans la délamination en 2D dans des stratifiés en FRP, a été développée et validée. Cette méthode, valide pour des fissures qui se propagent sous l'action de tensions hors plan, permet de réduire considérablement les travaux expérimentaux et numériques.

Cette investigation de la fracture bidirectionnelle a été étendue aux panneaux sandwich en GFRP/balsa dont le comportement au décollement en 2D a aussi été investigué de manière expérimentale. Des fissures internes circulaires ont été placées à l'interface entre le noyau en balsa et la peau en GFRP puis des charges statiques et de fatigue ont été appliquées pour ouvrir lesdites fissures. Des tensions d'étirement se sont développés de nouveau en activant des modes de fissuration de cisaillement, lesquels, en fonction de l'architecture du stratifié choisi pour la peau, ont entraîné différents comportements de propagation de la fissure. Les boucles d'hystérésis affichées par le couple charge-déplacement ont montré une augmentation de la rigidité cyclique en raison du raidissement causé par les tensions d'étirement. L'introduction de couches menant au développement du «fiber-bridging» dans l'interface entre la peau et le noyau, a donné lieu à une amélioration de la résistance au décollement sous charges statiques. Par contre, sous charges de fatigue, son efficacité à la fracture a été trouvée fortement dépendante de l'amplitude de charge investiguée. Des rapports de charges plus élevés ont amélioré le comportement à la fatigue suite à une réduction de l'écrasement des fibres.

### **Mot clés**

Propagation de fissures en deux dimensions, délamination, décollement, fiber-bridging, taux de restitution d'énergie, éléments finis, fatigue, stratifié, panneau sandwich, polymère renforcé de fibres de verre.



# Resumen

Los materiales compuestos de polímeros reforzados con fibras (FRP) son actualmente seleccionados para la concepción y diseño de elementos portantes ligeros y eficaces en una gran variedad de estructuras de ingeniería. Particularmente, los paneles sándwich con núcleos de baja densidad y pieles de polímeros reforzados con fibra de vidrio (GFRP) constituyen una de las aplicaciones más habituales de FRP en el campo de la ingeniería civil. La resistencia de las estructuras construidas en FRP puede verse considerablemente reducida debido a la existencia y propagación de fisuras entre las diferentes capas de un laminado (delaminación) o entre el núcleo y la piel de un panel sándwich (despegue). Aunque en estructuras en servicio estas fisuras pueden expandirse en todas direcciones — variando por tanto el tamaño del frente de grieta — la mayor parte de los trabajos de investigación existentes emplean probetas de fractura unidireccional (1D) en la cuales las fisuras se propagan longitudinalmente manteniendo un ancho de grieta constante. Las propiedades de fractura obtenidas con dichas probetas pueden por tanto conllevar a una predicción errónea del comportamiento a rotura de las estructuras. Esta investigación estudia la propagación bidimensional (2D) de fisuras en laminados de GFRP y paneles sándwich de GFRP/balsa con el objetivo de establecer un enfoque más realista del daño por delaminación y despegue en estructuras de FRP y así obtener una mejor caracterización de su comportamiento a fractura.

La delaminación en 2D en laminados de GFRP con fisuras internas sometidas a sollicitaciones de tracción fuera del plano fue investigada experimentalmente. El aumento no proporcional del área de la fisura 2D durante su propagación resultó en un incremento constante de la carga de apertura aplicada. Asimismo, el análisis de las diferentes respuestas estructurales reveló una rigidización de la parte abierta de los laminados debido a tensiones de tracción en el plano que surgieron como resultado de las condiciones de contorno existentes.

El efecto de esta rigidización así como el conjunto de mecanismos de fractura asociados se analizó a través de una investigación numérica con elementos finitos. En comparación con los casos unidireccionales, los resultados confirmaron un aumento del 50% en la tasa de restitución energética (SERR, i.e. tenacidad) requerida para la propagación de la fisura. Este resultado fue correlacionado con el aumento de la cantidad de fibras que unen las caras de la fisura — formando un puente de fibras a gran escala (FB, «fiber-bridging») — que a su vez fue causado por un aumento global de la rigidez a flexión y por la rigidización debido a la aparición de las tensiones de tracción en el plano del laminado.

Un método numérico destinado a la determinación del valor medio del SERR implicado en la delaminación 2D en laminados de FRP fue desarrollado y validado. Este método, adecuado para fisuras que se propagan bajo la acción de tensiones de tracción fuera del plano (i.e. modo I de fractura), permite reducir considerablemente los esfuerzos experimentales y numéricos.

La fractura bidireccional fue también investigada en paneles sándwich de GFRP/balsa cuyo comportamiento al despegue 2D fue estudiado experimentalmente. Fisuras circulares fueron introducidas en la interfaz núcleo/piel aplicando cargas cuasi-estáticas y de fatiga para abrir dicha fisura. Al igual que en los laminados, tensiones de tracción en el plano surgieron en la parte abierta de la piel, activando modos de fractura a cortante que, en función de la arquitectura del laminado, desencadenaron diferentes modos de propagación de fisura. Los bucles de histéresis manifestados por el par carga-desplazamiento mostraron un aumento de la rigidez cíclica debido a la rigidización ocasionada por las tensiones de tracción en el plano. La introducción en la interfaz núcleo/piel de laminas propensas a desarrollar «fiber-bridging» contribuyó a una mejora de la resistencia al despegue bajo cargas cuasi-estáticas. Por el contrario, bajo cargas de fatiga, su eficiencia dependió en gran medida de la amplitud de carga investigada. Razones de carga más elevadas mejoraron el comportamiento a fatiga debido a una reducción del grado de aplastamiento de las fibras.

### **Palabras clave**

Propagación de fisura en dos dimensiones, delaminación, despegue, fiber-bridging, tenacidad, elementos finitos, fatiga, laminado, panel sándwich, polímero reforzado con fibra de vidrio.

# Table of Contents

<b>Preface</b>	<b>v</b>
<b>Acknowledgements</b>	<b>vii</b>
<b>Agradecimientos</b>	<b>xi</b>
<b>Abstract</b>	<b>xv</b>
<b>Résumé</b>	<b>xvii</b>
<b>Resumen</b>	<b>xix</b>
<b>Table of contents</b>	<b>xxi</b>
<b>List of Figures</b>	<b>xxv</b>
<b>List of Tables</b>	<b>xxxix</b>
 <b>Chapter 1   Introduction</b>	 <b>1</b>
1.1 Context and motivation	1
1.2 Objectives	4
1.3 Methodology	4
1.4 Thesis organization	5
References	7
 <b>Chapter 2   Two-dimensional delamination. <i>Experimental investigation</i></b>	 <b>13</b>
2.1 Introduction	13
2.2 Experimental investigation	15
2.2.1 Material description	15
2.2.2 Specimen description and elastic properties	17
2.2.3 Experimental set-up, instrumentation and measurements	20
2.3 Experimental results	23
2.3.1 Load-displacement responses and crack propagation measurements	23
2.3.2 Crack propagation patterns	28

2.3.3	Compliance behavior	31
2.4	Discussion	32
2.4.1	Increasing load behavior	32
2.4.2	Stiffness-related mechanisms	33
2.5	Conclusions	36
	References	37
<b>Chapter 3</b>	<b>Two-dimensional delamination. <i>Numerical investigation</i></b>	<b>41</b>
3.1	Introduction	41
3.2	Experimental methods	44
3.2.1	Previous experimental investigation of laminated plates	44
3.2.2	Experimental investigation of Mode I DCB specimens	46
3.3	Numerical methods	48
3.3.1	Description of numerical model of laminated plates	48
3.3.2	Description of numerical model of DCB specimens	49
3.3.3	Cohesive zone modeling	50
3.4	Experimental results and discussion	51
3.4.1	Experimental results for laminated plates	51
3.4.2	Experimental results for DCB specimens	54
3.5	Numerical results and discussion	55
3.5.1	DCB specimens	55
3.5.2	Laminated plates	56
3.5.3	Influence of shape of traction-separation law	60
3.6	Conclusions	61
	References	62
<b>Chapter 4</b>	<b>Two-dimensional fracture characterization. <i>A numerically-based method</i></b>	<b>67</b>
4.1	Introduction	67
4.2	Experimental investigation of laminated plates: results and discussion	69
4.2.1	Previous results and discussion	69
4.2.2	Effects of stiffness variations on fiber-bridging development	71
4.3	Previous numerical results of CFM plates	72
4.4	New total SERR derivation method	73
4.5	Validation of the method and discussion	76
4.5.1	CFM laminates	76
4.5.2	W50.50 laminates	77
4.5.3	W60.40 laminates	81
4.6	Conclusions	83
	References	84
<b>Chapter 5</b>	<b>Two-dimensional debonding. <i>Quasi-static experimental investigation</i></b>	<b>89</b>
5.1	Introduction	89
5.2	Experimental program	91
5.2.1	Material description	91
5.2.2	Specimen description and fabrication	92
5.2.3	Experimental set-up and instrumentation	94
5.3	Experimental results	96
5.3.1	Load and crack-opening displacement responses	96
5.3.2	Compliance behavior	97

5.3.3	Crack propagation behavior	98
5.3.4	Radial and circumferential strain distribution	99
5.4	Discussion	100
5.4.1	Load and crack-opening displacement responses	100
5.4.2	Compliance behavior	101
5.4.3	Analysis of strain profiles	102
5.4.4	Stretching-induced shear fracture modes	106
5.5	Conclusions	107
	References	108
<b>Chapter 6</b>	<b>Two-dimensional debonding. <i>Fatigue experimental investigation</i></b>	<b>113</b>
6.1	Introduction	113
6.2	Experimental program	115
6.2.1	Material description	115
6.2.2	Specimen description	116
6.2.3	Experimental set-up, loading and instrumentation	116
6.3	Experimental results	120
6.3.1	Crack growth and displacement responses in SPA panels	120
6.3.2	Crack growth and displacement responses in SPB panels	121
6.3.3	Crack area growth rate	123
6.3.4	Load-displacement hysteresis loops and stiffness degradation	124
6.3.5	Radial and circumferential strain distribution	125
6.3.6	Evolution of face sheet surface temperature	126
6.4	Discussion	128
6.4.1	Load vs displacement control in 1D and 2D fatigue experiments	128
6.4.2	Effect of local damage in loading region	129
6.4.3	<i>R</i> -ratio effects	130
6.4.4	Load-displacement hysteresis loops and stretching stiffening effect	131
6.4.5	Derivation and evolution of in-plane stretching strains	133
6.4.6	Location and evolution of inflection points	134
6.5	Conclusions	135
	References	136
<b>Chapter 7</b>	<b>Conclusions and future work</b>	<b>143</b>
7.1	Conclusions	143
7.1.1	Two-dimensional effects on delamination and debonding fracture behavior	143
7.1.2	Influence of 2D effects on fiber-bridging development	145
7.1.3	Fiber architecture effects	145
7.1.4	Numerically-based method for 2D delamination fracture characterization	146
7.2	Original contributions	147
7.3	Recommendations for future work	148
7.3.1	Quasi-static 2D crack growth under shear-dominated fracture modes	148
7.3.2	Further validation of developed numerically-based method	148
7.3.3	Numerical investigation of 2D delamination considering local variation of total SERR	149
7.3.4	Numerical investigation of quasi-static and fatigue 2D debonding in GFRP/balsa sandwich panels	149
7.3.5	Investigation of fatigue 2D debonding under displacement control	150

7.3.6 Investigation of fatigue 2D debonding in sandwich panels with pure woven face sheet configuration under different $R$ -ratios	150
7.3.7 Establishment of fracture energy correction factors to include 2D effects	150
References	151
<b>Appendix A   Vacuum infusion procedure for GFRP laminated plates</b>	<b>155</b>
<b>Appendix B   GFRP laminated plate experiments</b>	<b>161</b>
<b>Appendix C   Effect of stiffness variation on fiber-bridging development</b>	<b>171</b>
<b>Appendix D   Vacuum infusion procedure for GFRP/balsa sandwich panels</b>	<b>179</b>
<b>Appendix E   Quasi-static sandwich experiments</b>	<b>185</b>
<b>Appendix F   Fatigue sandwich experiments</b>	<b>191</b>
<b>Curriculum Vitae</b>	<b>203</b>

# List of Figures

## Chapter 1 | Introduction

Figure 1.1	Haramain High Speed Railway (HHR) Jeddah Station: GFRP-foam sandwich roof, Saudi Arabia 2014; (a) lifting of one the 42 independently-manufactured modules; (b) general view after construction finalization [6]	2
Figure 1.2	(a) Novartis Campus Entrance Building: GFRP-PUR sandwich roof, Switzerland, 2006 [7]; (b) CSCOR-Paris: GFRP-foam sandwich domes, France, 2015 [6]	2
Figure 1.3	(a) Avançon bridge: road bridge with GFRP-balsa sandwich deck, Switzerland, 2012 [14]; (b) Clavières bridge: pedestrian bridge with GFRP-balsa sandwich deck, Switzerland, 2013 [15]	3
Figure 1.4	(a) Full scale four-point bending experiment on beam with variable depth [7]; (b) Twin-shaped composite beam (TSCB): pedestrian bridge with CFRP-PET sandwich structure [20]	3

## Chapter 2 | Two-dimensional delamination. *Experimental investigation*

Figure 2.1	Detail of glass fiber reinforcements	16
Figure 2.2	GFRP plate configuration; dimensions in mm	19
Figure 2.3	Assembling of loading system; (a) general view; (b) A'A section (unloaded/closed) view; (c) detailed description of assembling sequence; (d) A'A section (loaded/open). Dimensions in mm	20
Figure 2.4	(a) Experimental set-up and (b) instrumentation layout	21
Figure 2.5	Layout of crack measuring system. N, S, E and W are orthogonal directions and NE, SE, NW and SW diagonal directions	21
Figure 2.6	DIC measurements of plate W50.50.1; (a) area and path of interest (example image); (b) evolution of out-of-plane deformed profiles and location of crack tip	22

Figure 2.7	Load and crack lengths vs opening displacement curves; (a) W50.50.1; (b) W50.50.2	23
Figure 2.8	Load and crack lengths vs opening displacement curves; (a) W60.40.1; (b) W60.40.2	24
Figure 2.9	Load and crack lengths vs opening displacement curves; (a) W70.30.1; (b) W70.30.2	24
Figure 2.10	Load and crack lengths vs opening displacement curves; (a) CFM.1; (b) CFM.2	24
Figure 2.11	Load and crack lengths vs opening displacement curves; (a) MD pair; (b) W80.20 pair	25
Figure 2.12	Example of deformation in plate W50.50.1 at (a) limit of symmetric propagation and (b) beyond limit	25
Figure 2.13	Displacement of LVDTs at corners of plate W50.50.1 vs load	27
Figure 2.14	Crack propagation pattern for W50.50 pair (limit of symmetric propagation marked in blue)	28
Figure 2.15	Crack propagation pattern for W60.40 pair (limit of symmetric propagation marked in blue)	29
Figure 2.16	Crack propagation pattern for W70.30 pair	29
Figure 2.17	Crack propagation pattern for W80.20 pair	30
Figure 2.18	Crack propagation pattern for CFM pair	30
Figure 2.19	Crack propagation pattern for MD pair	31
Figure 2.20	Progressive back-calculated propagation perimeters for (a) W50.50.1, (b) W60.40.1 and (c) CFM.1	31
Figure 2.21	Compliance vs crack area for (a) W50.50 pair and (b) W60.40 pair	32
Figure 2.22	Compliance vs crack area for (a) W70.30 pair and (b) CFM pair	32
Figure 2.23	Identification of stiffening and softening regions on: (a) compliance vs crack area of W50.50.1; (b) load-displacement curves of plates W50.50.1 and W50.50.2	33
Figure 2.24	Identification of stiffening and softening regions on load-displacement curves of (a) W60.40 pair and (b) CFM pair	34
Figure 2.25	FE model stress results for plate W50.50.1; (a) total radial stresses; (b) total circumferential stresses (MPa)	35
Figure 2.26	Load vs stretching stresses obtained at measured section (Figure 2.25) from FE model	35

### Chapter 3 | Two-dimensional delamination. Numerical investigation

Figure 3.1	Detail of glass fiber reinforcement (a) and crack propagation pattern in plate CFM.1 (b). Units in mm	43
Figure 3.2	Experimental set-up; (a) experiment on CFM.2 AND crack measuring system layout; (b) layout of set-up	44



Figure 3.3	DCB configurations; (a) in-house developed loading blocks (piano hinges); (b) patented [37] loading blocks; dimensions see Table 3.4.	45
Figure 3.4	DCB experimental set-up; (a) general view; (b) example of image from upper camera (Camera 1 in (a)); (c) DCB specimen with drawn grid ruler used for measurement of crack length; (d) example of image from side camera (Camera 2 in (a))	47
Figure 3.5	Description of finite element model of laminated plate	48
Figure 3.6	Schematic general fracture section of Mode I delamination with fiber-bridging	49
Figure 3.7	Description of traction-separation law	50
Figure 3.8	Load and crack length vs opening displacement curves of CFM plates	52
Figure 3.9	Comparison of growth of crack area in plate and equivalent DCB	53
Figure 3.10	Comparison of experimental and numerical crack area vs compliance of CFM plates	53
Figure 3.11	Comparison of experimental and numerical load-displacement curves of DCBs	54
Figure 3.12	Fiber-bridging zone; (a) DCB-25-2; (b) DCB-60-2	54
Figure 3.13	Experimental R-curves obtained from DCB specimens	55
Figure 3.14	Traction-separation curves used in numerical models	56
Figure 3.15	Comparison of experimental and numerical load-displacement curves of CFM plates using cohesive parameters and total SERR from DCBs	57
Figure 3.16	Comparison of experimental and numerical load and crack lengths vs opening displacement curves of CFM plates	57
Figure 3.17	Numerical R-curve of laminated plate	58
Figure 3.18	Description of general behavior of crack area vs compliance curves	59
Figure 3.19	Comparison of experimental and numerical curves of DCB-25 (1-2) and DCB-25-3 (cut from plate CFM.1)	60
Figure 3.20	Influence of shape of cohesive law in DCB-100-2: with and without bridging law	60
Figure 3.21	(a) Influence of shape of cohesive law in plates: with and without bridging law; (b) zoom of region indicated in (a)	61

#### **Chapter 4 | Two-dimensional fracture characterization. A numerically-based method**

Figure 4.1	Experimental set-up and crack measuring system	69
Figure 4.2	Crack propagation patterns in plates (a) CFM.1, (b) W50.50.1 and (c) W60.40.2. Dimensions in mm	70

Figure 4.3	Experimental and numerical load vs opening displacement curves of CFM plates and slopes in Region B	71
Figure 4.4	(a) Experimental load vs opening displacement curves of W50.50 plates; (b) extraction of experimental slopes	71
Figure 4.5	(a) Experimental load vs opening displacement curves of W60.40 plates; (b) extraction of experimental slopes	72
Figure 4.6	Explanatory layout of radial and circumferential fiber-bridging development (not to scale)	72
Figure 4.7	Traction-separation curves used in numerical models; (a) with softening including bridging law used for CFM; (b) with linear softening used for total SERR derivation in proposed method ( $G_{tot}$ for CFM and $\bar{G}_{tot}$ for woven plates)	73
Figure 4.8	Numerical load vs opening displacement curves obtained using different values of $G_{tot}$ and a linear softening cohesive law (see Figure 4.9(b)) compared to experimental curves	74
Figure 4.9	Numerical $\alpha$ vs $G_{tot}$ curve obtained for CFM laminates	74
Figure 4.10	General description of linear traction-separation laws varying along crack front	76
Figure 4.11	Description of finite element model of W50.50 laminated plate. Dimensions in mm	77
Figure 4.12	Numerical load vs opening displacement curves obtained for W50.50 laminates using different values of $\bar{G}_{tot}$ and a linear softening cohesive law (see Figure 4.9(b)) compared to experimental curves	78
Figure 4.13	Numerical $\alpha$ vs $\bar{G}_{tot}$ curve obtained for W50.50 laminates	79
Figure 4.14	(a) Experimental load-displacement curves and (b) R-curves of W50.50 DCB specimens	80
Figure 4.15	Example of out-of-plane displacement profile at cracked region in W50.50 plates. Dimensions in mm	81
Figure 4.16	Description of finite element model of W60.40 laminated plate. Dimensions in mm	82
Figure 4.17	Numerical load vs opening displacement curves obtained for W60.40 laminates using different values of $\bar{G}_{tot}$ and a linear softening cohesive law (see Figure 4.9(b)) compared to experimental curves	82
Figure 4.18	Numerical $\alpha$ vs $\bar{G}_{tot}$ curve obtained for W60.40 laminates	83

## Chapter 5 | Two-dimensional debonding. *Quasi-static experimental investigation*

Figure 5.1	Detail of glass fiber reinforcements used	92
Figure 5.2	Sandwich panel layout; (a) Top view and (b) Side view of section AA' in (a). Dimensions in mm	92

Figure 5.3	Fabrication sequence	93
Figure 5.4	Experimental set-up	95
Figure 5.5	Crack monitoring schema (common to all panels) and crack propagation pattern of sandwich panel SPA.1	95
Figure 5.6	Load and total radial crack length vs opening displacement curves	96
Figure 5.7	Detail of loading region in SPA.1 after 75 mm of radial propagation (i.e. 105 mm of total radial crack length)	97
Figure 5.8	Compliance vs crack area curves	97
Figure 5.9	Crack interfaces of (a) sandwich panel SPA.2 and (b) sandwich panel SPB.2	99
Figure 5.10	Face sheet top surface in-plane strain distributions extracted from DIC; (a) in radial direction and (b) in circumferential direction for SPA.2	99
Figure 5.11	Results obtained from face sheet top surface of panel SPA.2 at total radial crack length of 88 mm; (a) out-of-plane DIC radial deflection profiles; (b) radial strain profiles extracted and derived from DIC experimental results	101
Figure 5.12	Qualitative sketch of effect of stretching and fiber-bridging traction on radial strain profile of face sheet (not to scale)	103
Figure 5.13	Comparison of calculated radial stretching strains of SPA.2 at total radial crack lengths of 80, 88 and 105 mm; values at 60% of total crack length	105
Figure 5.14	Comparison of calculated radial stretching strains of SPB.2 at total radial crack lengths of 65, 70 and 75 mm; values at 70% of total crack length	105
Figure 5.15	Evolution of inflection point with crack propagation for (a) SPA.2 and (b) SPB.2	106

## Chapter 6 | Two-dimensional debonding. *Fatigue experimental investigation*

Figure 6.1	Sandwich panel layout; (a) Top view and (b) Side view of section AA' in (a). Dimensions in mm	115
Figure 6.2	Experimental set-up	117
Figure 6.3	Crack monitoring schema (common to all panels) and circular crack propagation pattern of sandwich panels SPA.1F	118
Figure 6.4	Total radial crack length vs number of cycle curves of SPA configuration panels	121
Figure 6.5	Displacement increment vs number of cycle of SPA configuration panels	121
Figure 6.6	Total radial crack length vs number of cycle curves of SBP configuration panels	122

Figure 6.7	Displacement increment vs number of cycle of SPB configuration panels	122
Figure 6.8	Crack area growth rate vs total crack area	123
Figure 6.9	Load-displacement hysteresis loops of SPA.1F panel	124
Figure 6.10	Hysteresis area per cycle vs normalized number of cycles of SPA panels	125
Figure 6.11	Global stiffness vs number of cycles	125
Figure 6.12	Crack area growth rate vs global stiffness	126
Figure 6.13	Global stiffness vs total crack area	126
Figure 6.14	Face sheet top surface in-plane strain distributions extracted from DIC; (a) in radial directions and (b) in circumferential direction for SPA.1F	127
Figure 6.15	Surface temperature before last fatigue cycles in four of performed experiments	127
Figure 6.16	Schematic comparison between load and displacement control in (a) 1D and (b) 2D fatigue fracture experiments	128
Figure 6.17	(a) Load-displacement hysteresis loops and (b) loading part compliances vs load curves at 0.6 million cycles and 3 million cycles; results for SPA.1F panel	131
Figure 6.18	Results obtained from face sheet top surface of panel SPA.1F at maximum deformation state at cycle 0.5M; (a) out of plane radial deflection profile; (b) radial strain profiles; all data derived from DIC	132
Figure 6.19	Comparison of calculated radial stretching strains in fatigue SPA.1F and static SPA.2 [37] panels	133
Figure 6.20	Evolution of inflection point with crack propagation in fatigue SPA.1F and static SPA.2 [37] panels	134

# List of Tables

## Chapter 1 | Introduction

Table 1.1	Thesis core chapter organization	6
-----------	----------------------------------	---

## Chapter 2 | Two-dimensional delamination. *Experimental investigation*

Table 2.1	Material properties	16
Table 2.2	Description of GFRP plates	16
Table 2.3	Elastic properties of GFRP plates	18
Table 2.4	Load and displacement values for initiation and maximums	26

## Chapter 3 | Two-dimensional delamination. *Numerical investigation*

Table 3.1	Material properties	45
Table 3.2	Description of GFRP laminated plates	45
Table 3.3	Elastic properties of laminated plates	46
Table 3.4	Geometrical and elastic properties of fracture mechanics (DCB) specimens	46

## Chapter 4 | Two-dimensional fracture characterization. *A numerically-based method*

Table 4.1	Material properties	70
Table 4.2	Description of GFRP laminated plates	70
Table 4.3	Elastic properties of laminated plates used in FE models	77

## Chapter 5 | Two-dimensional debonding. *Quasi-static experimental investigation*

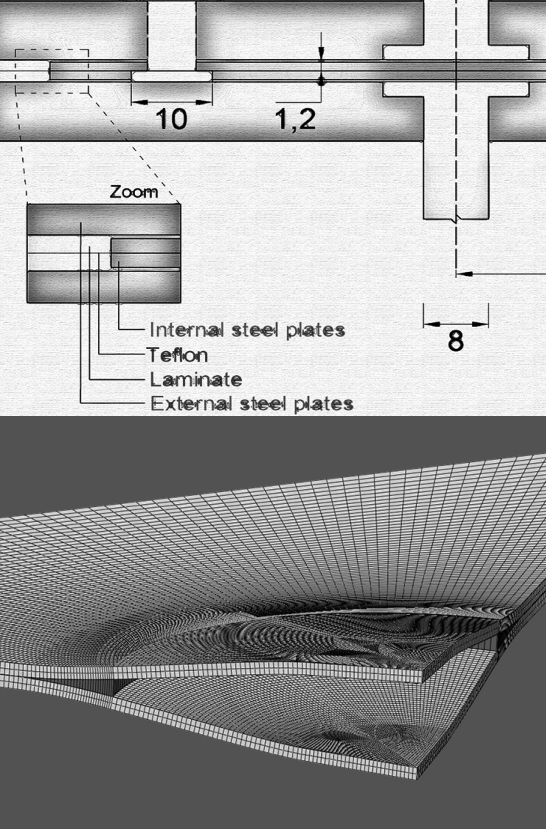
Table 5.1	Material properties	92
Table 5.2	Description of GFRP/balsa sandwich panels	93

Table 5.3	Load-displacement values at initiation, maximum loads and minimum compliances	98
-----------	---	----

**Chapter 6 | Two-dimensional debonding. *Fatigue experimental investigation***

Table 6.1	Material properties	115
Table 6.2	Description of GFRP/balsa sandwich panels	116
Table 6.3	Summary of fatigue experiments and results	118
Table 6.4	Description and values of ULS material safety factor coefficients	119

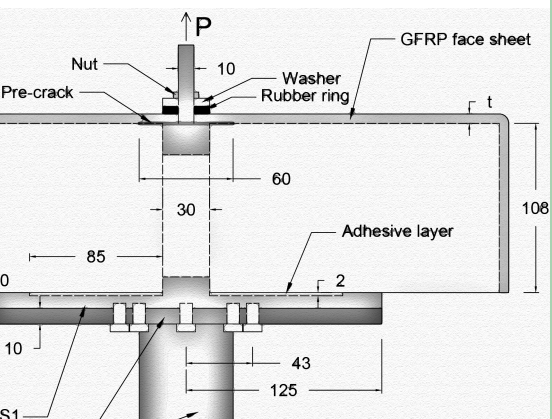




**Step 2:** performance of FE analyses using the same separation law in all directions. Different values of  $\alpha$  are used. At least three FE analyses with three different values of  $\alpha$ .

**Step 3:** extraction of the numerical load-displacement curves (i.e. for each analysis) and calculation of the critical load  $P_{crit}$  from the last linear part of the curves.

**Step 4:** with the obtained  $\alpha - \bar{G}_{I,II}$  results, determine the best fitting (a linear equation in the cases presented).





# Chapter 1

## Introduction

### 1.1 Context and motivation

Civil engineering projects relating to bridge and building structures increasingly necessitate construction methods capable of reducing construction times and thus provide rapid project delivery. Swift on-site installation is especially relevant in replacement and rehabilitation projects where minimum interference with user routine is desired. Consequently, prefabricated solutions are being increasingly adopted, also assuring an exhaustive safety and quality control difficult to attain using traditional on-site construction methods.

Due to the significant expense and severe traffic disruptions that intensive bridge maintenance interventions entail, new bridge designs targeting reduced maintenance costs and the assurance of structural durability are currently being developed by the bridge engineering community. Deck deterioration due to wear, de-icing salts, temperature gradients and freeze-thaw cycles, concrete ageing and deterioration and corrosion of steel members and steel reinforcement of concrete are listed among the most common deficiencies typically identified in the existing bridge inventory [1]. These deficiencies are in fact not restricted to bridges but are endemic to all built structures such as buildings, industrial structures or pipelines. Hence, advanced materials offering improved resistance to environmental actions are increasingly required.

New civil engineering projects, particularly in building construction, often involve geometrically complex shapes that require complex structural solutions for which conventional construction materials and building techniques are not adapted. This constitutes a further new challenge for the engineering community worldwide.



Figure 1.1 – Haramain High Speed Railway (HHR) Jeddah Station: GFRP-foam sandwich roof, Saudi Arabia 2014; (a) lifting of one of the 42 independently-manufactured modules; (b) general view after construction finalization [6]



Figure 1.2 – (a) Novartis Campus Entrance Building: GFRP-PUR sandwich roof, Switzerland, 2006 [7]; (b) CSCOR-Paris: GFRP-foam sandwich domes, France, 2015 [6]

Fiber-reinforced polymer (FRP) composite materials have proved to be a competitive construction solution as they offer advantageous properties for bridge and building applications such as high strength- and stiffness-to-weight ratios, good resistance against fatigue and environmental actions, rapid installation and geometrical versatility [2,3]. Lightweight FRP structural elements, able to adopt complex shapes and resistant to environmental actions, can be prefabricated and then easily transported and installed on the construction site [3-5], thus providing an effective solution to all the previously described current challenges.

Composite sandwich structural elements, typically composed of laminated glass fiber-reinforced polymer (GFRP) face sheets and foam cores, are currently used in building construction, particularly roof structures (see Figures 1.1 and 1.2) [6, 7]. In cases where the shear resistance and stiffness of the foam core is insufficient, reinforcing GFRP webs must be added to the core [7,8].

Regarding bridge construction, commercial GFRP decks consisting of adhesively-bonded pultruded profiles (e.g. DuraSpan or Asset [9]) have been increasingly used both to replace existing reinforced-concrete decks and in new constructions [10-12]. Due to the span limitations of pultruded GFRP decks [2], composite sandwich bridge deck solutions, which offer great thickness flexibility, have been used for larger spans [4, 13-15]. For bridge application, where a uniform support for the upper face sheet in contact with wheel loads is required, balsa cores (which also provide sufficient shear capacity) are particularly advantageous (see examples of GFRP/balsa decks in Figure 1.3)[4, 13, 14].



Figure 1.3 – (a) Avançon bridge: road bridge with GFRP-balsa sandwich deck, Switzerland, 2012 [14]; (b) Clavières bridge: pedestrian bridge with GFRP-balsa sandwich deck, Switzerland, 2013 [15]

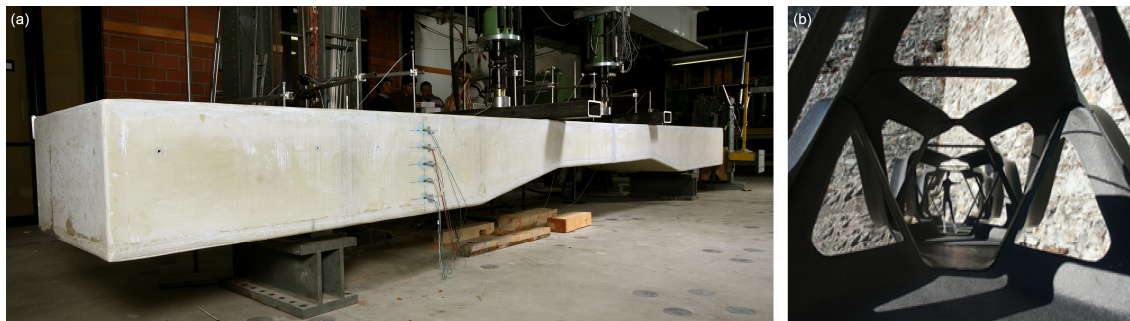


Figure 1.4 – (a) Full scale four-point bending experiment on beam with variable depth [7]; (b) Twin-shaped composite beam (TSCB): pedestrian bridge with CFRP-PET sandwich structure [20]

The load-bearing capacity and thus structural integrity of FRP structural members can be significantly limited by delamination and debonding damage which is usually triggered by interlaminar defects in laminated elements or disbonds at the face sheet/core interface in sandwich panels [16-18] that may arise either during manufacturing or due to impacts during the service life of the structure. These types of cracks (i.e. interlaminar defects and disbonds) may grow under out-of-plane tensile stresses (i.e. Mode I fracture) and in-plane shear stresses (Mode II and III fracture) [16]. Although crack propagation typically occurs under a combination of the three fracture modes, Mode I-dominated scenarios are also common in civil engineering structures. For instance, the existence of disbonds in structural composite sandwich elements under pure compression or bending may induce premature face sheet wrinkling [19] causing the disbonds to open and thus propagate primarily under Mode I. Likewise, geometrical changes in the structure (see Figure 1.4(a), [7]) or curved geometries (see Figure 1.4(b), [20]) can also lead to significant out-of-plane tensile stresses and thus Mode I-dominated delamination and debonding scenarios [21]. Mode I-dominated debonding in sandwich panels in particular is considered the most critical phenomenon as the face sheet is separated from the core [18, 22].

Extensive research has been conducted on the quasi-static and fatigue characterization of the delamination and debonding behavior of composite materials [22-28], focusing on one-dimensional (1D) fracture specimens where the crack propagates with an approximately constant crack width in the longitudinal direction of the specimens. Nevertheless, these particular fracture conditions are not likely to be

found in actual structural members, where delamination and debonding damage may span all around the perimeter, constantly modifying the size of the crack front. Thus, more realistic fracture approaches, providing new insight regarding the transition from small-scale 1D delamination experiments to real delamination and debonding scenarios, are required.

## 1.2 Objectives

The aim of this research is to investigate the two-dimensional (2D) crack growth under out-of-plane tensile loads in GFRP laminates and GFRP/balsa sandwich panels and thus provide a more realistic approach to delamination and debonding damage in actual FRP structural members. The following objectives were therefore defined:

1. Experimental investigation of the 2D quasi-static delamination behavior in FRP laminates presenting embedded defects subjected to out-of-plane tensile loads, evaluation of fiber architecture effects on the fracture process and identification of potential behavioral differences compared to 1D delamination (i.e. 2D effects).
2. Numerical simulation of one of the experimentally studied 2D delamination cases to investigate the influence of 2D effects in the delamination fracture process.
3. Two-dimensional fracture characterization through the establishment of a simple method suitable for determining the total strain energy release rate (SERR) value involved in 2D in-plane delamination cases where an opening fracture mode (i.e. Mode I) is dominant.
4. Investigation of 2D quasi-static debonding behavior in FRP sandwich composites presenting embedded disbonds subjected to out-of-plane tensile loads, evaluation of the benefits of including plies prone to develop fiber-bridging at the face sheet/core interface and identification of 2D effects.
5. Investigation of 2D fatigue debonding behavior in FRP sandwich composites presenting embedded disbonds subjected to out-of-plane tensile loads and identification of 2D and  $R$ -ratio effects.

## 1.3 Methodology

The methodology adopted to attain the objectives of this research is as follows:

- 1.a Development of a new experimental set-up and procedure suitable for investigating the propagation of 2D internal defects under out-of-plane tensile loads in FRP laminated plates.
- 1.b Experimental investigation of 2D delamination behavior of six configurations of GFRP/epoxy laminated plates with circular embedded pre-cracks subjected to out-of-plane quasi-static loads.
- 2.a Numerical modeling of the 2D delamination behavior in order to characterize the fracture properties, focusing on one of the investigated plate configurations.

- 2.b Experimental investigation of 1D double cantilever beam (DCB) specimens with the same layup configuration as the laminated plates investigated in 2.a.
- 3.a Development of a numerically-based method to determine the 2D SERR involved in delamination cases where defects propagate under Mode I-dominated conditions.
- 3.b Numerical simulations of three laminated plate configurations to validate the developed method.
- 4.a Establishment of a new experimental set-up and procedure suitable for investigating the propagation of 2D disbonds under out-of-plane tensile loads in FRP sandwich panels.
- 4.b Experimental investigation of the quasi-static 2D debonding behavior of two configurations of GFRP/balsa sandwich panels with circular embedded pre-cracks at the face sheet/core interface subjected to out-of-plane loads.
5. Experimental investigation of fatigue 2D debonding behavior using a similar experimental set-up and sandwich panel configurations as in the quasi-static investigation (Objective 4, Methodologies 4.a,b).

## 1.4 Thesis organization

The research work presented in this thesis is divided into five core chapters, which address the five objectives introduced in Section 1.2, and an additional chapter summarizing the conclusions of the research and future prospects. The general organization of the core chapters of the thesis is shown in Table 1.1.

A summary of the main content of each chapter is presented in the following:

- Chapter 2: The 2D delamination fracture behavior of GFRP composite laminates presenting embedded defects subjected to quasi-static out-of-plane tensile loads is experimentally investigated. A total of six different types of fiber architecture are examined and circular pre-cracks are introduced in the center and at the midplane of the laminates. The obtained load-bearing and compliance responses are analyzed and the differences between 1D and 2D delamination are discussed.
- Chapter 3: The numerical investigation of the 2D in-plane crack propagation in laminated plates with circular embedded pre-cracks is carried out to simulate the 2D delamination behavior of one of the laminated plate configurations experimentally studied in Chapter 2. Additionally, double cantilever beam (DCB) 1D fracture experiments are performed and their delamination behavior is numerically simulated. Three-dimensional finite element (FE) models are developed for the investigation using cohesive elements to simulate the fracture interface. The 1D and 2D fracture properties are compared, providing a thorough analysis of the 2D effects and their influence in the 2D fracture process.
- Chapter 4: A new numerically-based method suitable for determining the total SERR involved in 2D Mode I-dominated delamination in FRP laminates under

&gt; Table 1.1 – Thesis core chapter organization

Investigated 2D fracture	Loading conditions	Methodology	Main chapters	Appendices	Papers
<b>Delamination of GFRP laminated plates</b>	Quasi-static	- Development of experimental set-up and procedure - Experimental investigation	Chapter 2	A, B	1
		- Numerical investigation focusing on one type of laminated plates - Experimental investigation of DCB specimens	Chapter 3	A, B, C	2
		- Development of a numerically- based method for total 2D SERR determination - Numerical simulations	Chapter 4	C	3
<b>Debonding of GFRP/balsa sandwich panels</b>	Quasi-static	- Development of experimental set-up and procedure - Experimental investigation	Chapter 5	D, E	4
	Fatigue	- Experimental investigation	Chapter 6	D, F	5

opening loads is proposed. The method is developed based on findings reported in Chapter 3. The experimental results obtained from three types of the GFRP/epoxy laminated plates investigated in Chapter 2 are used to validate the method.

- Chapter 5: The 2D quasi-static debonding behavior of GFRP/balsa sandwich panels with embedded circular disbonds at the face sheet/core interface subjected to out-of-plane tensile loads is experimentally investigated. Two different face sheet configurations are studied and their load-bearing and fracture performance is compared. The crack paths are analyzed by means of post-mortem cuts and correlated with the in-plane strains measured on the face sheets.
- Chapter 6: The 2D fatigue debonding behavior of GFRP/balsa sandwich panels with embedded circular disbonds at the face sheet/core interface subjected to out-of-plane loads is experimentally investigated. The same configurations as in the quasi-static investigation presented in Chapter 5 is used and their fatigue fracture performance is compared. The fatigue crack growth rate behavior is discussed and compared to that typically observed in 1D fracture experiments. The shape of the load-displacement loops and causes of the recorded hysteresis are discussed. The global stiffness degradation, also shown by the load-displacement loops, is also discussed. Furthermore, the influence of the  $R$ -ratio on the developing fiber-bridging is analyzed and the in-plane stretching strains are quantified.

- Chapter 7: The main conclusions of the conducted research are presented and suggestions for future research are formulated.

Supplementary information concerning the main chapters of the thesis is provided in six appendices (see Table 1.1):

- Appendix A: Vacuum infusion procedure for GFRP laminated plates.
- Appendix B: GFRP laminated plate experiments.
- Appendix C: Effect of stiffness variation on fiber-bridging development.
- Appendix D: Vacuum infusion procedure for GFRP/balsa sandwich panels.
- Appendix E: Quasi-static debonding experiments.
- Appendix F: Fatigue debonding experiments.

The results of this thesis have been published in five journal papers. The five papers are listed below and correspond to the five main chapters of the thesis (see Table 1.1):

1. Cameselle-Molares A, Vassilopoulos A.P, Keller T. Experimental investigation of two-dimensional delamination in GFRP laminates. *Eng Fract Mech* 2018; 203; 152-171.
2. Cameselle-Molares A, Renart J, Turon A, Vassilopoulos A.P, Keller T. Numerical simulation of two-dimensional in-plane crack propagation in FRP laminates. *Compos Struct* 2018; 200; 396-407.
3. Cameselle-Molares A, Renart J, Turon A, Vassilopoulos A.P, Keller T. Numerically-based method for fracture characterization of Mode I-dominated two-dimensional delamination in FRP laminates. *Compos Struct* 2019; 214; 143-152.
4. Cameselle-Molares A, Vassilopoulos A.P, Keller T. Two-dimensional quasi-static debonding in GFRP/balsa sandwich panels. *Compos Struct* 2019; 215; 391-401.
5. Cameselle-Molares A, Vassilopoulos A.P, Keller T. Two-dimensional fatigue debonding in GFRP/balsa sandwich panels. *Int J Fatigue* 2019; 125; 72-84..

## References

1. Karbhari, V.M., Zhao, L. Use of composites for 21st century civil infrastructure. *Comput. Methods Appl. Mech. Eng.*, 2000; 185(2-4): 433-454.
2. Keller, T. Recent all-composite and hybrid fiber-reinforced polymer bridges and buildings. *Prog. Struct. Eng. Mater.*, 2001; 3(2): 132-140.
3. Uddin, N. *Developments in Fiber-Reinforced Polymer (FRP) Composites for Civil Engineering*. First edition, Woodhead Publishing; 2013.
4. Keller, T., Rothe, J., De Castro, J., Osei-Antwi, M. GFRP-Balsa Sandwich Bridge Deck: Concept, Design and Experimental validation. *J. Compos. Constr.*, 2013; 18(2): 0413043.
5. Lee, S.W., Hong, K.J., Park, S. Current and future applications of glass-fiber-reinforced polymer decks in Korea. *Struct. Eng. Int.*, 2010; 20(4): 405-408.
6. Durand, S. Technical specificities when designing with composite materials – case of building and architecture. In: Ferrier, E., Benzarti, K., Caron, J-F. (eds) *Proceedings of the 9<sup>th</sup> International*



*Conference on Fiber-Reinforced Polymer (FRP) Composites in Civil Engineering, CICE*, 17-19 July 2018, Paris, France.

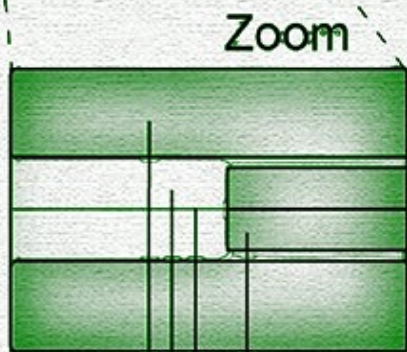
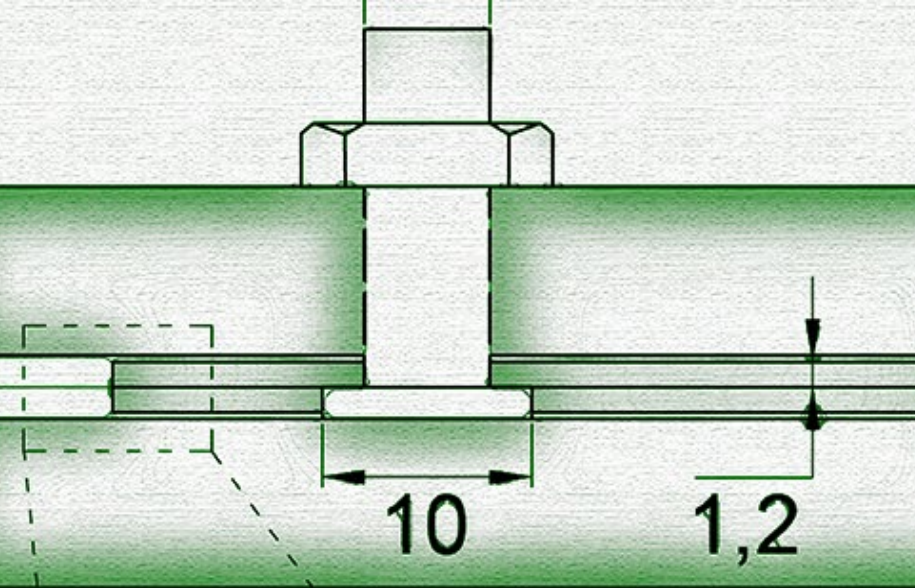
7. Keller, T., Haas, C., Vallée, T. Structural concept, design and experimental verification of a glass fiber-reinforced polymer sandwich roof structure. *J. Compos. Constr.*, 2008; 12(4): 454-468.
8. Correia, J.R., Garrido, M., Gonilha, J.A., Branco, F.A., Reis, L.G. GFRP sandwich panels with PU foam and PP honeycomb cores for civil engineering structural applications: Effects of introducing strengthening ribs. *Int. J. Struct. Integrity*, 2012; 3(2): 127-147.
9. Yanes-Armas, S., de Castro, J., Keller, T. System transverse in-plane shear stiffness of pultruded GFRP bridge decks. *Eng. Struct.*, 2016; 107: 34-46.
10. Keller, T. *Use of fibre reinforced polymers in bridge construction*. Structural engineering documents, 7. Zurich: International Association for Bridge and Structural Engineering IABSE; 2003.
11. Hollaway L. A review of the present and future utilization of FRP composites in the civil infrastructure with reference to their important in-service properties. *Constr. Build. Mater.*, 2010; 24(12): 2419-2445.
12. Sá, M., Correia, J., Gomes, A., Silvestre, N. The Glass Fiber-Reinforced Polymer-Steel Hybrid Footbridge of Saint Mateus Park, Portugal: From Conceptual Design to In Situ Assessment. *Struct. Eng. Inter.*, 2018; 27:4; 575-580.
13. Osei-Antwi, M., De Castro, J., Vassilopoulos, A.P., Keller, T. Structural limits of FRP-balsa sandwich decks in bridge construction. *Composites: Part B*, 2014; 63: 77-84.
14. Osei-Antwi, M., De Castro, J., Vassilopoulos, A.P., Keller, T. FRP-balsa Composite Sandwich Bridge Deck with Complex Core Assembly. *J. Compos. Constr.*, 2013; 17(6): 04013011.
15. Lavanchy, S., Plumey, S., Beuchat, T. Lightweight durable composite deck offers solution on bridge dynamics. *Footbridge 2014, 5<sup>th</sup> International Conference, Footbridges: Past, present and future*, 16-18 July 2014, London, United Kingdom.
16. Sridharan, S (ed). *Delamination behavior of composites*. 1<sup>st</sup> ed., Woodhead Publishing and CRC Press; 2018.
17. Cantwell, W.J., Davies, P. A test technique for assessing core-skin adhesion in composite sandwich structures. *Journal of Material Science Letters*, 1994; 13: 203-205.
18. Ratcliffe, J.G., Reeder, J.R. Sizing a single cantilever beam specimen for characterizing facesheet-core peel debonding in sandwich structure. *J. Compos. Mat.*, 2011; 45(25): 2669-2684.
19. Rani, E., Grant, P., Ashforth, C. *Composite structures: effects of defects*. 1<sup>st</sup> ed. Hoboken NJ: John Wiley & Sons; 2018.
20. Brogini, F., Diviani, D., Rüegg, D., Ambrosini, M., Keller, T. Twin-shaped CFRP-sandwich pedestrian bridge. *Proceedings of the 8<sup>th</sup> International Conference on Fiber-Reinforced Polymer (FRP) Composites in Civil Engineering, CICE*, 14-16 December 2016, Hong-Kong, China.
21. Kedward, K.T., Wilson, R.S., McLean, S.K. Flexure of simply curved composite shapes. *Composites*, 1989; 20(6): 527-536.
22. Saseendran, V., Berggreen, C., Krueger, R. Mode mixity analysis of face/core debonds in a single cantilever beam sandwich specimen. *J. Sandwich Structures and Materials*, 2018; 0(0): 1-31.
23. Benzeggagh, M.L., Kenane, M. Measurement of mixed-mode delamination fracture toughness of unidirectional glass/epoxy composites with mixed-mode bending apparatus. *Compos. Sci. Technol*, 1996; 56: 439-49.
24. Brunner, A.J. Experimental aspects of Mode I and Mode II fracture toughness testing of fiber-reinforced polymer-matrix composites. *Compt. Method. Appl. M.*, 200; 185(2-4): 161-172.



25. Li, X., Carlsson, L.A. The tilted sandwich debond (TSD) specimen for face/core interface fracture characterization. *J. Sandwich Structures and Materials*, 1999; 1: 60-75.
26. Turon A., Camanho, P.P., Costa, J., Dávila, C.G. A damage model for the simulation of delamination in advanced composites under variable-mode loading. *Mech. Mater.*, 2006; 38(11): 1072-89.
26. Berggreen, C., Simonsen, B.C., Borum, K.K. Experimental and numerical study of interface crack propagation in fam-cored sandwich beams. *J. Compos. Mat.*, 2007; 41(4): 493-520.
27. Manca, M., Quispitupa, A., Berggreen, C., Carlsson, L.A. Face/core debond fatigue crack growth characterization using the sandwich mixed mode bending specimen. *Composites: Part A*, 2012; 43:2120-2127.
27. Farmand-Ashtiani, E., Cugnoni, J., Botsis, J. Monitoring and characterization of the interfacial fracture in sandwich composites with embedded multiplexed optical sensors. *Composite Structures*, 2013; 96: 476-483.
28. Shafiq, B., Quispitupa, A. Fatigue characteristics of foam core sandwich composites. *Inter. J. Fat.*, 2006; 28(2): 96-102.



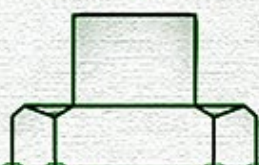




Internal steel plates  
Teflon  
Laminate  
External steel plates

A'A Section loaded

$P/6$



# Chapter 2

## Two-dimensional delamination

### *Experimental investigation*

#### 2.1 Introduction

Composite materials such as GFRPs (glass fiber-reinforced polymers) are commonly used for high performance load-bearing structural elements because of their high stiffness- and strength-to-weight ratios and great resistance to environmental impact (e.g. corrosion) [1]. The successful use of FRP for primary structural parts depends on its integrity and reliability. Delamination in laminated composites, which is likely to occur under compression, out-of-plane or shear loads, is one of the most common and critical types of damage. The relatively weak interlaminar strengths of laminates makes this failure mode particularly important for the integrity of composite structures. Due to the significant reduction in the load-bearing capacity of the structure caused by delamination, many experimental, analytical and numerical investigations have been carried out to characterize the fracture behavior of composite materials [1-6]. Research efforts have focused on beam-like specimens where the crack propagates with an approximately constant width of the crack front only in the longitudinal direction, i.e. one dimensional (1D) crack propagation occurs. However, delamination/debonding damage in real structures is not restricted to one direction but spans all around its contour. Few experimental or numerical investigations emulating the two-dimensional propagation of fully embedded pre-cracks in composite laminates or at the bonding interface between two adherends have been carried out.



Two-dimensional delamination under shear modes was investigated in [7] for carbon/epoxy laminates under three-point bending. An elliptical pre-crack was placed at the center and at the midplane of the laminate between two unidirectional ( $0^\circ$ ) plies. The fracture toughness along the crack front and the failure load were calculated analytically while only the latter was measured. Crack migration along the transverse direction was reported, causing an uneven propagation of the crack.

When damaged FRP sandwich structures are subjected to compressive loads, they tend to exhibit wrinkling of the thin laminates surrounding the damage, leading to delamination under opening and shear modes [8, 9]. Most of the work developed in this wrinkling-driven fracture framework is also restricted, as for standardized fracture procedures, to one-directional damage propagation [9, 10].

Several works have investigated the two-dimensional buckling and delamination in composite laminates under in-plane pure compression [11-15]. An analytical model able to predict critical values of applied strain preceding the two-dimensional crack propagation due to buckling is presented in [11]. Experimental and numerical analyses of CFRP (carbon fiber-reinforced polymer) laminates under pure compressive load with a circular eccentric delamination were used to evaluate the accuracy of the model. Intra-ply cracking occurred along the directions perpendicular to the fibers, as in [7], and only initiation values could be evaluated in this study. The value of the total critical strain energy released rate (SERR) used in the model was obtained from an energy-based damage propagation criterion. The critical SERR values of pure fracture modes used in this criterion were obtained from standard fracture specimens. Further analytical, numerical and experimental investigations can be found in [12-15]. However, the fracture mechanics parameters used in combination with the analytical and numerical formulations developed for 2D scenarios were again derived from 1D standard experiments.

A numerical study of the two-dimensional fracture behavior of flat and curved honeycomb sandwich panels containing a circular disbond at one of the face sheet/core interfaces is conducted in [16, 17]. Two loading conditions were considered: in-plane loads and ground-air-ground pressurization. The SERR was evaluated along the disbond using the virtual crack closure technique (VCCT). Standard 1D fracture mechanics specimens were also used to determine the critical SERR of the 2D laminate.

Experimental work to determine the Mode I critical energy release rate ( $G_{Ic}$ ) under external out-of-plane opening loading at the interface of two circular plexiglass (PMMA) plates bonded together with epoxy was presented in [18]. A circular pre-crack was inserted at the center of one interface and a tensile load was applied to propagate the pre-crack. An expression to calculate  $G_{Ic}$  for this configuration was developed. The flexural rigidity and deflection formulations at the center of isotropic plates were used to obtain the expression for the compliance. Assuming that the perimeter of the circular crack area (i.e.  $b=2\pi a$ ,  $a$  being the radius of the crack) is equivalent to the width of the crack in a standard double cantilever beam (DCB), a closed expression for  $G_{Ic}$  independent of the dimension of the crack was obtained. The described assumption

might be refutable for two reasons: first in the general expression for  $G_{Ic}$ , the compliance is derived with respect to the crack area, and therefore the chosen value of  $b$  multiplied by the radius  $a$  should give the value of the cracked area, a condition not fulfilled in this case; second, in this type of experiment, the length of the crack front increases as the crack propagates, and it is therefore a variable and cannot be treated as a constant for the derivation of the compliance. To the authors' knowledge, no other experimental investigation of two-dimensional delamination under an external out-of-plane tensile load has been reported.

In this work, the main objective was the experimental investigation of the two-dimensional (2D) delamination behavior in GFRP/epoxy plates and to identify potential differences in the behavior compared to 1D delamination. For that purpose, a novel design and experimental set-up suitable for the investigation of the 2D delamination behavior of laminates with internal circular disbands, subjected to opening loads, similar to the loads applied in a Mode I DCB specimen, was developed. Tensile experiments were performed to progressively open the crack. The load, introduced via an in-house developed loading system, was measured throughout the experiments as well as the crack propagation in the different directions, which was recorded digitally and visually. Based on the experimental results, the evolution of the crack front and consequently the fracture behavior could be analyzed. To understand the different phenomena observed, an FE simulation up to crack initiation was conducted for one of the plates.

## 2.2 Experimental investigation

### 2.2.1 Material description

Six different types of glass fiber reinforcements were used to fabricate the laminates: four types of woven fabrics with different proportions of reinforcement in the warp/weft directions (50/50 (W50.50) of 390-g/m<sup>2</sup> weight provided by Swiss-Composite, Switzerland, and 60/40 (W60.40), 70/30 (W70.30), and 80/20 (W80.20) of 500, 510 and 400-g/m<sup>2</sup> weight respectively, supplied by Tissa Glasweberei AG, Switzerland); a long continuous filament mat (CFM) with a weight of 600-g/m<sup>2</sup> and no binder or stitching, provided by Owens Corning (United States); and a multidirectional (quadraxial 0/±45°/90°) sewed (not stitched) fabric (MD) of 800-g/m<sup>2</sup> weight supplied by Swiss-Composite (Switzerland). Photos of the different reinforcements are presented in Figure 2.1. These fiber architectures were selected with two objectives: 1) to obtain different propagation patterns starting from a circular pre-crack, and 2) to propagate the crack at the midplane and thus avoiding crack migration phenomena (i.e. preventing the crack from jumping between layers) which would complicate the understanding of the results.

The selected matrix was an epoxy resin (Sika Biresin CR83) intended for infusion techniques and supplied by Global Tool Trading AG, Switzerland. The combination of

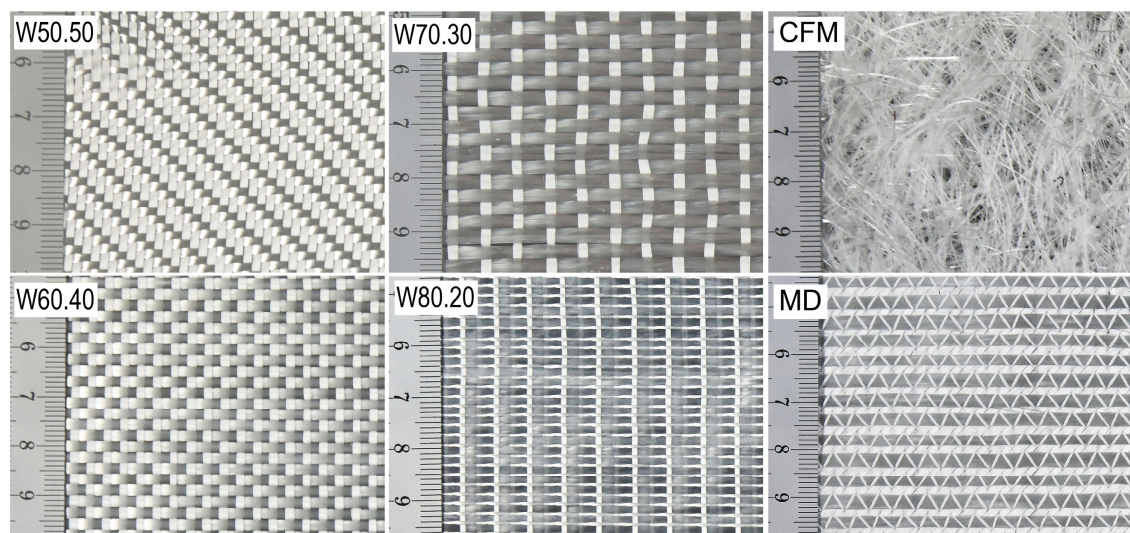


Figure 2.1 – Detail of glass fiber reinforcements

> Table 2.1 – Material properties

Material	$E$ (GPa)	$G$ (GPa)	$\nu$ (-)	$\rho$ (g/cm <sup>3</sup> )
Epoxy resin	2.96	1.30	0.35	1.14
E-glass	72.00	29.50	0.22	2.55
E-CR <sup>*</sup> glass	80.00	32.80	0.22	2.62

<sup>\*</sup>CR: Corrosion-resistant

> Table 2.2 – Description of GFRP plates

Plate type	No. of layers/ type of reinforcement	Dimensions (mm) (width x height x avg. thickness)
MD.1 / MD.2	4 / MD glass	480 x 480 x 3.27 / 480 x 480 x 3.74
W50.50.1 / W50.50.2	8 / W50.50 glass	460 x 460 x 3.33 / 480 x 480 x 3.53
W60.40.1 / W60.40.2	6 / W60.40 glass	410 x 410 x 3.05 / 410 x 410 x 3.06
W70.30.1 / W70.30.2	6 / W70.30 glass	400 x 400 x 3.36 / 400 x 400 x 3.35
W80.20.1 / W80.20.2	8 / W80.20 glass	410 x 410 x 3.62 / 410 x 410 x 3.51
CFM.1 / CFM.2	6 / CFM glass	420 x 420 x 7.50 / 420 x 420 x 6.99

this resin with the selected reinforcements resulted in highly translucent laminates for the case of CFM and medium translucent laminates for the remainder, this being an important requirement for this investigation where the crack propagates inside the plate and visual access to the crack front is essential. The properties of the glass fibers and resin are reported in Table 2.1 (manufacturer data [19-22]). All the reinforcements consisted of E-glass, except for the CFM which was made of E-CR glass.



## 2.2.2 Specimen description and elastic properties

The experimental program was conducted on twelve GFRP plates, two for each type of reinforcement. The pairs of plates were labeled accordingly (i.e. W50.50.1/2, W60.40.1/2, W70.30.1/2, W80.20.1/2, CFM.1/2 and MD.1/2) and their layup and geometrical description are presented in Table 2.2.

The elastic properties of the laminates were estimated based on the fiber volume fraction, calculated as  $f = w / (\rho_f d)$ , where  $w$  is the weight of the reinforcement,  $\rho_f$  the density of the glass fibers and  $d$  the thickness of the plate. For the woven (W) laminates, the in-plane E-moduli were calculated using Equation 2.1 [23, 24]:

$$E_{1,2} = m_{1,2}(E_r + (E_f - E_r)f + E_{90}) \quad (2.1)$$

where  $m_{1,2}$  are parameters indicating the proportion of reinforcement for each direction (e.g. 0.5 for both directions in W50.50);  $E_r$  and  $E_f$  are the E-moduli of the resin and fiber respectively;  $f$  is the fiber volume fraction and  $E_{90}$  is the E-modulus in the 90° direction of a unidirectional layer with the same fiber volume fraction as the woven plate calculated by the Halpin-Tsai formulation [24]. The out-of-plane E-modulus  $E_3$  equals  $E_{90}$ . The in-plane E-modulus for the continuous filament mat laminates (CFM) was calculated according to Equation 2.2 [25]:

$$E_1 = E_2 = \frac{3}{8}E_0 + \frac{5}{8}E_{90} \quad (2.2)$$

where  $E_0$  and  $E_{90}$  are the E-moduli in the 0° and 90° directions of a unidirectional layer with the same volume fraction as the CFM plate. The out-of-plane E-modulus was calculated with the same formulation as for the woven laminates. The Poisson's ratios for the CFM laminates were extracted from the database in [23] and for the woven laminates, Equations 2.3 - 2.5 were used [23]:

$$\nu_{12} = (\nu_r - (\nu_r - \nu_f)f)m_1 \left[ 1 + \frac{E_{90}}{E_r + (E_f - E_r)f} \right] \quad (2.3)$$

$$\nu_{13} = (\nu_r - (\nu_r - \nu_f)f)m_1 f \quad (2.4)$$

$$\nu_{23} = (\nu_r - (\nu_r - \nu_f)f)m_2 f \quad (2.5)$$

where  $\nu_r$  and  $\nu_f$  are the Poisson ratios of the resin and fiber. Finally, the shear moduli of the woven laminates were calculated using Equations 2.6 - 2.8 [23, 24]:

$$G_{12} = G_r \frac{1 + \zeta \mu f}{1 - \mu f} \quad (2.6)$$

$$G_{13} = G_r \frac{1 + \zeta \mu f m_1}{1 - \mu f m_1} \quad (2.7)$$

$$G_{23} = G_r \frac{1 + \zeta \mu f m_2}{1 - \mu f m_2} \quad (2.8)$$

where  $G_r$  is the shear modulus of the resin,  $\zeta = 1$  for fibers of circular cross-section and  $\mu$  is a parameter calculated with Equation 2.9:

$$\mu = \left( \frac{G_f}{G_r} - 1 \right) / \left( \frac{G_f}{G_r} + \zeta \right) \quad (2.9)$$

The shear modulus  $G_{12}$  of the CFM laminates was calculated with the general isotropic material formulation and  $G_{13}$  and  $G_{23}$  were calculated using the same formulation as that indicated for W50.50 laminates. There is no empirical formulation available to determine the elastic properties of MD specimens. Therefore, Composite Laminate Theory (CLT) was used to approximate  $E_1$ ,  $E_2$ ,  $G_{12}$ ,  $\nu_{12}$  values and the same procedure as for the woven laminates was followed to calculate the out-of-plane properties. The obtained values of one plate of each type are presented in Table 2.3.

All the GFRP laminates were symmetric with respect to both the midplane and each of the halves separately. Likewise, they were all fabricated by a vacuum infusion process. The plate configuration is shown in Figure 2.2 and the fabrication procedure is described in the following. First, three layers of release agent were applied over the polypropylene substrate to facilitate the demolding of the plates. Then half of the reinforcement layers (i.e. up to the midplane) were placed and lightly fixed with tape to the substrate. To introduce the load in a distributed manner, two stainless steel inserts of 1.2-mm thickness and 100-mm diameter were placed at the center of the reinforcements. Between them, a Teflon film of 13- $\mu$ m thickness and 180-mm diameter was placed to introduce the pre-crack (see Figure 2.2). To ensure that both steel inserts and the Teflon remained vertically aligned during the infusion process, preventing them from sliding, a very small pin was welded at the center of one of the steel plates and a small hole was drilled into the other so that a local shear bearing connection was created and no relative movements between them occur during the infusion process. Finally the remaining layers were placed and fixed and the whole system was infused. The thicknesses of the plates around the inserts were slightly greater than for the rest of the laminate. Their sufficient distance from the crack front is enough to make this difference unnoticeable with regard to the fracture behavior.

> Table 2.3 – Elastic properties of GFRP plates

Plate type	$f(\%)$	$E_1$ (GPa)	$E_2$ (GPa)	$E_3$ (GPa)	$G_{12}$ (GPa)	$G_{13}$ (GPa)	$G_{23}$ (GPa)	$\nu_{12}$ (-)	$\nu_{13}$ (-)	$\nu_{23}$ (-)
MD.1	0.38	15.45	15.45	7.54	4.35	1.85	1.85	0.32	0.30	0.30
W50.50.1	0.37	17.79	17.79	7.25	2.62	1.83	1.83	0.19	0.33	0.33
W60.40.1	0.39	22.30	14.86	7.57	1.76	2.00	1.73	0.23	0.32	0.33
W70.30.1	0.36	24.28	10.41	7.07	2.56	2.07	1.58	0.27	0.32	0.34
W80.20.1	0.35	27.03	6.76	6.90	2.51	2.18	1.48	0.31	0.31	0.34
CFM.1	0.18	9.34	9.34	4.68	3.51	1.54	1.54	0.33	0.30	0.30

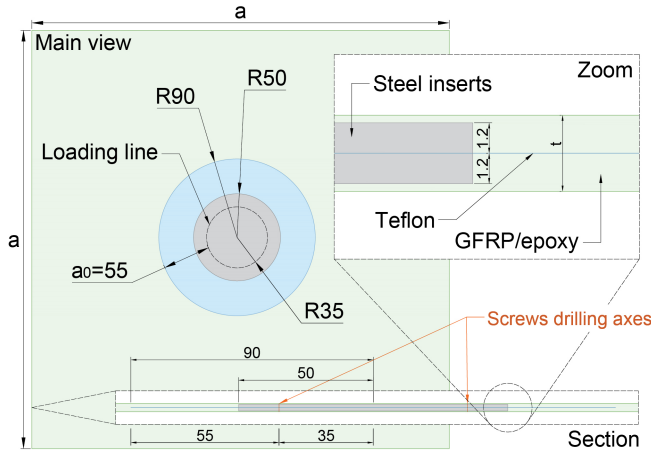


Figure 2.2 – GFRP plate configuration; dimensions in mm

The infusion was performed from side to side of the specimens. To obtain a good impregnation of the entire laminate, especially around the steel insert where the flow is particularly impeded, the infusion speed was carefully regulated. Likewise, for the multiaxial and woven reinforcements whose fiber architecture makes them harder to impregnate, flow meshes were placed above and below the plates and were connected to their own resin inlet. The plates with continuous filament mat reinforcement only required the upper flow mesh with the corresponding resin inlet. To eliminate the air inside the resin before the infusion, a degassing process was carried out. The laminates were cured under vacuum for at least 16 hours at room temperature and subsequently, once demolded, post-cured at 70°C for eight hours.

The procedure developed for the introduction of the out-of-plane load into the infused plates is detailed in Figure 2.3, with the different steps of the procedure indicated with the numbers in red color. First, six holes of 10-mm diameter were drilled starting from the bottom side of the plate until the midplane, where the diameter was changed to 6-mm diameter to complete the hole from the midplane to the other side of the plate (Figure 2.3(c), Steps 1 and 2). The same procedure was followed from the top side but with an alternated location of the holes (i.e. again six holes but rotated by 30° with respect to the center). All the holes were drilled along a radial length of 35 mm from the center of the plate, delimiting thus the loading line (see Figure 2.2). Subtracting the radial length of the loading line from that of the Teflon (i.e. 90 mm) resulted in a pre-crack of 55 mm radial length. Six downward facing screws were then placed followed by six upward facing ones (Figure 2.3(c), Step 3). The latter were immediately tightened to an 8-mm thickness and 100-mm diameter upper steel plate (Figure 2.3(c), Steps 5 and 6), which was pierced in advance with six holes of Ø6 and an additional centered hole for a screw of Ø8 mm. This central screw was also inserted in advance (Step 4) and intended for the assembling of a hinge (see Figure 2.3(a)) that connected the specimen to the grips of the machine. Finally the downward facing screws were also tightened to their

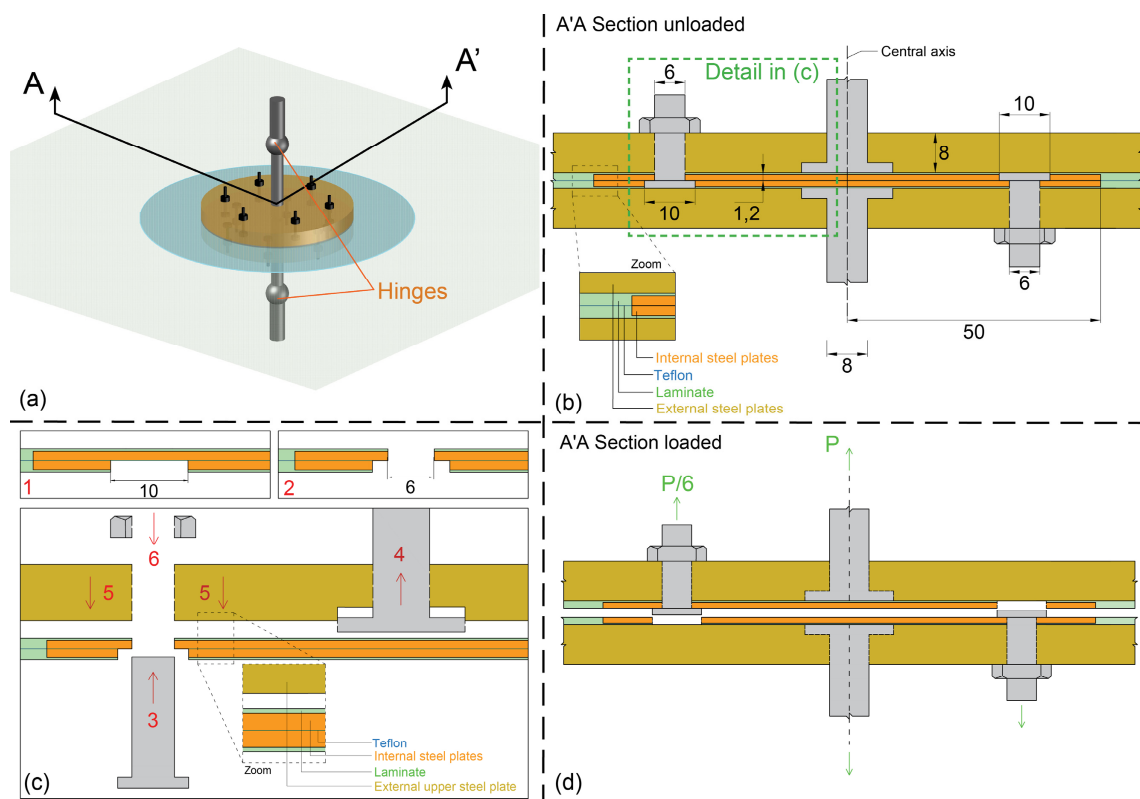


Figure 2.3 – Assembling of loading system; (a) general view; (b) A'A section (unloaded/closed) view; (c) detailed description of assembling sequence; (d) A'A section (loaded/open). Dimensions in mm

corresponding lower steel plate and the hinges were assembled. The hinges assured that any small specimen rotation would not damage the loading cell of the machine. Consequently, the centrally applied load was distributed by the (sufficiently stiff) upper and lower external steel plates to the upper and lower groups of six screws, which opened the system via the internal steel plates, as shown in Figure 2.3(d).

### 2.2.3 Experimental set-up, instrumentation and measurements

The experiments were performed under displacement-control on a W+B electromechanic machine of 50-kN capacity at a rate of 1.5 mm/min, a temperature of  $24 \pm 2^\circ\text{C}$  and relative humidity of  $38 \pm 5\%$ . The experimental set-up and instrumentation layout are shown in Figure 2.4. Once the load-introduction system was assembled, the plate was placed and fixed within the grips of the machine, by adjusting first the bottom hinge and then, with the help of a level so that the plate is completely horizontal, the upper hinge.

Due to the nature of the experiment and difficulty of measuring the entire contour of the crack, three different measuring systems were employed: the 3D Digital Image Correlation System (DIC), a digital camera and visual measurements. Eight rulers starting from the end of the pre-crack were drawn on the plates corresponding to eight directions of propagation, named after the cardinal directions (see Figure 2.5). The

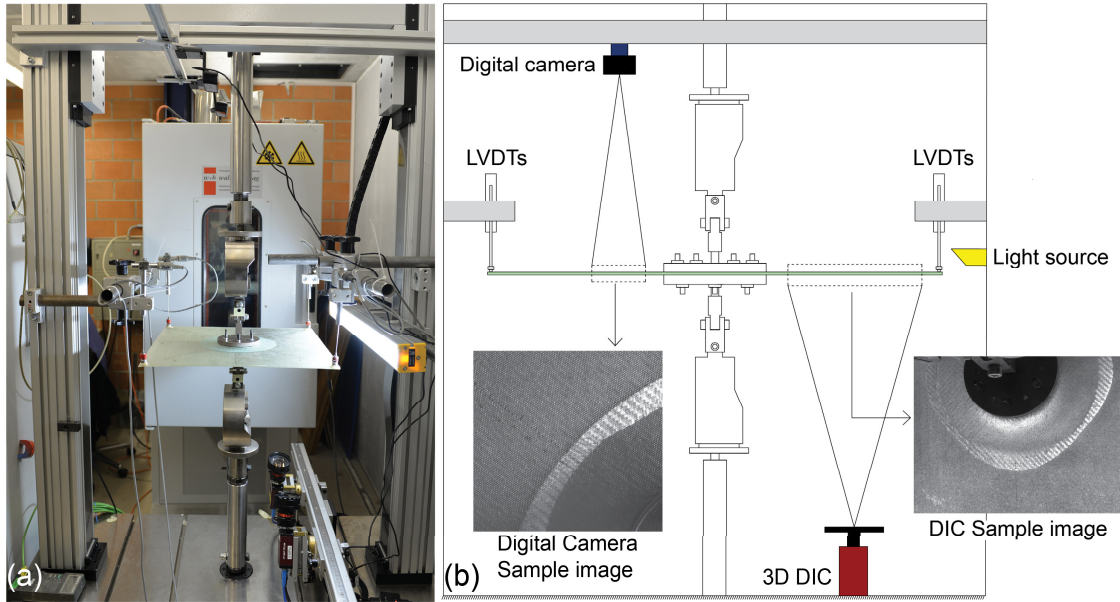


Figure 2.4 – (a) Experimental set-up and (b) instrumentation layout

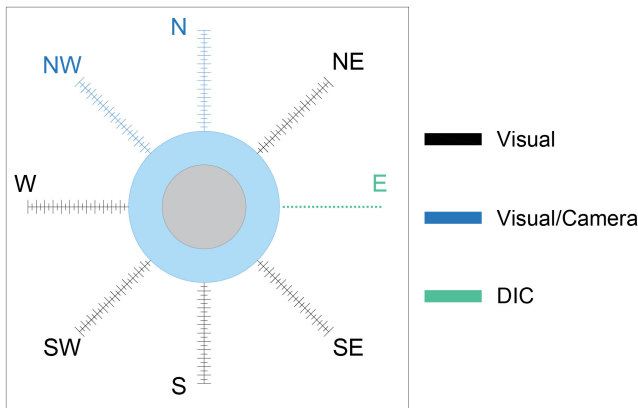


Figure 2.5 – Layout of crack measuring system. N, S, E and W are orthogonal directions and NE, SE, NW and SW diagonal directions

propagation along the east (“E”) direction was measured by the DIC system (accuracy of  $\pm 0.005$  mm). Due to the set-up requirements, the two DIC cameras were placed below the plate (Figure 2.4(b)). A random  $\leq 0.1$  mm speckle pattern using black spray paint was applied over the surface (see Figure 2.4). The ruler corresponding to this direction, drawn on the bottom surface, was slightly different from the others as small black points 2.5 mm apart were used instead of continuous lines so that the general DIC pattern was not disturbed (Figure 2.5). The calibration area around this dotted line was approximately 50 mm wide and 100 mm long. In order to obtain clear, good quality images, a source of white light was employed with a semi-opaque diffusor. The set-up was the same for all the plates except for the CFM laminates, where a layer of white paint was additionally applied before the black speckle pattern due to the high transparency of these specimens causing reflections and affecting the quality of the measurements during the experiment. The acquisition frequency of the images was set

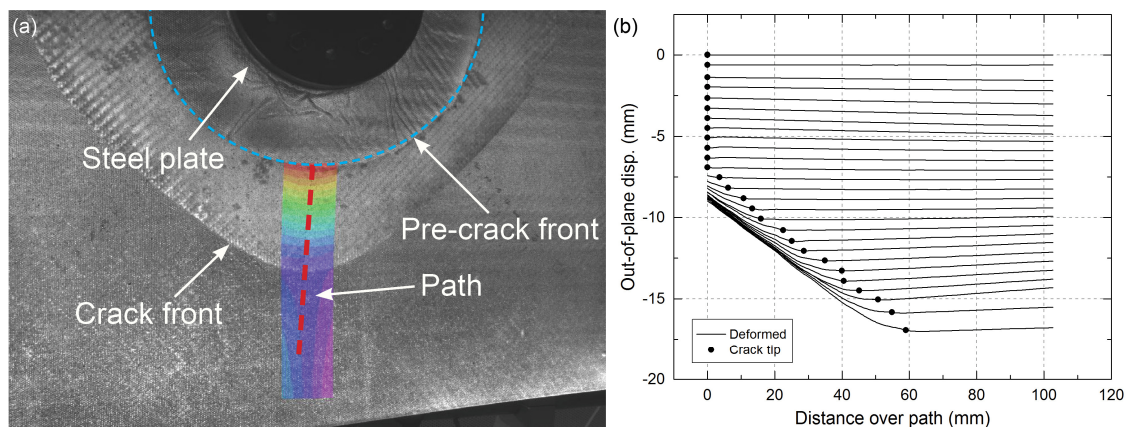


Figure 2.6 – DIC measurements of plate W50.50.1; (a) area and path of interest (example image); (b) evolution of out-of-plane deformed profiles and location of crack tip

to 0.2 Hz. The processing of the results was carried out using Vic-3D software from Correlated Solutions Inc. [26]. In Figure 2.6 (a) an example of the measuring area and the selected path of interest are presented. The path is superposed on the dotted ruler and therefore starts at the end of the pre-crack in that direction. The values of the out-of-plane displacements were extracted along the path and the crack tip was defined by means of a numerical script as the point where the deformed profile of the path changes from straight to curved. An example of the profiles obtained for the plate W50.50.1 is presented in Figure 2.6(b) and the corresponding load and displacement values for the indicated crack tips can be found in Figure 2.7(a). Positive values correspond to deformation towards the location of the DIC cameras and negative values to the opposite direction. During deformation, two contributions to the out-of-plane displacements were measured by the DIC system: the solid rigid movement of the whole plate in the negative direction (i.e. upwards together with the loading frame of the machine) and the out-of-plane deformation due to the opening of the crack in the positive direction. Therefore, as a result of the positive contribution of the opening of the crack and as can be observed in Figure 2.6(b), the out-of-plane displacement values in the cracked region (i.e. curved part of the profiles) are smaller in absolute terms than in the non-cracked region. The obtained results were cross-checked with the corresponding values observed in the DIC pictures by means of the drawn dotted ruler and a very good agreement was found.

The direction of propagation monitored with the digital camera was either north (“N”) or northwest (“NW”) depending on the type of reinforcement and the illumination requirements. The diagonal “NW” direction was selected for W50.50 plates providing that the crack was expected to propagate along the orthogonal directions equally and one of them, the “E” direction, was already recorded by the DIC. For the rest of the woven plates, where the crack propagated differently along the two orthogonal directions, the “N” direction was monitored. The illumination affected the measurements of the CFM plates whose transparency made it hard to measure the “N” direction with the digital camera due to the high intensity of the reflections in the pictures. Therefore, the “NW” direction was selected. The images were taken from above the plate (see Figure 2.4(b)) and consequently the rulers were drawn on the upper surface of the plates. The acquisition

frequency was set, as for the DIC, to 0.2 Hz and each picture was recorded with the corresponding values of the load and displacement. Post-processing visual work based on the images was performed. The type of image obtained by the camera during the experiment can be observed in Figure 2.4 (b, “Digital Camera Sample Image”).

Along the remaining directions, where the rulers were also drawn on the upper surface, the crack front was recorded visually. Every time the crack propagated 2.5 mm, measured over the rulers, the values of the crack front along all these directions were registered together with the load and the displacement.

To record the boundary movements, four Linear Variable Differential Transducers (LVDTs, accuracy of  $\pm 0.02$  mm) were installed (Figure 2.4(b)) to measure the displacement of the four corners. The load and the displacement at the center of the plates (out-of-plane) were obtained from the machine (accuracy of  $\pm 0.11\%$ ). The whole experiment was likewise recorded with a video camera.

## 2.3 Experimental results

### 2.3.1 Load-displacement responses and crack propagation measurements

Continuously increasing load-opening displacement curves were obtained for all the experiments, also after crack initiation (Figure 2.7 to 2.11). For plates W50.50, W60.40 and MD, the experiments were stopped after the load started to decrease. For plates W70.30, CFM and W80.20, the crack propagation was automatically interrupted by the matrix failure and therefore a sharp decrease in the loads can be observed in Figure 2.9, 2.10 and 2.11(b), respectively. The values of the maximum load and displacement achieved for each specimen are presented in Table 2.4.

As mentioned in the previous section, the vertical displacements on the four corners were recorded by the LVDTs. Different values were recorded depending on the corner for all the plates except for the CFM pair, where the four corners presented approximately

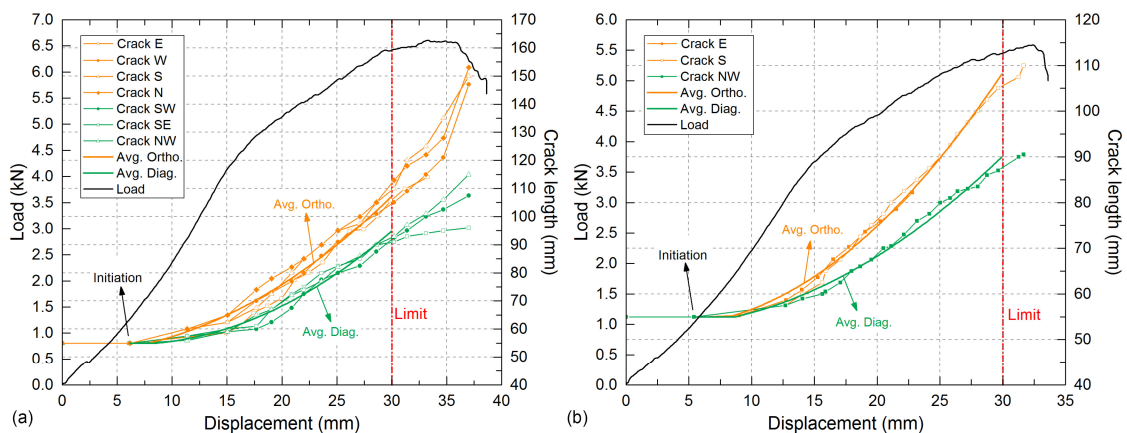


Figure 2.7 – Load and crack lengths vs opening displacement curves; (a) W50.50.1; (b) W50.50.2



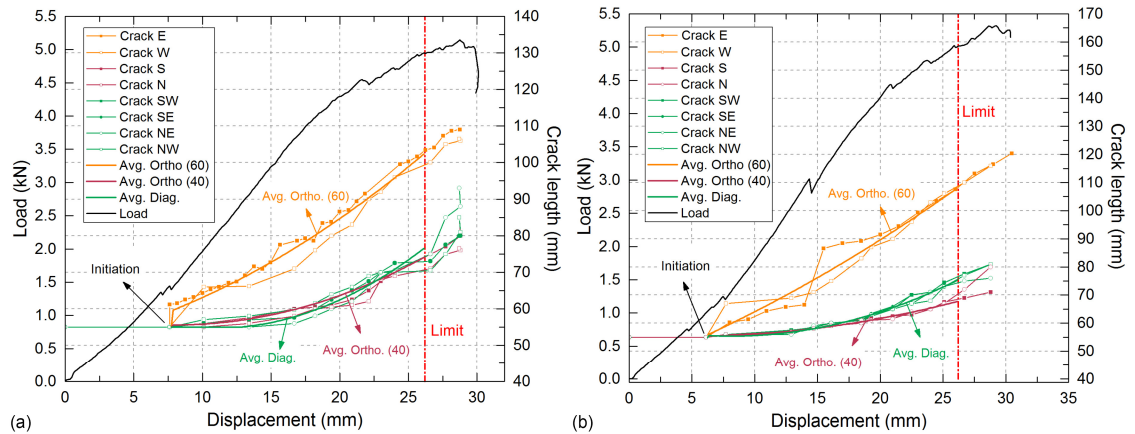


Figure 2.8 – Load and crack lengths vs opening displacement curves; (a) W60.40.1; (b) W60.40.2

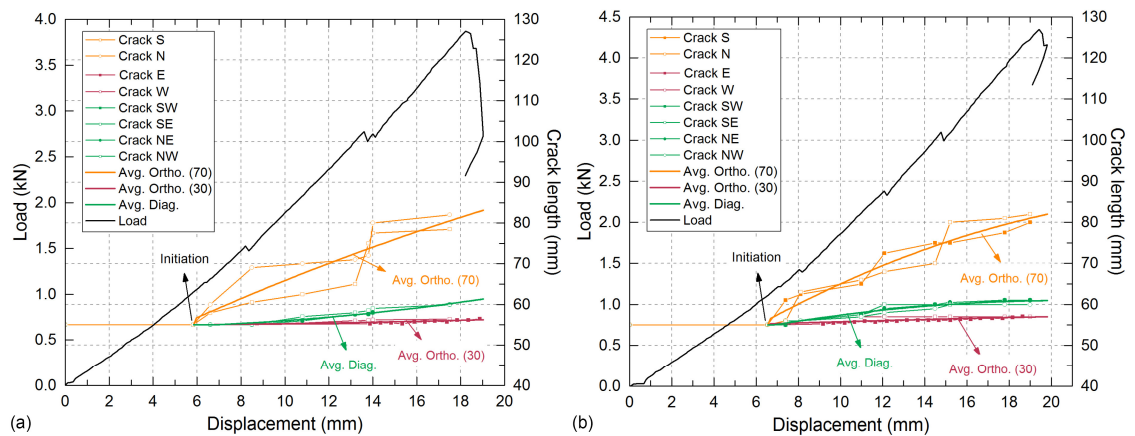


Figure 2.9 – Load and crack lengths vs opening displacement curves; (a) W70.30.1; (b) W70.30.2

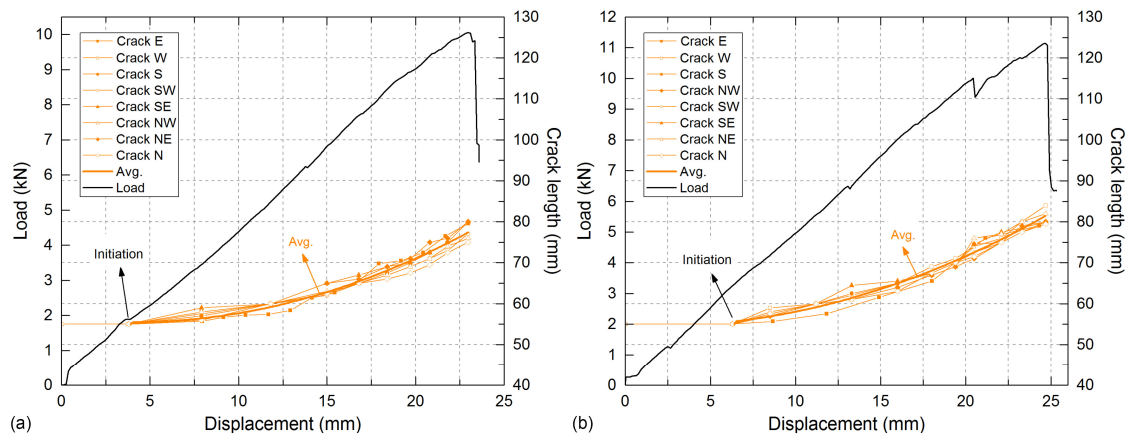


Figure 2.10 – Load and crack lengths vs opening displacement curves; (a) CFM.1; (b) CFM.2



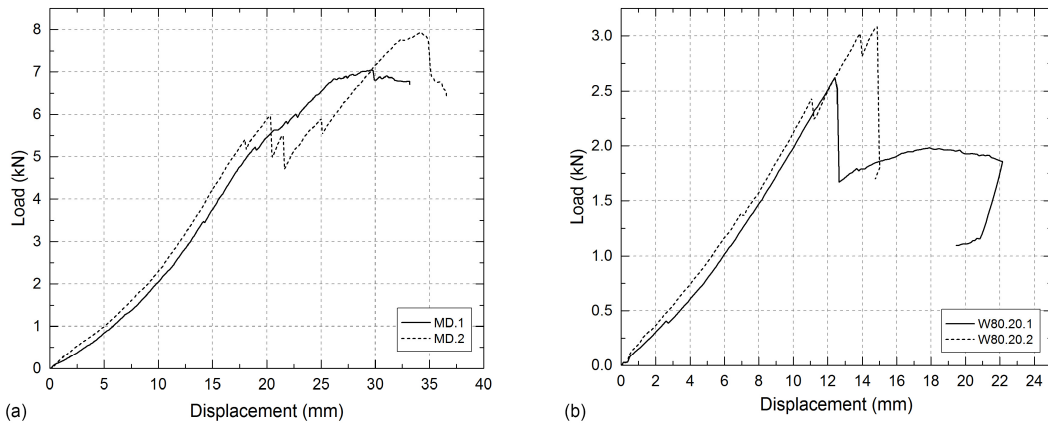


Figure 2.11 – Load vs opening displacement curves; (a) MD pair; (b) W80.20 pair

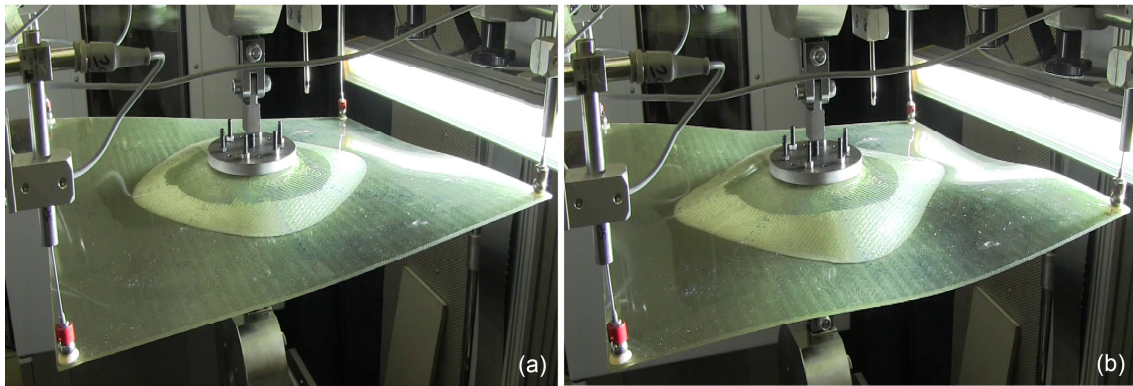


Figure 2.12 – Example of deformation in plate W50.50.1 at (a) limit of symmetric propagation and (b) beyond limit

the same displacement values. One of the reasons for these differences in the vertical displacements of the boundaries of the plates was the variation in stiffness depending on the direction of propagation. As a result, the crack tip along the stiffest directions (e.g. the orthogonal directions for W50.50) exhibited the greatest opening and therefore a greater propagation and vertical movement of the un-cracked region in that direction. Also, depending on the propagation direction, distances from the crack tip to the free end were different (longer in the diagonal and shorter in the orthogonal directions), also affecting the magnitude of these vertical movements: the further the free end from the crack tip, the greater the vertical displacement. The combination of both effects led to the recorded boundary behavior, unique for each type of reinforcement. Initially, the crack propagations were not affected by these boundary displacements and a symmetric and stable propagation could be observed. When the boundary displacements became higher, they started to influence the crack front and the symmetry in the growth was lost (see Figure 2.12). The limits of the symmetric behavior were obtained based on the data registered during the experiment (i.e. during the experiments, load, displacement and crack length measurements along all the directions were noted when the loss in symmetry was noticed). A subsequent revision of all the digitally recorded data was performed to corroborate the in-situ registered data. As an example, the obtained curve of corner and opening displacements vs the the load for specimen W50.50.1 is shown

> Table 2.4 – Load and displacement values for initiation and maximums

Plate	Initiation		Maximum	
	Disp. (mm)	Load (kN)	Disp. (mm)	Load (kN)
MD.1	11.13	2.31	29.63	7.04
MD.2	7.98	1.66	34.27	7.93
W50.50.1	6.10	1.27	33.04	6.60
W50.50.2	5.40	1.03	32.40	5.60
W60.40.1	7.61	1.42	28.74	5.15
W60.40.2	6.14	1.00	29.14	5.32
W70.30.1	5.83	1.03	18.22	3.87
W70.30.2	6.54	1.11	19.43	4.38
W80.20.1	4.04	0.61	12.41	2.62
W80.20.2	4.10	0.72	14.88	3.08
CFM.1	3.79	1.89	22.97	10.05
CFM.2	6.29	3.24	24.67	11.14

in Figure 2.13. It can be seen that for this type of plate the corners exhibited a similar behavior in a two-by-two trend, with the displacement of the “NW”/”SE” pair being higher than for the “NE”/”SW” pair. The opening displacement at the limit was 30 mm and is indicated with a red dashed line. In this case, from the limit onwards, the displacements of the corners became unstable, and the measurements for the “NW”/”SE” pair were lost.

The advance of the crack front was measured up to the end of the experiments for all the plates. However, only the results concerning plates W50.50, W60.40, W70.30 and CFM are described in the following since the results obtained for the W80.20 plates (Figure 2.11(b)) were very similar to those for W70.30 and the output obtained from the MD plates (Figure 2.11(a)) was not conclusive due to the crack jumping and the consequent asymmetry in the propagation. A further description of the crack propagation patterns will be given in Section 2.3.2.

The crack lengths vs opening displacement responses of the W50.50 pair are shown in Figure 2.7. Crack length values in the “NE” direction for W50.50.1 are missing due to technical problems with the digital camera during the experiment and for W50.50.2, which was the first specimen of woven reinforcement investigated, only the “E”, “NW” and “S” directions were measured, the first two by digital means (DIC and digital camera respectively) and the third visually. For the remainder of the plates the full set of measurements was obtained. The orange lines represent the orthogonal directions

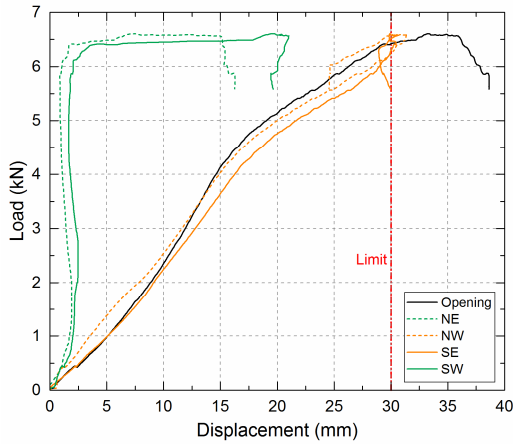


Figure 2.13 – Displacement of LVDTs at corners of plate W50.50.1 vs load

(i.e.  $0/90^\circ$ , both equally reinforced in this case) and the green lines represent the diagonal directions (i.e.  $\pm 45^\circ$ ). It can be observed that the measured lengths along the diagonal directions remained fairly consistent with each other as well as for the orthogonal directions, indicating a practically symmetric growth of the crack front. The limit of the symmetric behavior corresponded, as previously indicated, to a 30-mm opening displacement and is marked with a dashed vertical red line. It is evident in Figure 2.7(a) how the values between the diagonal crack lengths and also between the orthogonal crack lengths began to diverge from this point onwards. Additionally, in order to obtain a continuous evaluation of the crack front, average curves for the orthogonal and diagonal directions were derived by means of parabolic expressions, as shown in Figure 2.7.

The same representation is shown in Figure 2.8 for the W60.40 plates. Here, the orange lines represent the orthogonal directions with 60% reinforcement, the red lines the orthogonal directions with 40% of reinforcement and the green lines the diagonal directions. Some sudden crack propagations occurred in the case of the W60.40.2 specimen in the 60% directions as can be observed in both the load and crack length curves (sharp variations) showing a subsequent very rapid recovery of the load. The corresponding average crack length curves were also plotted for the three groups of directions. The limit of symmetric propagation in this case corresponded to a displacement of 26.2 mm also indicated with a red vertical dotted line. It can be observed that, as expected, it was along the most reinforced directions (orange lines) that the crack front propagated the furthest. Initially, the propagation along the less reinforced directions was slightly greater than along the diagonals. Once the crack fronts advanced sufficiently further, the behavior was inverted and the propagation along the 40% reinforced directions became smaller (see Figure 2.8).

The results obtained for plates type W70.30 are shown in Figure 2.9. As for the W60.40, the three main directions are represented in orange (orthogonal of 70%), red (orthogonal of 30%) and green (diagonals). The average curves are also added for each direction. This type of laminate exhibited a less smooth crack propagation than the previous plates, with two sudden propagations in the most reinforced directions for

W70.30.1 (Figure 2.9(a)) and three for W70.30.2 (Figure 2.9(b)), also showing a subsequent rapid recovery of the load. It can be observed how the crack barely propagated along the least reinforced direction. In this case, the crack did not propagate far enough to lose the symmetrical crack shape.

The load and crack lengths vs the displacement curves for CFM plates are presented in Figure 2.10. Due to the concentric growth of the crack up to the failure of the matrix near the holes, the values of the crack lengths showed the same trend. The CFM.2 plate exhibited two small sudden crack propagations reflected in both the load and crack lengths (Figure 2.10(b)) followed by a rapid recovery.

The initiation points are indicated for all the plates in Figure 2.7 to 2.10 and the corresponding load and displacement values are given in Table 2.4. As can be observed in the figures, no specific change in the load could be noticed for most of the plates except for the W60.40 pair and CFM.1 where a small load fluctuation was registered. The values were obtained in situ during the experiments (i.e. when the crack propagation was initiated, the load and displacement values were noted) and a subsequent revision of all the digitally recorded data (pictures from digital camera and DIC) was performed to corroborate them.

### 2.3.2 Crack propagation patterns

The different crack propagation patterns obtained are shown in Figures 2.14-2.19. All these pictures were taken with a black background in order to improve the contrast and better identify the propagated crack area except for the CFM plates where, due to their high translucency, a white background was selected.

Crack propagation in the W50.50 plates advanced symmetrically to the orthogonal axes up to around 30 mm of propagation in the diagonal directions and 50 mm of propagation in the orthogonal directions in both plates. The shape of the crack front for the last symmetric contour for W50.50.1 is drawn in blue in Figure 2.14. From this point onwards, the boundary displacements started to affect the specimens' propagation behavior, impeding the crack growth in some directions (e.g. "NE") and favoring others

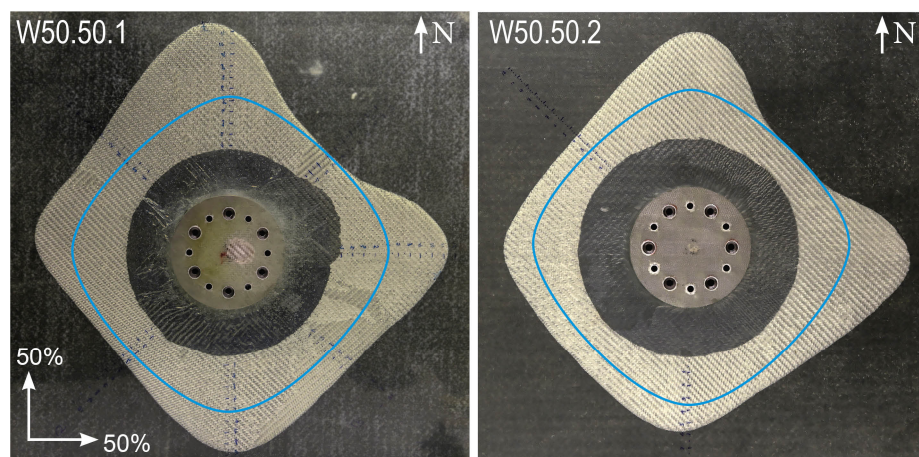


Figure 2.14 – Crack propagation pattern for W50.50 pair (limit of symmetric propagation marked in blue)



(e.g. “N”). A similar performance was found for the W60.40 laminates where the crack grew symmetrically to a propagation length of around 45 mm in the orthogonal directions of 60% reinforcement, 15 mm in the orthogonal directions of 40% reinforcement and 20 mm in the diagonal directions. In Figure 2.15 the shape of the last symmetric crack front for the plate W60.40.1 is also indicated in blue. Plates W70.30 and W80.20 only propagated 2 mm in the less reinforced directions and 20–30 mm in the more reinforced directions before they failed due to matrix cracking starting from the holes (see Figure 2.16 and Figure 2.17). For the CFM laminates a concentric circular crack front propagation was observed as expected for an in-plane isotropic reinforcement. A propagation along the entire contour of 22.5 mm and 25 mm for CFM.1 and CFM.2 respectively was achieved before they also failed as a result of matrix failure initiating from the holes (Figure 2.18). The crack initiated and propagated in all of these plates between the adjacent plies of the pre-crack (i.e. the midplane).

For the MD plates the propagation was symmetric only at the very beginning of the experiments (2–3 mm of propagation) for both plates but, as soon as the crack propagated further, crack migration phenomena occurred all around the contour creating

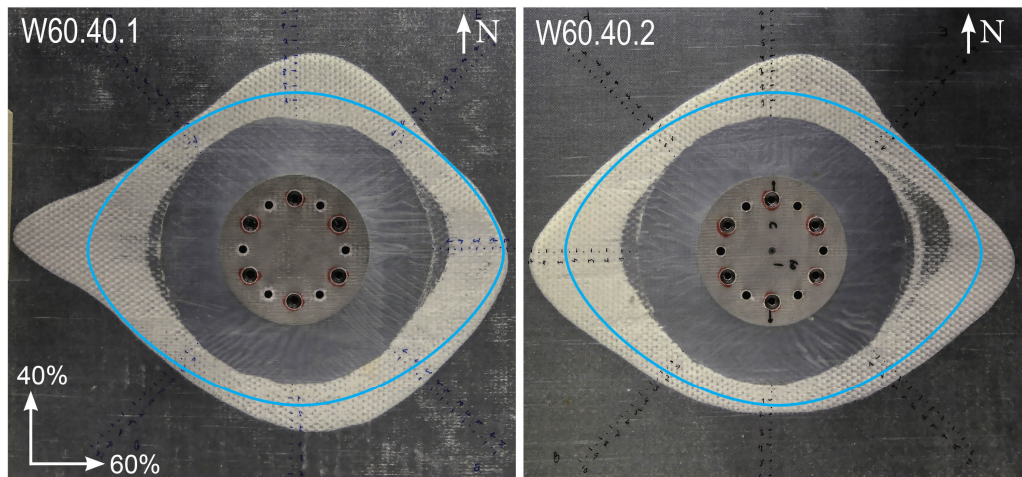


Figure 2.15 – Crack propagation pattern for W60.40 pair (limit of symmetric propagation marked in blue)

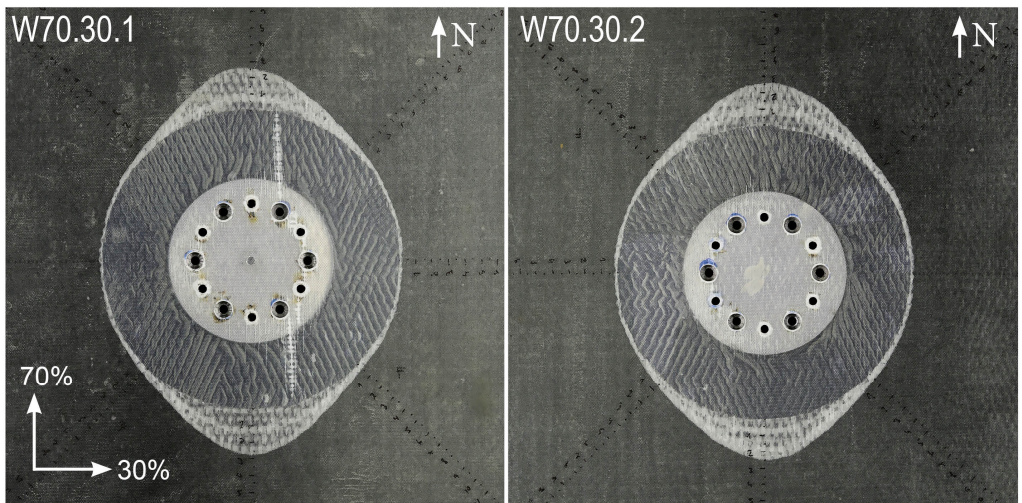


Figure 2.16 – Crack propagation pattern for W70.30 pair

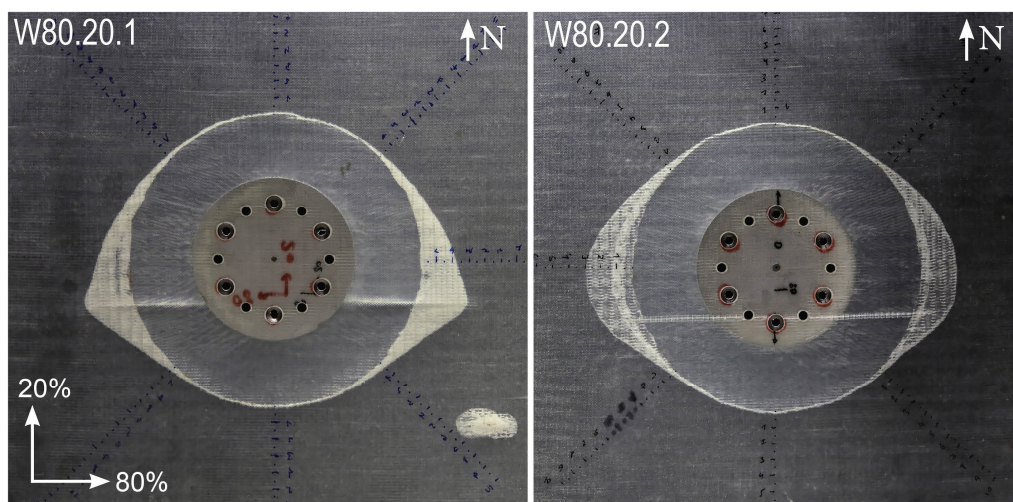


Figure 2.17 – Crack propagation pattern for W80.20 pair

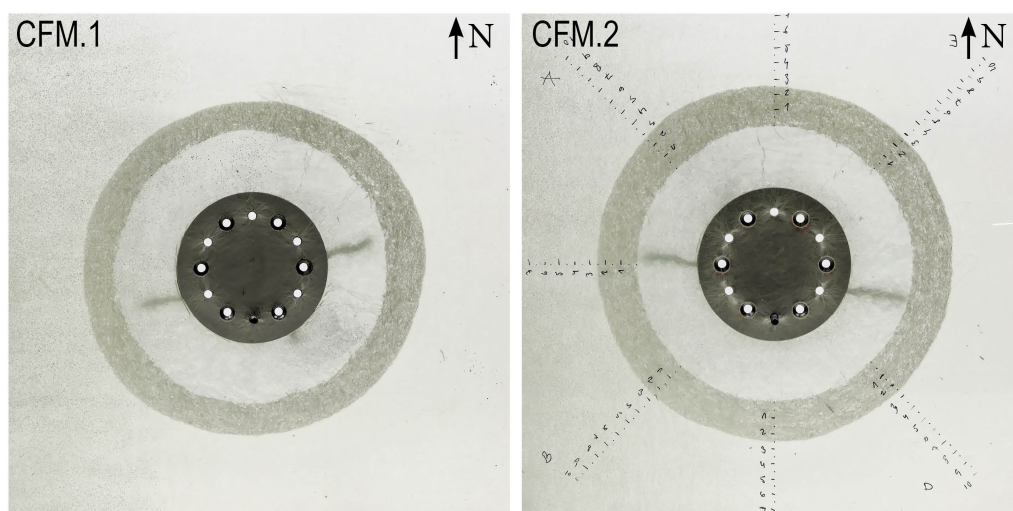


Figure 2.18 – Crack propagation pattern for CFM pair

a non-symmetric propagation pattern that was not even repeatable from one plate to the other (Figure 2.19). As previously mentioned in Section 2.2.1, in the MD reinforcement, and unlike in the W (woven) reinforcement, the different directions were sewed together (each direction one layer). Given the results, it is evident that this sewing was not sufficient to join the layers firmly together, i.e. enable them to behave as a single layer and permit the crack to propagate in the plate's midplane. Therefore the crack started to migrate from one layer to another depending on the direction of propagation as might have occurred for a laminate with unidirectional reinforcements stacked in different directions.

Based on the derived average curves of crack-length along the different directions of propagation vs the opening displacement (see Figure 2.7 to 2.10) a back-calculation of the crack front was performed for each increment of the experiment. The advance of the crack front is represented for three of the plates, W50.50.1 (Figure 2.20(a)), W60.40.1



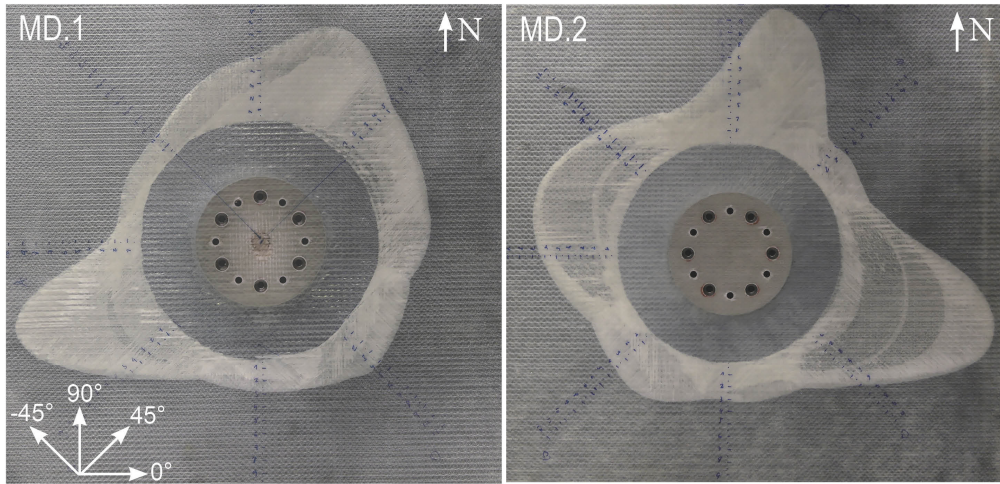


Figure 2.19 – Crack propagation pattern for MD pair

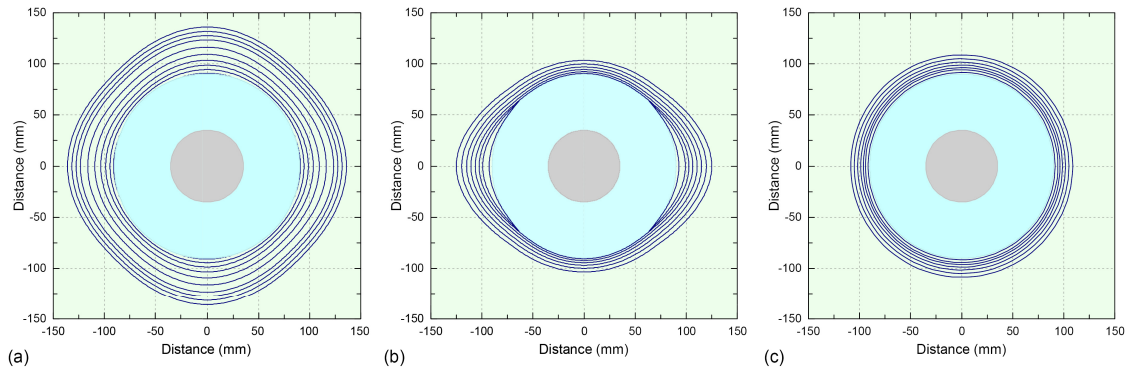


Figure 2.20 – Progressive back-calculated propagation perimeters for (a) W50.50.1, (b) W60.40.1 and (c) CFM.1

(Figure 2.20(b)) and CFM.1 (Figure 2.20(c)). The last contour corresponds to the last crack front before the loss of symmetry for the woven plates (also specified as previously indicated with a blue contour in Figure 2.14 and Figure 2.15). Correspondingly, the last contour of the CFM is the last before the failure of the matrix. It can be observed how the average curves are able to reproduce the symmetry with respect to the orthogonal axis shown in the experiments.

### 2.3.3 Compliance behavior

As has been described, the experimental values of the crack lengths along the different directions were used to derive the corresponding average curves, providing continuous evaluation of the crack propagation fronts. The area of the crack was calculated for each increment as the area between the obtained crack front and the loading line (as for the standard fracture mechanics experiments), i.e. a 70-mm diameter circle passing through the center of the screws that constitute the loading points (see Figure 2.2). The compliance, calculated as  $\delta/P$ ,  $\delta$  being the opening displacement and  $P$  the load, plotted against the crack area is shown for W50.50 (Figure 2.21(a)), W60.40 (Figure 2.21(b)), W70.30 (Figure 2.22(a)) and CFM (Figure 2.22(b)). The crack initiation points are indicated. Woven laminates W50.50 and W60.40 exhibited comparable

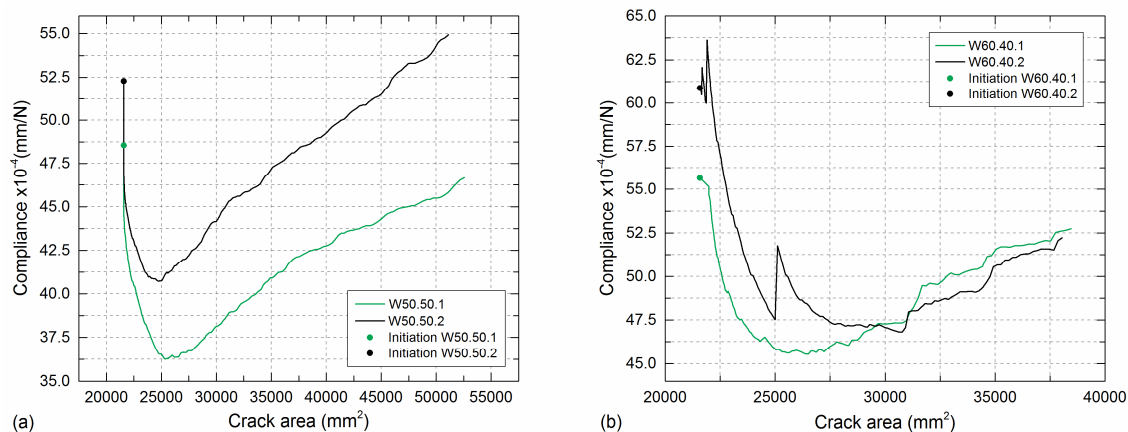


Figure 2.21 – Compliance vs crack area for (a) W50.50 pair and (b) W60.40 pair

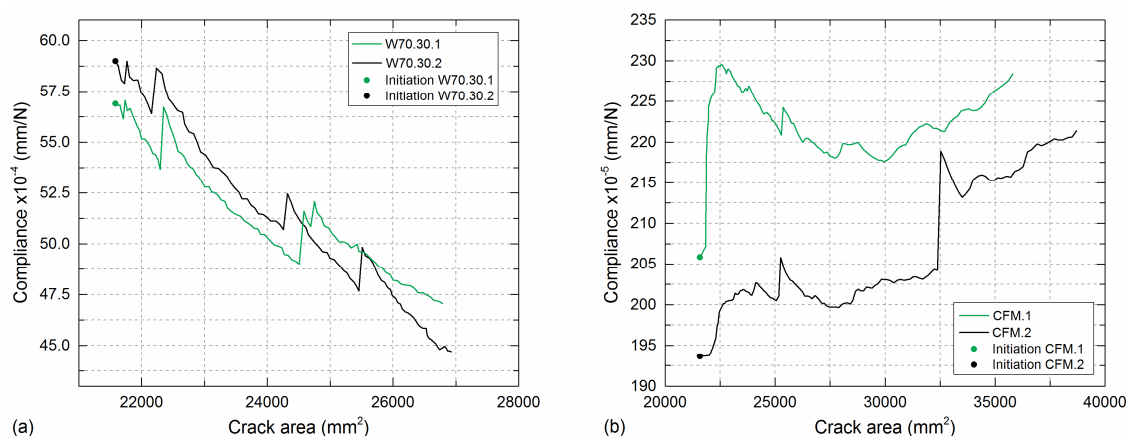


Figure 2.22 – Compliance vs crack area for (a) W70.30 pair and (b) CFM pair

behavior, i.e. first a descending branch down to a minimum and then an ascending branch corresponding respectively to a stiffening and subsequent softening of the system. Only the first descending part was developed for the W70.30 plates (Figure 2.22(a)) where the crack propagation was significantly less than in the other plates. The W80.20 specimens behaved in the same manner. For the CFM plates, a third branch appeared, apart from the descending and ascending parts already described for the previous plates, showing an increase in the compliance during the initial propagation of the crack (Figure 2.22(b)).

## 2.4 Discussion

### 2.4.1 Increasing load behavior

As described in Section 2.3.1, a continuously increasing load-opening displacement behavior was monitored from the beginning of all experiments up to the loss of symmetry of propagation or failure of the specimen, depending on the plate. In contrast to the results shown in this chapter, the load in standard fracture mechanics experiments always decreases once the crack starts to propagate. This contradictory behavior can be understood by comparing how the crack grows in both cases. For



fracture mechanics experiments, or any beam-like experiment where the crack width is constant and the length of the crack front also remains practically constant, the crack area grows proportionally throughout the entire experiment. For the two-dimensional experiments presented here, the crack was embedded inside the laminate and consequently, since the crack area started to grow symmetrically with respect to the orthogonal axes, the length of the crack front increased accordingly. As a result, a disproportionate growth of the crack area occurred, whose increments were higher as the crack advanced, forcing the load to increase in order to continue the propagation of the crack.

When the boundary displacements started to affect the propagation of the crack, the length of the crack fronts ceased to increase symmetrically. Some of the directions of the crack fronts were constrained by the boundary deformation of the plate and some other directions were favored (see “W” in Figure 2.15 (W60.40.1)). This caused a reduction of the crack front length and consequently a decrease in the load (Figures 2.7, 2.8 and 2.11(a)).

### 2.4.2 Stiffness-related mechanisms

Three different mechanisms affecting the specimens' stiffness could be distinguished in the experiments: stretching, fiber bridging and crack propagation. When thin beams, plates or shells are subjected to transversal loads and their boundary conditions are fixed on both sides in such a way that their deformation will cause in-plane tension, the structure will become significantly stiffer with increasing deformation [28]. This phenomenon is called stretching and is normally disregarded for standard fracture mechanics experiments as it barely affects the propagation of the crack. For the specimens investigated here, the boundary conditions caused stretching to become a significant stiffening mechanism. As the crack opened under the out-of-plane tensile load, two curvatures appeared: the radial and the circumferential, see Figure 2.12. The frame-like boundary of the plates prevented the plate from moving radially (i.e. horizontally), causing the corresponding radial stretching. Likewise, the embedded geometric nature of the crack prevented the plate from moving in the circumferential direction, causing the corresponding circumferential stretching. The plates were therefore

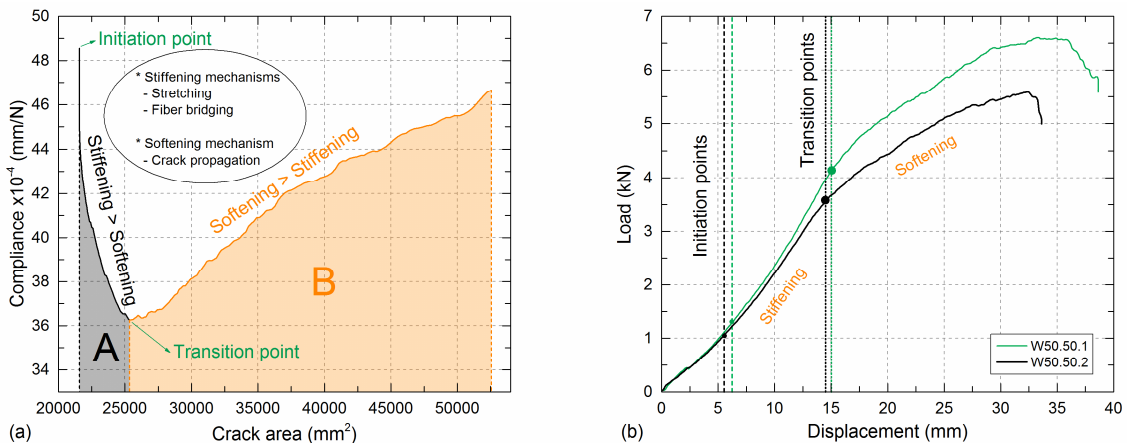


Figure 2.23 – Identification of stiffening and softening regions on: (a) compliance vs crack area of W50.50.1; (b) load-displacement curves of plates W50.50.1 and W50.50.2

subjected to a bi-directional stretching phenomenon. Once the crack started propagating, two additional mechanisms were activated, fiber bridging, as an additional stiffening mechanism, and crack propagation itself as a softening mechanism. The fiber bridging was not measured and due to the nature of the experiment it could not be observed either, but it was expected to exist mainly for the CFM specimens and on a much smaller scale for the rest of the specimens. Typically, for a standard fracture experiment, crack propagation is the dominant mechanism after crack initiation, leading to a continuous upwards behavior of the compliance. On the contrary, for these two-dimensional experiments, the stiffening mechanisms (mainly stretching) played an important role in the performance of the specimens, prevailing over the softening due to crack propagation and thus significantly affecting the results. Since the experimental compliance results did not correspond uniquely to the propagation of the crack as for standard fracture specimens, the fracture resistance cannot be directly derived from the experiments.

Based on the curves presented in Figure 2.21(a), an identification of the stiffening and softening regions in both the compliance vs crack curve (for W50.50.1) and load vs displacement curve (for both W50.50 specimens) was carried out in Figure 2.23. Two regions were differentiated on the compliance vs crack area curve. The first region, designated “A”, which spans from crack initiation (called “initiation point”) up to a minimum (called “transition point”), represents the interval where the stiffening mechanisms (stretching and fiber bridging) prevail over the softening mechanisms (crack propagation), causing the corresponding decrease in compliance. Only when the softening due to crack propagation becomes the dominant mechanism, prevailing over the others (at the transition point) does the compliance start to grow, then entering the second region, designated “B” (Figure 2.23(a)).

The same differentiation procedure in the compliance vs crack curve can be established for the W60.40, W70.30 and CFM plates in Figure 2.21(b), 2.22(a) and 2.22(b) respectively by identifying the minimum values as from which the general trend of the compliance increases. Only a part of region A could be identified in Figure 2.22(a), signifying that for plates W70.30 the crack did not propagate sufficiently

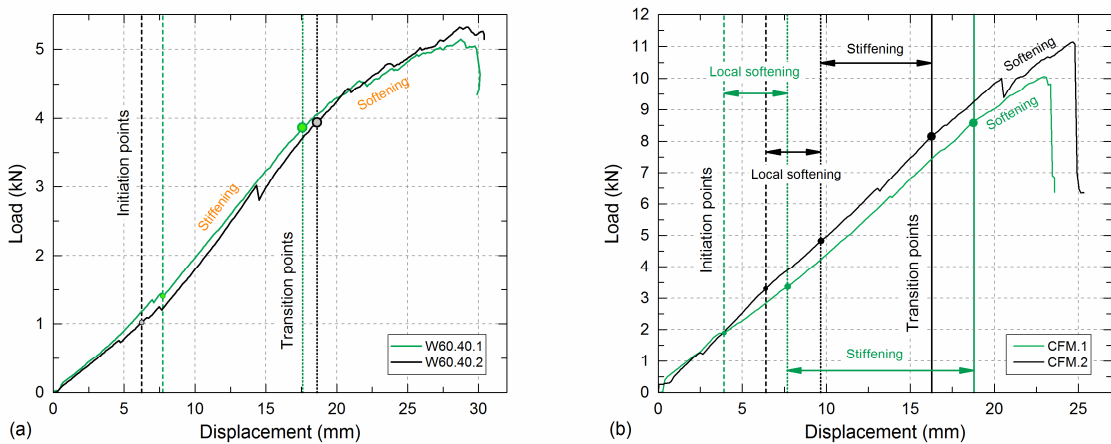


Figure 2.24 – Identification of stiffening and softening regions on load-displacement curves of (a) W60.40 pair and (b) CFM pair

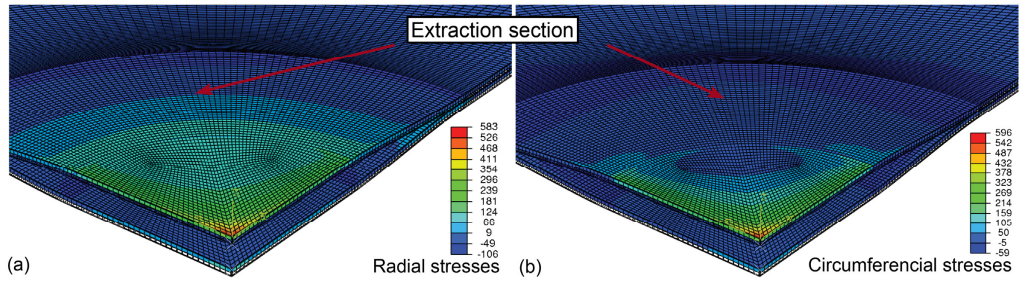


Figure 2.25 – FE model stress results for plate W50.50.1; (a) total radial stresses; (b) total circumferential stresses (MPa)

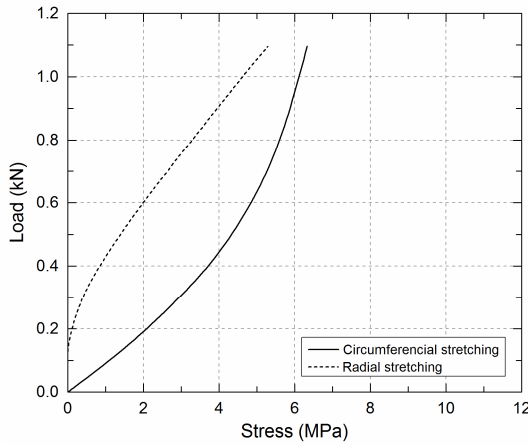


Figure 2.26 – Load vs stretching stresses obtained at measured section (Figure 2.25) from FE model

to become the dominant mechanism (i.e. the failure of the matrix occurred before the transition point was reached). For the CFM plates (Figure 2.22(b)), an initial ascending part of the compliance could be observed, which was attributed to isolated initial slipping at the loading blocks and this part was therefore not considered in the further analysis. All the regions and points of interest were likewise identified in the corresponding load-displacement curves for the W60.40 (Figure 2.24(a)) and CFM (Figure 2.24(b)) plates.

Based on the compliance vs crack area curves, the thresholds indicating initiation of crack propagation were plotted with dashed lines for each pair of plates and the thresholds representing the transition from a dominant stiffening behavior to a dominant softening behavior were plotted with dotted lines. It is evident how the stiffening zones corresponded to an increase of the load vs displacement slope and correspondingly, how the softening zones after the transition points corresponded to a decrease of the slope.

In order to confirm the presence of a stretching mechanism and its contribution to the stiffening of the plates, an FE model using the commercial finite element analysis (FEA) software Abaqus 6.14.1 was developed (Figure 2.25). The plate chosen for the model development was the W50.50.1, and a total displacement corresponding to the experimental value of initiation was applied, i.e. the behavior before crack propagation was simulated. Based on the boundary movements, the diagonals of the plate were taken as the two axes of symmetry and only one quarter of the model was built. The steel inserts and the external loading blocks were not modeled. Instead, the nodes of the inner faces of the loading areas were tied together with a rigid body condition to shell elements of eight nodes and reduced integration (CS8R) from Abaqus/Standard [27] were used. The

mesh comprises 75,146 nodes and 56,664 elements, with two elements through the thickness of each of the halves above and below the midplane half plate. The size of the mesh varied from 0.6 mm close to the crack to 4 mm far from the crack. A static standard calculation taking large displacements into account was carried out. The engineering constants employed to define the material are presented in Table 2.3. The stress results are plotted in a cylindrical coordinate system and the values in the radial and circumferential directions are shown in Figure 2.25(a) and (b) respectively. The values at a specific through-thickness section (indicated as “extraction section” in Figure 2.25), located at  $\rho=68$  mm and  $\varphi=\pi/4$ , were extracted and the stretching stresses were calculated in both directions by subtracting the bending stresses from the total stresses obtained. The result of the stretching stresses vs the load is presented in Figure 2.26. It can be observed that the stretching in the circumferential direction grows slightly faster than in the radial direction, reaching a proportion of 55%/45% (circumferential/radial) at the end of the simulation. Consequently, as the plates deformed under the out-of-plane loading, they were subjected to bending and stretching stresses, the latter causing a considerable double stiffening effect capable of retarding the softening of the system when the crack started to propagate.

## 2.5 Conclusions

The 2D delamination behavior of composite laminates with a circular embedded pre-crack under quasi-static out-of-plane loading has been experimentally investigated. Different fiber architectures were selected to obtain different propagation patterns starting from a circular pre-crack. Two plates of each type were investigated and the crack propagation modes and load-bearing and compliance behavior were analyzed. Furthermore, an FE model corresponding to one of the plates was developed in order to study the stretching effects and their contribution to the stiffening of the system. The following conclusions were drawn:

1. An experimental design suitable for investigating the 2D propagation of an embedded pre-crack under out-of-plane opening loading was successfully developed. The different methods employed for the measurement of crack propagation were consistent and reliable.
2. Increasing loads, also after crack initiation, were obtained as a result of a continuously increasing crack front length and a consequently disproportionate increase in the propagation area. This is intrinsic to an embedded crack that grows all around its contour.
3. As the plates started to deform under the out-of-plane loading, stretching stresses appeared in both the radial and circumferential directions as a result of the geometrical constraints. Consequently, the plates were subjected to a dual stiffening effect.
4. Stretching of the specimens and also fiber bridging mainly for the CFM specimens (both stiffening mechanisms) were capable of delaying the general softening of the system that typically occurs once the crack started to propagate.

The threshold indicating the point where softening due to crack propagation became the dominant mechanism could be clearly identified as the minimum in the compliance vs crack area curves.

5. Regarding the type of reinforcement, different propagation modes and patterns were obtained, the most reinforced direction being the one experiencing the greatest crack propagation. In the woven and continuous filament mat reinforcements, the crack remained in the mid-plane and propagated symmetrically with respect to the orthogonal axes, whereas for the multiaxial reinforcement (non-woven) crack migration effects occurred and non-symmetrical propagation was observed.
6. Out-of-plane displacements of the boundaries of the plates were measured for all specimens as a result of the different rates of crack propagation and distances to the free end along the crack front. The propagation of the crack was unaffected by these boundary effects up to a recognizable limit. From this limit onwards, the results were not considered.
7. The FE model developed for one of the woven plates simulating the experimental behavior up to crack initiation showed that the stretching stresses in the circumferential direction increased slightly faster than in the radial direction. Significant values were reached in both directions, thus confirming the experimental results, i.e. the activation of this mechanism.

## References

1. Bakis, C., et al., Fiber-reinforced polymer composites for construction-state-of-the-art review. *Journal of Composites for Construction*, 2002; 6(2): 73-87.
2. Benzeggagh, M.L., Kenane, M. Measurement of mixed-mode delamination fracture toughness of unidirectional glass/epoxy composites with mixed-mode bending apparatus. *Compos. Sci. Technol.*, 1996; 56: 439-449.
3. ASTM D5528-13: Standard test method for mode I interlaminar fracture toughness for unidirectional fiber-reinforced polymer matrix composites, in *Annual book of ASTM standards: adhesive section 15.03*.
4. ASTM D6671/D6671M - 13e1: Standard test method for mixed mode I-mode II interlaminar fracture toughness for unidirectional fiber-reinforced polymer matrix composites, in *Annual book of ASTM standards: adhesive section 15.03*.
5. Turon, A., Dávila, C.G., Camanho, P.P., Costa, J. An engineering solution for mesh size effects in the simulation of delamination using cohesive zone models. *Eng. Fract. Mech.*, 2007; 74: 1665-1682.
6. Shahverdi M, Vassilopoulos AP, Keller T. Modeling effects of asymmetry and fiber bridging on Mode I fracture behavior of bonded pultruded composite joints. *Eng Fract Mech*, 2013; 99: 335-348.
7. Chatterjee, S.N., Dick, W.A., Byron Pipes, R. Mixed-mode delamination fracture in laminated composites. *Compos. Sci. Technol.*, 1986; 25: 49-67.
8. Carlsson, L.A., Kardomateas, G.A. *Structural and Failure Mechanics of Sandwich Composites*, 2011; *Solid Mechanics and its Applications* vol. 121; Springer.
9. Rasmus, C., Østergaard, C. Buckling driven debonding in sandwich columns. *Int. J. Solids Struct.*, 2008; 45: 1264-1282.

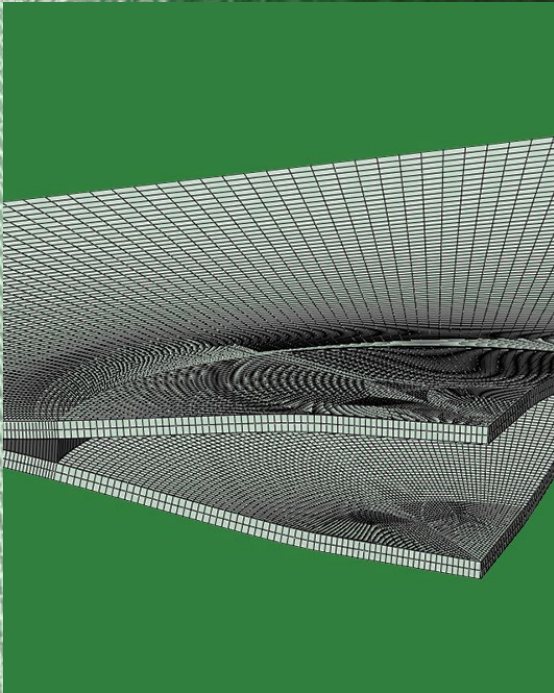
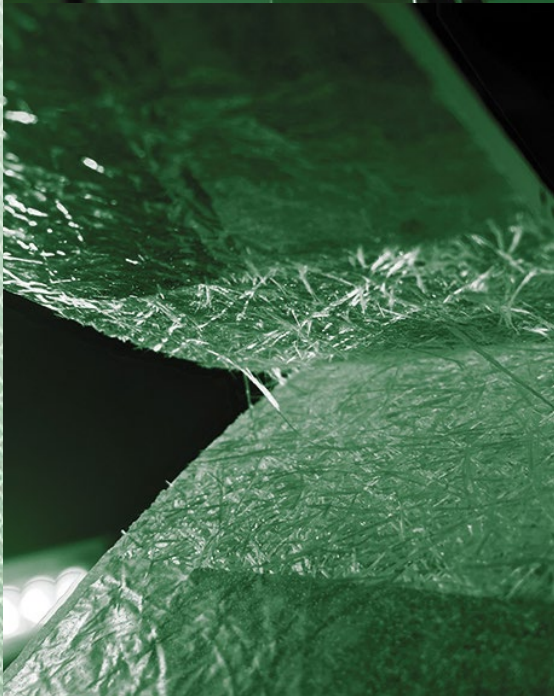
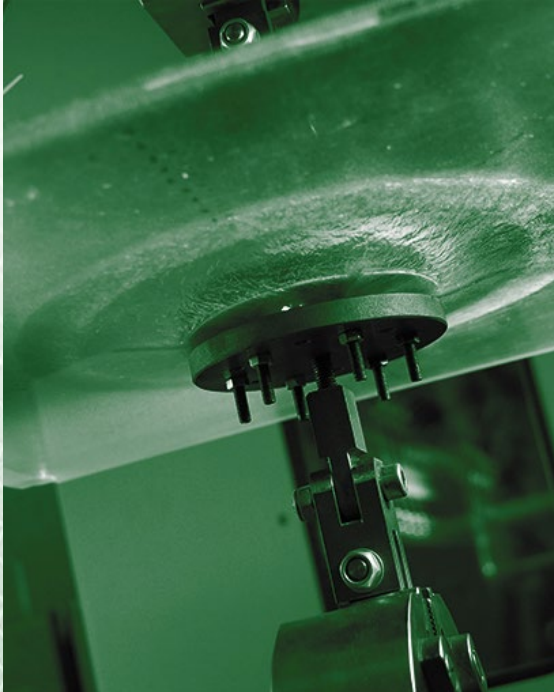
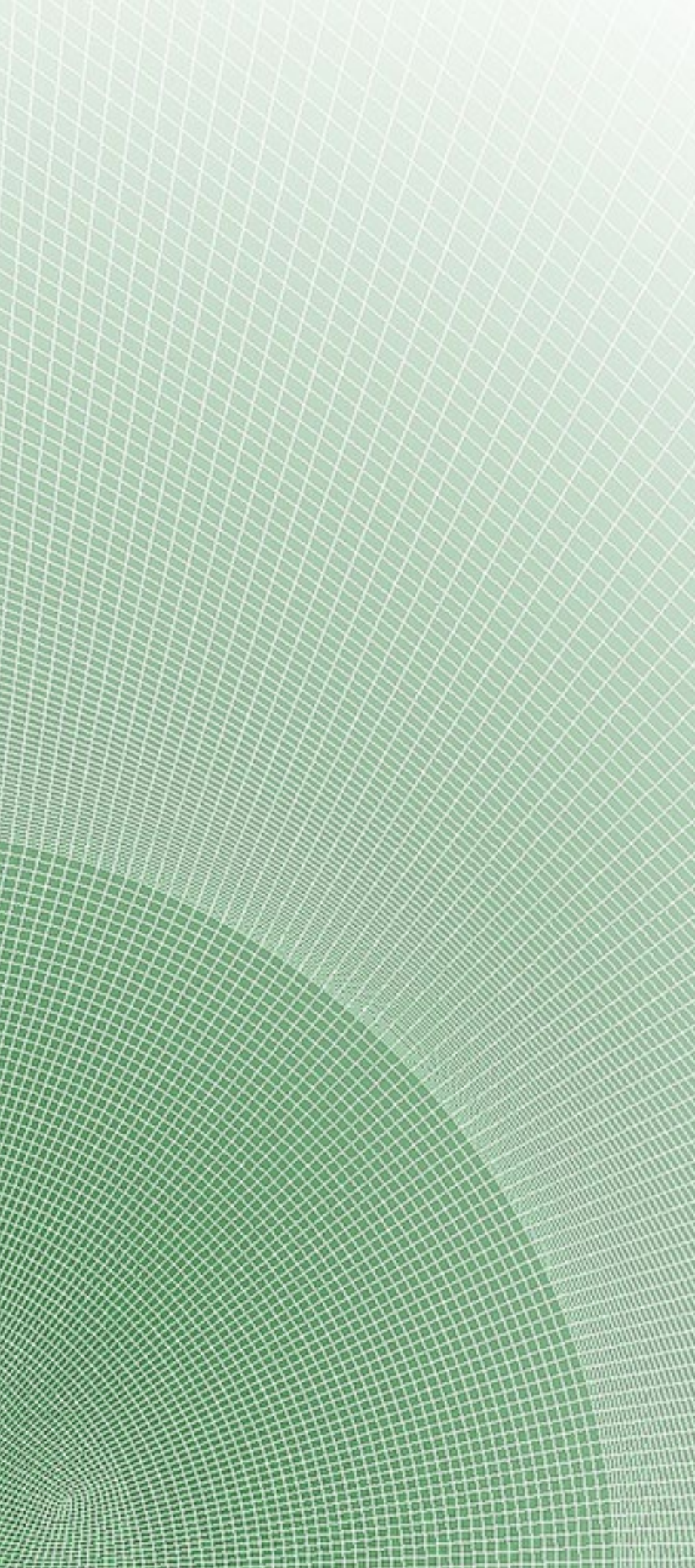
10. Kinawy M., Butler, R., Hunt, G.W. Bending strength of delaminated aerospace composites. Phil. Trans. R. Soc. A, 2012; 370: 1780-1979.
11. Butler, R., Rhead, A.T, Liu, W., Kontis, N. Compressive strength of delaminated aerospace composites. Phil. Trans. R. Soc. A, 2012; 370:1759-1779.
12. Nilsson K.F., Thesken J.C., Sindelar P, Giannakopoulos A.E., Storakers B. A theoretical and experimental investigation of buckling induced delamination growth. J. Mech. Phys. Solids, 1993; 41(4): 749-782.
13. Riccio A., Raimondo A., Di Caprio F., Scaramuzzino F. Delaminations buckling and growth phenomena in stiffened composite panel under compression. Part II: a numerical study. Journal of Composite Materials, 2014; 48(3); 2857-2870.
14. Rhead A.T., Butler R., Hunt G.W. Compressive strength of composite laminates with delamination induced interaction of panel and sublaminar buckling modes. Composite Structures, 2017; 171; 326-334.
15. Nilsson K.F., Asp L.E., Alpman J.E., Nystedt L. Delamination buckling and growth for delaminations at different depth in a slender composite panel. Int. J. Solid Struct., 2007; 38; 3039-3071.
16. Chen, Z.M., Krueger, R., Rinker, M. Facesheet/Core Disbond Growth in Honeycomb Sandwich Panels Subjected to Ground-Air-Ground Pressurization and In-Plane Loading. In: 11th International Conference on Sandwich Structures ICSS-11, Ft. Lauderdale, USA, March, 2016.
17. Rinker, M., Krueger, R., Ratcliffe, J. Analysis of an Aircraft Honeycomb Sandwich Panel with Circular Face Sheet/Core Disbond Subjected to Ground-Air Pressurization. NASA/CR-2013-217974, 2013.
18. Kumar, P., Reddy, S.R. Experimental determination of interlaminar  $G_{Ic}$  using a fully embedded centre-cracked specimen. Eng. Fract. Mech., 1998; 59(2): 183-189.
19. Owen's Corning Reinforcements Composite Solutions Guide. <[http://www.ocvreinforcements.com/pdf/library/Composite\\_Solutions\\_Guide\\_100360\\_E\\_finalprintable.pdf](http://www.ocvreinforcements.com/pdf/library/Composite_Solutions_Guide_100360_E_finalprintable.pdf)> (Accessed 26 March 2018).
20. Swiss Composite Product Catalogue. <<https://www.swiss-composite.ch/pdf/Produkteuebersicht.pdf>> (Accessed 16 October 2017).
21. Tissa Glasweber AG website. <<http://www.tissa.ch/i4Def.aspx?tabindex=0&tabid=500&lang=en>> (Accessed 16 October 2017).
22. Sika datasheet product. <[https://deu.sika.com/dms/getdocument.get/dd4b783e-bfa5-32e3-a705-f9f548f6b326/Biresin\\_CR83\\_eng.pdf](https://deu.sika.com/dms/getdocument.get/dd4b783e-bfa5-32e3-a705-f9f548f6b326/Biresin_CR83_eng.pdf)> (Accessed 19 October 2017).
23. Ascione L, Caron J-F, Godonou P, Van IJselmuiden K, Knippers J, Mottram T, et al. Prospect for new guidance in the design of FRP: Support to the implementation, harmonization and further development of the Eurocodes. Publications Office of the European Union; 2016. Report No. EUR 27666 EN. doi: <http://dx.doi.org/10.2788/22306>.
24. Jones R. M. Mechanics of Composite Materials, 1999; 2nd Edition: Taylor and Francis.
25. Gay D., Hoa S.V. Composite Materials, Design and Application, 2007; 2nd Edition: CRC Press, Taylor and Francis.
26. Correlated Solutions Inc. VIC 3D-v7 reference manual. Columbia, USA: Correlated Solutions.
27. Abaqus Inc. Abaqus analysis user's manual, version 6.14-1. 2014. Providence, RI, USA.
28. Howell L.L. Compliant Mechanisms, 2001: John Wiley & Sons Inc.

---

**Contributions:** Aida Comeselle Molares conceived, designed and performed the experimental campaign under the supervision of Prof. Thomas Keller and Dr. Anastasios Vassilopoulos. The analysis of the results was carried out by Aida Comeselle Molares in collaboration with Prof. Thomas Keller and Dr. Anastasios Vassilopoulos.









## Chapter 3

# Two-dimensional delamination

## *Numerical investigation*

### 3.1 Introduction

Despite the good structural performance of fiber-reinforced composite materials (FRPs) [1], mechanisms such as delamination in laminated components may lead to a considerable reduction in the load-bearing capacity of the structure. Significant efforts have been devoted to the investigation of the delamination fracture behavior of laminated composites [2-4]. Pure and mixed-mode fracture behaviors have been widely investigated, i.e. beam-like specimens such as the double cantilever beam (DCB) for Mode I, end-loaded split (ELS) for Mode II or mixed-mode bending for mixed-Mode I/II, have all been extensively used and standardized [5-7]. However, some of the conditions required by these types of experiments, such as a constant crack width or single direction of propagation, may not correspond to the actual delamination damage growth that occurs in FRP structures. In many scenarios, delamination damage may develop all around the contour of a defect with an increasing length of the front of the propagating crack. Furthermore, accurate determination of the strain energy release rate (SERR) is a key factor for damage-tolerant structural design and therefore the development of new fracture experimental designs better able to represent realistic scenarios is needed. Some investigations studying the two-dimensional (2D) propagation of an embedded pre-crack in composite materials can be found in [8-13]. Various sources of delamination are considered: buckling-driven delamination in [8-11] or out-of-plane deformation of the laminate around a disbond due to differences in pressure in [12-13]. However, in all of them, the fracture properties were assumed to

be those obtained from the previously mentioned standard beam-like specimens with one-dimensional (1D) crack propagation.

When a material undergoes deformation and damage, different toughening mechanisms may be activated, increasing the energy dissipation level. These damage mechanisms can be considered intrinsic or extrinsic, depending on whether they appear behind or in front of the crack tip respectively [14]. Intrinsic damage is related to the fracture resistance of a material and typically associated with plasticity in ductile materials such as metals or soft polymers, e.g., thermoplastics. On the other hand, extrinsic damage appears in front of the crack and is the main source of toughening in quasi-brittle materials such as thermoset FRPs. Fiber-bridging, matrix cracking and fiber pull-outs are some of the processes considered as extrinsic damage [15, 16], which occur in the fracture process zone (FPZ). Fiber-bridging is considered the most efficient of these to reduce the strain/stress level at the crack tip [15, 17] and thus increase the SERR value required to further extend the crack. This behavior is reflected in the resistance curves (R-curves) which typically present initially increasing SERR values for small crack lengths, and then reach a steady-state plateau for crack lengths corresponding to fully developed fiber-bridging [17, 18]. When the length of the fiber-bridging is comparable to or greater than one of the dimensions of the specimen/component in which the crack is propagating (usually called large-scale bridging, LSB), the R-curve has been proved to be size and geometry dependent [19-21]. The prediction of the structural response by means of linear elastic fracture mechanics (LEFMs) only applies for small FPZs where the damage can be reduced to one point (the crack tip), i.e. no significant extrinsic mechanisms develop. If this condition does not apply, more complex methods are required [22-24]. Cohesive zone models (CZMs) [25-27] have been widely and successfully used for the simulation of fracture in many quasi-brittle materials [14] and have been proved particularly accurate in cases of materials developing a long FPZ with a high fiber-bridging contribution [28, 29]. In the cohesive model the cohesive stresses (also named tractions) inside the FPZ tend to close the crack. The cohesive law describes the evolution of these tractions as a function of the crack-opening displacement. Based on this, the bridging fibers are considered as tractions along the bridging length, resulting in the so-called bridging law [24] that has usually been considered as a material property regardless of the size and geometry of the system [19, 30, 31]. This implies the assumption of the value of the SERR at the steady state as a material property [32]. Nevertheless, as previously mentioned, the R-curves of materials presenting LSB are strongly dependent on the specimen's geometry and therefore any experimentally or numerically derived bridging law cannot be considered as a material property. Although some studies have described effects of thickness variation in the increasing part of the R-curves [28], recent investigations [15, 17, 32, 33] have also reported a high influence of this parameter on the steady-state SERR value (plateau of the R-curve) of DCB specimens, proving a considerable influence of stiffness in the development of the fracture mechanisms and fiber-bridging in particular. Micromechanical models of DCB specimens with different

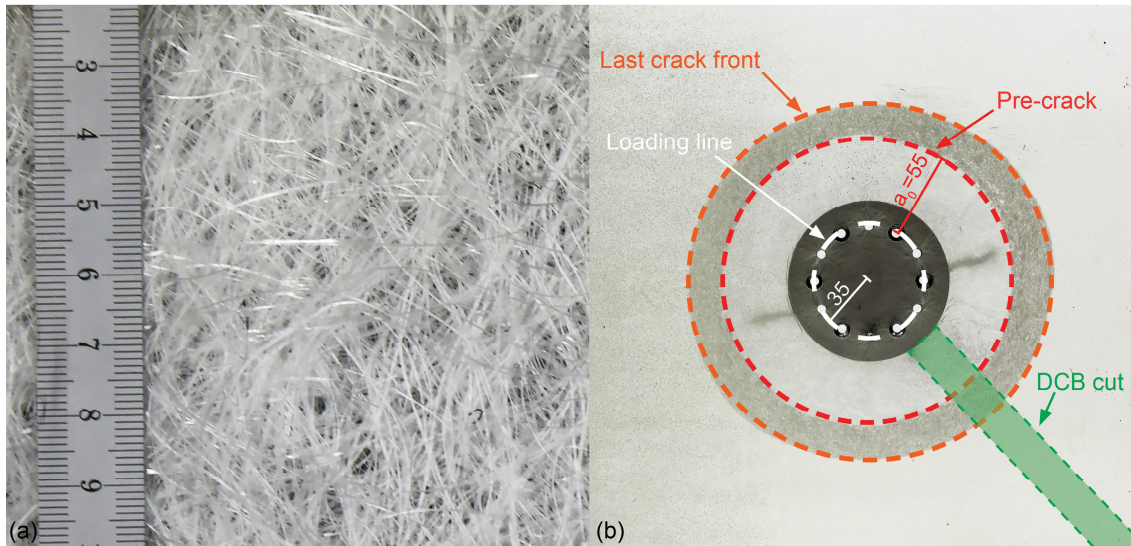


Figure 3.1 – Detail of glass fiber reinforcement (a) and crack propagation pattern in plate CFM.1 (b). Units in mm

thicknesses were developed in [15] showing that the extension of the fiber-bridging was dependent on the curvature of the arms. Thicker, therefore stiffer, and less curved arms presented longer bridging lengths and thus increased fiber-bridging.

The experimental fracture behavior of laminated FRP plates with an embedded circular pre-crack (i.e. 2D delamination) and subjected to quasi-static out-of-plane opening loads – similar to the loads applied in a DCB – was investigated in [34]. The results of these experiments showed that due to the boundary conditions inherent to an embedded pre-crack growing in a plate, stretching stresses appeared in the circumferential and radial directions resulting in a stiffening of the plate, in addition to the general increase in the flexural stiffness that occurs due to the transition from the (1D) beam to the (2D) plate configuration [34].

The objective of this work was the numerical investigation of the 2D in-plane crack propagation in two of the laminated plates presented in [34], in order to better understand the nature of the aforementioned additional stiffening effects and the associated mechanisms. The material system of the selected plates was glass/epoxy with a long continuous filament mat reinforcement whose nature led to the development of a considerable amount of fiber-bridging. For the sake of comparison and to understand the transition from standard 1D fracture experiments to 2D crack propagation scenarios, DCB specimens with different widths were further experimentally investigated. Three-dimensional finite element models were developed to simulate the experimental fracture responses of the plates and the DCBs using cohesive elements to take into account the fracture mechanisms acting on the FPZ. The influence of the parameters of the traction-separation laws on the load-displacement curves of the two investigated configurations was analyzed.

## 3.2 Experimental methods

### 3.2.1 Previous experimental investigation of laminated plates

The 2D delamination behavior of FRP laminated plates under quasi-static out-of-plane opening loading was experimentally investigated in [34]. The experimental program was conducted on twelve GFRP/epoxy plates comprising different glass reinforcements. The investigation presented here involves the two plates with six layers of long continuous glass filament mat reinforcement (CFM). A detail of the fiber reinforcement is given in Figure 3.1(a) and the properties of the glass fibers and epoxy resin are given in Table 3.1 (manufacturer data [35, 36]). The plates were fabricated using a vacuum infusion process with an embedded circular pre-crack in the center and at the midplane. The layup and geometrical description are presented in Table 3.2 and the crack propagation pattern obtained for one of the plates is shown in Figure 3.1(b). An example of the experimental set-up for the CFM.2 plate is presented in Figure 3.2(a). Due to the high translucency of the laminates, the crack tip could be precisely identified through the occurring whitening of the delaminated areas. To monitor the position of the crack tip three different measuring systems were employed: a 3D Digital Image Correlation System (DIC), a digital camera and visual measurements (see Figure 3.2 (a, b)). Eight rulers starting from the end of the pre-crack were drawn on the plates corresponding to eight directions of propagation, named after the cardinal directions (see “Crack measuring system” in Figure 3.2(a)). The propagation along the east (“E”) direction was measured by the DIC system (0.2 Hz of acquisition frequency and accuracy of  $\pm 0.005$  mm). The direction of propagation monitored with the digital camera (also acquisition frequency of 0.2 Hz) was northwest (“NW”). Along the remaining directions, the crack front was recorded visually and in-situ during the experiments. From these experimental values, average curves (one per plate) of radial

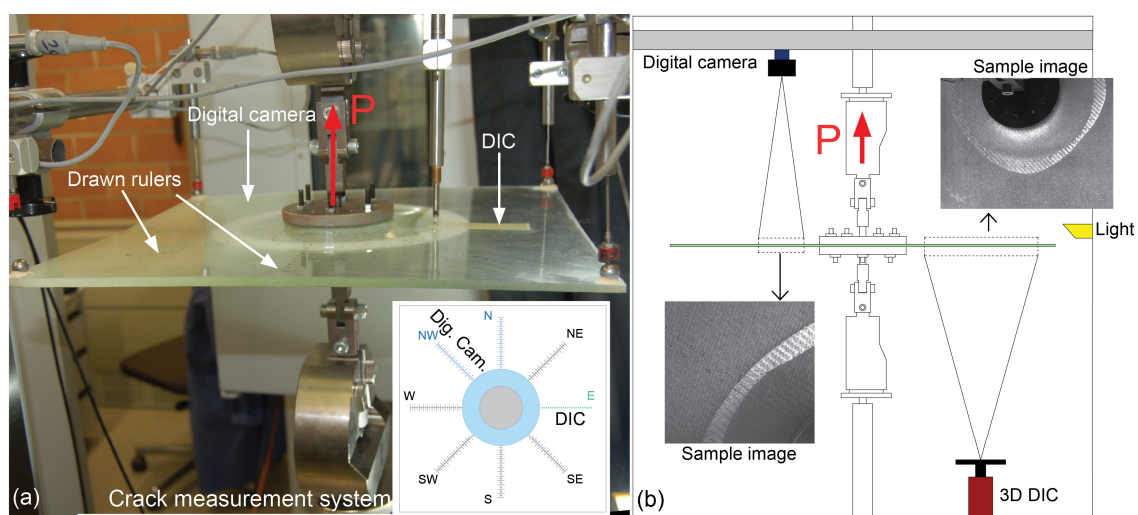


Figure 3.2 – Experimental set-up; (a) experiment on CFM.2 AND crack measuring system layout; (b) layout of set-up

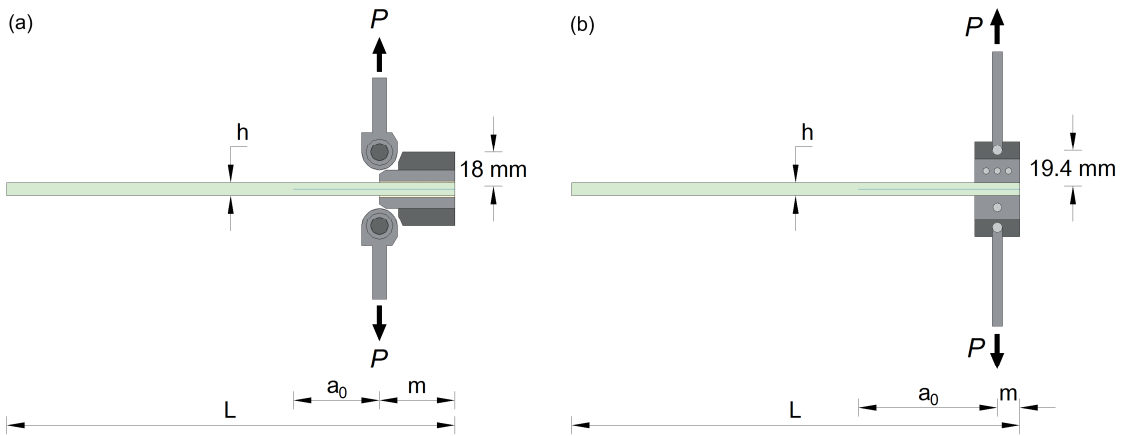


Figure 3.3 – DCB configurations; (a) in-house developed loading blocks (piano hinges); (b) patented [37] loading blocks; dimensions see Table 3.4.

> Table 3.1 – Material properties

Material	$E$ (GPa)	$G$ (GPa)	$\nu$ (-)	$\rho$ (g/cm <sup>3</sup> )
Epoxy resin	2.96	1.30	0.35	1.14
E-CR <sup>*</sup> glass	80.00	32.80	0.22	2.62

<sup>\*</sup>Corrosion-resistant

> Table 3.2 – Description of GFRP laminated plates

Plate type	No. of layers	Dimensions (mm) (width x height x avg. thickness)
CFM.1	6	420 x 420 x 7.50
CFM.2	6	420 x 420 x 6.99

crack length were obtained and used to derive a continuous progression of the circular crack area. The load and opening displacement were obtained from the machine (W+B electromechanic machine of 50-kN capacity,  $\pm 0.11\%$  accuracy). Further details concerning the measuring methodologies can be found in [34].

A DCB specimen of 25-mm width and 220-mm length was radially cut from the CFM.1 plate, see Figure 3.1(b), to perform a cantilever beam bending test at different clamping distances on the un-cracked region and derive the in-plane E-moduli of the plate. An experimental value of 8.64 GPa was obtained and used in the numerical model of the plates. This value differed by less than 10% from the analytically estimated value (see [34]) (see Table 3.3). The in-plane shear modulus was calculated for an isotropic material with a previously estimated in-plane Poisson ratio and the remaining out-of-plane properties were assumed to be the estimated values. These updated values were used for all the numerical simulations of the plates presented.

&gt; Table 3.3 – Elastic properties of laminated plates

	$E_1 = E_2$ (GPa)	$E_3$ (GPa)	$G_{12}$ (GPa)	$G_{13} = G_{23}$ (GPa)	$\nu_{12}$ (-)	$\nu_{13} = \nu_{23}$ (-)
Estimated in [34] (CFM.1)	9.34	4.68	3.51	1.54	0.33	0.30
Used in FEM	8.64*	4.68	3.25*	1.54	0.33	0.30

\* Updated values from the DCB test

&gt; Table 3.4 – Geometrical and elastic properties of fracture mechanics (DCB) specimens

	$b$ (mm)	$h$ (mm)	$L$ (mm)	$m$ (mm)	$a_0$ (mm)	$E_1 = E_2$ (GPa)	$E_3$ (GPa)	$G_{12}$ (GPa)	$G_{13} = G_{23}$ (GPa)	$\nu_{12}$ (-)	$\nu_{13} = \nu_{23}$ (-)
DCB-25 #1-2	25	7.64	250	42	50	9.22					
DCB-25-3*	25	7.50	220	12.50	42	8.64					
DCB-40 #1-2	40			42	50		4.64	3.47	1.54		
DCB-40 #3-5	40	7.64		25	30	9.22				0.33	0.30
DCB-60 #1-3	60		250	42	50						
DCB-100 #1-3	100	6.80		42	50	10.03	4.90	3.77	1.57		

\*Specimen cut from plate CFM.1, see Figure 3.1(b)

### 3.2.2 Experimental investigation of Mode I DCB specimens

Double cantilever beam (DCB) specimens were used to determine the Mode I SERR (see Figure 3.3). The same material system (long continuous glass filament mat reinforcement/epoxy resin) and lay-up (six layers of 600 g/m<sup>2</sup>) as those of the previously studied plates were used. A vacuum infusion process was employed for fabrication of the laminates and a Teflon film of 13- $\mu$ m thickness was placed at the midplane to introduce the pre-cracks. The infusion and curing protocols were identical to those of the plates (see [34] for further details). Once cured, the DCB specimens were cut from the laminates by means of a water jet machine. Specimens of four different widths,  $b$ , (25, 40, 60 and 100 mm) were investigated to determine any possible influence of this parameter on the experimental SERR. Two fabrications were carried out and due to small differences in the vacuum level of the pump, small discrepancies in thickness,  $h$ , and consequently in the E-modulus existed. Specimens of 25- and 40-mm width were cut from the first fabrication, with an average thickness value of 7.64 $\pm$ 0.01-mm while specimens of 60- and 100-mm width were cut from the second fabrication, with a corresponding average thickness of 6.80 $\pm$ 0.01-mm. As mentioned above, another DCB specimen of 25-mm width (DCB-25-3) was cut directly in the radial direction from the CFM.1 plate.

To allow the transfer of the load from the loading frame to the specimens, two different types of loading blocks were used. For all the DCB specimens except DCB-25-3, adhesively-bonded “in-house fabricated” piano-hinged loading blocks (see Figure 3.3(a)) were employed.



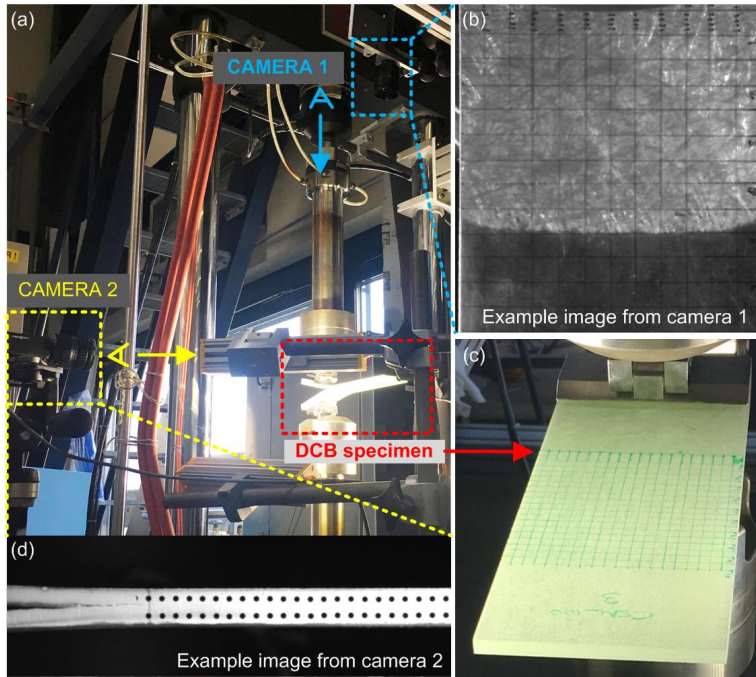


Figure 3.4 – DCB experimental set-up; (a) general view; (b) example of image from upper camera (Camera 1 in (a)); (c) DCB specimen with drawn grid ruler used for measurement of crack length; (d) example of image from side camera (Camera 2 in (a))

For specimen DCB-25-3, patented [37] mechanically-fixed loading blocks were used (Figure 3.3(b)). The geometrical and elastic properties of the DCB specimens are presented in Table 3.4.

The experiments were performed under displacement-control on a 100-kN MTS Landmark servo-hydraulic testing rig with a load cell of 25 kN calibrated to 20% of its maximum capacity at a rate of 2.5 mm/min. All the experiments were conducted under laboratory conditions,  $21 \pm 3^\circ\text{C}$  and  $40 \pm 10\%$  RH.

The experimental set-up and instrumentation layout are shown in Figure 3.4(a). The crack length was monitored with a digital camera (camera 1 in Figure 3.4(a)) placed above the highly translucent specimens focusing on the grid ruler drawn over the upper surface (see Figure 3.4(b and c)). The grid size was set to 1 mm over the first centimeter after the crack tip and to 5 mm over the rest of the length. The acquisition frequency was set to 0.2 Hz and each picture was registered with the corresponding load and displacement values recorded by the machine (accuracy of  $\pm 0.5\%$ ). Additionally, in order to monitor the bridging length from the side of the specimens, a second digital camera (camera 2 in Figure 3.4(a)), also synchronized with the machine, was used. The same acquisition frequency was set and the opening displacement between the arms was monitored by pairs of black dots (with an accuracy of  $10^{-5}$  m) marked at equal intervals of around 2 mm on the upper and lower lateral surfaces of the specimens (see Figure 3.4(d)).

### 3.3 Numerical methods

#### 3.3.1 Description of numerical model of laminated plates

A finite element (FE) model was developed to simulate the delamination behavior of the CFM plates using the commercial finite element analysis (FEA) software ABAQUS 6.14.1. The dimensions of the model are presented in Figure 3.5. The built-in continuum shell element of eight nodes and reduced integration (CS8R) from Abaqus/Standard was used to mesh the GFRP bulk material [38]. Two through-thickness elements were assigned to each of the halves (in relation to the midplane) of the plate, which, after a sensitivity analysis, proved to be sufficient to capture the bending behavior accurately. A single zero-thickness layer of three-dimensional cohesive elements of eight nodes (Abaqus COH3D8 [38]) was implemented at the midplane of the un-cracked region (Figure 3.5). To assure a correct dissipation of energy during delamination, a minimum of fifteen elements in the cohesive zone length (CZL) (i.e. the length along the plane of the crack along which the cohesive forces were acting) was guaranteed throughout the analysis [39]. The greatest dimension of the elements of the model varied from 0.6 mm in the un-cracked region close to the pre-crack to 4 mm at the boundaries. The engineering constants used to define the bulk material are presented in Table 3.3. The nonlinear geometry (NLGEOM) option was used to account for large deformation effects.

Two symmetry planes (D1 and D2) coincident with the diagonals of the plates were considered and therefore corresponding symmetric boundary conditions were applied (see Figure 3.5). The steel inserts and external loading blocks [34] were not explicitly modeled. Instead, the nodes of the inner faces of the loading areas (spanning from the center of the plates to the loading circumference, i.e. a radius of 35 mm, “referenced areas” in Figure 3.5 and [34]) were tied by means of a rigid body condition [38] to reference points (indicated in Figure 3.5) where the boundary conditions were applied. An out-of-plane displacement condition (in-plane displacements constrained) was

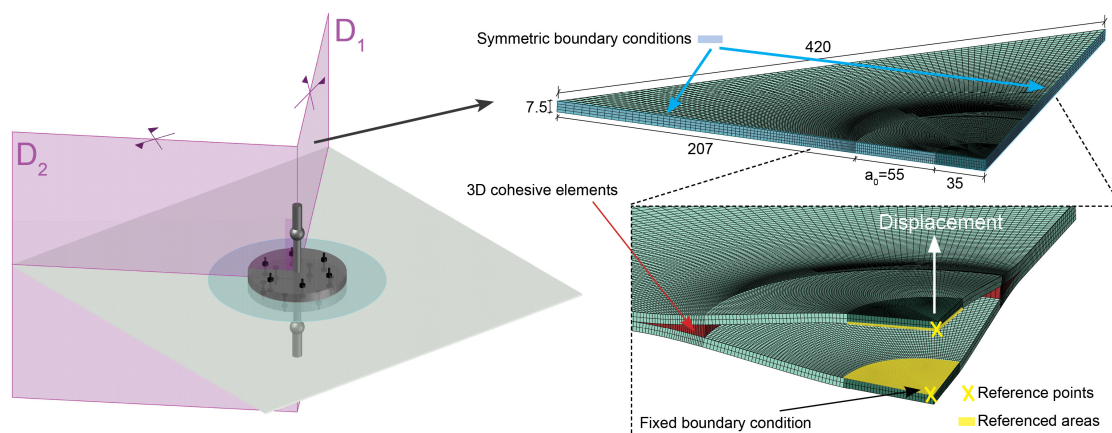


Figure 3.5 – Description of finite element model of laminated plate



applied to the upper reference point and a pinned condition (all displacements constrained) to the bottom reference point. To capture the behavior of the complex loading system, whose rotations were partially impeded due to the upper and lower external steel plates, equivalent in-plane E-moduli and shear modulus, stiffer than the values used for the bulk material (see Table 3.3), were calibrated for these regions by an iterative procedure to fit the initial slope of the experimental curves. Resulting fitted values were  $E_1=E_2=42$  GPa and  $G_{12}=15.8$  GPa. The model comprised 75,146 nodes and 56,664 elements. As in the experiments, the boundary edges of the plate were free.

To determine any possible contribution of shear fracture modes (Mode II and Mode III) in addition to the obvious opening fracture mode (Mode I), the shear displacements in the cohesive elements were also computed. Insignificant and close-to-zero values were always obtained assuring a pure opening mode propagation of the crack.

### 3.3.2 Description of numerical model of DCB specimens

For the numerical simulation of the DCB experiments, the FEA software ABAQUS 6.14.1 was also employed. The two GFRP beams were modeled with 3D built-in continuum shell elements (CS8R) as for the plate and a single zero-thickness layer of three-dimensional cohesive elements (Abaqus COH3D8 [38])) was also implemented at the midplane in the un-cracked region. A minimum of ten cohesive elements in the cohesive zone length (CZL) are guaranteed for these models. Likewise, the greatest dimension of the elements varies from 0.83 mm in the un-cracked zone to 0.26 mm close to the pre-crack. The loading blocks were not modeled and the DCBs were only simulated from the loading line onwards (i.e. according to Figure 3.3, only from  $a_0$ ). The boundary conditions were applied at the bottom (pinned condition) and top edges (out-of-plane opening displacement condition). The engineering constants used to define the bulk material are listed in Table 3.4 and as for the plates, the nonlinear geometry (NLGEOM) option was used to account for large deformation effects. One FE model for each of the DCB configurations presented in Table 3.4 was performed.

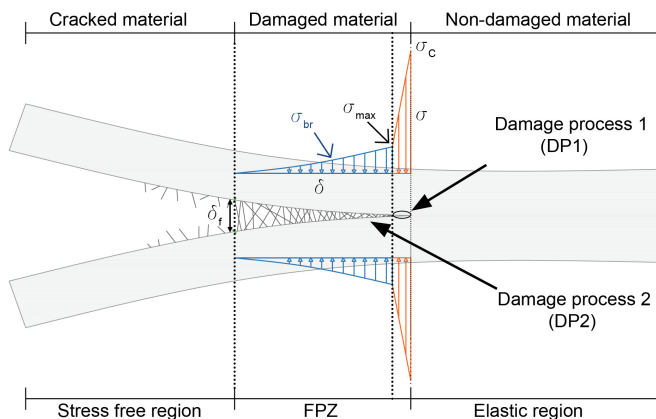


Figure 3.6 – Schematic general fracture section of Mode I delamination with fiber-bridging

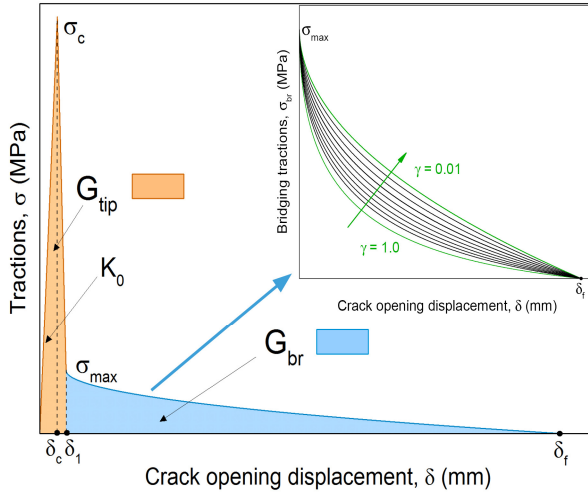


Figure 3.7 – Description of traction-separation law

### 3.3.3 Cohesive zone modeling

In Mode I delamination, cohesive elements are defined by their “traction-separation” response where the normal traction,  $\sigma$ , over the fracture process zone (FPZ) is a function of the local crack-opening displacement  $\delta$  as illustrated in Figures 3.6-3.7. Once the FPZ is fully developed, the maximum crack opening,  $\delta_f$ , is achieved and tractions vanish. Two different damage processes can be distinguished in composite materials in the presence of fiber-bridging. The first is related to damage and micro-fractures of the matrix (epoxy) in the process zone in front of the crack tip (DP1 in Figure 3.6) while the second corresponds to the fiber-bridging behind the crack (DP2). As investigated in literature [18, 29], the traction-separation law suitable for the simulation of delamination under the effect of fiber-bridging is the result of the combination of i) the traditional cohesive law, where damage evolves according to a linear softening (from damage initiation traction,  $\sigma_c$ , to the maximum bridging traction,  $\sigma_{max}$ ), and ii) the bridging law, where damage evolves according to bridging stress functions (from  $\sigma_{max}$  to zero tractions). The former corresponds to the initial part of the traction-separation law in Figure 3.6 (in orange) and the latter to the second part (in blue). The traction-separation law used in this work to define the behavior of the cohesive elements is shown in Figure 3.7. The first part of the law (in orange) is attributed to the initial damage growth in the DP1 zone and the area under this bilinear part equals the strain energy release rate (SERR) at the crack tip,  $G_{tip}$ , corresponding to the energy required for crack initiation. The second part (in blue) corresponds to the SERR due to the fiber-bridging,  $G_{br}$ . The addition of these two SERR values equals the total area under the traction-separation law, which will be referred hereafter as  $G_{tot}$  (i.e.  $G_{tot} = G_{tip} + G_{br}$ ). The bridging tractions are given by [18]:

$$\sigma_{br}(\delta) = e^{-\gamma\sqrt{\delta-\delta_c}} \sigma_{max} \left( 1 - \sqrt{\frac{\delta-\delta_c}{\delta_f-\delta_c}} \right), \quad \delta_c \leq \delta \leq \delta_f \quad (3.1)$$

where  $\delta$  is the crack-opening displacement (COD),  $\sigma_{max}$  and  $\delta_l$  are the maximum bridging traction and the corresponding COD and  $\delta_f$  is the COD at the end of the bridging zone. Likewise,  $\gamma$  is the parameter governing the bridging tractions' profile. As can be observed in the zoom of the bridging tractions in Figure 3.7, the smaller the value of  $\gamma$  (for fixed values of  $\sigma_{max}$  and  $\delta_f$  the greater the area under the curve, and thus the greater the value of  $G_{br}$ ). The overall traction-separation response is defined as:

$$\sigma = (1 - D(\delta))K_0 \delta \quad (3.2)$$

$$D(\delta) = \begin{cases} 0 & \text{for } 0 \leq \delta \leq \delta_c \\ 1 - \frac{\alpha\delta + \beta}{K_0\delta} & \text{for } \delta_c \leq \delta \leq \delta_l \\ 1 - \frac{\sigma_{br}}{K_0\delta} & \text{for } \delta > \delta_l \end{cases} \quad (3.3)$$

where  $\sigma_c$  is the general cohesive traction,  $D$  is the damage,  $K_0$  is the initial cohesive stiffness and  $\alpha$  and  $\beta$  are:

$$\alpha = \frac{\sigma_c - \sigma_{max}}{\delta_c - \delta_l} \quad (3.4)$$

$$\beta = \sigma_c - \alpha\delta_c \quad (3.5)$$

where  $\sigma_c$  and  $\delta_c$  are the corresponding values of the traction and COD for damage initiation.

The presented traction-separation law was implemented in the FE model by means of a user material subroutine (UMAT) written in FORTRAN programming language. The damage definition ( $D(\delta)$ ) was changed according to the formulation presented (Equations 3.2-3.5). Details and theoretical background of the formulation of the original UMAT can be found in [40, 41].

### 3.4 Experimental results and discussion

#### 3.4.1 Experimental results for laminated plates

The experimental results previously obtained for the two laminated plates under study in this investigation (CFM) are summarized in the following. In Figure 3.8 the load vs displacement and average crack-length vs displacement curves are shown for CFM plates.

In Figure 3.8 it can be observed that, even after crack initiation, a continuously increasing load-opening displacement behavior was obtained up to specimen failure. This behavior differed from the load-displacement behavior in fracture mechanics experiments such as DCB, where the load tends to decrease during crack propagation, due to the different crack growth pattern observed in each system. In a DCB (or any beam-like fracture experiment) the length of the crack front remains almost constant and perpendicular to the direction of propagation for each increment in the length of

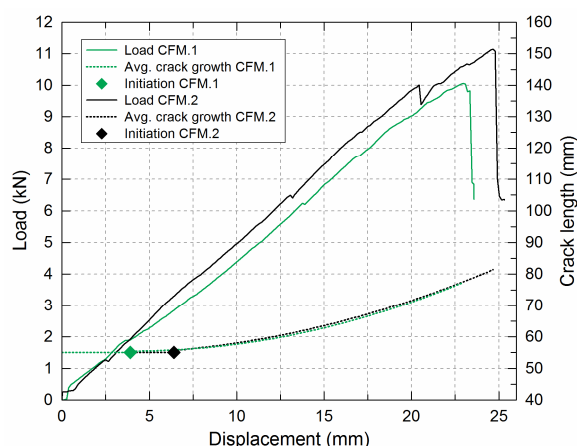


Figure 3.8. – Load and crack length vs opening displacement curves of CFM plates

the crack and therefore the cracked area grows proportionally to the crack length. However, in a 2D fracture experiment, the crack front (perimeter of the concentric circles) increases for each increment in the radial direction, causing a non-proportional growth of the crack area in relation to the propagation distance and forcing the load to increase to maintain the crack propagation (i.e. more energy is needed to advance the crack by the same increment). This difference in the growth of the area of the crack between the two configurations is presented in Figure 3.9 using the numerical results of the plate and of the DCB-40(1-2). The crack areas represented in this figure correspond to propagated crack areas and therefore the area of the pre-cracks is not considered. To compare the results, the crack area in the DCB was calculated by considering a width equal to the length of the perimeter of the pre-crack in the plate ( $2\pi \cdot 90$  mm) (see Figure 3.9). In the horizontal axis two values can be read: crack length for the DCB and crack radius for the plate. It can be observed that the growth of the crack area is greater in the plate than in the equivalent DCB and how this difference increases as the crack propagates.

The curves illustrating the crack area vs the compliance (calculated as  $\delta/P$ ,  $\delta$  being the opening displacement and  $P$  the load) of the plates are shown in Figure 3.10. The area was calculated for each increment as the area between the crack front and the loading line, i.e. a 35-mm radius circle passing through the center of the screws that constitute the loading points (see Figure 3.1). Based on the compliances, two main different regions could be differentiated (A and B in Figure 3.10). In region A, a decreasing behavior of the compliance was observed (i.e. stiffening of the plate) down to a minimum value (transition point, TP). From the TP onwards (Region B), the compliance started to increase (i.e. softening of the plate). The decreasing behavior of region A in the curve of the CFM.2 plate was however less accentuated than for the CFM.1 plate.

The initial ascending branch of the compliance curve immediately after crack initiation was attributed to an initial readjustment between the loading system and the specimen. The changes in the stiffness were caused by three different mechanisms

activated during the opening of the plates: stretching, fiber-bridging and crack propagation. Two curvatures could be distinguished as the plate opened: the radial and the circumferential. The frame-like boundary of the plates, i.e. the undamaged zone around the crack which did not deform and thus acting like a frame, led to the radial stretching of the out-of-plane deforming open part of the plates. Likewise, as the crack was embedded in the plate, the elongation in the circumferential direction during the out-of-plane deformation was also constrained, causing the corresponding circumferential stretching. Therefore, the plate was subjected to a biaxial stretching and thus a biaxial stiffening effect. Once the crack started propagating, the other two mechanisms were activated: the fiber-bridging, contributing to the stiffening of the plate, and the crack propagation itself, causing the softening of the system. The stiffening mechanisms prevailed over the softening up to the TP. Beyond the TP, the softening was the dominant mechanism. Typically, for a standard (1D) fracture experiment, crack propagation is the dominant mechanism after crack initiation, always leading to an upward trend of the compliance curve. Further discussion and details can be found in [34].

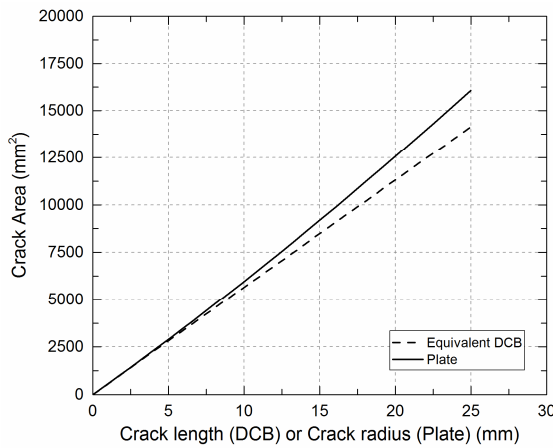


Figure 3.9 – Comparison of growth of crack area in plate and equivalent DCB

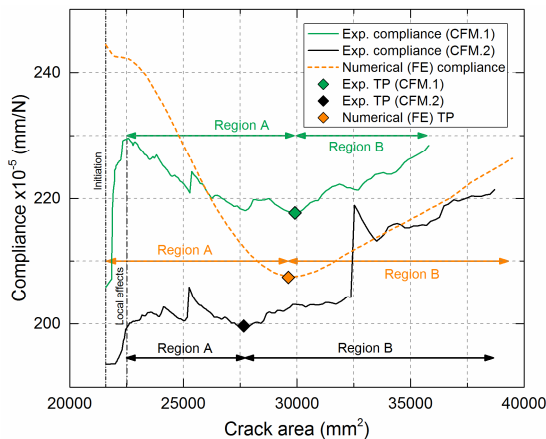


Figure 3.10 – Comparison of experimental and numerical crack area vs compliance of CFM plates

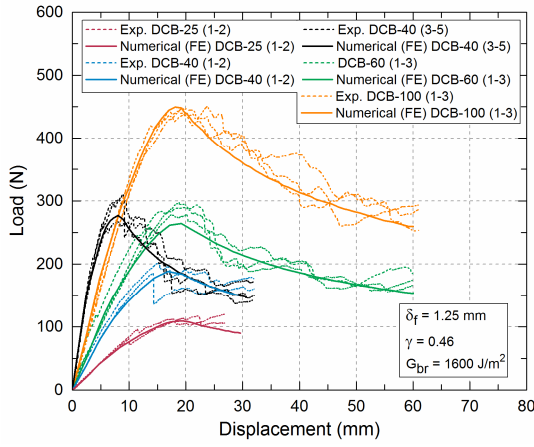


Figure 3.11 – Comparison of experimental and numerical load-displacement curves of DCBs

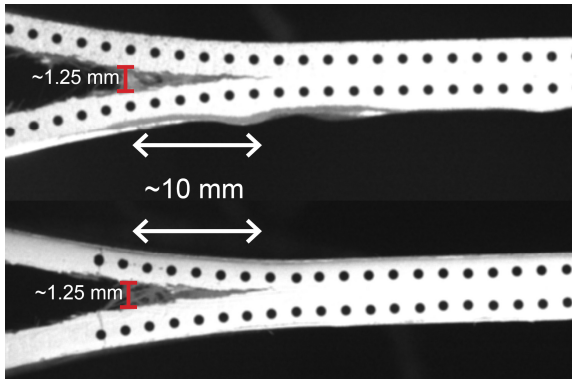


Figure 3.12 – Fiber-bridging zone; (a) DCB-25-2; (b) DCB-60-2

### 3.4.2 Experimental results for DCB specimens

The experimental load-displacement responses of the new set of DCB specimens described in Section 3.2.2 are presented in Figure 3.11. Typical curves of this type of specimens (increase of the load up to a maximum followed by decrease) can be observed. Representative side views of the fiber-bridging for two specimens are presented in Figure 3.12. For the calculation of the total SERR of the specimens,  $G_{tot}$ , the experimental compliance method (ECM) was used. The  $G_{tot}$  derived from the experiments is the sum of the SERR at the crack tip,  $G_{tip}$ , and the SERR due to the fiber-bridging,  $G_{br}$ . The expression used for the calculation based on the experimental compliance was the following [42]:

$$G_{tot} = G_{tip} + G_{br} = \frac{P^2}{2b} \frac{\partial C}{\partial a} \quad (3.6)$$

where  $P$  is the load,  $b$  is the specimen width,  $C$  is the compliance and  $a$  is the crack length. The R-curves obtained for all the DCB specimens are shown in Figure 3.13. According to these curves, values of 400 J/m<sup>2</sup> and 2000 J/m<sup>2</sup> respectively were assigned to  $G_{tip}$  and  $G_{tot}$ . The length of the fiber-bridging observed in the side views of the

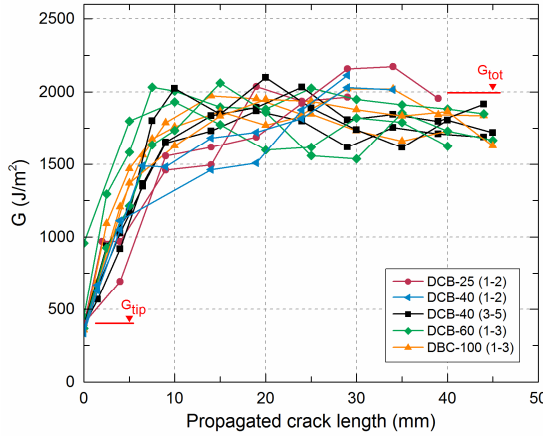


Figure 3.13 – Experimental R-curves obtained from DCB specimens

specimens (see Figure 3.12) are in good agreement with the lengths inferred from the R-curves (i.e. the crack length corresponding to the starting point of the plateau of the crack propagation value, see Figure 13). A value of  $\sim 10$  mm for the fiber-bridging length was obtained along with a maximum COD,  $\delta_f$ , of  $\sim 1.25$  mm (see Figure 3.12). Likewise, as can be observed in Figure 3.13, similar R-curves were obtained (considering the typical scatter) regardless of the width.

### 3.5 Numerical results and discussion

#### 3.5.1 DCB specimens

The traction-separation law described in Section 3.3.3 was implemented in the cohesive elements of the FE model developed for the DCB specimens presented in Section 3.3.2. The experimentally obtained SERR values of  $G_{tip}=400$  J/m<sup>2</sup> and  $G_{tot}=2000$  J/m<sup>2</sup> (i.e.  $G_{br}=1600$  J/m<sup>2</sup>) and the maximum COD ( $\delta_f=1.25$  mm) were assigned. According to [43, 44], the maximum traction for damage initiation was assumed to be equal to 30% of the tensile strength of the matrix (84 MPa, manufacturer data [36]), i.e.  $\sigma_c=25.2$  MPa. The initial cohesive stiffness,  $K_0$ , was taken as being equal to 100,000 MPa/mm [40] and the resulting value of  $\delta_i$  was 0.027 mm. The values of the maximum bridging traction,  $\sigma_{max}$ , and the bridging traction decay ratio,  $\gamma$ , were estimated iteratively to fit the numerical with the experimental load-displacement responses. Corresponding values of  $\sigma_{max}=5$  MPa and  $\gamma=0.46$  were obtained to maintain the  $G_{tot}$  equal to 2000 J/m<sup>2</sup>. The same traction-separation law was used for all DCB specimens and is presented in Figure 3.14. The numerical load-displacement curves obtained for the new set of DCB specimens are shown in Figure 3.11. As can be observed, the experimental curves are in good agreement with the numerical prediction.

As mentioned in Section 3.2.2, a wide range of DCB specimen widths was selected in order to study the influence of the width on the total SERR. As previously described, the reinforcement is composed of long continuous glass filaments randomly distributed



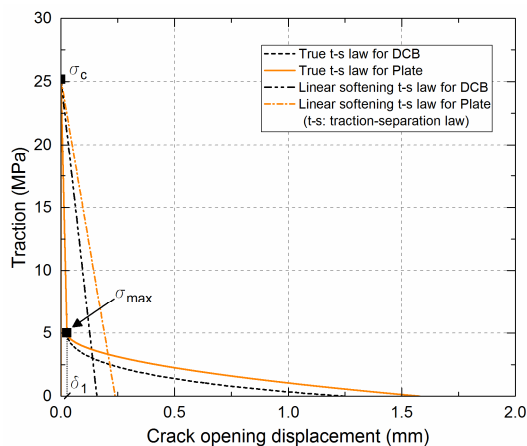


Figure 3.14 – Traction-separation curves used in numerical models

in-plane and although no influence of the width has been reported in the literature for unidirectional-fiber DCB specimens, a possible effect of the anchorage length (which increases with width) on the fiber-bridging behavior was considered. However, in view of the experimental R-curves presented in Figure 3.13 and the validity of the same bridging parameters for all specimens (see numerical load-displacement curves in Figure 3.11), it can be concluded that the width of the DCB specimens has no influence on the fracture results, at least in the range investigated here. Therefore, the development of the fiber-bridging has been proved to be independent of the length of the fibers in mat-like reinforcements.

### 3.5.2 Laminated plates

The same type of traction-separation law was implemented in the cohesive elements of the FE model of the plates. Initially, the same traction-separation law obtained for the DCB specimens was used (see Figure 3.14), the total value of the SERR being therefore equal to  $G_{tot}=2000 \text{ J/m}^2$ . However, the numerical load-displacement response obtained with these values did not correspond to the experimental curves, leading to an underestimation of the experimental load, as shown in Figure 3.15. In order to better approach the experimental behavior, a fitting process was carried out. The values of  $K_0$ ,  $G_{tip}$ ,  $\sigma_c$  and  $\sigma_{max}$  (typically matrix-dominated values) were kept constant and the same as those obtained from the DCB specimens. The adjustment of the law was accomplished by fitting the value of  $G_{br}$  and therefore modifying the values of  $\gamma$  and  $\delta_f$ . The selected values that allowed the FE model to predict the experimental behavior were  $\gamma=0.01$  and  $\delta_f=1.58 \text{ mm}$  which lead to a  $G_{br}$  value of  $2600 \text{ J/m}^2$  and therefore to a  $G_{tot}$  value of  $3000 \text{ J/m}^2$ . The obtained traction-separation law is presented in Figure 3.14. The revised numerical load-displacement and crack length-displacement curves are shown in Figure 3.16. A very good agreement with the experimental results was obtained. The numerically determined initiation of the crack (see Figure 3.16) was taken as the point where the first cohesive element reached a COD equal to  $\delta_f=0.027 \text{ mm}$  (see Figure 3.7 and Figure 3.14) and therefore the point where the SERR equaled  $G_{tip}$ . It can be observed

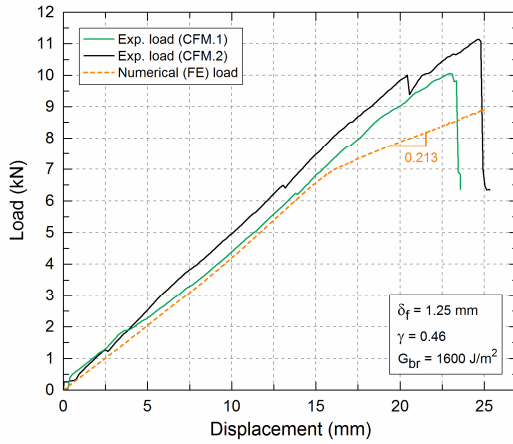


Figure 3.15 – Comparison of experimental and numerical load-displacement curves of CFM plates using cohesive parameters and total SERR from DCBs

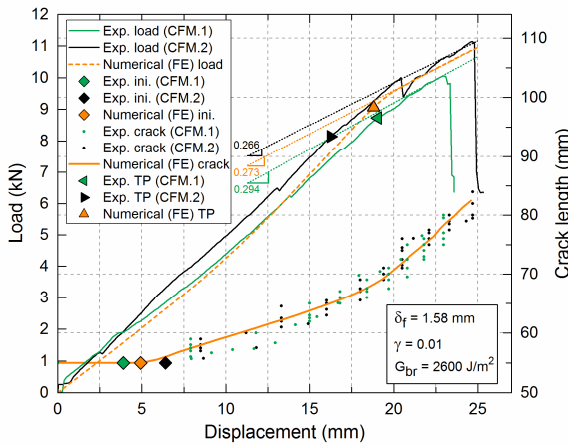


Figure 3.16 – Comparison of experimental and numerical load and crack lengths vs opening displacement curves of CFM plates

that the numerical initiation value was between the experimental initiation values of the two plates, proving that the initial part of the traction-separation law (up to  $\delta_i$  in Figure 3.7) is independent of any size or geometry change. The second part of the law (from  $\delta_i$  to  $\delta_f$  in Figure 3.7) was however the varying part, proving that the fiber-bridging is not a material property and is likely to vary under different configurations of the same material system.

In Figure 3.10 the numerical compliance vs crack area is shown, also presenting good agreement with the trend of the experimental curves. The initial increasing behavior of the experimental compliance was not reproduced in the numerical results, proving that its attribution to local slipping effects was correct. The TP (see Section 3.4.1) is indicated in both the experimental and numerical curves. As for the initiation value in Figure 3.16, the numerical TP was between the two experimental results, also obtaining a good agreement with the latter.

The numerically derived R-curve is shown in Figure 3.17. The numerical value of the crack area at the TP in Figure 10 coincides with the numerical value of the fully developed bridging area in the numerical R-curve (see Figure 3.17). Consequently, with

the value of the area at the TP obtained from the compliance vs crack area curve, the value of the bridging area of the plate can be directly obtained. The numerical value of this crack area was  $\sim 29600 \text{ mm}^2$  which corresponded to a propagated radial length measured from the front of the pre-crack of  $\sim 13.2 \text{ mm}$ . As described in Section 3.4.1, the TP corresponds to the change in behavior of the compliance when the general softening due to the propagation of the crack dominated over the stiffening mechanisms (stretching and fiber-bridging). Therefore, as a result of the identification of the fully developed bridging area with the TP, any decrease or increase in the bridging area would lead the compliance vs crack area curve moving to the left or right respectively (Figure 3.18). The initiation point, proved to be a material property, would not change. Moreover, this correspondence between the TP and the full development of the fiber-bridging justifies the change of the increasing load-displacement curve from non-linear to linear (see TPs in Figure 3.16). Before the TP the stiffening mechanisms were dominant and therefore the load increased non-linearly. However, the TP was the point where the softening started to dominate and the fiber-bridging was fully developed, achieving an equilibrium between stiffening and softening and entering the plateau of the R-curve (Figure 3.17). Therefore, the linearization of the increasing load (beyond the TP) can be related to the stabilization of the crack propagation.

The fitting of the traction-separation law revealed a dependency between the slope of the load after the TP and the value of  $G_{br}$  (controlled by the parameters  $\gamma$  and  $\delta_f$ ) and therefore between the values of TP and  $G_{tot}$ . The slope obtained with a value of  $G_{tot}=2000 \text{ J/m}^2$  was 0.213 (see Figure 3.15) while the slope obtained with a value of  $G_{tot}=3000 \text{ J/m}^2$  was 0.273 (see Figure 3.16). Thus the greater the value of  $G_{tot}$ , the greater the value of the slope. Likewise, the numerical slope was also between the two experimental values (0.266 and 0.294).

The total value of the SERR obtained from the FEM of the plates was 50% higher than the total SERR derived from the DCB specimens, increasing from  $2000 \text{ J/m}^2$  to  $3000 \text{ J/m}^2$ . This increase in the  $G_{tot}$ , and thus in the R-curve, was directly related to the

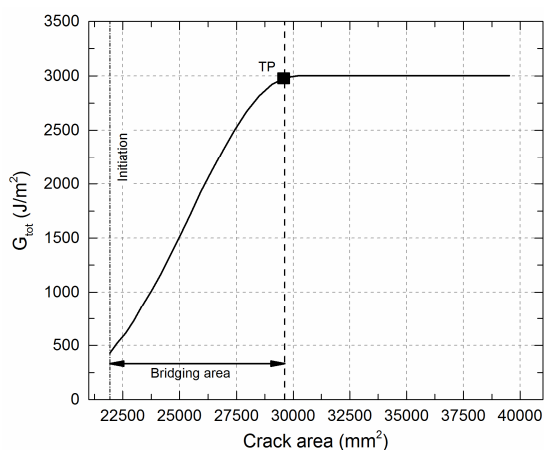


Figure 3.17 – Numerical R-curve of laminated plate

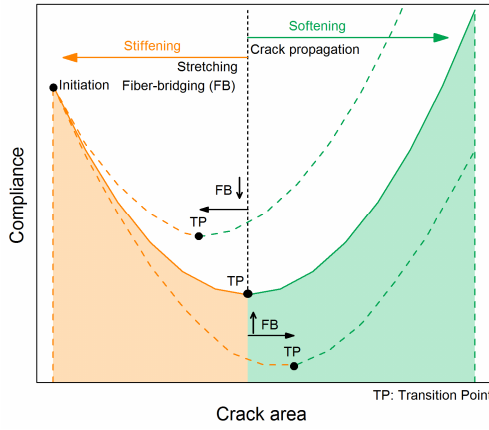


Figure 3.18 – Description of general behavior of crack area vs compliance curves

difference in stiffness between the DCB specimens and the plates. In terms of flexural stiffness, the plate was several times stiffer than any of the investigated DCB specimens. Furthermore, the biaxial stretching of the deformed part of the plate (radially and circumferentially) resulted in a biaxial “stress stiffening” effect. Consequently, more fiber-bridging than in the DCB specimens developed in the plates. Due to the in-plane isotropy of the plate, the opening of the crack was the same all along its contour (i.e. circumferential concentric growth) restraining the fiber-bridging to develop only in the radial direction, in spite of the bi-dimensionality of the crack propagation. The fiber-bridging length and  $\delta_f$  were higher in the plates than in the DCB specimens (13.2 vs 10 mm and 1.58 vs 1.25 mm respectively). The rate of decay of the bridging tractions,  $\gamma$ , was considerably smaller in the plates (0.01 vs 0.46 in the DCB specimens) and became the main parameter responsible for the increase of the  $G_{br}$  and thus of the  $G_{tot}$ . The lower the rate of decay, the lower the reduction in the bridging traction for a specific crack opening along the bridging zone (see Figure 3.7). Therefore, the increase of the stiffness in the plates contributed to the development of a fiber-bridging capable of maintaining higher bridging tractions during the opening of the crack.

The difference in the amount of fiber-bridging developed in the DCB specimens and the plates was also determined by comparing the experimental and numerical load-displacement results obtained for DCB-25-3 (cut from CFM.1), presented in Figure 3.19. For the sake of comparison, the experimental and numerical results obtained for the other DCB specimens of the same width (DCB-25 (1-2)) were also added in Figure 3.19. The numerical response of DCB-25-3 was obtained by implementing the same traction-separation law as for the rest of the DCB specimens but resulted in an underestimation of the load. Typically, for standard fracture load-displacement curves, two different regions can be identified regarding the shape of the traction-separation law [16]. The first region (region 1 in Figure 3.19) depends on the shape of the traction-separation law and corresponds to the development of the fiber-bridging. The second (region 2 in Figure 3.19), once the fiber-bridging is fully developed, depends exclusively on the value of  $G_{tot}$  (i.e. the total area under the traction-separation law). This second region can be clearly identified in Figure 3.19 for DCB-25-3 as the region where the

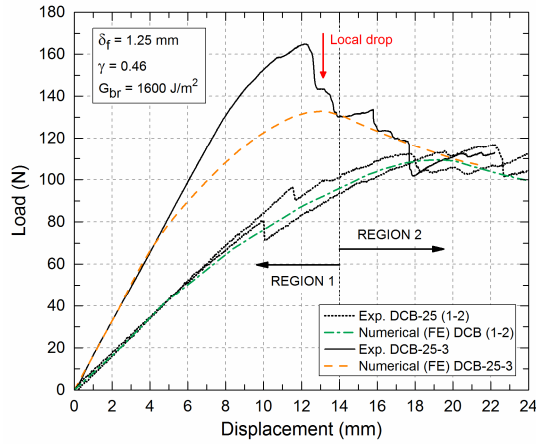


Figure 3.19 – Comparison of experimental and numerical curves of DCB-25 (1-2) and DCB-25-3 (cut from plate CFM.1)

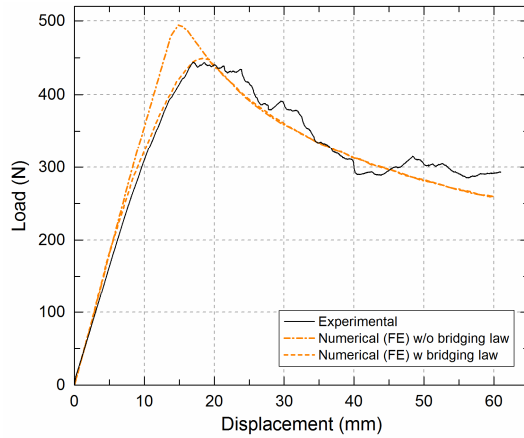


Figure 3.20 – Influence of shape of cohesive law in DCB-100-2: with and without bridging law

numerical results match the experimental results. It is also evident that the  $G_{tot}$ -dominated region of DCB-25-3 overlapped the same region in DCB-25 (1-2) (i.e. both  $G_{tot}$  values were the same). The length of the radius of the fully developed bridging area in the plates was found to be 13.2 mm and the length of the propagated crack (measured from the end of the pre-crack) of DCB-25-3 cut from CFM.1 was 22.5 mm. Therefore, a 13.2-mm bridging length was already present in DCB-25-3 before the experiment. However, as the DCB opened, the new fiber-bridging was developing up to the bridging length corresponding to the DCB configuration ( $\sim 10$  mm) and consequently, a drop in the load was registered (see Figure 3.19) as a result of the loss in the amount of fiber-bridging.

### 3.5.3 Influence of shape of traction-separation law

A different type of traction-separation law was implemented in the FE models to compare the influence of the shape of the law on the load-displacement response of the DCB specimens and the laminated plates. In both cases, a law with a linear softening (see Figure 3.14) from  $\sigma_c$  onwards, without explicitly taking into account fiber-bridging, was selected for the comparison. The value of the  $G_{tot}$  was the same as for the traction-

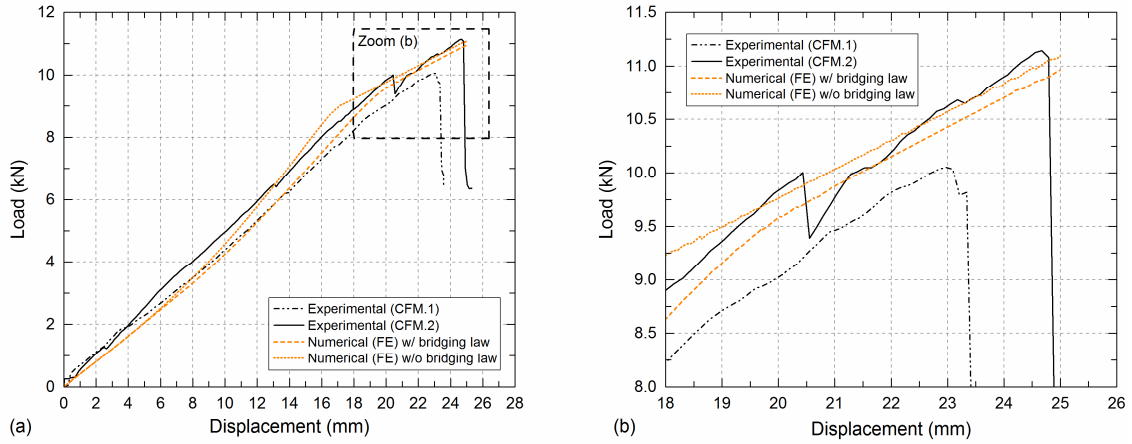


Figure 3.21 – (a) Influence of shape of cohesive law in plates: with and without bridging law; (b) zoom of region indicated in (a)

separation laws obtained with fiber-bridging (i.e. 2000 J/m<sup>2</sup> for the DCB and 3000 J/m<sup>2</sup> for the plate). The chosen DCB specimen was the DCB-100-2 and the corresponding results are presented in Figure 3.20. It can be observed how the  $G_{tot}$ -dominated regions (region 2) of both overlapped, similarly to what occurred in Figure 3.19 with the DCB-25 specimens while initially (region 1) their behavior differed due to the differences in the shape of the traction-separation law. However, a different behavior was obtained from the plate (see Figure 3.21). In this case, instead of an overlapping of the  $G_{tot}$ -dominated regions, parallel curves were obtained, as the value of  $G_{tot}$  is the same. Consequently, the shape of the traction-separation law chosen to simulate the fracture behavior in plates affected not only the load-displacement results during the development of the bridging area (i.e. up to the TP) but also the rest of the curve, leading to the overestimation of the load in this case. This behavior proves the previously discussed relationship between the slope of the load-displacement curve after the TP and the value of  $G_{tot}$ .

### 3.6 Conclusions

A numerical investigation of the 2D in-plane crack propagation in laminated plates with an embedded circular pre-crack was carried out in order to simulate the fracture behavior of the same plates that were experimentally investigated in a previous work [34]. Additional DCB experiments were performed to study the transition from 1D to 2D crack propagation scenarios. Three-dimensional FE models were developed to simulate the exhibited experimental fracture behaviors in both experimental configurations and cohesive elements were used to model the FPZ and a detailed analysis of the results was presented. The following conclusions can be drawn from this work:

1. The selected shape of the traction-separation law was able to model the fracture behavior of the plates, reproducing the trend in the behavior shown in the experimental load vs displacement and compliance vs crack area curves. By

calibrating the law to fit the experimental and the numerical values, the total SERR and fiber-bridging values of the plates were determined.

2. The stress stiffening of the plates (due to the stretching) together with the increase in the flexural stiffness (from beam to plate) led to an increase of the developed fiber-bridging area, causing a 50% increase of the total SERR compared to the total SERR obtained from the DCB specimens. Taking into account the stiffness effects on the fracture mechanisms, more efficient damage-tolerant structural designs can be developed for large-scale bridging scenarios.
3. The stiffness variations of the plates were reflected in the compliance vs crack area curves, which exhibited first a decreasing behavior down to a minimum (transition point) after which it started to increase. This transition point represented the threshold between the stiffening and softening mechanism predominance.
4. The fully developed fiber-bridging area in the plates was correlated with the crack area at the transition point of the compliance vs crack area curves. Any increase or decrease in the amount of fiber-bridging would be reflected in this curve by anticipating or delaying the appearance of the transition point. Therefore, the area of the fiber-bridging can be directly obtained from the experimental compliance without any further experimental measurement.
5. The transition point was also correlated to the change from non-linear to linear increasing of the load, confirming the full development of the fiber-bridging and achievement of an equilibrium between the stiffening and softening mechanisms existing in the plates.
6. The slope of the load vs displacement curve in the linear part (i.e. after the transition point) was correlated to the total SERR. Higher slopes corresponded to higher total SERR values and vice versa.

## References

1. Bakis, C., et al., Fiber-reinforced polymer composites for construction-state-of-the-art review. *Journal of Composites for Construction*, 2002; 6(2): 73-87.
2. Williams J.G. On the calculation of energy release rates for cracked laminates. *Int. J. Fract.*, 1988; 36(2): 101-119.
3. Brunner A.J.. Experimental aspects of Mode I and Mode II fracture toughness testing of fiber-reinforced polymer-matrix composites. *Compt. Method. Appl. M.*, 2000; 185(2-4): 161-172.
4. Choi N.S., Kinloch A.J., Williams J.G.. Delamination fracture of multidirectional carbon-fiber/epoxy composites under Mode I, Mode II and mixed-Mode I/II loading. *J. Compos. Mater.*, 1999; 31(1): 73-100.
5. Benzeggagh, M.L., Kenane, M. Measurement of mixed-mode delamination fracture toughness of unidirectional glass/epoxy composites with mixed-mode bending apparatus. *Compos. Sci. Technol.*, 1996; 56: 439-449.
6. ASTM D5528-13: Standard test method for mode I interlaminar fracture toughness for unidirectional fiber-reinforced polymer matrix composites, in *Annual book of ASTM standards: adhesive section 15.03*.



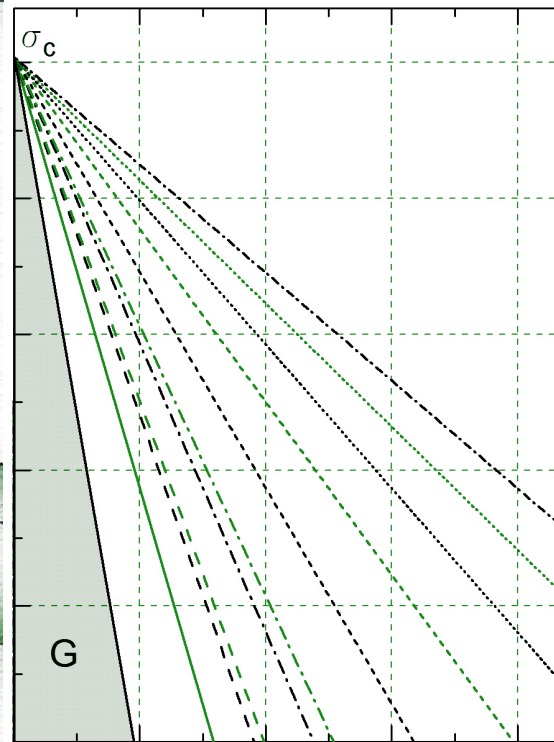
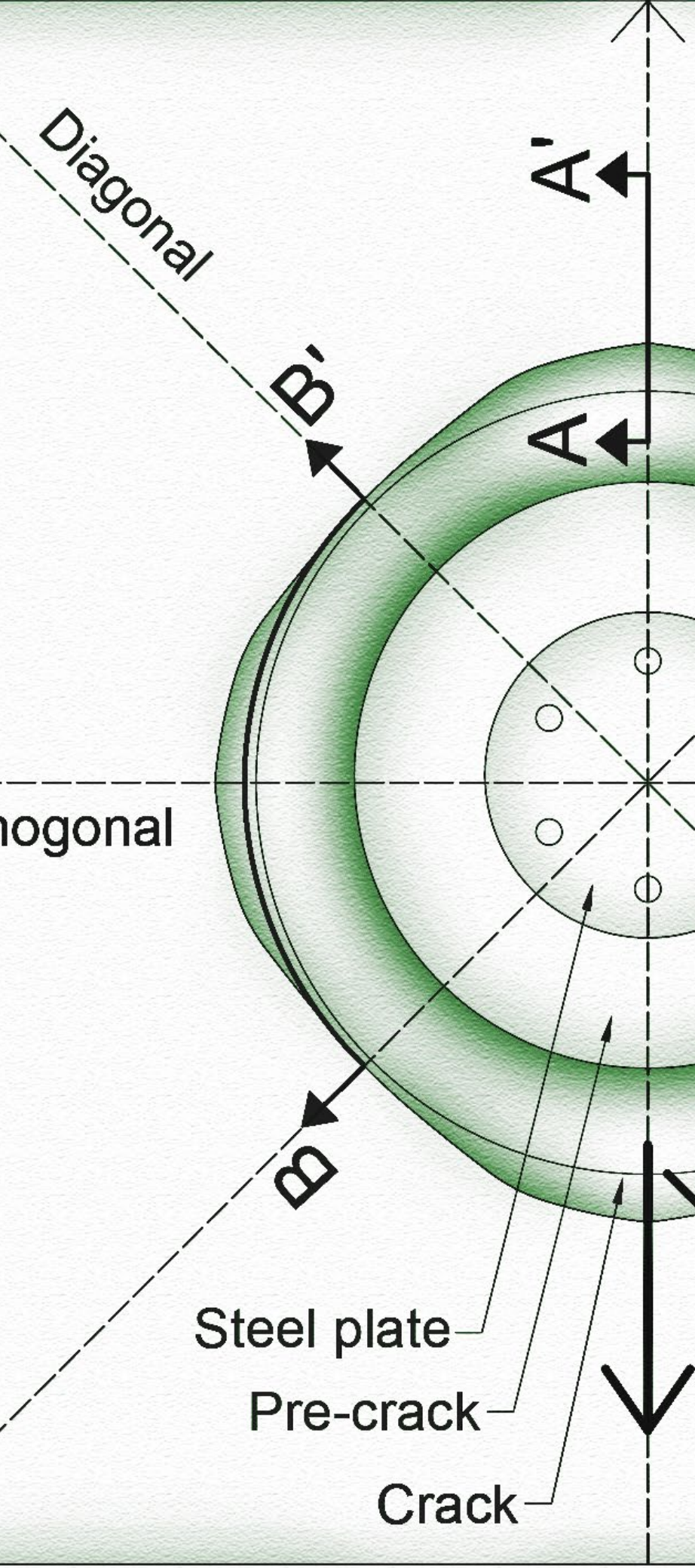
7. ASTM D6671/D6671M - 13e1: Standard test method for mixed mode I-mode II interlaminar fracture toughness for unidirectional fiber-reinforced polymer matrix composites, in Annual book of ASTM standards: adhesive section 15.03.
8. Butler, R., Rhead, A.T., Liu, W., Kontis, N. Compressive strength of delaminated aerospace composites. *Phil. Trans. R. Soc. A*, 2012; 370:1759-1779.
9. Nilsson K.F., Thesken J.C., Sindelar P., Giannakopoulos A.E., Storakers B. A theoretical and experimental investigation of buckling induced delamination growth. *J. Mech. Phys. Solids*, 1993; 41(4): 749-782.
10. Riccio A., Raimondo A., Di Caprio F., Scaramuzzino F. Delaminations buckling and growth phenomena in stiffened composite panel under compression. Part II: a numerical study. *Journal of Composite Materials*, 2014; 48(3); 2857-2870.
11. Rhead A.T., Butler R., Hunt G.W. Compressive strength of composite laminates with delamination induced interaction of panel and sublaminar buckling modes. *Composite Structures*, 2017; 171; 326-334.
12. Chen, Z.M., Krueger, R., Rinker, M. Facesheet/Core Disbond Growth in Honeycomb Sandwich Panels Subjected to Ground-Air-Ground Pressurization and In-Plane Loading. In: 11th International Conference on Sandwich Structures ICSS-11, Ft. Lauderdale, USA, March, 2016.
13. Rinker, M., Krueger, R., Ratcliffe, J. Analysis of an Aircraft Honeycomb Sandwich Panel with Circular Face Sheet/Core Disbond Subjected to Ground-Air Pressurization. NASA/CR-2013-217974, 2013.
14. Launey M.E., Ritchie R.O. On the fracture toughness of advanced materials. *Adv. Mater.*, 2009; 21; 2103-2110.
15. Canal L.P., Alfano M., Botsis J. A multi-scale based cohesive zone model for the analysis of thickness scaling effect in fiber bridging. *Comp. Science and Tech.*, 2017; 139; 90-98.
16. Ortega A., Maimí P., González E.V., Trias D. Characterization of the translaminar fracture cohesive law. *Composites: Part A*, 2016; 91; 501-509.
17. Manshadi B.D., Farmand-Ashtiani E., Botsis J., Vassilopoulos A.P. An iterative analytical/experimental study of bridging in delamination of the double cantilever beam specimen. *Composites: Part A*, 2014; 61; 43-50.
18. Frossard G., Cugnoni J., Gmür T., Botsis J. Mode I interlaminar fracture of carbon epoxy laminates: effects of ply thickness. *Composites: Part A*, 2016; 91; 1-8.
19. Suo Z., Bao G., Fan B. Delamination R-curve phenomena due to damage. *J. Mech. Phys. Solids*, 1992; 40 (1): 1-16.
20. Manshadi B.D., Vassilopoulos A.P., Botsis J. A combined experimental/numerical study of the scaling effects on mode I delamination of GFRP. *Comp. Science and Tech.*, 2013; 83; 32-39.
21. Sørensen B.F., Gamstedt E.K., Østergaard R.C., Goutianos S. Micromechanical model of cross-over fibre bridging-Prediction of mixed mode bridging laws. *Mechanics of Materials*, 2008; 40; 220-234.
22. Shaverdi M., Vassilopoulos A.P., Keller T. Modelling effects of asymmetry and fiber bridging on Mode I fracture behavior of bonded pultruded composite joints. *Eng. Fract. Mech.*, 2013; 99; 335-348.
23. Cameselle-Molares A., Roohollah S., Shaverdi M., Vassilopoulos A.P., Keller T. Fracture mechanics-based progressive damage modelling of adhesively bonded fibre-reinforced polymer joints. *Fatigue Fract. Eng. Mater. Struct.*, 2017; 40(12): 2183-2193.
24. Pappas G, Canal L.P., Botsis J. Characterization of intralaminar mode I fracture of AS4/PPS composites using inverse identification and micromechanics. *Composites: Part A*, 2016; 91; 117-126.
25. Barenblatt G.I. The formation of equilibrium crack during brittle fracture: general ideas and hypothesis, axially-symmetric cracks. *J. Appl. Math. Mech.*, 1959; 23; 622-636.
26. Dugdale D. Yielding of steel sheets containing slits. *J. Mech. Phys. Solids*, 1960; 8(2); 100-104.

27. Barenblatt G.I. The mathematical theory of equilibrium cracks in brittle fracture. *Adv. Appl. Mech.*, 1962; 7; 55-129.
28. Sørensen B.F., Jacobsen T.K. Large-scale bridging in composites: R-curves and bridging laws. *Composites: Part A*, 1998; 29A; 1443-1451.
29. Sorensen L., Botsis J., Gmür Th., Humbert L. Bridging tractions in mode I delamination: Measurements and simulations. *Comp. Sci. and Tech.*, 2008; 68; 2350-2358.
30. Morel S., Lespine C., Coureau J.L., Planas J., Dourado N. Bilinear softening parameters and equivalent LEFM R-curve in quasibrittle failure. *Inter. J. of Solids and Struct.*, 2010; 47; 837-850.
31. Bao G., Suo Z. Remarks on crack-bridging concepts. *Appl. Mech. Rev.*, 1992; 45(8); 355-366.
32. Farmand-Ashtiani E., Cugnoni J., Botsis J. Specimen thickness dependence of large scale fiber bridging in mode I interlaminar fracture of carbon epoxy composite. *Inter. J. of Solids and Struct.*, 2015; 55; 58-65.
33. Pappas G., Botsis J. Intralaminar fracture of unidirectional carbon/epoxy composite: experimental results and numerical analysis. *Inter. J. of Solids and Struct.*, 2016; 85-86; 114-124.
34. Cameselle-Molares A., Vassilopoulos A.P., Keller T. Experimental investigation of two-dimensional delamination in GFRP laminates. *Eng. Fract. Mech.*, 2018; 203; 152-171.
35. Owen's Corning Reinforcements Composite Solutions Guide. <[http://www.ocvreinforcements.com/pdf/library/Composite\\_Solutions\\_Guide\\_100360\\_E\\_finalprintable.pdf](http://www.ocvreinforcements.com/pdf/library/Composite_Solutions_Guide_100360_E_finalprintable.pdf)> (Accessed 26 March 2018).
36. Sika datasheet product. <[https://deu.sika.com/dms/getdocument.get/dd4b783e-bfa5-32e3-a705-f9f548f6b326/Biresin\\_CR83\\_eng.pdf](https://deu.sika.com/dms/getdocument.get/dd4b783e-bfa5-32e3-a705-f9f548f6b326/Biresin_CR83_eng.pdf)> (Accessed 19 October 2017).
37. Renart J., Blanco N., Pajares E., Costa J., Lazcano S., Santacruz G. Side Clamped Beam (SCB) hinge system for delamination tests in beam-type composite specimens. *Comp. Sc. and Tech.*, 2011; 71; 1023-1029.
38. Abaqus Inc. Abaqus analysis user's manual, version 6.14-1. 2014. Providence, RI, USA.
39. Soto A., González E.V., Maimí P., Turon A., Sainz de Aja J.R., de la Escalera F.M. Cohesive zone length of orthotropic material undergoing delamination. *Eng. Fract. Mech.*, 2016; 159; 174-188.
40. Turon A., Camanho P.P., Costa J., Dávila C.G. A damage model for the simulation of delamination in advanced composites under variable-mode loading. *Mechanics of Materials*, 2006; 38(11): 1072-1089.
41. Turon A., Camanho P.P., Costa J., Renart J. Accurate simulation of delamination growth under mixed-mode loading using cohesive elements: Definition of interlaminar strengths and elastic stiffness. *Composite Structures*, 2010; 92(8): 1857-1864.
42. Anderson Ted. *Fracture mechanics*. 2<sup>nd</sup> ed. Texas: CRP; 1995.
43. Heidari-Rarani M., Shokrieh M.M., Camanho P.P. Finite element modeling of mode I delamination growth in laminated DCB specimens with R-curve effects. *Composites: Part B*; 2013; 45; 897-903.
44. Camanho P.P., Dávila C.G., Ambur D.R. Numerical simulation of delamination growth in composite materials. NASA/TP-2001-211041. Hampton: NASA Langley Research Center; 2001.

---

**Contributions:** Aida Cameselle Molares conceived, designed and performed the experimental campaign under the supervision of Prof. Thomas Keller, Dr. Jordi Renart and Dr. Anastasios Vassilopoulos. The numerical model was developed by Aida Cameselle Molares under the supervision of Dr. Jordi Renart and Dr. Albert Turon. The analysis of the results was carried out by Aida Cameselle Molares in collaboration with Dr. Jordi Renart, Prof. Thomas Keller and Dr. Anastasios Vassilopoulos.



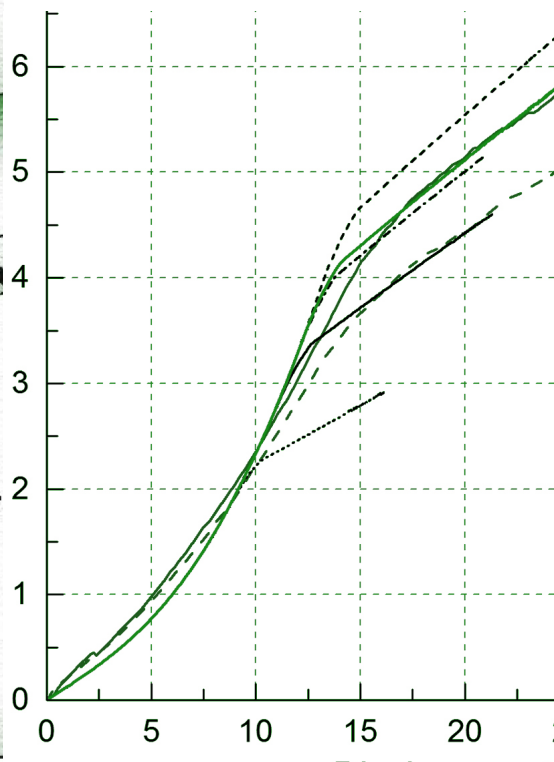


separation law in all directions. Different at least three FE analyses with three different

**Step 3:** extraction of the numerical load (i.e. for each analysis) and calculation of the last linear part of the curves.

**Step 4:** with the obtained  $\alpha - \bar{G}_{tot}$ , results the best fitting (a linear equation in the case of

**Step 5:** determination of the experimental results for each of the available specimens.



# Chapter 4

## Two-dimensional fracture characterization

### *A numerically-based method*

#### 4.1 Introduction

Traditionally, most delamination or debonding investigations of fiber-reinforced polymer (FRP) materials have been limited to beam-like specimens such as double cantilever beams (DCBs) for opening fracture modes (Mode I) or end-loaded split (ELS) and mixed-mode bending (MMB) for shear modes (Mode II and mixed-Mode I/II respectively) [1-4]. The fracture values obtained from these standard fracture mechanics experiments were often employed in the prediction of the damage response in more complex structural components [5, 6]. Nevertheless, some conditions inherent to the standard beam-like specimens, e.g. constant crack width or unique direction of crack propagation (1D), do not correspond to real delamination scenarios, where cracks propagate in the delamination plane (2D) without any space or shape restrictions. Thus, fracture properties derived from 1D experiments may not be applicable for the prediction of the fracture behavior of actual structural components.

A more realistic description of the 2D fracture behavior was suggested by the authors by performing experimental [7] and numerical [8] investigations of 2D delamination in laminated GFRP plates with embedded cracks growing under opening loads. The transparency of the laminates enabled the crack front to be monitored during the fracture process. In [8], a significant increase in the total SERR (i.e. the SERR achieved after the full development of the fiber-bridging) involved in the 2D delamination, when compared to the total SERR value derived from standard (1D)

fracture experiments, was reported. This increase was caused by an increase in the amount of fiber-bridging developed as a result of two factors: 1) the increment in the flexural stiffness (from beam to plate), and 2) stress stiffening due to the in-plane stretching of the delaminated regions of the plates (as a result of the boundary conditions inherent to an embedded crack), which both reduced the rotation of the crack faces. In 1D delamination cases where non-negligible fracture process zones (FPZs) with significant fiber-bridging developed, a flexural stiffness dependency of the total SERR was already observed [9-16].

The compliance results obtained in [7] for the 2D laminated plates were affected not only by the propagation of the crack but also by the additional stress stiffening due to the stretching of the cracked region. Thus, existing compliance-based data reduction methods used to derive the total SERR in beam-like specimens [2-4, 17], where the required compliance values after crack initiation only reflect the propagation of the crack, are no longer applicable in 2D delamination cases. Furthermore, the required monitoring of the 2D crack front, i.e. the crack length in the different directions, is not simple in cases of opaque laminates. The contour integral method (*J*-integral) [11, 14, 18, 19], which can provide closed formulations that do not depend on the compliance or the crack length, generally requires measuring the rotations of the specimens however, which leads to complex experimental set-ups in 2D delamination cases.

In order to estimate the total SERR involved in 2D delamination, numerical simulations using cohesive elements to model the crack interface were carried out in [8]. A complex traction-separation law combining linear and exponential softening was implemented in the numerical model to define the cohesive behavior. The different cohesive parameters of the law were iteratively adjusted to simulate the experimental load-displacement and crack-displacement curves, thus involving considerable time and computational cost. The measurement of the 2D crack front, visually accessible thanks to the translucency of the GFRP plates, was therefore essential in this process.

To overcome these difficulties, a novel and simpler numerically-based method, suitable for determining the total SERR involved in Mode I-dominated 2D in-plane delamination of FRP laminated plates with internal embedded defects and subjected to opening loads, is presented, applied and validated in this work. The method is based on two particular findings reported in the former work [8], i.e. 1) the existing dependence between the slope of the load-displacement curve exhibited after the full development of the FPZ and the value of the total SERR, and 2) the independence of the latter from the selected shape of the traction-separation laws. As a result, cohesive elements with simple traction-separation laws are used and only the slope of the linear part of the experimental load-displacement results is required to apply the method. Since no monitoring of the crack front is necessary either, this implies a considerable simplification of both the experimental and numerical demands. The backbone of the method is based on an inverse analysis [20-25] where, through the fitting of the above-defined experimental slope, the total SERR is obtained. However the method builds up on the above-mentioned novel findings and their combination and allows the



estimation of the total SERR in 2D crack propagation under Mode I and opening in an affordable way, i.e. without excessive experimental and numerical efforts.

The relevant previous experimental [7] and numerical [8] results, necessary for understanding the new method, are summarized in Sections 4.2 and 4.3 respectively. Section 4.2 is complemented with an extended discussion of the experimental results, not included in the previous work. The new method is described in Section 4.4 and validated in Section 4.5.

## 4.2 Experimental investigation of laminated plates: results and discussion

### 4.2.1 Previous results and discussion

An experimental investigation of the 2D delamination behavior of GFRP/epoxy laminated plates under quasi-static out-of-plane opening loading was presented in [7]. A circular embedded pre-crack was introduced in the center and midplane of the plates. The experimental set-up, similar for all the laminates, is presented in Figure 4.1. A total of six pairs of plates, using six different types of glass reinforcements, were investigated. The investigation presented here involves the continuous filament mat reinforcement (plates CFM.1/2) and two types of woven fabrics with different proportions of reinforcement in the warp/weft directions, i.e. 50/50 (plates W50.50.1/2) and 60/40 (plates W60.40.1/2). The properties of the epoxy resin and glass fibers are given in Table 4.1 (manufacturer data [26, 27]). The layup and geometrical description of the six plates are summarized in Table 4.2. Further details concerning the experimental program can be found in [7].

The crack propagation patterns obtained for one plate of each pair for the CFM, W50.50 and W60.40 plates are shown in Figure 4.2. Results beyond the “last symmetric crack front” are not considered [7]. The experimental load vs displacement curves obtained are shown in Figures 4.3, 4.4(a) and 4.5(a) for the CFM, W50.50 and W60.40 pairs

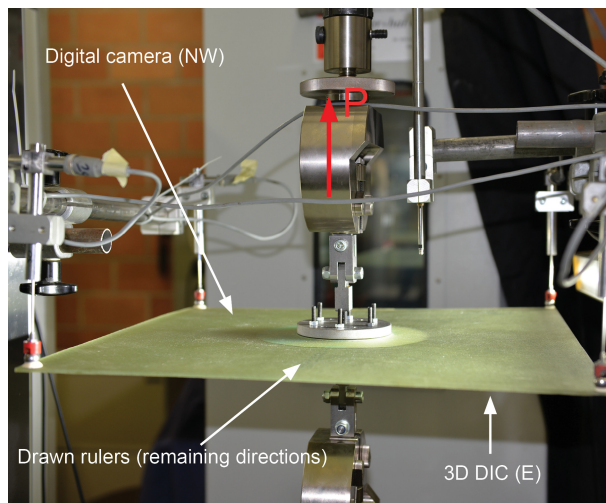


Figure 4.1 – Experimental set-up and crack measuring system



of plates respectively. The load increased continuously up to specimen failure as a result of the non-proportional growth of the crack area [7]. Based on the compliance results (i.e.  $\delta/P$ , where  $\delta$  is the displacement and  $P$  is the load), two different regions were identified. Region A (indicated for the first plate of each pair) corresponds to the region where the experimental compliance decreased (i.e. stiffening of the system) and Region B to the region where it increased (i.e. softening of the region). The changing point in the compliance behavior (“transition point”, TP) is indicated for all plates. The stiffening was caused by the stretching of the opening part of the plates as a result of the boundary conditions and the fiber-bridging generated in front of the crack tip. The softening was caused by the propagation of the crack itself. Both stiffening mechanisms were capable of delaying the softening of the system after crack initiation, i.e. Region A (stiffening) extended for all cases much further than the visual crack initiation, indicated also for all plates (denominated “Ini”), see Figures 4.3-4.5. A more detailed discussion and further results can be found in [7].

> Table 4.1 – Material properties

Material	$E$ (GPa)	$G$ (GPa)	$\nu$ (-)	$\rho$ (g/cm <sup>3</sup> )
Epoxy resin	2.96	1.30	0.35	1.14
E-CR <sup>*</sup> glass (for CFM)	80.00	32.80	0.22	2.62
E-glass (for woven)	72.00	29.50	0.22	2.55

<sup>\*</sup>Corrosion-resistant

> Table 4.2 – Description of GFRP laminated plates

Plate type	No. of layers	Reinforcement weight per layer (g/m <sup>2</sup> )	Dimensions (m) (width x height x avg. thickness)
CFM.1 / CFM.2	6	600	420 x 420 x 7.50 / 420 x 420 x 6.99
W50.50.1 / W50.50.2	8	390	460 x 460 x 3.33 / 480 x 480 x 3.53
W60.40.1 / W60.40.2	6	500	410 x 410 x 3.05 / 410 x 410 x 3.06

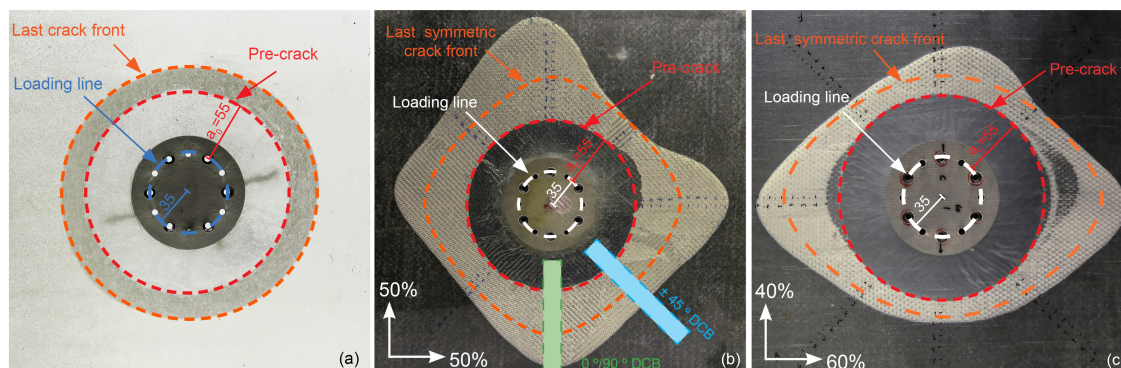


Figure 4.2 –Crack propagation patterns in plates (a) CFM.1, (b) W50.50.1 and (c) W60.40.2. Dimensions in mm

### 4.2.2 Effects of stiffness variations on fiber-bridging development

Depending on the fiber architecture, the shape of the defect and the boundary conditions, 2D cracks may propagate following different patterns that can potentially lead to a non-homogeneous development of fiber-bridging along the crack front. As a result, the amount of total SERR required to propagate the crack can vary depending on the direction of propagation. Such behavior occurred in the W50.50 and W60.40 plates, whose woven fiber architecture caused the crack to propagate differently depending on the stiffness in the direction of propagation (see Figure 4.2(b, c)) and thus the potential fiber-bridging to develop radially and circumferentially. To illustrate this behavior, an analysis of an arbitrary crack front following the propagation pattern of the W50.50 plates is presented in Figure 4.6. As the crack propagated faster in the orthogonal directions (the stiffest with fibers at  $0/90^\circ$ ) than along the diagonal directions (the least stiff with fibers at  $\pm 45^\circ$ ), an uneven deformation of the opened part of the plate occurred, exhibiting the largest opening along the orthogonal directions and the smallest along the diagonal directions (see Sections AA' in Figure 4.6). This resulted in an additional circumferential opening and therefore to develop fiber-bridging both radially and circumferentially (circumferential Section BB'). The directions of propagation and

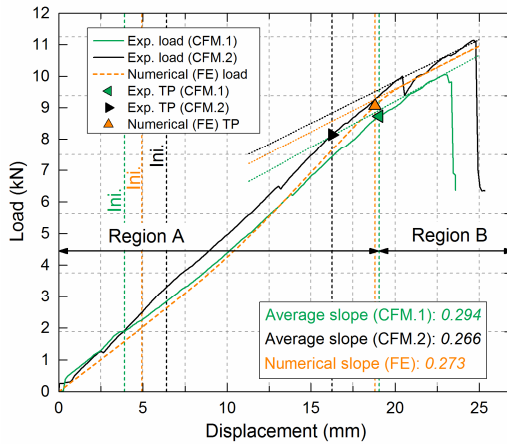


Figure 4.3 – Experimental and numerical load vs opening displacement curves of CFM plates and slopes in Region B

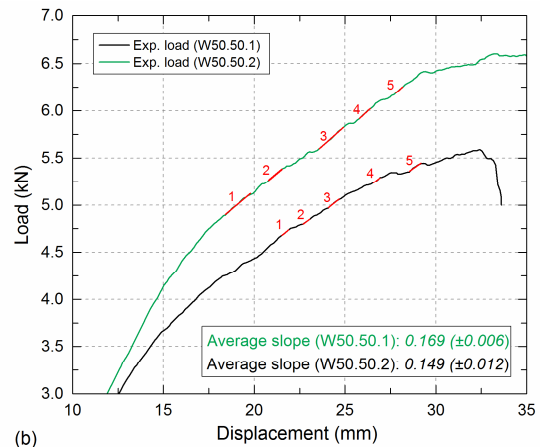
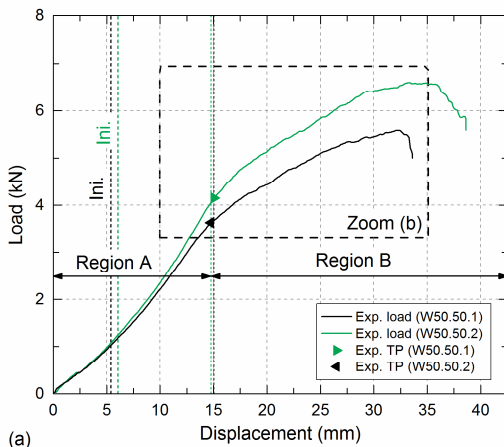


Figure 4.4 – (a) Experimental load vs opening displacement curves of W50.50 plates; (b) extraction of experimental slopes

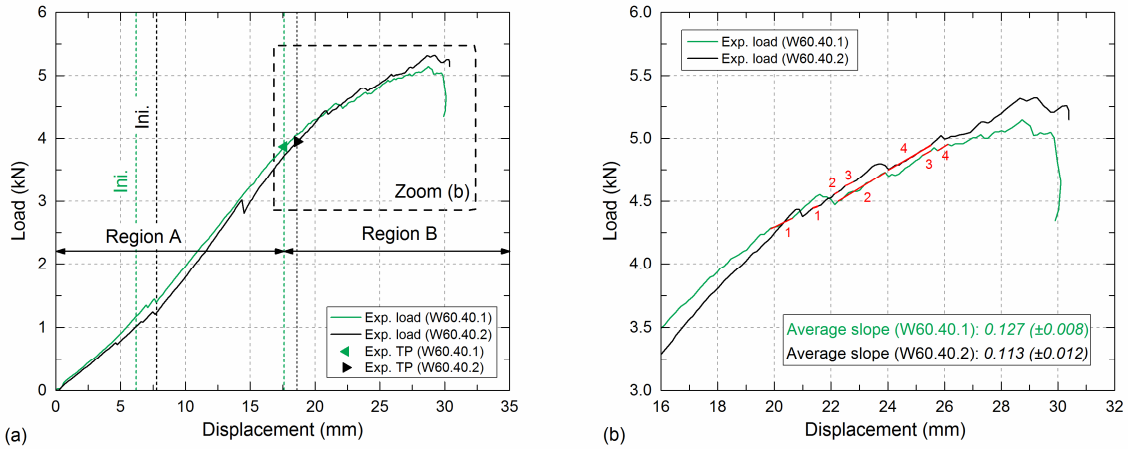


Figure 4.5 – (a) Experimental load vs opening displacement curves of W60.40 plates; (b) extraction of experimental slopes

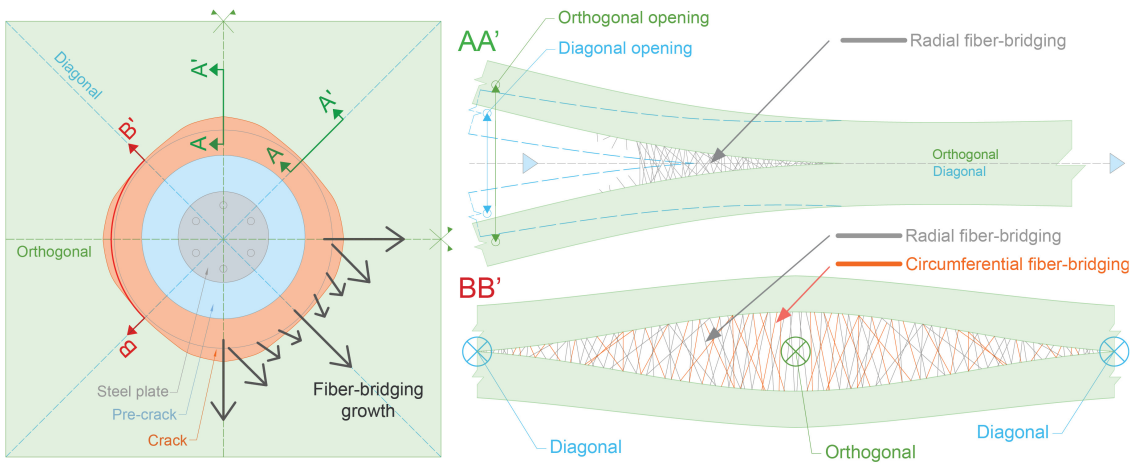


Figure 4.6 – Explanatory layout of radial and circumferential fiber-bridging development (not to scale)

fiber-bridging growth are indicated with arrows in Figure 4.6. Due to the symmetric growth of the crack, only radial fiber-bridging developed along exactly the orthogonal and diagonal directions. However, the circumferential fiber-bridging was already present in close proximity to both directions. Consequently, the total SERR required to propagate the crack varied depending on the direction of propagation, being higher in those regions where more fiber-bridging developed. Similar behavior can be concluded for the W60.40 plates.

Only in particular cases, such as the in-plane isotropic CFM plates where the crack propagated similarly in all directions and therefore the fiber-bridging developed strictly radially (i.e. concentrically from the circular pre-crack, see Figure 4.2(a)), is the required amount of total SERR the same all along the crack front.

### 4.3 Previous numerical results of CFM plates

A numerical investigation of the CFM plates was presented in [8] and the relevant results used to derive and validate the new method are summarized in the following. A three-dimensional finite element model was developed for the simulation of the experimental fracture response using cohesive elements. The traction-separation law

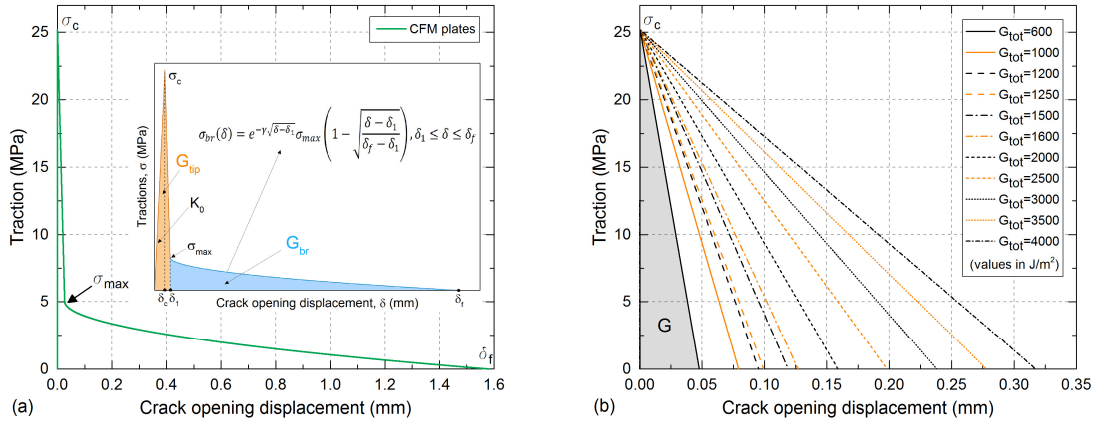


Figure 4.7 – Traction-separation curves used in numerical models; (a) with softening including bridging law used for CFM; (b) with linear softening used for total SERR derivation in proposed method ( $G_{tot}$  for CFM and  $\bar{G}_{tot}$  for woven plates)

used to model the behavior of the cohesive elements, shown in Figure 4.7(a), was a combination of two different laws: first, a linear softening law corresponding to the initial damage growth and second, an exponential softening law representing the fiber-bridging traction. The areas under the first and second parts equal the SERRs involved in crack initiation and fiber-bridging development respectively ( $G_{tip}$  and  $G_{br}$ ). As discussed in [8],  $G_{tip}$  is a material property and  $G_{br}$  depends on the geometry and size of the investigated specimen. The addition of these two values corresponds to the total area under the traction-separation law (i.e. to the total SERR) and will be hereafter denoted as  $G_{tot}$  which therefore is also geometrical and size dependent. Further details regarding the numerical model and cohesive formulation can be found in [8].

The numerical load-displacement response obtained is shown in Figure 4.3. Several relationships between the parameters of the traction-separation law and the load-displacement curves were observed [8]. The transition point (TP), which marked the full development of the FPZ, was reflected in the load-displacement curves as the change from an initially non-linear to a purely linear increasing behavior (see Figure 4.3, Region B beyond the TP). It was further concluded that the slope of this linear part depended only on the value of the total SERR – i.e. greater slopes corresponded to greater total SERR values and vice versa – and was thus completely independent of the shape of the traction-separation law [8]. The method presented in this work was developed based on this last finding.

#### 4.4 New total SERR derivation method

As mentioned in the introduction, existing fracture data reduction methods are not appropriate for determining the total SERR involved in 2D delamination. In order to overcome this problem, a numerically-based method to determine the total SERR involved in the Mode I-dominated 2D delamination of laminates with an embedded defect under opening loads was developed. The new method is based on the above-mentioned relationship between the total SERR ( $G_{tot}$ ) and the slope of the load-displacement curves developed beyond the TP (hereafter referred to simply as

“slope”). The method is described and applied for the in-plane isotropic CFM plates in the following and validated in Section 4.5 with the experimental results obtained for the orthotropic W50.50 and W60.40 plates.

Initially a three-dimensional (3D) FE model (of the CFM plate) with the elastic properties and geometry of the investigated plate and a zero-thickness layer of cohesive elements in the plane of the crack is developed (analogously to the one described in [8]). Considering that the slope was found to be dependent of the area under the traction-separation law (i.e.  $G_{tot}$ ) but independent of the shape of the traction-separation law, a simple traction-separation law with linear softening is used, in contrast to the model in [8], to define the cohesive behavior (see Figure 4.7(b)) and implemented through a user material subroutine (UMAT) [8, 28]. The maximum traction for damage initiation is assumed to be 30% of the tensile strength of the matrix (84 MPa, [8, 27]), according to [8, 29], resulting in a value of  $\sigma_c = 25.2$  MPa and the initial stiffness,  $K_0$ , is set to 100,000 MPa/mm [8, 28, 30]. Subsequently, five simulations with different values of  $G_{tot}$  (i.e. different areas under the traction-separation law and therefore different values of maximum opening), ranging from 2000 to 4000 J/m<sup>2</sup>, are

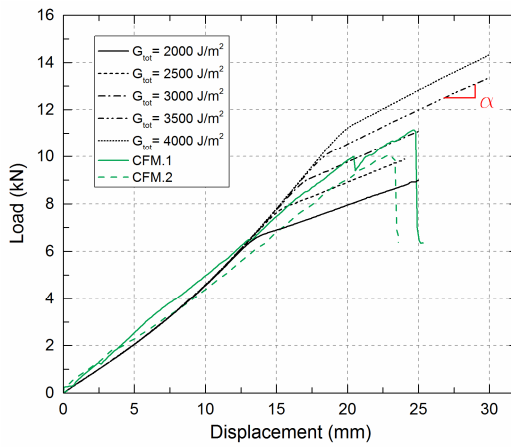


Figure 4.8 – Numerical load vs opening displacement curves obtained using different values of  $G_{tot}$  and a linear-softening cohesive law (see Figure 4.9(b)) compared to experimental curves

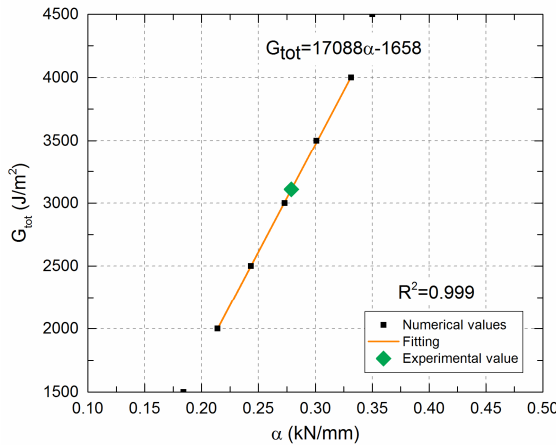


Figure 4.9 – Numerical  $\alpha$  vs  $G_{tot}$  curve obtained for CFM laminates

performed. The numerically obtained load-displacement curves are shown in Figure 4.8. It can be observed that increasing slopes (denoted by “ $\alpha$ ”) correspond to higher values of  $G_{tot}$  and higher loads. The  $\alpha - G_{tot}$  values for each simulation are represented in Figure 4.9, revealing a linear relationship between them; the equation of the fitted linear behavior is likewise indicated. Using the average value of the experimental slopes (0.280, see Figure 4.3 and [7]), and entering the fitted equation, a value for  $G_{tot}$  of 3109 J/m<sup>2</sup> is obtained.

As discussed in Section 4.2.2, the total SERR ( $G_{tot}$ ) required to propagate the crack may vary along the crack front depending on the fiber architecture, crack shape or boundary conditions. However, the load-displacement curve reflects the overall fracture behavior of the plates and therefore the slope ( $\alpha$ ) correlates with the overall or mean  $G_{tot}$  value required to propagate the 2D crack, hereafter denominated  $\bar{G}_{tot}$ :

$$\bar{G}_{tot} = \frac{\sum_{i=1}^n G_{tot,i} \cdot A_i}{A_{tot}} \quad (4.1)$$

where  $G_{tot,i}$  is the total SERR required to locally propagate a crack area,  $A_i$ , along a particular direction and  $A_{tot}$  is the total propagated area (i.e. the summation of all  $A_i$ ).

Similarly, and corresponding to the different  $G_{tot}$  values (ranging from a minimum to a maximum), different traction-separation laws may apply depending on the direction of propagation, see Figure 4.10. However, in line with the mean value of  $G_{tot}$ , a mean traction-separation law, independent of the direction, can be, and is, assumed in the proposed method, thus simplifying the FE model significantly. In the case of the isotropic CFM plates, the same value of  $G_{tot}$  is required to propagate the crack in all directions (i.e.  $G_{tot} = G_{tot,min} = G_{tot,max} = \bar{G}_{tot}$ ) and therefore the mean traction-separation law coincides with the traction-separation law in every direction.

The new method can thus be broken down into the following six steps:

**Step 1:** development of an FE model comprising the geometry and elastic properties of the specimen with cohesive elements placed at the delamination interface.

**Step 2:** performance of FE analyses using the same simple linear-softening traction-separation law in all directions. Different values of  $\bar{G}_{tot}$  are assigned to each analysis; at least three FE analyses with three different values of  $\bar{G}_{tot}$  must be performed.

**Step 3:** extraction of the numerical load-displacement curves for each value of  $\bar{G}_{tot}$  (i.e. for each analysis) and calculation of the corresponding values of the slope,  $\alpha$ , of the last linear part of the curves.

**Step 4:** with the obtained  $\alpha - \bar{G}_{tot}$  results, determination of the curve that provides the best fitting (a linear equation in the cases presented in this work).

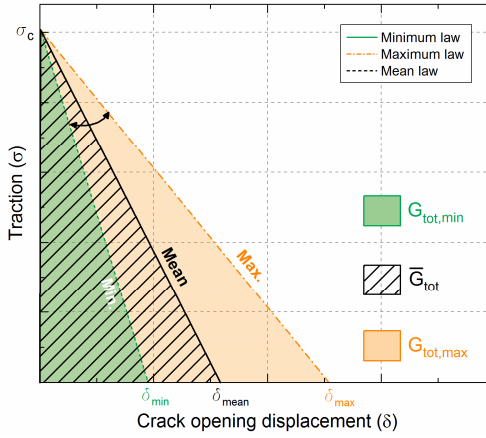


Figure 4.10 – General description of linear traction-separation laws varying along crack front

**Step 5:** determination of the experimental slope of the linear part of the curves for each of the available specimens.

**Step 6:** using the fitted equation derived in Step 4 and with the average value of the experimental slopes obtained in Step 5, determination of the value of  $\bar{G}_{tot}$ .

The presented method does not require the crack front to be measured during the experiment in order to derive the total SERR, thereby avoiding any uncertainty linked to the location of the crack tip. The only experimental requirement is the load-displacement curve. Particularly in the case of 2D delamination of embedded cracks in opaque FRP materials such as carbon fiber-reinforced polymers (CFRPs), where measurement of the crack front is not visually possible, this represents a significant advantage. Furthermore, considering that the slope used in the method corresponds to a mean  $G_{tot}$  value, the procedure is valid for any fiber architecture, crack shape and boundary conditions. This  $\bar{G}_{tot}$  value underestimates the  $G_{tot}$  in some regions and overestimates it in others, therefore resulting in an inaccurate propagation pattern. However, the aim of the method is not to determine the exact shape of the propagated crack, but to obtain a total SERR value that indicates whether a 2D crack propagates or not. In cases where an accurate prediction of the load-displacement behavior between crack initiation and the TP (see Figures 4.3-4.5) and the crack propagation pattern is required, further modeling with varying traction-separation laws and optimized shape might be necessary, as shown in [8]. The value of the total 2D SERR provided by the presented method constitutes a valuable starting point for any further optimization of the traction-separation law.

## 4.5 Validation of the method and discussion

### 4.5.1 CFM laminates

The result of total SERR obtained by applying the described method for the CFM plates ( $\bar{G}_{tot} = 3109 \text{ J/m}^2$ ) only differs by 3.5% from the numerically estimated value in [8] of  $3000 \text{ J/m}^2$ , where the complete load-displacement curve and the crack propagation pattern were accurately reproduced, representing therefore a first validation of the method.



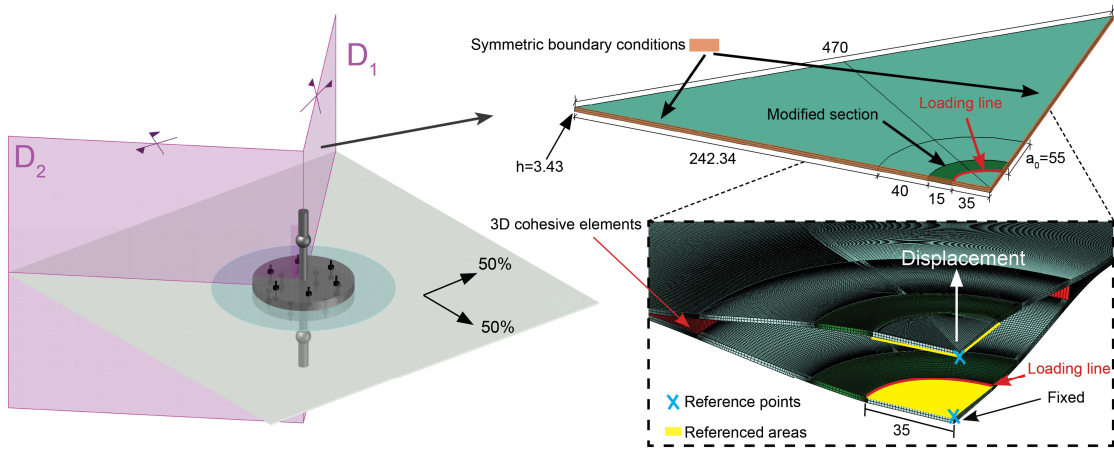


Figure 4.11 – Description of finite element model of W50.50 laminated plate. Dimensions in mm

> Table 4.3 – Elastic properties of laminated plates used in FE models

Plate type	$E_1$ (GPa)	$E_2$ (GPa)	$E_3$ (GPa)	$G_{12}$ (GPa)	$G_{13}$ (GPa)	$G_{23}$ (GPa)	$\nu_{12}$ (-)	$\nu_{13}$ (-)	$\nu_{23}$ (-)
W50.50	17.79	17.79	7.25	2.62	1.83	1.83	0.19	0.33	0.33
W50.50 <sup>(M)</sup>	89.51	89.51	46.82	30.42	6.43	6.43	0.25	0.30	0.30
W60.40	22.30	14.86	7.57	1.76	2.00	1.73	0.23	0.32	0.33
W60.40 <sup>(M)</sup>	131.99	111.69	116.63	33.57	11.74	7.48	0.29	0.29	0.30

<sup>(M)</sup>Modified section (woven reinforcement + steel)

#### 4.5.2 W50.50 laminates

##### Validation

To further validate the method, the described procedure was applied to determine the value of the total SERR associated with the delamination experiments on the W50.50 plates described in Section 4.2.1 and [7]. According to Step 1, a 3D finite element model was developed using the commercial finite element analysis (FEA) software ABAQUS 6.14.1. The geometry and dimensions of the model are shown in Figure 4.11. Only one quarter of the plate was modeled using the symmetry planes (D1 and D2) conforming to the experimentally recorded vertical movements of the free edges (see [7]). Symmetric boundary conditions were applied accordingly. The thickness of the laminate was selected as the average of the experimental thicknesses (i.e. 3.43 mm, see Table 4.2). As mentioned in Section 4.2.1, two steel inserts of 1.2-mm thickness and 100-mm diameter were used as part of the loading system [7], but, for the sake of simplicity, neither they nor the rest of the components of the loading system were explicitly modeled. Alternatively, all the nodes in the inner faces located inside the area delimited by the loading line (“reference area” in Figure 4.11) were tied with a rigid body condition [31] to reference points. The boundary conditions were applied to the reference points, i.e. in-plane displacements and all the rotations constrained in the top reference point and all displacements and rotations constrained in the bottom reference

point. However, since the radius of this loading line is 35 mm and the radius of the steel inserts 50 mm, there was a remaining 15 mm of deforming plate (i.e. not included in the rigid body condition) with a modified section of both GFRP laminate and steel. Measuring the thickness of the laminate in this area, an average value of 0.8 mm was obtained which, added to the 1.2-mm thickness of the steel inserts, resulted in a section of 2-mm thickness. The properties of this modified section were calculated by applying the Composite Laminate Theory (CLT) for the in-plane properties and the Rule of Mixtures (ROM) for the out-of-plane properties. The engineering constants used for the laminate (W50.50) and modified section (W50.50+steel) are presented in Table 4.3.

A single zero-thickness layer of three-dimensional built-in cohesive elements of eight nodes (Abaqus/Standard COH3D8, [31]) was implemented at the midplane of the un-cracked region (i.e. the delamination interface, see Figure 4.11). The bulk material (GFRP) was meshed using built-in continuum shell elements of eight nodes and reduced integration (Abaqus/Standard CS8R, [31]). Two through-thickness elements were assigned to each of the halves of the plate (i.e. above and below the delamination interface), this being sufficient to accurately capture the bending behavior (see [8]). A finer mesh was assigned around the end of the pre-crack (indicated as  $a_0$  in Figure 4.11) and at the previously described section-transition zone (from modified steel/GFRP to pure GFRP section). The largest dimension of the elements was 0.981 mm at the end of the pre-crack and 0.552 mm in the section-transition zone. Close to the free edges, elements with a maximum dimension of 3.258 mm were used. The model comprised 387,440 nodes and 299,988 elements.

To determine whether, apart from the dominant opening mode (Mode I), shear fracture modes (Mode II and Mode III) were contributing to the propagation of the crack, shear displacements in the cohesive elements were also computed. Insignificant values were obtained throughout the simulation, confirming a pure opening mode at the crack tip.

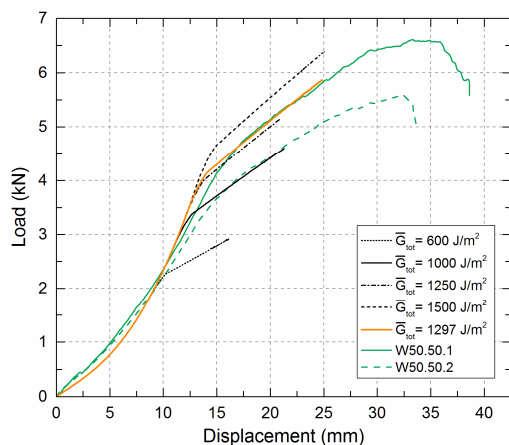


Figure 4.12 – Numerical load vs opening displacement curves obtained for W50.50 laminates using different values of  $G_{0t}$  and a linear-softening cohesive law (see Figure 4.9(b)) compared to experimental curves

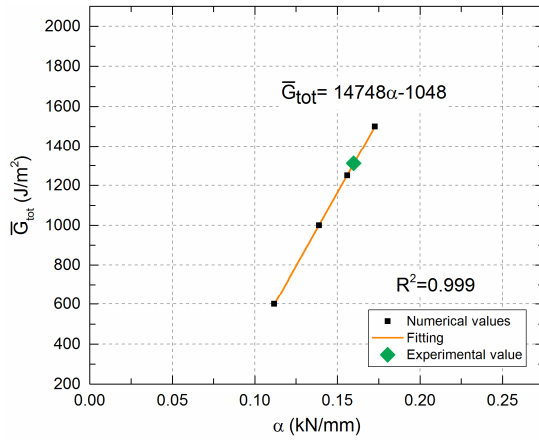


Figure 4.13 – Numerical  $\alpha$  vs  $\bar{G}_{tot}$  curve obtained for W50.50 laminates

In Step 2, four FE analyses were performed considering four different values of  $\bar{G}_{tot}$  (600, 1000, 1250 and 1500 J/m<sup>2</sup>). The traction-separation laws used corresponding to the indicated values of  $\bar{G}_{tot}$ , are also presented in Figure 4.7(b) (again implemented through a UMAT). Subsequently, and according to Step 3, the numerical load-displacement curves were extracted (see Figure 4.12), and the slopes ( $\alpha$ ) corresponding to each value of  $\bar{G}_{tot}$  were derived; the  $\alpha$  -  $\bar{G}_{tot}$  pairs obtained are plotted in Figure 4.13. A linear relationship was also obtained and the equation of the fitted line is likewise indicated.

Due to the nature of the woven reinforcement, a typical “run-arrest” behavior [32] in the experimental load-displacement curves was obtained (see Figure 4.4(a)). Therefore, to determine the experimental slopes (Step 4), only the segments between the small jumps were considered (see Figure 4.4(b)), i.e. 4 to 5 segments were selected in a way to minimize their standard deviation. Each of the computed segments is indicated in red with ordinal numbers. An average slope was obtained for each of the plates. Finally, and following Steps 5 and 6, the mean value of both experimental slopes (i.e. 0.159) was entered in the fitted equation in Figure 4.13. A value of  $\bar{G}_{tot} = 1297$  J/m<sup>2</sup> was obtained. A new simulation using this value and also a simple linear-softening traction-separation law was then performed. The resulting load-displacement curve is shown in Figure 4.12. A fairly good agreement with the experimental results, beyond the TP, was obtained. The slopes compared well while the average load level of the two experiments was only slightly overestimated (approximately a 10%); the latter was attributed to the experimental scatter exhibited for this type of plate, which was higher than in the CFM (Figure 4.3) and W60.40 (Figure 4.5) plates.

### **Comparison with DCB fracture results and discussion**

For comparison between the 2D total SERR obtained in the previous section and the 1D total SERR corresponding to the same fiber architecture, DCB specimens were fabricated and investigated. In order to examine whether the stiffness (different depending on the orientation of the woven fabrics) had any effect on the 1D fracture behavior, one specimen with the layers of woven fabric oriented at 0/90° and another

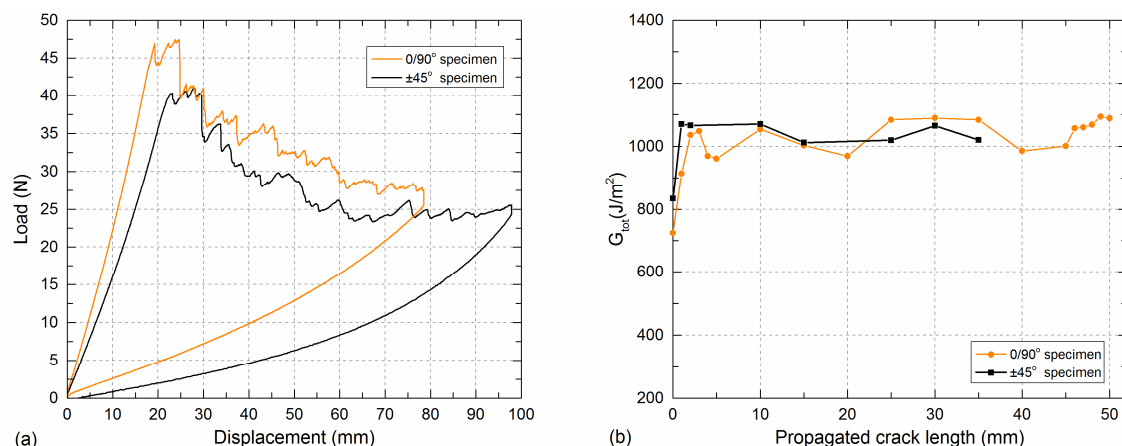


Figure 4.14 – (a) Experimental load-displacement curves and (b) R-curves of W50.50 DCB specimens

at  $\pm 45^\circ$  degrees (both with respect to the longitudinal direction of the DCB specimen) were investigated, as indicated in Figure 4.2(b). The specimens were 25 mm wide and 6.55 mm thick. They were cut from a new laminate fabricated with the same lay-up as that used in the W50.50 plates (i.e. eight layers of reinforcement - see Table 4.2) using the vacuum infusion technique. A Teflon film of 13  $\mu\text{m}$  thickness was placed at the midplane to introduce the pre-crack. Similar infusion and curing protocols to those of the plates were used [7]. The load was transferred from the loading frame to the specimens with patented mechanically fixed loading blocks [33]. The experiments were performed under displacement-control on a 5-kN MTS Insight electromechanical machine with a load cell calibrated from 1 to 100% of its maximum capacity at a displacement rate of 5 mm/min. All the experiments were conducted under laboratory conditions,  $23 \pm 2^\circ\text{C}$  and  $50 \pm 5\%$  RH and according to the ISO 15024 standard [2]. The crack length was monitored from one side of the specimen where a thin coat of white paint was applied. A video acquisition system comprising a Canon 550D digital camera installed on a travelling fixture was employed to optically monitor the crack. Vertical markers were drawn each millimeter between a 1- and 5-mm distance from the crack tip and each 5 millimeters from a 5- to 50-mm distance.

The experimental load vs displacement curves for the two configurations of DCB ( $0/90^\circ$  and  $\pm 45^\circ$ ) are presented in Figure 4.14(a). They exhibited the so-called “run-arrest” behavior [32] in the descending branch due to the unstable crack propagation typical of woven fabric composites. The total strain energy release rate ( $G_{tot}$ ) was calculated using the experimental compliance method (ECM) [34] and the derived R-curves are shown in Figure 4.14(b). It can be observed that similar values were obtained for both specimens, leading to the conclusion that there were no relevant differences in the 1D fracture behavior as a result of the orientation of the fabric. A limited amount of fiber-bridging was observed (Figure 4.14(b), with an increase of  $G_{tot}$  from approx. 800 to 1000 J/m²), which is typical in woven fabric DCB specimens [32].

Similarly to what was observed in the CFM plates (see [8]), where the total SERR increased by 50% in comparison to the DCB specimens due to an increase in the fiber-bridging, the

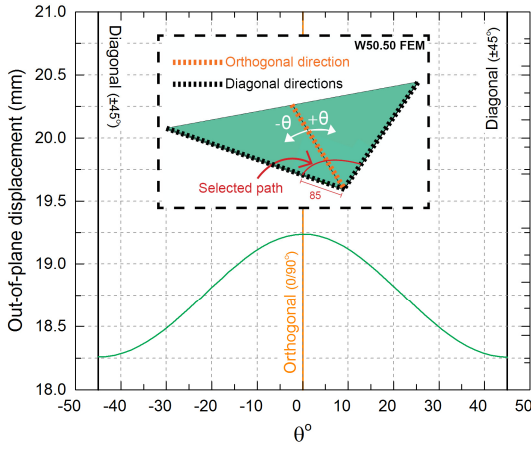


Figure 4.15 – Example of out-of-plane displacement profile at cracked region in W50.50 plates. Dimensions in mm

total SERR value obtained for the W50.50 plates was approximately 30% higher than the total SERR derived from the DCB specimens ( $\sim 1300$  vs  $\sim 1000$  J/m<sup>2</sup>). This increase was likewise assumed to also be caused by an increase in the fiber-bridging. This is further confirmation of the influence of the stiffness-related effects (see [8]) in 2D delamination cases.

As discussed in Section 4.2.2, additional transversal fiber-bridging developed in the case of the W50.50 plates as a result of the uneven opening of the deformed part of the plate. To confirm this, the out-of-plane displacement profile along a circumferential path at an 85-mm distance from the center of the plate (i.e. 5 mm before the end of the pre-crack), extracted from the last FE model (i.e. with a  $\bar{G}_{tot} = 1297$  J/m<sup>2</sup>) at an opening displacement of  $\sim 26$  mm, is presented in Figure 4.15. It can be observed that along the stiffest direction (i.e. the orthogonal 0/90° direction) the out-of-plane displacement was significantly higher than along the diagonal directions ( $\pm 45^\circ$ ), causing the transversal crack growth and corresponding fiber-bridging. Therefore, the transversal fiber-bridging constitutes a further 2D effect, which can also be likewise amplified by the stiffness-related effects. In cases where no fiber-bridging develops, none of the described 2D effects would apply.

### 4.5.3 W60.40 laminates

A last validation of the method was carried out using the experimental results of the W60.40 plates. The 3D FE model (Step 1) was developed also using the commercial FEA software ABAQUS 6.14.1 and its geometry and dimensions are shown in Figure 4.16. Half of the plate was modeled using the symmetry plane “A” according to the experimental behavior of the free edges (see [7]) and a symmetric boundary condition was correspondingly applied. The thickness of the laminate was the average of the experimental thicknesses, i.e. 3.055 mm (Table 4.2). As in the FE model of the W50.50 plates, the loading system was not explicitly modeled and all the nodes in the inner faces inside the loading line were tied using a rigid body condition [31] to reference points (Figure 4.16). The boundary conditions (same as for the W50.50 model) were applied to the reference points. The same method as that described in Section 4.5.2 to characterize

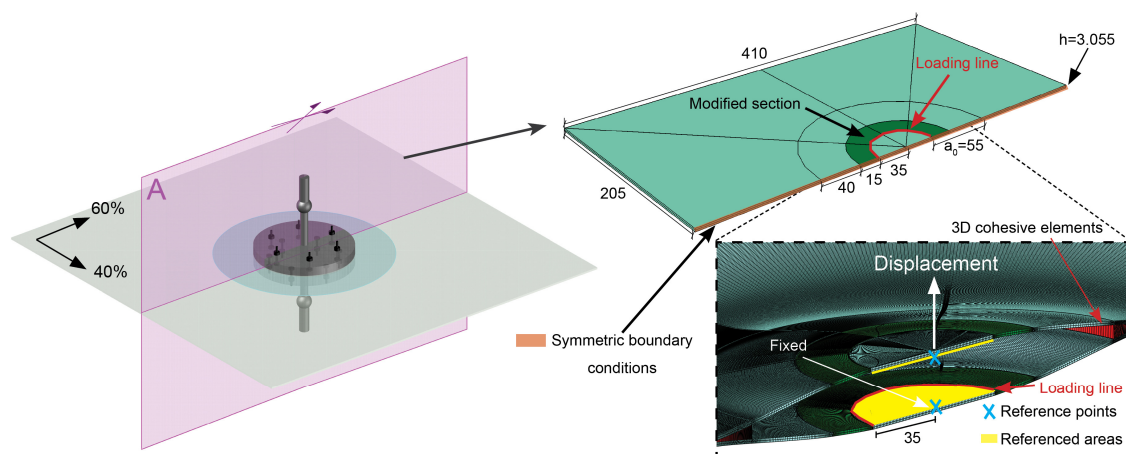


Figure 4.16 – Description of finite element model of W60.40 laminated plate. Dimensions in mm

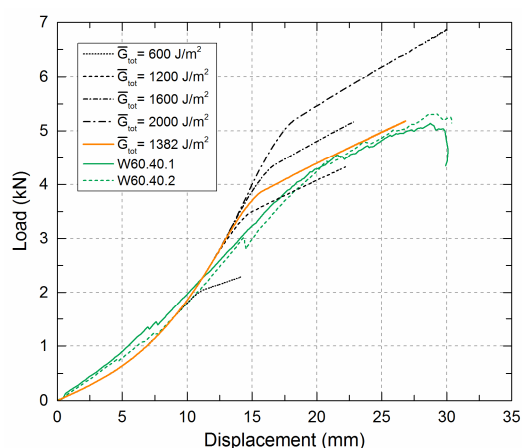


Figure 4.17 – Numerical load vs opening displacement curves obtained for W60.40 laminates using different values of  $\bar{G}_{tot}$  and a linear-softening cohesive law (see Figure 4.9(b)) compared to experimental curves

the modified section of steel and GFRP was followed. The engineering constants used to define the pure bulk material (GFRP) and the composite section are presented in Table 4.3. The same type of elements as in the W50.50 FE model were used in both bulk and cohesive sections (see Section 4.5.2). The largest dimension of the elements close to the end of the pre-crack was 0.896 mm. Also a finer mesh was used at the transition from the modified GFRP/steel section to pure GFRP section, with elements whose largest dimension was 0.495 mm. Elements of 2.562 mm (also the largest dimension) were used close to the boundaries. The model comprised 642,806 nodes and 490,880 elements and insignificant values of cohesive shear displacement were also obtained throughout the simulation, again confirming a pure opening fracture mode. No contribution of shear fracture modes was found.

Four different values of  $\bar{G}_{tot}$  (600, 1200, 1600 and 2000 J/m<sup>2</sup>) were used to evaluate the  $\alpha - \bar{G}_{tot}$  behavior (one simulation for each value, Step 2). The traction-separation laws used (also the same in all directions as for the W50.50 plates) are shown in Figure 4.7(b) and the numerical load-displacement curves obtained for each simulation are presented in Figure 4.17 (Step 3). The extracted  $\alpha - \bar{G}_{tot}$  pairs are represented in



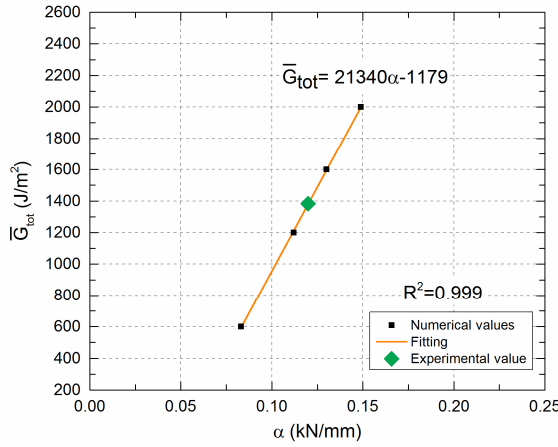


Figure 4.18 – Numerical  $\alpha$  vs  $\bar{G}_{tot}$  curve obtained for W60.40 laminates

Figure 4.18 together with the equation also fitting a linear behavior (Step 4). Again, due to the woven nature of the reinforcement, a “run-arrest” behavior occurred and the experimental slopes (Step 5) were thus again determined by considering only the segments between the irregularities (see Figure 4.5(b)) following the same procedure as in Section 4.5.2. The mean value of both experimental slopes was 0.120, which, according to the fitted equation in Figure 4.18, provided a value of  $\bar{G}_{tot} = 1382 \text{ J/m}^2$  (Step 6). As for the W50.50 plates, a new simulation using this value and also a simple linear-softening traction-separation law was performed. The load-displacement curve obtained is shown in Figure 4.17. Good agreement with the experimental results for the slope and load level of the linear part of the curves was obtained.

## 4.6 Conclusions

A numerically-based method to determine the total SERR involved in the Mode I-dominated 2D delamination of GFRP laminates with internal embedded defects and subjected to opening loads was presented in this work. The method is based on the relationship between the slope of the load-displacement curves after the full development of the FPZ and the total SERR involved in the delamination process. The equation relating both parameters (linear for the studied cases) is derived from three-dimensional FE analysis using simple linear-softening cohesive zone models. The above-mentioned slope and total SERR correspond to the overall 2D fracture behavior. Thus, the same mean linear-softening traction-separation law is implemented in every direction, simplifying considerably the computational effort. The total 2D SERR is obtained by substituting the corresponding slope of the load-displacement experimental curves in the derived equation. Even though with this method the total SERR value along certain directions may be locally overestimated or underestimated, therefore resulting in an inaccurate crack propagation pattern, it can however assure that no unstable propagation of the crack area occurs. The method is thus suitable for damage-tolerant designs. The crack front does not need to be monitored throughout the experiment since the load-displacement curves are the only experimental input required. This constitutes a considerable simplification in the experimental process,



reducing time and instrumentation, particularly in opaque laminates offering no visual access to the crack.

The method was validated using the experimental results obtained for three types of GFRP/epoxy plates with different fiber architectures. Further validation with different materials is however still recommended. The presented method is valid for any fiber architecture, crack shape and boundary conditions in Mode I-dominated and opening loading cases. If shear fracture mode contributions would arise, the presented method would not be applicable.

The total SERR obtained by applying the method for one of the validation plates (W50.50) was compared to the total SERR obtained from DCB specimens composed of the same material. The total SERR obtained for the plates was 30% greater than for the DCBs. As for the CFM plates, this was caused by an increment in the amount of fiber-bridging, which in this case developed both radially and circumferentially, as a result of the increase in the bending stiffness (from beam to plate), its uneven distribution and the stress-stiffening effect. This constitutes further confirmation of the relevant role of stiffness effects on the development of fracture mechanisms in 2D delamination.

## References

1. Benzeggagh, M.L., Kenane, M. Measurement of mixed-mode delamination fracture toughness of unidirectional glass/epoxy composites with mixed-mode bending apparatus. *Compos. Sci. Technol.*, 1996; 56: 439–449.
2. ISO 15024:2001: Fibre-reinforced plastic composites — Determination of the mode I interlaminar fracture toughness, GIC, for unidirectionally reinforced materials (83.120 – Reinforced Plastics).
3. ISO 15114:2014: Fibre-reinforced plastic composites — Determination of the mode II fracture resistance for unidirectionally reinforced materials using the calibrated end-loaded split (C-ELS) test and an effective crack length approach (83.120 – Reinforced Plastics).
4. ASTM D6671/D6671M - 13e1: Standard test method for mixed mode I-mode II interlaminar fracture toughness for unidirectional fiber-reinforced polymer matrix composites, in *Annual book of ASTM standards: adhesive section* 15.03.
5. Chen, Z.M., Krueger, R., Rinker, M. Facesheet/Core Disbond Growth in Honeycomb Sandwich Panels Subjected to Ground-Air-Ground Pressurization and In-Plane Loading. In: *11th International Conference on Sandwich Structures ICSS-11*, Ft. Lauderdale, USA, March, 2016.
6. Riccio A., Gigliotti M. A novel numerical delamination growth initiation approach for the preliminary design of damage tolerant composite structures. *J. Comp. Mat.*, 2007;41(16):1939:1960.
7. Cameselle-Molares A., Vassilopoulos A.P., Keller T. Experimental investigation of two-dimensional delamination in GFRP laminates. *Eng. Frac. Mech.*, 2018; 203: 152-171.
8. Cameselle-Molares A., Vassilopoulos A.P., Renart J., Turon A., Keller T. Numerical simulation of two-dimensional in-plane crack propagation in FRP laminates. *Comp. Struc.* 2018; 200: 396-407.
9. Shaverdi M., Vassilopoulos A.P., Keller T. Modelling effects of asymmetry and fiber bridging on Mode I fracture behavior of bonded pultruded composite joints. *Eng. Fract. Mech.*, 2013; 99: 335-348.

10. Cameselle-Molares A., Roohollah S., Shaverdi M., Vassilopoulos A.P., Keller T. Fracture mechanics-based progressive damage modelling of adhesively bonded fibre-reinforced polymer joints. *Fatigue Fract. Eng. Mater. Struct.*, 2017; 40(12): 2183-2193.
11. Pappas G, Canal L.P., Botsis J. Characterization of intralaminar mode I fracture of AS4/PPS composites using inverse identification and micromechanics. *Composites: Part A*, 2016; 91: 117-126.
12. Suo Z., Bao G., Fan B. Delamination R-curve phenomena due to damage. *J. Mech. Phys. Solids*, 1992; 40 (1): 1-16.
13. Manshadi B.D., Vassilopoulos A.P., Botsis J. A combined experimental/numerical study of the scaling effects on mode I delamination of GFRP. *Comp. Science and Tech.*, 2013; 83: 32-39.
14. Canal L.P., Alfano M., Botsis J. A multi-scale based cohesive zone model for the analysis of thickness scaling effect in fiber bridging. *Comp. Science and Tech.*, 2017; 139: 90-98.
15. Bao G., Suo Z. Remarks on crack-bridging concepts. *Appl. Mech. Rev.*, 1992; 45(8); 355-366.
16. Farmand-Ashtiani E., Cugnoni J., Botsis J. Specimen thickness dependence of large scale fiber bridging in mode I interlaminar fracture of carbon epoxy composite. *Inter. J. of Solids and Struct.*, 2015; 55: 58-65.
17. Blackman B.R.K., Kinloch A.J., Paraschi M. The determination of the mode II adhesive fracture resistance,  $G_{IIc}$ , of structural adhesive joints: an effective crack length approach. *Eng. Fract. Mech.*, 2005; 72: 877-897.
18. Rice J. A path independent integral and the approximate analysis of stain concentration by notches and cracks. *J. Appl. Mech.*, 1968; 35:379-386.
19. Pérez-Galmés M., Renart J., Sarrado C., Rodríguez-Bellido A., Costa J. A data reduction method based on the J-integral to obtain the interlaminar fracture toughness in a mode II end-loaded split (ELS) test. *Composites: Part A*, 2016;90:670-677.
20. Que N.S., Tin-Loi F. An optimization approach for indirect identification of cohesive crack properties. *Comput. Struct.*, 2002; 80: 1383-92.
21. Xu, Y., Li, X., Wang, X., Liang, L. Inverse parameter identification of cohesive zone model for simulating mixed-mode crack propagation. *Int. J. Solids and Struct.*, 2014; 51: 2400-2410.
22. Dourado N., de Moura M.F.S.F., de Moraes A.B., Pereira A.B. Bilinear approximations to the mode II delamination cohesive law using an inverse method. *Comp. Struct.*, 2015; 122: 361-366.
23. De Moura M.F.S.F., Moraes J.J.L., Dourado N. A new data reduction scheme for mode I wood fracture characterization using the double cantilever beam test. *Eng. Frac. Mech.*, 2008; 75: 3852-65.
24. Valoroso, N., Sessa, S., Lepore, M., Cricri, G. Identification of mode-I cohesive parameters for bonded interfaces based on DCB test. *Eng. Frac. Mech.*, 2013; 104: 56-79.
25. Ortega A., Maimí P., González E.V., Trias D. Characterization of the translaminar fracture cohesive law. *Composites: Part A*, 2016; 91: 501-509.
26. Owen's Corning Reinforcements Composite Solutions Guide. <[http://www.ocvreinforcements.com/pdf/library/Composite\\_Solutions\\_Guide\\_100360\\_E\\_finalprintable.pdf](http://www.ocvreinforcements.com/pdf/library/Composite_Solutions_Guide_100360_E_finalprintable.pdf)> (Accessed 26 March 2018).
27. Sika datasheet product. <[https://deu.sika.com/dms/getdocument.get/dd4b783e-bfa5-32e3-a705-f9f548f6b326/Biresin\\_CR83\\_eng.pdf](https://deu.sika.com/dms/getdocument.get/dd4b783e-bfa5-32e3-a705-f9f548f6b326/Biresin_CR83_eng.pdf)> (Accessed 19 October 2017).
28. Turon A., Camanho P.P., Costa J., Dávila C.G. A damage model for the simulation of delamination in advanced composites under variable-mode loading. *Mechanics of Materials*, 2006; 38(11): 1072-1089.

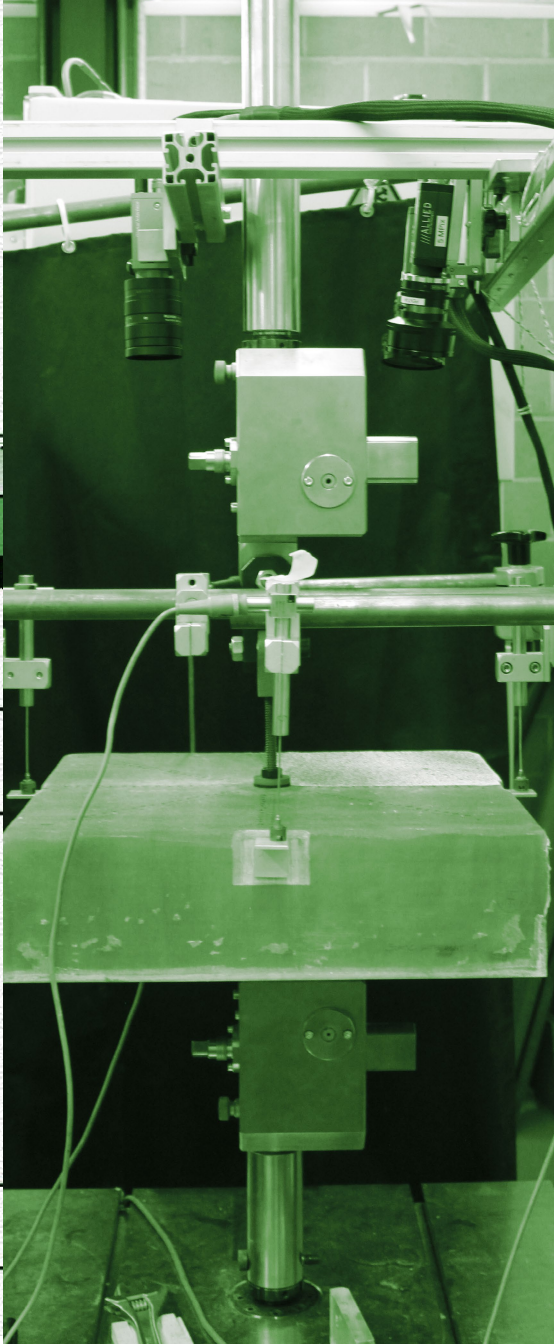
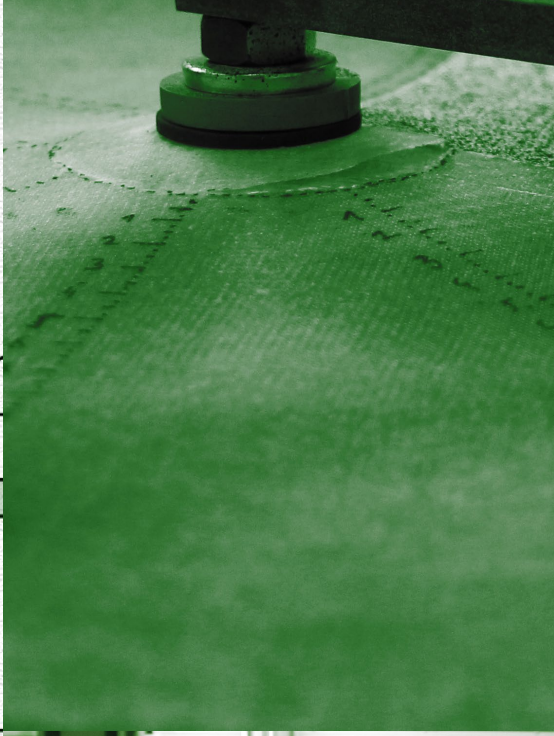
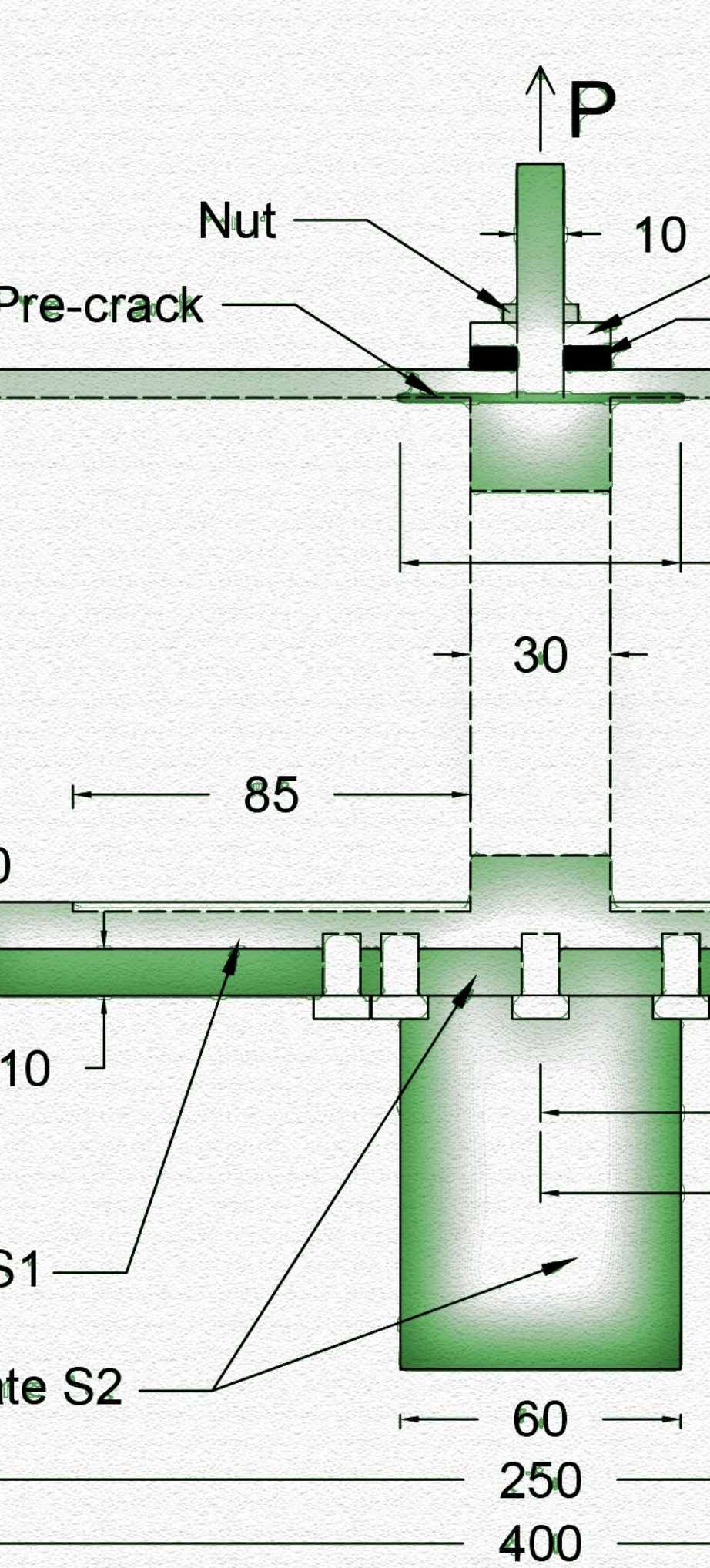
29. Camanho P.P., Dávila C.G., Ambur D.R. Numerical simulation of delamination growth in composite materials. NASA/TP-2001-211041. Hampton: NASA Langley Research Center; 2001.
30. Turon A., Camanho P.P., Costa J., Renart J. Accurate simulation of delamination growth under mixed-mode loading using cohesive elements: Definition of interlaminar strengths and elastic stiffness. *Composite Structures*, 2010; 92(8): 1857–1864.
31. Abaqus Inc. Abaqus analysis user's manual, version 6.14-1. 2014. Providence, RI, USA.
32. Blake S.P., Berube K.A., Lopez-Anido R.A. Interlaminar fracture toughness of woven E-glass fabric composites. *J. Comp. Mat.*, 2011; 46(13): 1583:1592.
33. Renart J., Blanco N., Pajares E., Costa J., Lazcano S., Santacruz G. Side Clamped Beam (SCB) hinge system for delamination tests in beam-type composite specimens. *Comp. Sc. and Tech.*, 2011; 71; 1023-1029.
34. Anderson Ted. *Fracture mechanics*. 2nd ed. Texas: CRP; 1995.

---

**Contributions:** Aida Cameselle Molares conceived, designed and performed the experimental campaign under the supervision of Prof. Thomas Keller, Dr. Jordi Renart and Dr. Anastasios Vassilopoulos. The numerically-based method model was developed by Aida Cameselle Molares under the supervision of Prof. Thomas Keller and Dr. Vassilopoulos. The analysis of the results was carried out by Aida Cameselle Molares in collaboration with Prof. Thomas Keller and Dr. Anastasios Vassilopoulos. Dr. Jordi Renart and Dr. Albert Turon provided advise in the development of the finite element models.







## Chapter 5

# Two-dimensional debonding

## *Quasi-static experimental investigation*

### 5.1 Introduction

Sandwich structures are currently used in a wide number of engineering applications where lightweight and efficient structural systems are required. Notably, systems formed by fiber-reinforced polymer (FRP) face sheets and low-density cores have been extensively and traditionally employed in the naval, aerospace or automotive industries. Thanks to the important advantages provided by FRP sandwich structures, such as high strength- and stiffness-to-weight ratios, rapid installation and versatility, the number of FRP sandwich structural elements used in civil infrastructure applications has increased [1-3]. Specifically, GFRP sandwich bridge decks offer great thickness flexibility, which constitutes a significant advantage for conceiving longer spans [4,5]. Honeycomb, foam (with shear GFRP webs) and balsa cores are usually employed in sandwich deck designs. Balsa cores are particularly advantageous due to their sufficient shear capacity and uniform support for the upper face sheet in contact with the frequent wheel loads [4-6].

When disbands between the face sheets and the core occur either during manufacturing or due to impacts during the structural life service, the bearing capacity and thus the structural integrity of a sandwich member may be affected [7,8]. Mode I-dominated debonding is considered the most critical phenomenon in sandwich structures [8,9]. The existence of disbands in structural elements under pure compression or bending may induce premature face sheet wrinkling [10] causing the



disbonds to open. Curved members subjected to tensile out-of-plane stresses may also lead to Mode I-dominated debonding scenarios.

To improve the face/core adhesion, layers of reinforcement with randomly oriented fibers such as chopped strand mat (CSM) or continuous filament mat (CFM) have been typically used in sandwich applications [11]. By adding these layers in the interface between the face sheet and core, a gradual stiffness transition zone is provided and the resin flow during fabrication of the panels is increased, thus avoiding dry areas. Furthermore, this type of layer is prone to develop fiber-bridging, providing additional fracture toughening of the interface and therefore improving the damage tolerance. The effect on the debonding fracture behavior of the layup at the face sheet/core interface of GFRP/foam sandwich panels, under different degrees of mode-mixity, was investigated in [12]. One of the examined face sheet's layups consisted of four layers of quadriaxial (90,45,0,-45) reinforcement, a layer of woven reinforcement and a layer of CFM. The latter was in contact with the core. Mode I-dominated loading caused the crack to propagate in the resin between the core and face sheet, while in Mode II-dominated loadings the crack migrated into the CFM layer causing the increase in fiber-bridging and fracture resistance. The crack never penetrated the woven layer. Additionally, for strongly Mode II-dominated cases, secondary cracks initiated between the woven layer and the quadriaxial plies.

Due to the critical importance of Mode I-dominated debonding in the structural performance of FRP sandwich elements, numerous test methods to evaluate and characterize the face sheet/core opening fracture behavior have been extensively discussed in the literature [7, 13-20]. Owing to the inherent elastic property mismatch at the interface between the core and the face sheets, crack propagation always occurs under a certain degree of mode-mixity [21]. Thus, of all the investigated specimen configurations, the single cantilever beam (SCB) method has been found to be the most appropriate as a compromise between experimental simplicity and Mode I-dominated loading conditions [8, 9, 22, 23]. Double cantilever beam specimens loaded by uneven moments (DCB-UBM) was also proved to be a suitable test method to characterize any mode-mixity, ranging from Mode I-dominated to Mode II-dominated, but it does however require a much more complex set-up [12].

All these experimental methods rely on beam-like one-dimensional (1D) specimens where the crack debonds with an approximately constant crack width in the longitudinal direction of the specimens. Nevertheless, debonding damage in actual structural members may span all around the perimeter, constantly modifying the size of the crack front.

An experimental investigation of the fracture delamination behavior of GFRP plates with embedded circular pre-cracks (i.e. 2D delamination) and subjected to out-of-plane opening loads was carried out in [24]. Results proved that, due to the boundary conditions inherent to an embedded crack growing in a laminated plate, a stiffening of the plates due to the appearance of in-plane stretching stresses occurred. Plates with a fiber architecture composed of layers of CFM were further numerically investigated in [25]. Results confirmed a 50% increase, compared to standard 1D DCB specimens with



the same layup, in the required strain energy release rate (SERR). The increase of the developed fiber-bridging, as a result of the increase in the flexural stiffness (1D beams vs 2D plates) together with the previously mentioned stress stiffening effect, was found to cause this SERR increase.

Currently, 1D debonding fracture properties are typically used in the numerical modeling of 2D debonding scenarios [26-28]. Nevertheless, 2D effects similar to those addressed in 2D delamination are expected to occur when fiber-bridging develops as a result of a 2D crack debonding in sandwich panels, therefore limiting the validity of 1D standard fracture results.

The main objective of this work was therefore to investigate the experimental 2D debonding in GFRP/balsa sandwich panels, thus extending the 2D fracture investigation initiated for 2D delamination in laminated plates in [24]. For this purpose, a new experimental set-up was developed. Circular embedded disbonds were introduced in the center of the face sheet/core interface and quasi-static out-of-plane tensile loads were applied to open the crack. In order to achieve a Mode-I-dominated loading and thus minimize the shear mode fracture contributions due to the elastic mismatch, the bottom of the sandwich panels was fixed, as in the set-up of the SCB. A total of four panels and two different face-sheet configurations were investigated: a pure woven layup and a combination of woven plies and CFM layers. The latter were placed at the face sheet/core interface to evaluate their effect on the debonding fracture performance. In view of the results from [24], a stretching of the face sheets and consequent shear mode contributions were expected. To quantify the magnitude of the stretching, in-plane strains were monitored throughout the experiments. Post-mortem cuts of the panels were made through the thickness to evaluate the crack propagation paths. Additionally, the influence of the fracture process zone (FPZ) on the experimentally obtained in-plane strain profiles and the evolution of the inflection points throughout the experiments were also discussed.

## 5.2 Experimental program

### 5.2.1 Material description

The face sheets of the investigated sandwich panels were fabricated with two types of glass fiber reinforcements: a 390-g/m<sup>2</sup> weight woven fabric (W) with a proportion of 50/50 in the warp/weft directions (provided by Swiss-Composite, Switzerland) and a long continuous filament mat (CFM) of 600-g/m<sup>2</sup> weight (provided by Owens Corning, United States). The fracture behavior of both types of reinforcement under Mode I-dominated conditions was individually investigated at the laminate level in [24]. Photos of the two reinforcements are shown in Figure 5.1. An epoxy resin (Sicommin SR8100) suitable for infusion techniques was selected. The properties of the glass fibers and resin can be found in Table 5.1 (manufacturer data [29-31]). Commercial BALTEK® VCB balsa wood was used for the core (supplied by Colevo, Switzerland). An average density of 228.40 kg/m<sup>3</sup> was determined for the provided pieces.

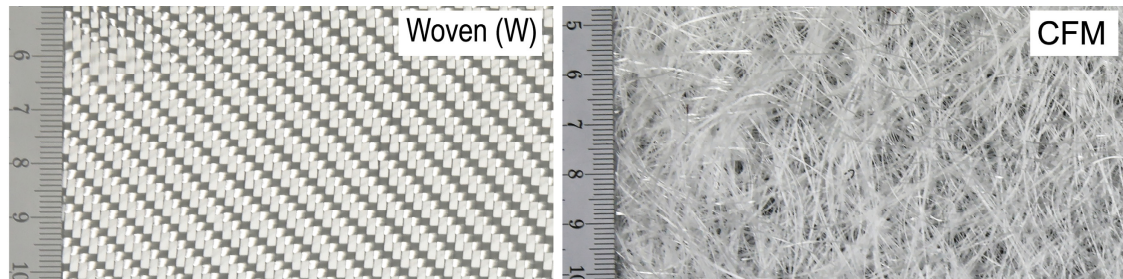


Figure 5.1 – Detail of glass fiber reinforcements used

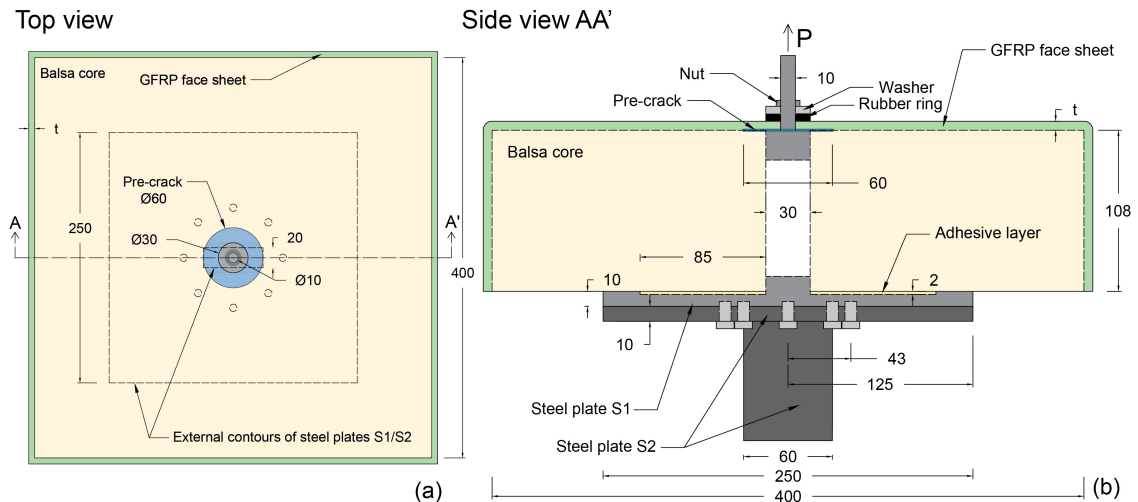


Figure 5.2 – Sandwich panel layout; (a) Top view and (b) Side view of section AA' in (a). Dimensions in mm

> Table 5.1 – Material properties

Material	$E$ (GPa)	$G$ (GPa)	$\nu$ (-)	$\rho$ (g/cm <sup>3</sup> )
Epoxy resin	3.00	1.30	0.35	1.14
E-glass (for woven)	72.00	29.50	0.22	2.55
E-CR <sup>*</sup> glass (for CFM)	80.00	32.80	0.22	2.62

<sup>\*</sup>CR: Corrosion-resistant

## 5.2.2 Specimen description and fabrication

The experimental program consisted of two pairs of GFRP/balsa sandwich panels with two different configurations of the GFRP face sheet (i.e. a total of four panels). The first configuration consisted of 18 plies of woven reinforcement (designated SPA) while for the second (SPB) a symmetric layup combining nine woven plies with two plies of CFM above and another two plies below was selected. The description of each panel type can be found in Table 5.2. The SPB layup was selected in order to obtain an axial and flexural stiffness comparable to those of the SPA configuration. The values were determined using Classic Laminate Theory (CLT). The lamina properties of each of the reinforcements used were estimated following the formulation presented in [24]. The values corresponding to each type of face sheet are given in Table 5.2 and, as can be observed, there is only a 13% and 17% difference in bending and axial stiffness respectively.

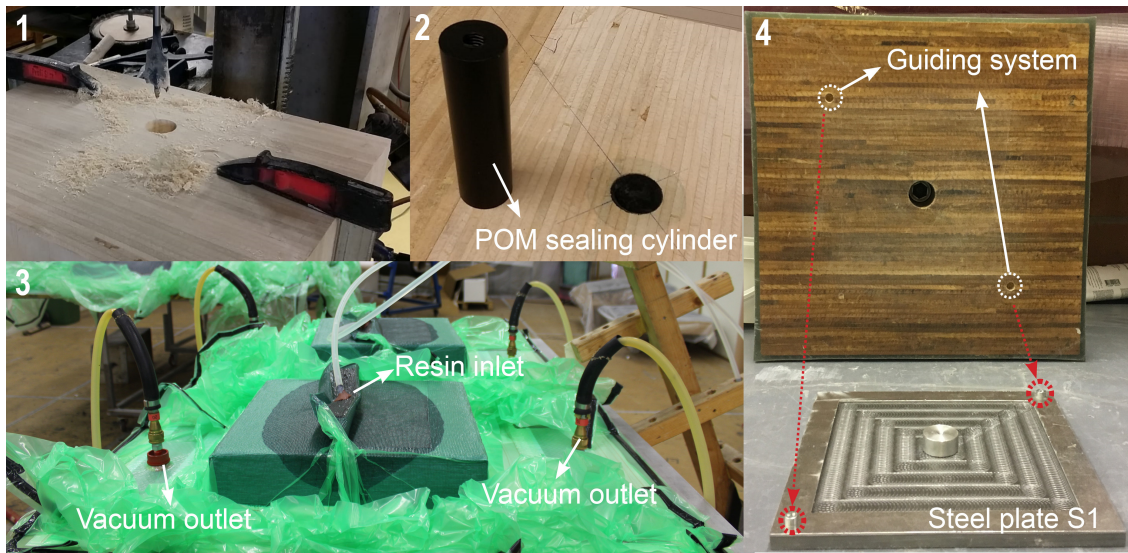


Figure 5.3 – Fabrication sequence

> Table 5.2 – Description of GFRP/balsa sandwich panels

Panel type	GFRP face sheet laminate				Dimensions of Baltek® VBC balsa core (mm)
	Layout	Thickness, $t$ (mm)	Axial stiffness (kN)	Bending stiffness (kN·mm <sup>2</sup> )	
SPA.1/2	(W) <sub>18</sub>	5	128.10	266.87	400 x 400 x 108
SPB.1/2	(CFM) <sub>2</sub> /(W) <sub>9</sub> /(CFM) <sub>2</sub>	6	106.01	230.90	400 x 400 x 108

Furthermore, a symmetrical layup was also selected to avoid any bending-extension coupling effect. The dimensions of the balsa core (see Table 5.2) were the same for all panels.

The layout of the sandwich panels is presented in Figure 5.2. As can be observed, a pre-crack between the GFRP face sheet and the balsa core of 60-mm diameter was created at the center of each panel. The opening load to propagate the pre-crack was transferred from the machine to the panels by means of a 30-mm head and 10-mm shank screw (see Figure 5.2). The perimeters of the surface of the head of the screw in contact with the face sheets were smoothed to remove sharp edges. Furthermore, the face sheets were anchored to the lateral sides of the balsa core to guarantee that no other cracks initiated distant from the pre-crack. The fabrication and assembling process followed to achieve the final design is described in the following.

First, in order to permit the subsequent insertion of the loading screw, a hole of 30-mm diameter was drilled in the center of the balsa core (see Figure 5.2(b) and Figure 5.3 (Step 1)). The vacuum infusion technique was employed to produce all the sandwich panels and therefore the above-mentioned hole in the balsa core was duly sealed before the infusion by a polyoxymethylene (POM) cylinder and mastic (see Figure 5.3, Step 2). A Teflon film of 13- $\mu$ m thickness was placed at the center of the balsa core (i.e. over the

sealed hole) to introduce the pre-crack and the layers of reinforcement were placed over it. To reinforce the top of the loading region (i.e. the center of the panels), three additional circular woven reinforcement layers of 60-mm diameter were added for both the investigated configurations. All the panels were infused with a centered resin inlet and two lateral resin outlets, as can be seen in Figure 5.3, Step 3. Following the infusion process, the panels were cured under vacuum for 12 hours at room temperature and subsequently eight hours at 45°C. Finally, after demolding the panels, the sealing POM cylinder was removed, a hole of 10-mm diameter was drilled at the center of the face sheets and the screw was inserted (Figure 5.2(b)).

To connect the bottom of the panels to the machine, a system of two steel plates was designed. One of the plates (designated S1, see Figure 5.2) was glued with an epoxy adhesive (Sikadur 330) to the bottom surface of each panel. The adhesive was applied inside a 200-mm width, 200-mm height and 2-mm depth volume carved on the top surface of S1 in order that, after placing the panels on top, an adhesive layer of 2-mm thickness was assured (see Figure 5.2 and 5.3, Step 4). Moreover, each S1 steel plate had an additional cylindrical steel element with the same diameter as that of the hole drilled in the balsa (i.e. 30 mm) to avoid any leaking of adhesive inside the hole. Thus a total adhesive surface of 39293 mm<sup>2</sup> was obtained. The correct alignment of all the elements in the vertical axis of the load was guaranteed by a guiding system consisting of two small cylindrical elements fixed on S1 and coincident with holes of the same dimensions at the bottom of the panels, as indicated in Figure 5.3, Step 4. The second steel plate, designated S2, consisted of two joined sub-elements: a horizontal element fixed by eight screws to S1 and a vertical element onto which the bottom grip was finally tightened (see Figure 5.2).

### 5.2.3 Experimental set-up and instrumentation

All the experiments were performed under displacement control at a rate of 1.5 mm/min. The tensile load was applied by a W+B electromechanical machine of 50-kN capacity at a temperature of 24±2°C and relative humidity of 38±5%. The experimental set-up is shown in Figure 5.4. The panels were first fixed and completely constrained by the bottom grip of the machine assuring, with the help of a level, that they were horizontal. The loading screw was then tightened to the surface of the panels by means of a nut, a washer and a rubber ring in order to evenly distribute the pressure (see Figure 5.2). Lastly, the panels were fixed to the top grip using an in-house developed hinge so that any small rotation of the screw due to crack propagation would not damage the loading cell of the machine.

The load and displacement during crack propagation were obtained from the machine (accuracy ±0.11%). In order to subtract from the total measured displacement the contribution due to the deformation of the core and bottom fixation and thus obtain the opening displacement, the panels were equipped with four Linear Variable Differential Transducers (LVDTs, accuracy of ±0.02 mm). To install them precisely at



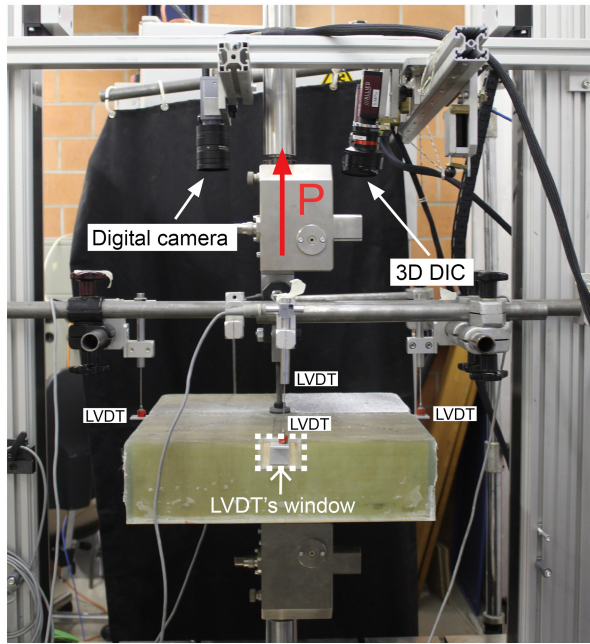


Figure 5.4 – Experimental set-up

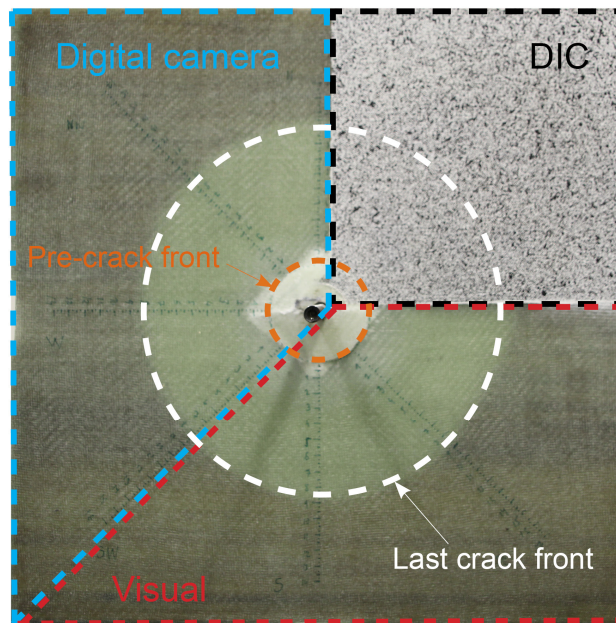


Figure 5.5 – Crack monitoring schema (common to all panels) and crack propagation pattern of sandwich panel SPA.1

the level of the interface between the face sheet and core, four windows were opened in the middle of each of the four lateral sides of the panels (see Figure 5.4).

Three measuring systems were used to monitor the 2D propagation of the crack: a digital camera, 3D Digital Image Correlation (DIC) and visual measurements, as presented in Figure 5.5. For each panel, six rulers starting from the end of the pre-crack and with markers every 2.5 mm were drawn on three quarters of the panel top surface (see Figure 5.5). The crack propagation along four of these rulers was monitored by a digital camera placed above the panels (see location in Figure 5.4) used to take pictures

of the area at an acquisition frequency of 0.2 Hz. The corresponding load and displacement values were recorded for each picture and the value of the crack front was determined by visually post-processing the images. The propagation along the remaining rulers was monitored in-situ by visual inspection. Thanks to the translucency of the face sheet laminates, the crack front was identified by the whitening of the delaminated areas. The 3D DIC system (accuracy  $\pm 0.005$  mm) was used in one quarter of the surface (see Figure 5.5) where a random speckle pattern was applied using white paint and black spray paint. The location of the 3D DIC cameras is shown in Figure 5.4. The acquisition frequency of the images was also 0.2 Hz. The change from straight to curved out-of-plane deformation profiles of the face sheet derived from the DIC was assumed as the crack front. The post-processing of the results was carried out using Vic-3D software from Correlated Solutions Inc. [32]). The DIC system was also used to extract the in-plane strain distributions in the measuring region with an accuracy of  $\pm 0.01\%$ .

## 5.3 Experimental results

### 5.3.1 Load and crack-opening displacement responses

The load and crack-opening displacement responses measured for the SPA and SPB configurations are shown in Figure 5.6. Since the cracks propagated concentrically throughout all the experiments, as can be observed for the SPA.1 panel in Figure 5.5, the values of the crack front in Figure 5.6 are given in terms of total radial crack length (i.e. with the 30-mm radius of pre-crack included). As can be observed, increasing curves after crack initiation were obtained for both configurations, as was also the case for the laminates investigated in [24]. Initially, before the initiation of the crack, similar stiffnesses were exhibited by the two configurations, confirming that the selected layups had comparable bending stiffness, as described in Section 5.2.2. After crack initiation, and during the first millimeters of crack propagation, no obvious variation of stiffness was observed. It then progressively decreased to a fairly constant stiffness (e.g. after 2 mm of opening displacement in SPA.2 panel) thus exhibiting a linear increase of the load. Such behavior (also exhibited in the laminated plates in [24, 25]) could be observed for all the panels.

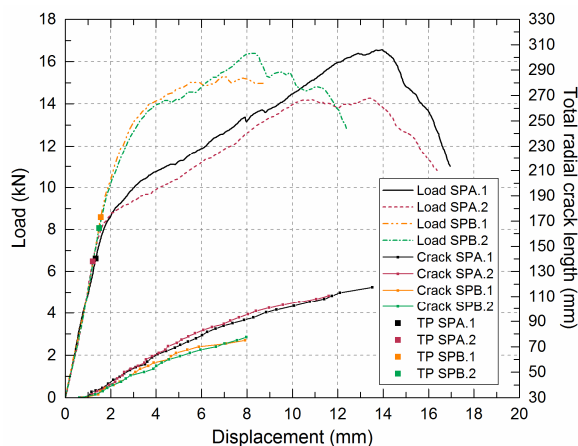


Figure 5.6 – Load and total radial crack length vs opening displacement curves

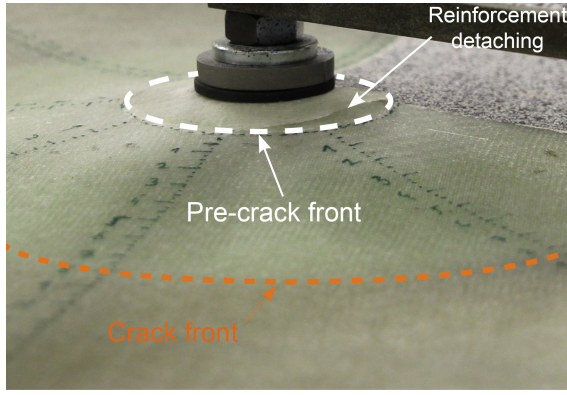


Figure 5.7 – Detail of loading region in SPA.1 after 75 mm of radial propagation (i.e. 105 mm of total radial crack length)

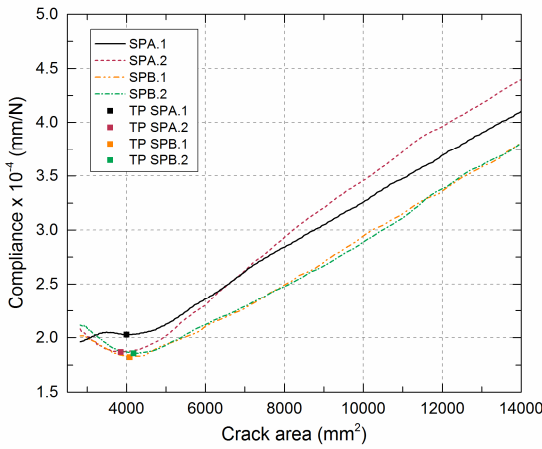


Figure 5.8 – Compliance vs crack area curves

As the crack propagated and the load and displacement increased, the additional woven circular layers of 60-mm diameter used to reinforce the loading region (see Section 5.2.2) started detaching, see Figure 5.7 (photo at 105-mm total radial crack length). However, due to the local effect they exerted, the detaching did not affect the global stiffness of any of the panels. Subsequently, towards the maximum load, local damage also started to develop in the laminate above the pre-crack, which finally prevented the load from increasing further. The load and displacement values at the maximum load are presented in Table 5.3 for each panel. The SPB panels achieved higher loads than the SPA panels. After the maximum loads were reached, the cracks stopped propagating. The last values of total radial crack lengths shown in Figure 5.6 correspond to the last crack fronts.

### 5.3.2 Compliance behavior

The compliance of each panel was calculated as  $\delta/P$ ,  $\delta$  being the opening displacement and  $P$  the load. In order to assign to each compliance value the corresponding crack area, a cubic fitting of the experimental total radial crack length for each configuration was carried out. The compliance vs crack area results are presented in Figure 5.8. Values are given from crack initiation up to a crack area value of 14000 mm<sup>2</sup> (i.e. 66.75 mm of total radial crack length). Although the curves would continue until the last value of



> Table 5.3 – Load-displacement values at initiation, maximum loads and minimum compliances

Panel	At initiation		At max. load		At min. compliance (TP)	
	Disp. (mm)	Load (kN)	Disp. (mm)	Load (kN)	Disp. (mm)	Load (kN)
SPA.1	0.79	4.05	13.90	16.56	1.34	6.61
SPA.2	0.74	3.54	10.89	14.21	1.21	6.47
SPB.1	0.77	3.84	7.07	15.28	1.56	8.58
SPB.2	0.62	2.96	8.23	16.41	1.50	8.06

propagation, a smaller horizontal segment was selected to better represent the initial behavior of the compliance. An initial decreasing trend was exhibited indicating a stiffening of the panels even after crack initiation. Then a minimum was reached and an increasing trend of the compliance was measured until the end of the experiment, consequently indicating a softening of the panels. This behavior was observed for all the panels. A local effect causing an increase of the compliance before the described decrease was recorded for panel SPA.1. The minima of the compliance are indicated with rectangular markers in Figure 5.8. Averaging the total crack area values of each pair of panels at the minimum compliances, values of 3927.6 mm<sup>2</sup> (i.e. a total radial crack length of 35.4 mm) and 4134.3 mm<sup>2</sup> (i.e. a total radial crack length of 36.3 mm) were obtained for the SPA and SPB configurations respectively. The load and displacement values corresponding to the minimum compliances of all the panels are presented in Table 5.3 and shown in Figure 5.6.

### 5.3.3 Crack propagation behavior

Post-mortem inspections of the cracks were carried out by cutting the panels through the thickness to provide direct access to the crack interface. In Figure 5.9 side images of the propagated cracks are shown for one panel of each configuration and drawings representing the observations are also included for better comprehension. Two different types of cracks were observed in both types of configuration that will hereafter be referred to as primary crack and secondary crack. The primary crack corresponded to the propagation of the pre-crack that was introduced into the interface between the face sheet and balsa core. The secondary crack was a new crack created during the experiments.

As can be observed, in the SPA panels the primary crack propagated throughout the whole experiment in the face sheet/core interface, without any migration. The secondary crack initiated in parallel to the primary crack between the first and second woven plies. Furthermore, the ultimate front of the primary crack corresponded to a shorter propagated radial crack length (referred to as “b” in Figure 5.9(a)) than the length corresponding to the ultimate crack front observed during the experiments (see Figure 5.6). A value of b=26 mm was observed for SPA.1 (i.e. at a total radial crack length of 56 mm) while a higher value of b=58 mm (i.e. at a total radial crack length of 88 mm) was observed for SPA.2. Therefore, the ultimate crack fronts observed from the top of the panels during the experiments corresponded to the front of the secondary crack.

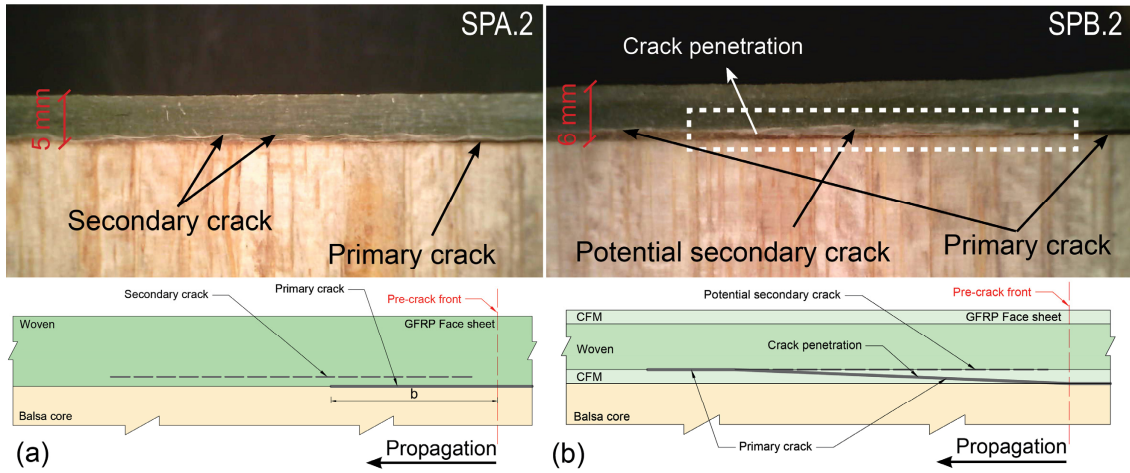


Figure 5.9 – Crack interfaces of (a) sandwich panel SPA.2 and (b) sandwich panel SPB.2

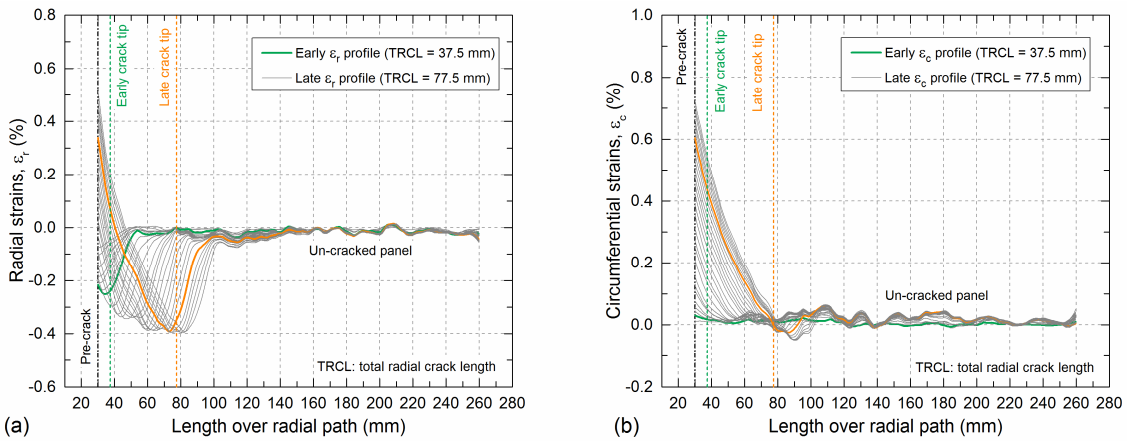


Figure 5.10 – Face sheet top surface in-plane strain distributions extracted from DIC; (a) in radial direction and (b) in circumferential direction for SPA.2

The point where the secondary crack overtook the primary crack could not be determined from the post-mortem inspection.

A different behavior of the primary crack was observed for the SPB panels (Figure 5.9(b)) in which shortly after crack initiation it already started to penetrate progressively into the CFM layer, thus generating dense fiber-bridging. After approximately 30 mm of radial propagation (i.e. a total radial crack length of 60 mm), the primary crack had completely migrated from the face sheet/core interface into the interface between the CFM and the first woven ply; the woven layer was not penetrated however. The secondary crack, also located between the CFM and the woven layers, either merged with the migrated primary crack or propagated backwards after migration of the primary crack – both scenarios are plausible.

### 5.3.4 Radial and circumferential strain distribution

The in-plane strains in the top surface of the face sheet were extracted from the 3D DIC measurements. In Figure 5.10, the radial and circumferential strain profiles corresponding to a radial path (starting from the end of the pre-crack) in the SPA.2 panel are presented. Two profiles are highlighted: an “early profile” (in green)

corresponding to a total radial crack length of 37.5 mm and a “late profile” (in orange) corresponding to a total radial crack length of 87.5 mm. The crack tips are also indicated for each of the highlighted profiles, permitting a clear distinction between the cracked and un-cracked regions. Observing the radial profiles in the cracked region, two types of profile can be distinguished depending on the size of the crack: a full compression strain profile for small cracks and strain profiles partially in compression and partially in tension for longer cracks. The circumferential strains in the cracked region remained in tension throughout the experiments. A typical compression state [33, 34] of the laminate in the un-cracked region could be observed throughout the experiment in both strain profiles. The magnitudes of these compression strains were greater in the radial than in the circumferential direction.

## 5.4 Discussion

### 5.4.1 Load and crack-opening displacement responses

Throughout the propagation of a 2D embedded crack, the length of the crack front (i.e. the perimeter of the crack) increased, contrasting with the typical 1D behavior of beam-like fracture mechanics experiments where the crack front length remains constant. Specifically, in the cases presented here, equal increments in the radial crack length led to increasing lengths of the concentric crack fronts. The resulting disproportional growth of the crack area forced the load to increase in order to maintain the crack propagation – again in contrast to 1D propagation where the load decreases – as can be observed for all the investigated panels in Figure 5.6. Further discussion regarding this 2D effect can be found in [24, 25].

Although all panels presented comparable bending stiffnesses, the SPB panels attained higher loads than the SPA panels (see Figure 5.6). For instance, comparing the linear part (after the progressive change of the stiffness) of the load-displacement curves of SPA.1 and SPB.1 panels, a load increase of  $\sim 3$  kN (i.e. a  $\sim 27\%$  increase) was registered. This enhancement originated as a result of the greater amount of fiber-bridging developed in the SPB panels where, as described in Section 5.3.3, the crack penetrated the CFM layers thus generating dense fiber-bridging. Additionally, as the crack never penetrated into the woven layers once migrated, the load-bearing part of the laminate (i.e. the woven layers) remained intact throughout the experiments. The effect of crack migration and the consequent dense fiber-bridging was also confirmed by the crack length vs displacement curves (see Figure 5.6), where an evident crack arrest in the SPB panels could be observed. Compared to the SPA panels, the total radial crack length was initially reduced by  $\sim 20\%$  and  $\sim 26\%$  for the last propagated crack front in the SPB experiments. It can thus be concluded that the inclusion of CFM layers between the face sheet and core considerably improved the 2D debonding behavior of the sandwich panels under the investigated loading.

The slight difference observed in the load-displacement curves of the SPA panels may be attributed to the crack propagation behavior detailed in Section 5.3.3 and not to experimental scatter. As described, even though similar propagation paths were

exhibited by both panels, the total radial crack length of the primary crack was shorter in SPA.1 than in SPA.2. Assuming that propagation in the resin of the face sheet/core interface (primary crack) required less energy than propagation between two woven plies (secondary crack), the longer the primary crack remained dominant (i.e. in SPA.2), the less energy (and consequently less load) was required. This is in agreement with the experimental results (Figure 5.6).

The concentric propagation of the crack in both configurations was directly related to the outer boundary conditions. The edges of the laminates in [24] were free and therefore the crack propagated differently depending on the stiffness of the direction of propagation (e.g. slower in the directions where the fibers were oriented at  $\pm 45^\circ$ ). However, the edges of the face sheet were completely fixed in this case, leading to a similar propagation all around the contour of the pre-crack.

### 5.4.2 Compliance behavior

The initially decreasing and then increasing trends in the experimental compliances of the 2D debonding experiments (shown in Figure 5.8) were in agreement with the results obtained for 2D delamination in the laminates [24]. Due to the similar 2D nature of the embedded cracks investigated in the laminates and in the studied sandwich panels, the same stiffness-related mechanisms affecting the exhibited compliance were developed: stretching (radial and circumferential) due to the geometrical constraints, fiber-bridging and crack propagation (see [24]). The first two mechanisms decreased the compliance (i.e. stiffened the system) while the propagation of the crack tended to increase the compliance (i.e. soften the system). Before the minimum point, hereafter designated “transition point” (TP) as in [24, 25], the stiffening mechanisms prevailed over the softening mechanism, while beyond the TP the crack propagation mechanism became dominant.

The stiffening mechanisms in the laminates developed widely before the propagation of the crack (and thus the softening) became dominant, exhibiting considerable descending branches in the compliances down to the TP [24]. However, the TP for all

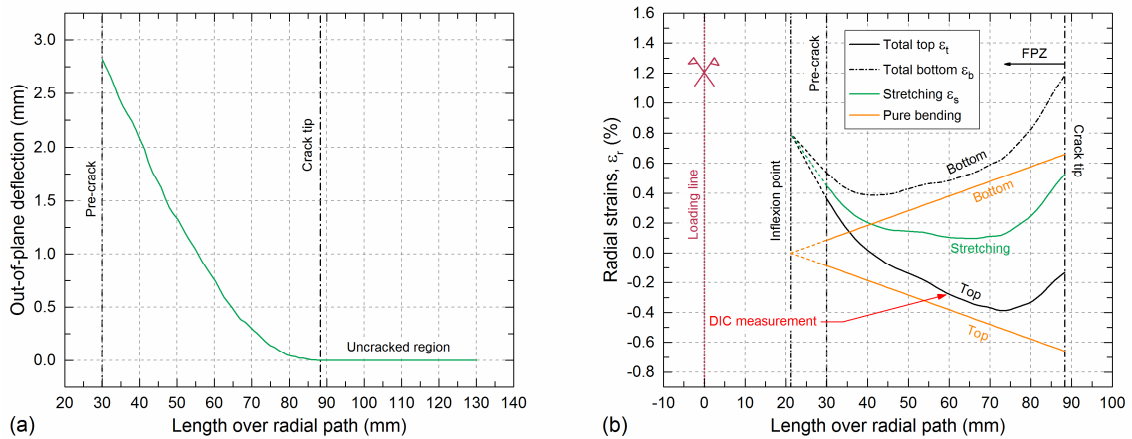


Figure 5.11 – Results obtained from face sheet top surface of panel SPA.2 at total radial crack length of 88 mm; (a) out-of-plane DIC radial deflection profiles; (b) radial strain profiles extracted and derived from DIC experimental results

the sandwich panels was reached almost immediately after crack initiation, exhibiting only a short branch of decreasing behavior in the compliance (Figure 5.8) and indicating an initial rapid crack growth and barely developed stiffening mechanisms. This earlier occurrence of the TP was caused by the smaller pre-crack area used in the sandwich panels ( $2827.4 \text{ mm}^2$  vs  $21598.5 \text{ mm}^2$  in laminates) and by the higher stiffness of the investigated face sheets compared to any of the laminated plates in [24], causing the cracks to initiate at low levels of opening displacement (see Table 5.3) with consequently barely deformed (and thus barely stretched) face sheets. Furthermore, the crack growth trend also differed. The laminated plates exhibited initially slow crack growth rates that progressively increased throughout the experiments [24]. Fast initial crack growth rates following a progressive decrease were however obtained for the sandwich panels (see Figure 5.6).

The TP in the laminates was particularly characteristic as it was found to correspond to the full development of the fiber-bridging area (see [25]) and the linearization of the load-displacement curves. However, the early appearance of the TP prior to any relevant development of the stiffening mechanisms meant that these conclusions were no longer valid for the investigated sandwich panels. Additionally, the described multi-crack scenarios for both panel configurations and the crack migration for the SPB panels (see Section 5.3.3) prevented any correlation to a single fiber-bridging area propagation in a single interface. Regarding the linearization of the load, although it could not be related to the TP (also shown in Figure 5.6), it still occurred, as for the laminated plates, i.e. equilibrium between the stiffening and softening mechanisms was present.

#### 5.4.3 Analysis of strain profiles

According to the experimental set-up, the center of the crack (i.e. the loading area) and the crack front could both be assumed as being fully constrained, with only free vertical movement at the loading area. Consequently, as the crack opened and the face sheet deformed, an inflection point appeared in the radial profile to allow the radial change of curvature, different at both ends. Theoretically, this inflection point would move away from the loading region as the crack propagated. Furthermore, under pure bending conditions, any change from a tension to compression strain state, such as those exhibited in Figure 5.10(a) in the radial strain profiles (i.e. zero strain points between the crack tip and pre-crack), would necessarily imply a change in the curvature of the deformed face sheet and therefore correspond to an inflection point. However, evaluating the out-of-plane deflections of the face sheet (also extracted from DIC measurements), no apparent inflection point existed at zero strain points (on the top surface). This could be attributed to the existence of the in-plane radial tensile strains (as a result of the radial stretching), which counteracted the compression strains in the compressed top surface (i.e. the one monitored with the DIC) and increased the tensile strains in the already tensioned bottom surface and thus shifted the zero strain point from its pure bending position. For the described boundary conditions, the circumferential curvature stayed constant and therefore only tensile strains appeared

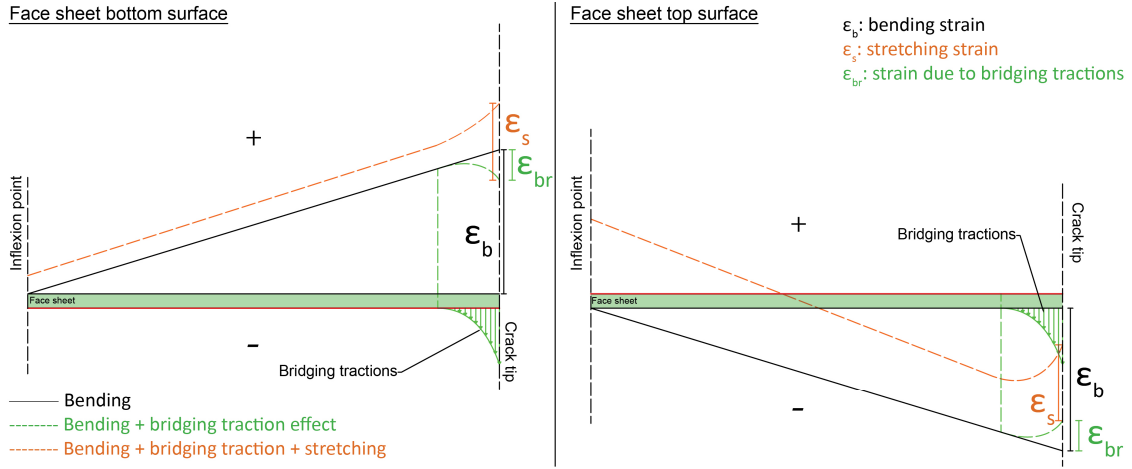


Figure 5.12 – Qualitative sketch of effect of stretching and fiber-bridging traction on radial strain profile of face sheet (not to scale)

in the top surface of the face sheet (Figure 5.10(b)). Consequently, the corresponding circumferential tensile stretching strains were contributing to simply increase the tensile strains in the top surface.

### ***Derivation of in-plane radial stretching strains***

An example of the radial out-of-plane deflection profile obtained from the top surface of the SPA.2 panel at a total radial crack length of 88 mm is shown in Figure 5.11(a). The corresponding radial strain profile (top surface of the face sheet) measured with the DIC is presented in Figure 5.11(b). As previously mentioned, no inflection point was visually apparent in the out-of-plane deflection profile at the zero radial strain point (i.e. at a total radial length of 40.85 mm) due to the superimposed stretching (tensile) strains. In order to determine the latter ( $\epsilon_s$  in Figure 5.11(b)), the following procedure was applied. First, a third order polynomial equation was fitted to the out-of-plane deflection profile so that a continuous description of the curvature (i.e. the second derivative of the deflection) was obtained. Then, using the values of the curvature, the thickness of the face sheet and strain profile at the top of the face sheet ( $\epsilon_t$ ), the strain profile on the bottom surface ( $\epsilon_b$ ) was calculated. Lastly, using the top and bottom strain values, the stretching strains were calculated. By subtracting the stretching strains from the total top and bottom total strains, the “pure” bending strain profiles were also obtained (see Figure 5.11(b)), representing the linear behavior inherent to a punctual load. For the sake of simplicity, a constant face sheet thickness of 5 mm was used during the calculation without any further consideration regarding the secondary crack propagation interface.

### ***Influence of the FPZ***

The developed fracture process zone (FPZ), generated mainly due to fiber-bridging, influenced the radial strain profiles immediately behind the crack tip. Theoretically, if the FPZ and the stretching did not exist, the strain profile on the top surface should start from a minimum value (i.e. a maximum compression) at the crack tip, decrease until the inflection point and increase up to a maximum value (i.e. maximum tensile

strain) at the loading point. A qualitative sketch showing this theoretical pure bending profile between the inflection point and the crack tip is presented in Figure 5.12 for both top and bottom surfaces (positive/negative signs indicate tensile/compressive strains). In the event of an FPZ zone with fiber-bridging developing in front of the crack tip, bridging tractions opposing the opening of the crack appear (see bridging traction profiles in Figure 5.12). Consequently, the original profile of pure bending (black profile) would be altered, reducing the tensile strains in the bottom surface and the compression in the top surface (green profile). Such an effect has been already reported elsewhere [33, 34]. However, when additional stretching strains appear, two scenarios regarding the strain behavior may apply. In the bottom surface, if the magnitude of the stretching strains is greater than the magnitude of the opposing strains from bridging traction, a continuously decreasing tensile strain profile at the FPZ would be obtained, i.e. the scenario shown in Figure 5.12 (orange profile). If the magnitude is smaller however, an initially increasing and then decreasing profile (as if only bridging tractions were acting) would be obtained. In both scenarios, in the top strain profile, where the region of the FPZ is in compression, a greater decrease would occur due to the stretching strains. As a result, the stretching values calculated from the measured top strains may not be accurate close to the FPZ, as the fiber-bridging effect is included and therefore the stretching values may be overestimated.

### ***Radial stretching strain evolution***

Based on the previously described procedure, the radial stretching strain profiles for two further total radial crack lengths (80 and 105 mm) of the SPA.2 panel were derived and are presented, together with the profile at 88 mm, in Figure 5.13. For the sake of comparison, the stretching strain values at 60% of the total radial crack length are indicated for each profile, guaranteeing a sufficient distance from the FPZ and thus avoiding any possible overestimation. As expected, an increasing trend of the stretching strains (both generally and particularly for the evaluated points) occurred as the crack propagated and the face sheet deformed.

Three stretching strain profiles at 65, 70 and 75-mm total crack lengths for SPB.2 panels are likewise shown in Figure 5.14. Considering that in the SPB panels the crack migration generated dense fiber-bridging and that particularly for the SPB.2 panel the crack had fully migrated after 60 mm of total radial crack length (see Section 5.3.3), any profile derived for shorter lengths would be highly affected by the generated fiber-bridging. Thus, as mentioned, profiles from 65 mm onwards were selected, leaving a short margin of total radial crack length to evaluate, as the last propagated crack front corresponded to a total radial length of 77.5 mm (Figure 5.6). The indicated strain values corresponded to 70% of the total crack length for each profile (values at 60%, as selected in Figure 5.13, would be affected by the damaging of the loading area). The increasing trend of the stretching strain profiles between the pre-crack and the FPZ with increasing crack length could again be observed. As the loading area was approached, the initial part of the 70 and 75-mm profiles exhibited a slightly decreasing value due to



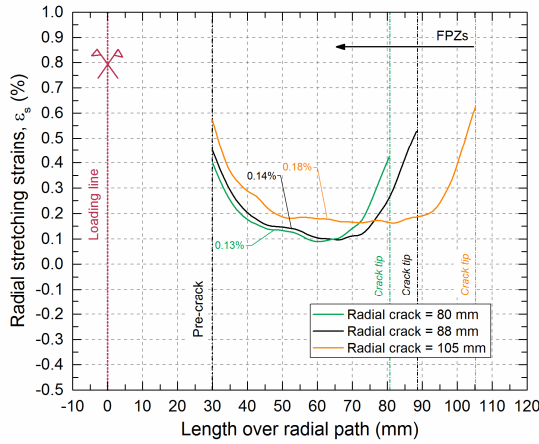


Figure 5.13 – Comparison of calculated radial stretching strains of SPA.2 at total radial crack lengths of 80, 88 and 105 mm; values at 60% of total crack length

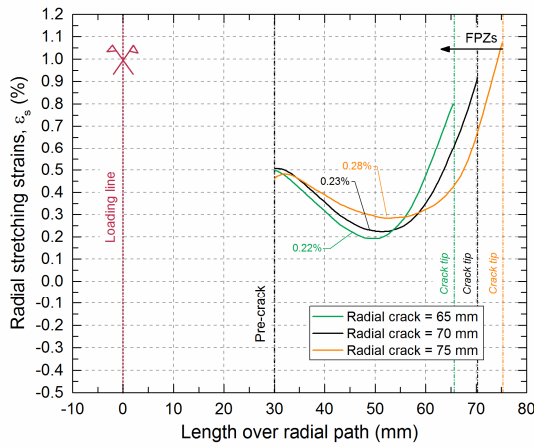


Figure 5.14 – Comparison of calculated radial stretching strains of SPB.2 at total radial crack lengths of 65, 70 and 75 mm; values at 70% of total crack length

the damage in this area (see also Section 5.3.1). The stretching strains were again calculated using the total thickness of the face sheet (i.e. 6 mm, see Table 5.2) without considering the (small) progressive reduction of the section due to migration of the crack.

The dense fiber-bridging developed in the SPB panels led to an increase of the load and crack arrest (compared to the SPA panels). Therefore, for similar crack lengths in both configurations, higher loads and opening displacements were exhibited in the SPB panels (see Figure 5.6). This was also reflected in the measured in-plane strains and is particularly evidenced in the higher stretching strains in SPB (Figure 5.14) compared to SPA (Figure 5.13).

### **Inflection point location**

By applying the previously described procedure (Figure 5.11) to the measured radial strains, even if the inflection points were located in the pre-crack area (i.e. outside the measuring area), they could always be found by extending the calculated linear pure bending profiles until they intersect (i.e. until zero strain), as shown in Figure 5.11(b). In the event of the inflection points being located in the measuring area, they could already be identified in the out-of-plane profile and the derived pure bending linear profiles would

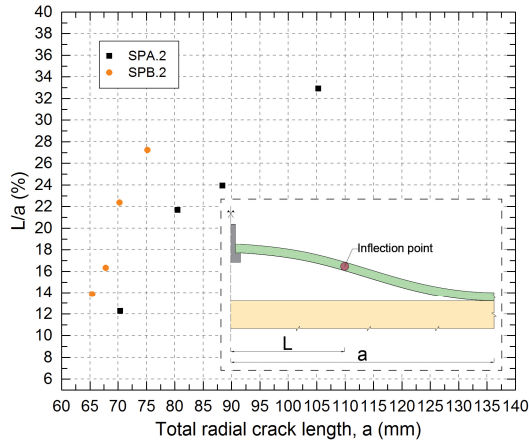


Figure 5.15 – Evolution of inflection point with crack propagation for (a) SPA.2 and (b) SPB.2

already intersect. In order to verify that at the inflection point only stretching stresses existed, the profiles of the total radial strains (top and bottom) and the stretching strain profile were also extended following the shown trend. The convergence point of the three profiles effectively matched the inflection point obtained from the pure bending profiles, thus confirming that only constant through-thickness tensile stresses existed.

The shift of the inflection point's location (with respect to the total radial crack length, i.e.  $L/a$ ) for panels SPA.2 and SPB.2 is shown in Figure 5.15. As a result of the propagation of the crack, the inflection point would move to the right (i.e. to the exterior of the face sheets). Considering however that, due to the damage caused to the loading region the corresponding boundary conditions evolved from an initial ideal full constraint of the rotations to their progressive partial release, the inflection point would move to the left (i.e. to the center of the face sheets). The effective location of the inflection point was thus the result of both opposing effects. For all the panels, the values of  $L/a$  at the investigated total radial crack lengths showed an increasing trend, revealing that despite the damage in the loading area, the general shift of the inflection point towards the exterior of the face sheet, as a result of the propagation of the crack, prevailed.

#### 5.4.4 Stretching-induced shear fracture modes

In the 2D delamination cases studied in [24], the crack propagated in the midplane. Therefore, as the crack opened, the upper and lower laminates of the cracked part of the plates deformed similarly thus developing the same stretching strains. As a result, no shear displacement, and thus no shear fracture mode contribution, occurred at the crack tip. However, in the 2D debonding of the sandwich panels, the stretching only developed in the face sheet and the core did not deform, thereby activating stretching-induced shear fracture modes. As mentioned in Section 5.1, the experimental set-up in the present investigation was developed (based on the SCB specimen) to minimize the shear mode fracture contributions resulting from the elastic property mismatch. Thus, the stretching strains developed in the face sheets were the main source of relevant shear fracture modes. As a result, the crack propagated under mixed-mode conditions (i.e. Mode I/shear modes). The greater the stretching strains, the greater the shear mode contribution.

The crack propagation paths observed in the post-mortem cuts (see Section 5.3.3) were a reflection of the effect of the stretching-induced shear modes on the crack propagation behavior. In the SPA panels, the shear modes caused the nucleation of a secondary crack, while in the SPB panels they led to the migration of the primary crack from the woven/CFM interface to the woven/CFM interface. Similar crack propagation behavior was found in [12] for 1D DCB-UBM specimens presenting a layup similar to the SPB configuration (at the face sheet/core interface level) and strong Mode II loading. Details are given in Section 5.1.

As reported in [25], there are two different 2D effects (not present in 1D cases) contributing to increase fiber-bridging developed under Mode I: 1) the increase in the flexural stiffness (from beam to plate) and 2) the stress stiffening of the deformed laminate due to the in-plane stretching. Both effects are consequences of the 2D nature of the crack and they thus apply in both delamination and debonding scenarios. In the 2D debonding cases investigated, the migration of the crack and nucleation of new crack surfaces, caused by the shear modes induced by the in-plane stretching of the face sheets, led to the development of additional fiber-bridging as the cracks opened. Specifically, the secondary crack in the SPA panels started and propagated in a woven/woven interface that, compared to a woven/core interface, naturally involved more fiber-bridging. Regarding the SPB panels, the migration of the crack through the two plies of CFM and subsequent propagation at the woven/CFM interface triggered high-density fiber-bridging. Taking into account the fact that the cracks kept propagating under Mode I, all the new fiber-bridging generated was also enhanced by the two previously mentioned and already known 2D effects. Thus, the stretching-induced mode-mixity can be considered as an additional 2D effect on cracks propagating under opening loads.

## 5.5 Conclusions

The 2D debonding in GFRP/balsa sandwich panels with embedded cracks subjected to quasi-static out-of-plane opening loads was experimentally studied. A total of four panels and two different face sheet configurations were investigated. The first configuration (SPA) consisted of a pure woven fabric (W) layup while in the second (SPB) continuous filament mat (CFM) layers were inserted above and below the woven plies. Circular pre-cracks were introduced in the interface between the balsa core and the face sheet. The load-bearing and compliance responses, crack propagation behavior and in-plane strain distributions of the face sheet were analyzed. The influence of the FPZ on the strain profiles and evolution of the inflection points throughout the experiments were likewise discussed. The following conclusions may be drawn from this work:

1. An experimental design appropriate for the investigation of the debonding behavior of 2D embedded cracks under out-of-plane loads in sandwich panels was developed. The design is able to capture the relevant 2D effects not occurring in 1D fracture experiments.

2. The introduction of plies prone to the development of fiber-bridging at the face sheet/core interface (i.e. CFM) resulted in an enhanced fracture resistance of SPB panels. An improved load-bearing performance (load increase of approx. 27%) and significant crack arrest (the propagation of the crack was reduced by 20 to 26%) were observed for the SPB compared to the SPA panels.
3. Due to the 2D nature of the investigated embedded cracks and the corresponding boundary conditions, in-plane tensile stretching strains appeared in the deformed face sheets as the cracks propagated. The magnitude of the radial stretching strains showed an increasing trend with increasing crack propagation in both the studied configurations. Due to the dense fiber-bridging and consequent crack arrest, the SPB panels required higher loads and opening displacements to propagate the crack than the SPA panels. As a result, higher stretching strains also developed in SPB panels (e.g. for an approx. 80 mm total radial crack length, stretching strains of 0.01 and 0.28 % developed in SPA and SPB panels respectively).
4. Due to the in-plane stretching strains, shear fracture mode contributions were activated throughout the experiments. As a result, the crack in the SPB panels migrated from the face sheet/core interface to the woven/CFM interface and a secondary crack initiated in the SPA panels between the first and second woven plies.
5. The stretching-induced mode-mixity constitutes an additional 2D effect in cracks propagating under opening loads. Depending on the layup, this can trigger different crack propagation behaviors (e.g. crack migration or nucleation of new crack surfaces). The other two (already known) 2D effects (i.e. increase in flexural stiffness and stress stiffening also caused by stretching) lead to an increase in the developing fiber-bridging. Thus, the additional fiber-bridging activated as a result of the stretching-induced mode-mixity (third 2D effect) is also increased by the two other 2D effects.
6. These three 2D effects on fiber-bridging do not occur in 1D Mode I-dominated fracture experiments. Their further quantification and separation, i.e. the investigation of the individual contributions, require further FE analysis, which constitutes the next step of this work.

## References

1. Keller, T. Recent all-composite and hybrid fiber-reinforced polymer bridges and buildings. *Prog. Struct. Eng. Mater.*, 2001; 3(2): 132-140.
2. Manalo, A., Aravinthan, T., Fam, A., Benmokrane, B. State-of-the-Art Review on FRP Sandwich Systems for Lightweight Civil Infrastructure. *J. Compos. Constr.*, 2017; 21(1): 04016068-1.
3. Uddin, N. *Developments in Fiber-Reinforced Polymer (FRP) Composites for Civil Engineering*. 1<sup>st</sup> ed. Woodhead Publishing; 2013.

4. Keller, T., Rothe, J., De Castro, J., Osei-Antwi, M. GFRP-Balsa Sandwich Bridge Deck: Concept, Design, and Experimental Validation. *J. Compos. Constr.*, 2013; 18(2): 04013043.
5. Osei-Antwi, M., De Castro, J., Vassilopoulos, A.P., Keller, T. Structural limits of FRP-balsa sandwich decks in bridge construction. *Composites: Part B*, 2014; 63: 77-84.
6. Osei-Antwi, M., De Castro, J., Vassilopoulos, A.P., Keller, T. FRP-Balsa Composite Sandwich Bridge Deck with Complex Core Assembly. *J. Compos. Constr.*, 2013; 17(6): 04013011.
7. Cantwell, W.J., Davies, P. A test technique for assessing core-skin adhesion in composite sandwich structures. *Journal of Material Science Letters*, 1994; 13: 203-205.
8. Ratcliffe, J.G, Reeder, J.R. Sizing a single cantilever beam specimen for characterizing facesheet-core peel debonding in sandwich structure. *Journal of Composite Materials*, 2011; 45(25): 2669-2684.
9. Saseendran, V., Berggreen, C., Krueger, R. Mode mixity analysis of face/core debonds in a single cantilever beam sandwich specimen. *J. Sandwich Structures and Materials*, 2018; 0(0): 1-31.
10. Rani, E., Grant P., Ashforth C. *Composite structures : effects of defects*. 1<sup>st</sup> ed. Hoboken, NJ: John Wiley & Sons; 2018.
11. Carlsson, L.A., Kardomateas, G.A. *Structural and Failure Mechanics of Sandwich Composites*. Solid Mechanics and its Applications, 121. Springer; 2011.
12. Lundsgaard-Larsen, C., Berggreen, C., Carlsson, L.A. Tailoring sandwich face/core interfaces for improved damage tolerance – Part II: experiments. *Appl. Compos. Mater.*, 2010; 17: 621-637.
13. Prasad, S., Carlsson, L.A. Debonding and crack kinking in foam core sandwich beams-II: experimental investigation. *Eng Fract Mechs*, 1994; 47(6): 825-841.
14. Cantwell, W.J., Scudamore, R. Ratcliffe, J., Davies, P. Interfacial fracture in sandwich laminates. *Comp. Sci. Tech.*, 1999; 54(14): 2079-2085.
15. Li, X., Carlsson, L.A. The tilted sandwich debond (TSD) specimen for face/core interface fracture characterization. *J. Sandwich Structures and Materials*, 1999; 1: 60-75.
16. Li, X., Carlsson, L.A. Elastic foundation analysis of tilted sandwich debond (TSD) specimen. *J. Sandwich Structures and Materials*, 2000; 2: 3-32.
17. Ratcliffe, J., Cantwell, W.J. A new test geometry for characterizing skin-core adhesion in thin-skinned sandwich structures. *Journal of Material Science Letters*, 2000; 19: 1365-1367.
18. Ural, A., Zehnder, A.T., Ingraffea, A.R. Fracture mechanics approach to facesheet delamination in honeycomb: measurement of energy release rate of adhesive bond. *Eng Fract Mechs*, 2003; 70: 93-103.
19. Shivakumar, K.N., Smith, S.A. in situ fracture toughness testing of core materials in sandwich panels. *Journal of Composite Materials*, 2004; 39(8): 655-668.
20. Berggreen, C., Simonsen, B.C., Borum, K.K. Experimental and numerical study of interface crack propagation in foam-cored sandwich beams. *Journal of Composite Materials*, 2007; 41(4): 493-520.
21. Hutchinson, J.W., Suo, Z. Mixed mode cracking in layered materials. *Adv. Appl. Mech.*, 1991; 29: 63-191.
22. Farmand-Ashtiani, E., Cugnoni, J., Botsis, J. Monitoring and characterization of the interfacial fracture in sandwich composites with embedded multiplexed optical sensors. *Composite Structures*, 2013; 96: 476-483.
23. Yoshida, K., Aoki, T. Beam on elastic foundation analysis of sandwich SCB specimen for debond fracture characterization. *Composite Structures*, 2018; 195: 83-92.

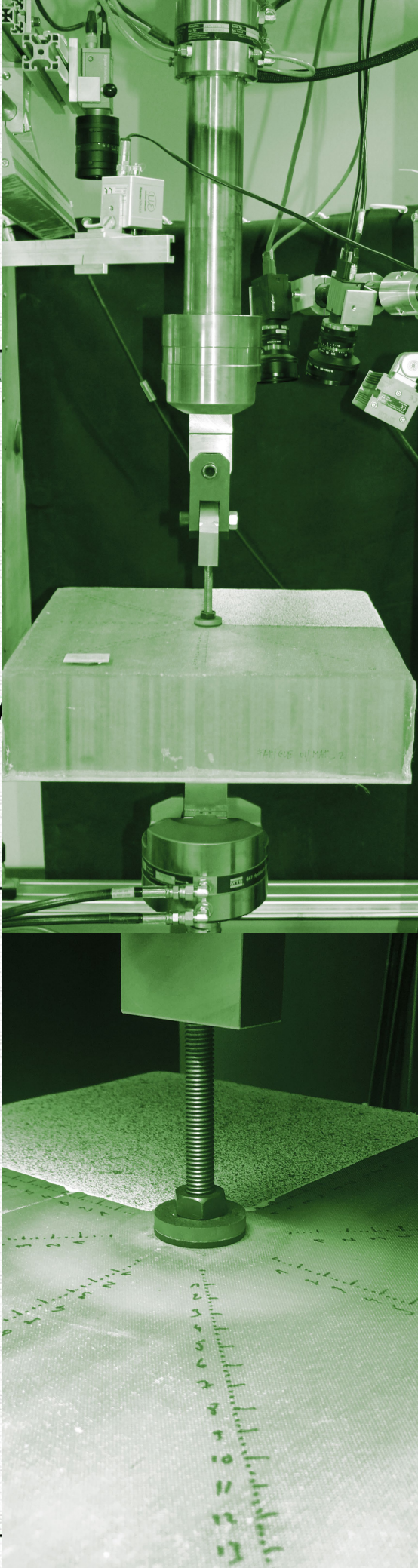
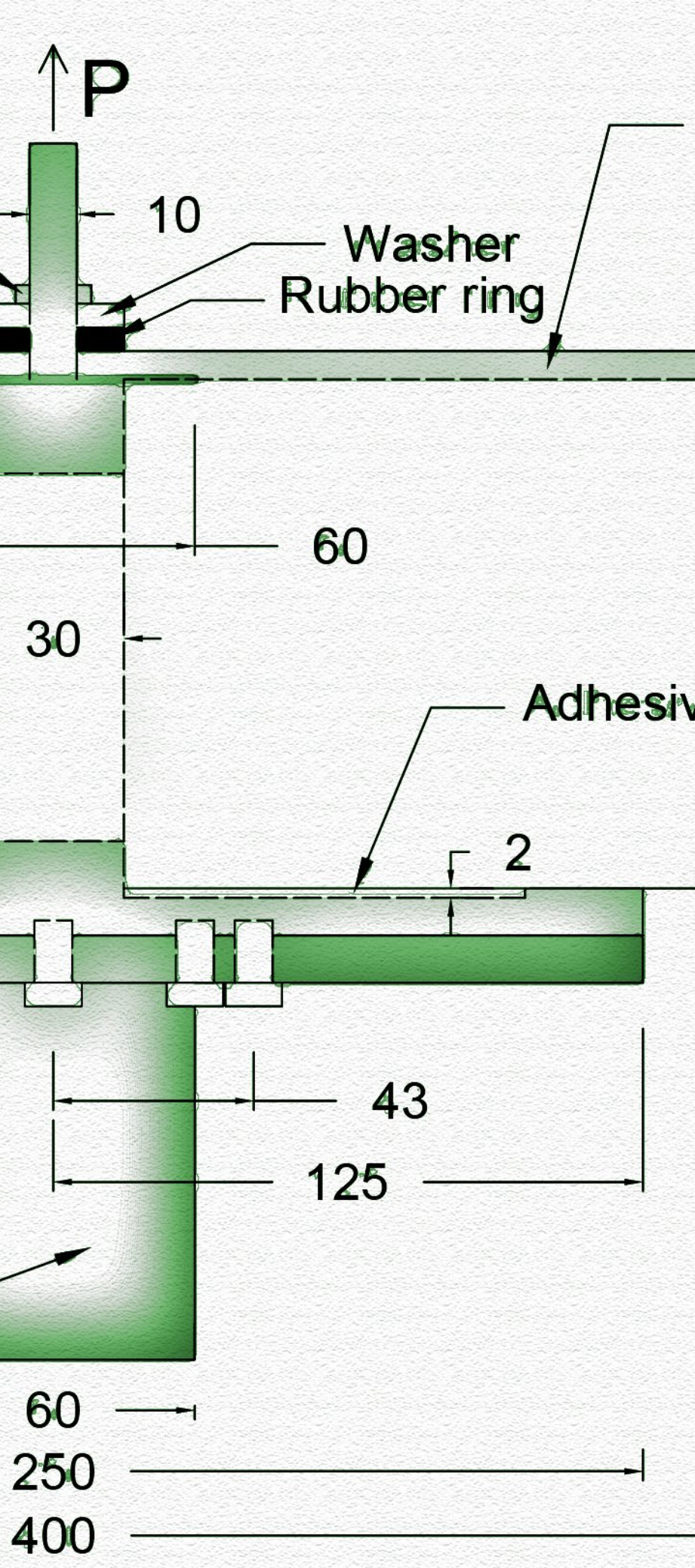
24. Cameselle-Molares A., Vassilopoulos A.P., Keller T. Experimental investigation of two-dimensional delamination in GFRP laminates. *Eng. Frac. Mech.*, 2018; 203: 152-171.
25. Cameselle-Molares A., Vassilopoulos A.P., Renart J., Turon A., Keller T. Numerical simulation of two-dimensional in-plane crack propagation in FRP laminates. *Comp. Struc.* 2018; 200: 396-407.
26. Chen, Z.M., Krueger, R., Rinker, M. Facesheet/Core Disbond Growth in Honeycomb Sandwich Panels Subjected to Ground-Air-Ground Pressurization and In-Plane Loading. In: 11th International Conference on Sandwich Structures ICSS-11, Ft. Lauderdale, USA, March, 2016.
27. Rinker, M., Krueger, R., Ratcliffe, J. Analysis of an Aircraft Honeycomb Sandwich Panel with Circular Face Sheet/Core Disbond Subjected to Ground-Air Pressurization. NASA/CR-2013-217974, 2013.
28. Moslemian, R., Quispitupa, A., Berggreen C., Hayman, B. Failure of uniformly compression loaded debond damaged sandwich panels – An experimental and numerical study. *J. Sandwich Structures and Materials*, 2012; 14(3): 297-324.
29. Swiss Composite Product Catalogue. <<https://www.swiss-composite.ch/pdf/Produkteuebersicht.pdf>> (Accessed 16 October 2017).
30. Owen's Corning Reinforcements Composite Solutions Guide. <[http://www.ocvreinforcements.com/pdf/library/Composite\\_Solutions\\_Guide\\_100360\\_E\\_finalprintable.pdf](http://www.ocvreinforcements.com/pdf/library/Composite_Solutions_Guide_100360_E_finalprintable.pdf)> (Accessed 26 March 2018).
31. Sicomin SR8100 resin datasheet. <<http://www.sicomin.com/datasheets/product-pdf94.pdf>> (Accessed 12 November 2018).
32. Correlated Solutions Inc. VIC 3D-v7 reference manual. Columbia, USA: Correlated Solutions.
33. Manshadi, B.D., Vassilopoulos, A.P., Botsis, J. A combined experimental/numerical study of the scaling effect on mode I delamination of GFRP. *Compo. Sci. Tech.*, 2013; 83: 32-39.
34. Pappas, G., Botsis, J. Intralaminar fracture of unidirectional carbon/epoxy composite: experimental results and numerical analysis. *Int. J. Solids and Struc.*, 2016; 85-86: 114-124.

---

**Contributions:** Aida Cameselle Molares conceived, designed and performed the experimental campaign under the supervision of Prof. Thomas Keller and Dr. Anastasios Vassilopoulos. The analysis of the results was carried out by Aida Cameselle Molares in collaboration with Prof. Thomas Keller and Dr. Anastasios Vassilopoulos.







# Chapter 6

## Two-dimensional debonding

### *Fatigue experimental investigation*

#### 6.1 Introduction

The number of fiber-reinforced polymer (FRP) sandwich components in high-performance load-bearing structures has considerably increased in recent decades thanks to their numerous advantages such as high strength- and stiffness-to-weight ratios, rapid installation and versatility. Specifically, in the civil engineering domain, glass fiber-reinforced polymer (GFRP) sandwich bridge decks have been increasingly employed mainly due to their easy and rapid assembly and their great shape and thickness flexibility [1-6]. Among the different core materials typically used in sandwich bridge decks, balsa cores have proved to be an advantageous choice due to a sufficient shear capacity and the uniform support to the upper face sheet (in contact with traffic loads) that they provide [4-6].

The load-bearing capacity of sandwich structural members can be compromised in the presence of disbonds between the face sheets and the core [7, 8]. Considering further that many structural components are subjected to both static and dynamic loads throughout their lifetime, accurate assessment of the debonding fracture behavior under both quasi-static and fatigue loading is essential for a reliable structural design. Since Mode I-dominated debonding is considered the most critical fracture mode in sandwich structures [8-10], particular emphasis has been placed on investigating debonding under tensile opening loads [7, 10-19]. The existence of disbonds in structural composite sandwich members under pure compression or bending may



induce premature face sheet wrinkling causing the disbond to open and thus propagate mainly under Mode I. Furthermore, geometrical changes or curved geometries can also lead to significant out-of-plane tensile stresses. Most of the existing studies focus on debonding under quasi-static loading, while only limited investigations of debonding under fatigue loading can be found in the literature [20-25].

Both quasi-static and fatigue debonding fracture behaviors in sandwich members are currently investigated through beam-like one-dimensional (1D) specimens [20-33] where the disbond propagates in the longitudinal direction maintaining an approximately constant crack width (i.e. the width of the specimen). Of all the available and not yet standardized specimen configurations, the single cantilever beam (SCB) specimen has been reported as being the most appropriate for characterizing the face sheet/core opening fracture behavior [8-10, 34]. These 1D conditions are not likely to be found in actual structural elements where the perimeter of embedded cracks may expand in all directions.

A more realistic fracture approach was studied in [35] where the two-dimensional (2D) delamination in GFRP plates with embedded circular pre-cracks subjected to out-of-plane quasi-static tensile loads was experimentally investigated. The results showed that a stiffening of the plates occurred, caused mainly by in-plane stretching stresses that developed in the opened parts of the laminates. The stretching occurred as a result of the boundary constraints inherent to a plate with an embedded crack. One of the studied plates was further numerically investigated in [36]. A 50% increase in the total strain energy released rate (SERR), compared to 1D double cantilever beam (DCB) specimens with the same layout as the plates, was found. The increase in flexural stiffness (1D beams vs 2D plates) and above-mentioned stress stiffening resulted in an increase of the total amount of fiber-bridging developed, which caused the corresponding SERR increase.

The 2D fracture investigation was further extended to quasi-static 2D debonding in GFRP/balsa sandwich panels and presented in [37]. Circular embedded pre-cracks were introduced in the face sheet/core interfaces and subjected to out-of-plane tensile loads. Due to the in-plane stretching strain that, as expected, also developed in the debonded part of the face sheets, significant shear fracture modes were activated throughout the propagation of the cracks, causing crack migration and nucleation of new crack surfaces.

All the previously described 2D fracture investigations were carried out under quasi-static loading conditions, however, 2D effects are also expected under fatigue loading conditions. To the authors' knowledge, no investigations of the 2D fatigue fracture behavior of sandwich panels have yet been reported in the literature.

Thus, the main objective of this work was to experimentally investigate the fatigue 2D debonding behavior in GFRP/balsa sandwich panels and identify the differences compared to 1D fatigue fracture. The same sandwich panel configurations as for the quasi-static investigation [37] were selected for this study. The experimental set-up was also similar to that developed for the quasi-static experiments. Circular embedded disbands were also introduced at the center of the face sheet/core interface and out-of-plane fatigue tensile loads were applied to open the crack. The experiments were

performed under load control and under different  $R$ -ratios. The crack growth and temperature on the surface of the face sheet were constantly monitored throughout all the experiments. Load-displacement hysteresis loops were also recorded in all the experiments. Their shape, the different causes of the increase of their inner area and the global stiffness degradation were discussed. Additionally, considering the results reported in [35-37], in-plane stretching of the opened part of the face sheet was also expected. In order to quantify the developed stretching, the in-plane strains in the top surface of the face sheets were also monitored throughout the experiments.

## 6.2 Experimental program

### 6.2.1 Material description

Two types of glass fiber reinforcement were used to fabricate the face sheets of the investigated sandwich panels: a 390-g/m<sup>2</sup> woven fabric (W) with the same proportion of reinforcement in the warp/weft directions (i.e. 50/50) and a 600-g/m<sup>2</sup> long continuous filament mat (CFM). The former was supplied by Swiss-Composite (Switzerland) and the latter by Owens Corning (United States). For the matrix, an epoxy resin (Sicommin SR8100) appropriate for vacuum infusion production was selected. The material properties of the resin and the glass fibers of each reinforcement are reported in Table 6.1 (manufacturer data [38-40]). Regarding the core, commercial BALTEK® VCB balsa wood (supplied by Colevo, Switzerland) was used. The average density of the provided balsa blocks was 228.40 kg/m<sup>3</sup>.

> Table 6.1 – Material properties

Material	$E$ (GPa)	$G$ (GPa)	$\nu$ (-)	$\rho$ (g/cm <sup>3</sup> )
Epoxy resin	3.00	1.30	0.35	1.14
E-glass (for woven)	72.00	29.50	0.22	2.55
E-CR* glass (for CFM)	80.00	32.80	0.22	2.62

\*CR: Corrosion-resistant

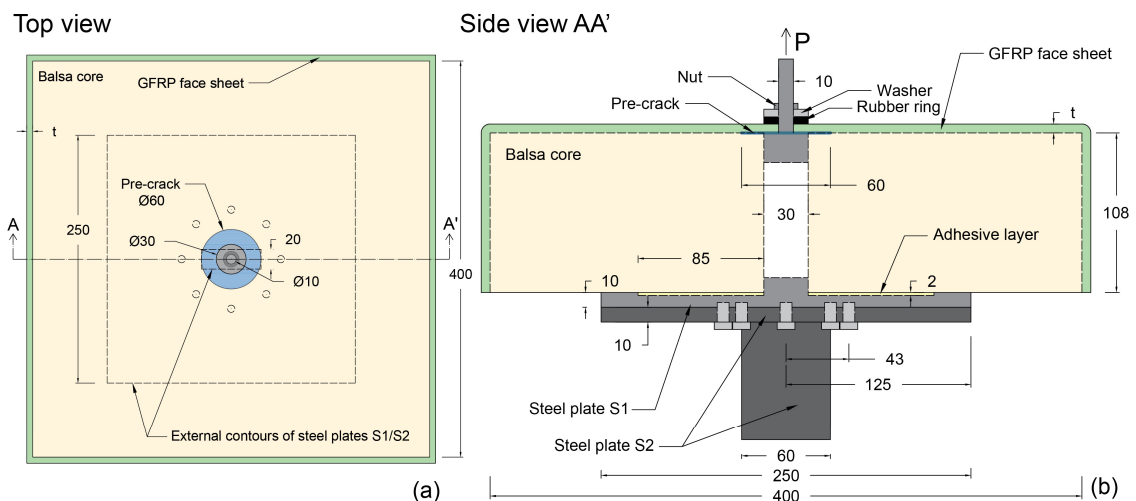


Figure 6.1 – Sandwich panel layout; (a) Top view and (b) Side view of section AA' in (a). Dimensions in mm

&gt; Table 6.2 – Description of GFRP/balsa sandwich panels

Panel type	GFRP face sheet laminate			Dimensions of	
	Layout	Thickness, t (mm)	Axial stiffness (kN)	Bending stiffness (kN·mm <sup>2</sup> )	Baltek VBC balsa core (mm)
SPA	(W) <sub>18</sub>	5	128.10	266.87	400 x 400 x 108
SPB	(CFM) <sub>2</sub> /(W) <sub>9</sub> /(CFM) <sub>2</sub>	6	106.01	230.90	400 x 400 x 108

### 6.2.2 Specimen description

Two different configurations of the GFRP face sheet were investigated. The first configuration (designated SPA) consisted of 18 plies of woven reinforcement (i.e. W18) and the second (SPB) of a symmetric layup combining nine plies of woven fabrics and two plies of CFM above and below (i.e. CFM2/W9/CFM2). The same configurations were experimentally investigated under quasi-static loading in [37]. The face sheet layups were selected so that they had comparable axial and flexural stiffnesses (see also [37]) and to avoid bending-extension coupling effects (i.e. they were symmetric). The same balsa core dimensions were used in all panels (see Table 6.2). A total of four panels, one pair of each configuration, were fabricated. The vacuum infusion technique was used to fabricate all the panels. The panels were cured under vacuum for at least 12 hours at room temperature and post-cured, also under vacuum, for eight hours at 45°C. The description and dimensions of each sandwich panel configuration are presented in Table 6.2. To differentiate static and fatigue experiments, an additional “F” is used in the panel denomination for the latter (e.g. SPA.1 for the first static and SPA.1F for the first fatigue panel).

A circular pre-crack of 60-mm diameter was introduced at the center of the face sheet/core interface using a 13- $\mu$ m thickness Teflon film. The load to open and propagate the pre-crack was applied by means of a 30-mm head and 10-mm shank screw. The layout of the sandwich panels (top and side views) is shown in Figure 6.1. As can be observed, the face sheets were anchored on the lateral sides to the balsa core to assure that no other crack distant from the pre-crack was created. The loading regions (i.e. the center of the panels where the screw is located) of all panels were reinforced with three additional circular 60-mm diameter layers of woven reinforcement. Further details regarding the fabrication and assembling process can be found in [37].

### 6.2.3 Experimental set-up, loading and instrumentation

The tensile load was applied by a 100-kN MTS Landmark servo-hydraulic experimental rig with a load cell of 25 kN calibrated to 20% of its maximum capacity at a temperature of 22±3°C and relative humidity of 40±5%. The experimental set-up is presented in Figure 6.2. The bottom of the panels was fixed and constrained to the bottom grip of the machine and the loading screw was then tightened to the surface of the panels with a nut, washer and rubber ring to distribute the pressures (Figure 6.1). Finally, an

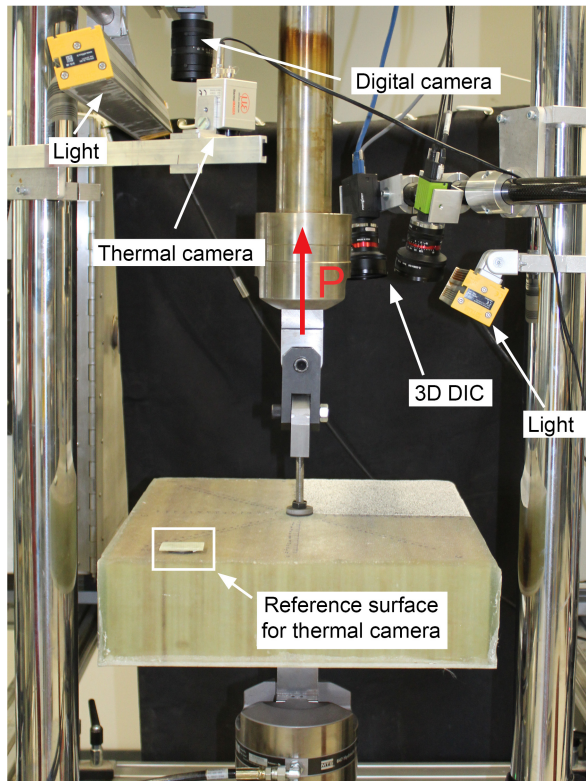


Figure 6.2 – Experimental set-up

in-house-developed hinge was placed between the loading screw and the upper grip to prevent any potential damage of the loading cell of the machine as a result of any small rotation of the screw. A level was used to guarantee the horizontality of the panels with respect to the vertical loading line. Initially, a quasi-static loading ramp was performed under displacement control at a rate of 1.5 mm/min until the mean fatigue load was achieved. Subsequently, the load control fatigue loading was initiated. This procedure was followed in all the experiments. The cyclic loading was performed initially and up to two million cycles at a frequency of 5 Hz. Subsequently, and until the end of the experiments, the frequency was increased to 10 Hz. The load and opening displacement were obtained from the machine (accuracy of  $\pm 0.5\%$ ) throughout the experiments. High acquisition frequencies were initially applied, recording load-displacement measurements at every cycle, followed by a progressive reduction. After two million cycles (i.e. at 10 Hz of fatigue loading), measurements were only recorded at every one million cycles. The data acquisition capability of the machine permitted a total of 20 load and displacement measurements per cycle at 5 Hz and 10 measurements/cycle at 10 Hz.

A total of five fatigue experiments were conducted on the four fabricated sandwich panels. A summary of the performed experiments is presented in Table 6.3. As can be seen, experiments under the same  $R$ -ratio of  $R=0.1$  were conducted on each of the two SPA panels (i.e. SPA.1F and SPA.2F). Regarding the SPB panels, and in order to evaluate the effect of the  $R$ -ratio on the fiber-bridging developed in SPB panels (which was expected to be dense based on the quasi-static results), three different  $R$ -ratios were

&gt; Table 6.3 – Summary of fatigue experiments and results

Experiment	$P_{max}$ (kN)	$\Delta P$ (kN)	$R$ -ratio	Number of cycles (x10 <sup>6</sup> )	Temperature at last cycle (°C)
SPA.1F	4.53	4.07	0.1	7.88 (failure)	54
SPA.2F				12.35 (failure)	59
SPB.1F	4.68	4.21	0.1	1.09 (failure)	52
SPB.2F1		2.34	0.5	12.5→	26.5
SPB.2F2		3.28	0.3	12.5→	35.6

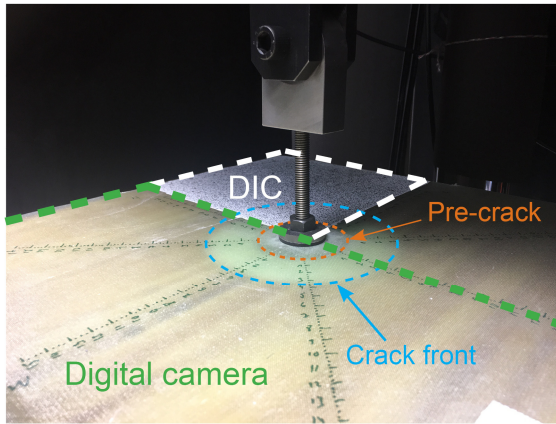


Figure 6.3 – Crack monitoring schema (common to all panels) and circular crack propagation pattern of sandwich panels SPA.1F

investigated:  $R=0.1$ , applied to one of the panels (SPB.1F), and  $R=0.5$  and  $0.3$ , both applied consecutively to the second panel due to the limited fatigue crack propagation exhibited under the first condition. After the first experiment at  $R=0.5$ , the panel was unloaded. Subsequently, the initial quasi-static ramp to reach the mean fatigue load corresponding to  $R=0.3$  was applied. The two experiments were designated SPB.2F1 and SPB.2F2 respectively (see Table 6.3). All experiments were performed until failure or until 12.5 million cycles which corresponded to a service life of 100 years for a bridge on main roads with low flow rates of lorries (see traffic category 3 in [41]).

The maximum fatigue loads were assigned based on the quasi-static results obtained for the same type of panels in [37]. Continuously increasing quasi-static loads were obtained throughout the experiments up to a maximum value, after which they decreased. These maximum values were considered as the characteristic [42] fracture resistance ( $P_k$ ) of the investigated sandwich panels. Thus, in order to evaluate the fatigue performance of the two configurations, their respective design fatigue resistance values ( $P_d$ ), calculated at ultimate limit state (ULS) level according to Eurocomp EUR 27666 [42], were used to calculate the maximum fatigue loads ( $P_{max}$ ) using Equation 6.1:

$$P_{max} = \frac{P_d}{\gamma_{Ff}} = \frac{\bar{P}_k}{\gamma_{mf} \cdot \gamma_{Ff}} = \frac{\bar{P}_k}{\gamma_{m,1} \cdot \gamma_{m,2} \cdot \gamma_{m,3} \cdot \gamma_{m,4} \cdot \gamma_{Ff}} \quad (6.1)$$

where  $\bar{P}_k$  is the average of the maximum registered quasi-static loads (see [37]),  $\gamma_{mf}$  is the partial safety factor for material and  $\gamma_{Ff}$  is the partial safety factor for fatigue actions ( $\gamma_{Ff} = 1.0$  unless agreed otherwise [42]). As indicated in Equation 6.1, four partial coefficients ( $\gamma_{m1,2,3,4}$ ) are comprised in  $\gamma_{mf}$ . Each takes into account different effects of material properties.



&gt; Table 6.4 – Description and values of ULS material safety factor coefficients [42]

Description	Nomenclature	Value
Property source <i>Properties derived from experiments</i>	$\gamma_{m,1}$	1.15
Manufacturing process <i>Resin infusion, fully post-cured</i>	$\gamma_{m,2}$	1.20
Temperature <i>Experiment temperature 25-50°C, HDT* 55-80°C</i>	$\gamma_{m,3}$	1.20
Fatigue <i>Periodic inspection and maintenance, poor accessibility</i>	$\gamma_{m,4}$	2.00

\*Resin heat distortion temperature

These effects, and the corresponding coefficient's values applicable to the investigated sandwich panels, are summarized in Table 6.4. Likewise, the calculated and applied maximum fatigue loads ( $P_{max}$ ), together with the load amplitudes ( $\Delta P$ ), are indicated in Table 6.3 for both configurations. The  $R$ -ratios were applied maintaining a constant value of the  $P_{max}$ .

The 2D crack propagation was monitored using two different systems: a digital camera and 3D Digital Image Correlation (DIC) system. A total of six rulers with markers every 2.5 mm were drawn on the surface of each panel, as can be observed in Figure 6.3. The crack propagation along these rulers was monitored by the digital camera located above the panels (see Figure 6.2). At the beginning of the experiments, images were taken every two seconds (i.e. acquisition frequency of 0.5 Hz). As the crack propagation rate decreased, the acquisition frequency was likewise progressively decreased. The target area was permanently illuminated with a non-heating LED EFFILUX bar of white light (Figure 6.2). The crack front was identified by the whitening of the delaminated areas recognizable thanks to the translucency of the face sheet laminates. The 3D DIC system (also located above the panels, see Figure 6.2) was used to measure the out-of-plane deformation and in-plane strain distributions (accuracy of  $\pm 0.005$  mm and  $\pm 0.01\%$  respectively) of the top surface of one quarter of the face sheets (see Figure 6.3). A random speckle pattern was applied on the measuring surface by means of white paint and black spray paint. The changes from straight to curved in the out-of-plane deformation profiles were assumed as being the crack front. The 3D DIC cameras had a maximum acquisition rate of 100 images/s. Therefore, a maximum of 20 images/cycle were recorded for each of the measured cycles at 5-Hz fatigue loading. Correspondingly, 10 images/cycles were recorded at 10 Hz. The cycle acquisition frequency was also varied throughout the experiments. During the first cycles, images were taken each 100 cycles and the frequency then progressively increased. From two million cycles and until the end of the experiments, images were taken every 50000 cycles. The DIC measuring area was also illuminated with a non-heating LED EFFILUX white light. The post-processing of the results was carried out using Vic-3D software from Correlated Solutions Inc. [43].

To verify whether the increase in the fatigue frequency from 5 to 10 Hz triggered a significant temperature increase at the crack front, the evolution of the temperature at the surface of the face sheets was monitored with an infrared (IR) thermal camera (accuracy of  $\pm 0.1^\circ\text{C}$ ) which was also located above the panels as can be seen in Figure 6.2. In order to have a reference surface where the temperature was not affected by the fatigue opening and crack growth, a piece of GFRP laminate isolated from the face sheets by means of hard rubber was glued to the outer part of the panels (see Figure 6.2). The image acquisition protocol was similar to that previously described for the digital camera.

## 6.3 Experimental results

### 6.3.1 Crack growth and displacement responses in SPA panels

The fatigue crack growth results, measured throughout the experiments on the SPA configuration (two different panels under  $R=0.1$ , see Table 6.3), are presented in Figure 6.4. Since (as expected based on the quasi-static results in [37]) the cracks propagated concentrically (see Figure 6.3), crack values are indicated as total radial crack lengths (i.e. with the 30-mm radius of the pre-crack included).

The cracks increased rapidly at the beginning of the two experiments, the growth rate then progressively decreased and finally approached a plateau after four million cycles. Almost identical total radial crack lengths were obtained and, although the exhibited plateaus differed slightly, similar mean values of total radial crack lengths were achieved (118.7 mm and 118.3 mm for SPA.1F and SPA.2F respectively). Both experiments ended before reaching the serviceability number of cycles (i.e. 12.5 million) due to the failure in the loading region where, as a result of the local damage of the face sheet, the screw was pulled out. The SPA.2F panel sustained almost 60% more cycles than SPA.1F, see Table 6.3. Consequently, a longer plateau was exhibited in the latter case.

As the crack propagated, the opening displacement values, both maximum ( $\delta_{max}$ ) and minimum ( $\delta_{min}$ ), increased to maintain the target maximum and minimum fatigue loads. In Figure 6.5 the consequently increasing displacement increment (i.e.  $\delta_{max} - \delta_{min}$ ) responses of both panels are presented. As can be observed, similar behaviors were exhibited up to approximately one million cycles. Then, the curves started to differ, i.e. the SPA.2F panel exhibited lower values. However, approximately the same displacement value was achieved before failure (3.7 and 3.6 mm for SPA.1F and SPA.2F respectively). The common general trend (i.e. fast initial increase followed by a progressive deceleration) is in agreement with the previously described crack propagation behavior.

After a certain degree of crack propagation, the additional layers of reinforcement inserted over the face sheet laminate in the loading region (see Section 6.2.2) started to detach in both panels. The cycle interval corresponding to this detaching process (from initiation to complete detachment) is indicated as “RD” (reinforcement detachment) in

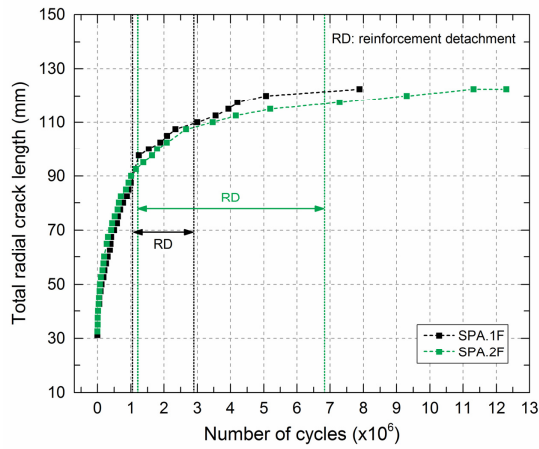


Figure 6.4 – Total radial crack length vs number of cycle curves of SPA configuration panels

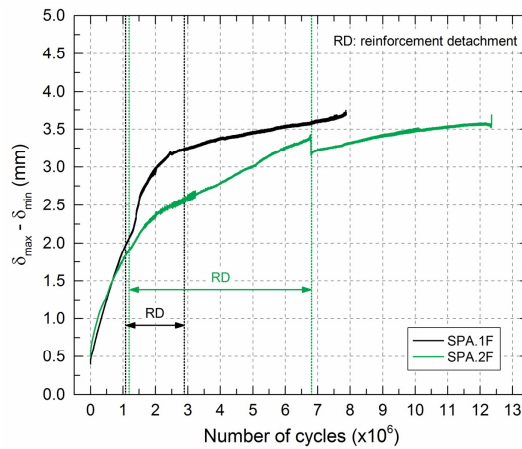


Figure 6.5 – Displacement increment vs number of cycle of SPA configuration panels

Figure 6.4 and Figure 6.5. The initiation occurred at similar total radial crack lengths (90.0 mm in SPA.1F and 92.5 mm in SPA.2F) and after a similar number of cycles ( $\sim 1$  and  $\sim 1.2$  million cycles respectively). The complete detachment of the layers occurred in both panels after the stabilization of the crack (i.e. already in the plateau region). However, the detachment process required more cycles in SPA.2F than in SPA.2F ( $\sim 2.9$  and  $\sim 6.8$  million cycles respectively).

### 6.3.2 Crack growth and displacement responses in SPB configuration panels

The fatigue crack growth results corresponding to the experiments on the SPB configuration are presented in Figure 6.6. As in the SPA panels, concentric crack propagation was obtained and thus crack values are also given in terms of total radial crack length. Depending on the selected  $R$ -ratio (see Table 6.3), very different fatigue behaviors were exhibited.

The crack in SPB.1F ( $R=0.1$ ) propagated rapidly throughout the experiment, without exhibiting any significant reduction in crack growth rate. At 105 mm of total radial crack length the loading region failed and the screw was pulled out. This occurred after 1.09 million cycles and thus much earlier than in either of the two SPA panels which were also loaded at  $R=0.1$  (see Section 6.3.1). Considering the short fatigue life

shown for the SPB configuration at  $R=0.1$ , a smaller amplitude ( $R=0.5$ ) was applied to the second panel (SPB.2F, Table 6.3). As can be observed in Figure 6.6, a plateau in the total radial crack length was quickly approached after a short initial rapid crack growth during the first 10 mm of radial propagation. Thus, almost no variation of the crack front was registered after approximately 1.5 million cycles. Furthermore, no noticeable damage occurred at the loading region. The experiment was stopped after the serviceability 12.5 million cycles were reached. In Table 6.3 the arrow indicates run-out specimens. Due to the reduced crack propagation (only 15 mm of radial increase) and the almost intact loading region after completing the SPB.2F1 experiment, a second experiment (i.e. SPB.2F2) under  $R=0.3$  was performed on the same panel. At this intermediate amplitude, the crack increased at a fairly constant rate throughout the experiment (see Figure 6.6). As for SPB.2F1, the experiment was stopped after the serviceability 12.5 million cycles were reached, which corresponded to a total radial crack length of 87.5 mm. More cycles would have been necessary to develop the plateau. Localized damage had already developed in the loading region.

The variation of the displacement increment during each of the three SPB experiments is shown in Figure 6.7. The results are in agreement with the above-mentioned crack growth behavior, showing a steep increase for SPB.1F, barely varying for SPB.2F1 and steadily increasing for SPB.2F2.

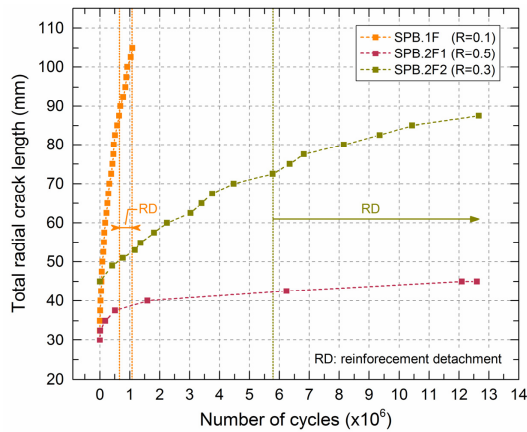


Figure 6.6 – Total radial crack length vs number of cycle curves of SBP configuration panels

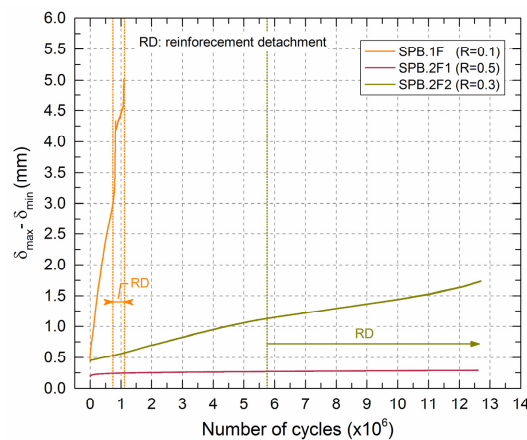


Figure 6.7 – Displacement increment vs number of cycle of SBP configuration panels

The detachment of the reinforcement layers was only observed in SPB.1F and SPB.2F2 (see “RD” in Figure 6.6 and Figure 6.7). In the SPB.1F experiment it initiated after 57.5 mm of radial propagation (i.e. a total radial crack length of 87.5 mm) and  $\sim 0.7$  million cycles. The complete detachment occurred simultaneously with the rapid local damage of the region. Regarding SPB.2F2, the detachment initiated at a total radial crack length of 72.5 mm and after  $\sim 8.5$  million cycles.

### 6.3.3 Crack area growth rate

To better understand the described changes in the propagation rates, the fatigue crack area growth rate (i.e.  $dA/dN$ , henceforth referred to simply as “crack growth rate”) vs the total crack area (i.e. with the pre-crack area included) curves are presented in Figure 6.8. An incremental polynomial fitting, similar to that recommended for 1D specimens in ASTM E647-15e1 [44], was used to calculate the crack growth rate. According to this method, a second-order polynomial is fitted to groups of a specific number of successive data points (seven here). The slope of the fitted equation at any point corresponded to the crack growth rate.

As can be observed in Figure 6.8, for all the experiments, the crack growth rate continuously decreased as the total crack area increased. Nevertheless, this decrease was not constant throughout the experiments, showing different behaviors depending on the experiment. Three regions could be identified for the two SPA experiments: 1) an initial region with a rapid decrease in the crack growth rate (from initiation to  $\sim 5000 \text{ mm}^2$  of total crack area); 2) an intermediate region exhibiting a moderate decrease in the crack growth rate and 3) a final region with again a rapid crack growth rate decrease (from  $\sim 40000 \text{ mm}^2$  of total crack area until the end of the experiments). The first region corresponded to the first 10 mm of radial crack propagation in Figure 6.4 and the last region to the exhibited plateau. Thus, the intermediate region corresponded to the major part of the fatigue experiments (see Figure 6.4).

Regarding the SPB experiments, a strong effect of the  $R$ -ratio, as already evident in Figure 6.6, was observed. The curve corresponding to  $R=0.1$  (SPB.1F) only showed the

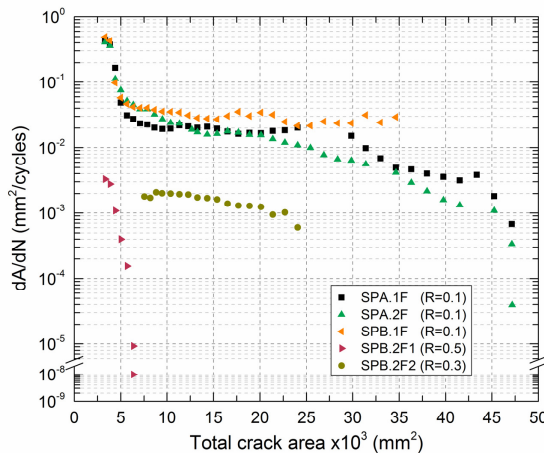


Figure 6.8 – Crack area growth rate vs total crack area

first and second regions (in Figure 6.8) due to the early failure of the panel (i.e. the plateau in Figure 6.6 was not reached). The three regions were exhibited in SPB.2F1 ( $R=0.5$ ) showing a rapid crack growth rate decrease from  $\sim 0.003 \text{ mm}^2/\text{cycle}$  to  $\sim 0.002 \text{ mm}^2/\text{cycle}$  (at the beginning of the experiment), followed by a more moderate decrease down to  $\sim 10^{-5} \text{ mm}^2/\text{cycle}$  and again a rapid crack growth down to  $\sim 10^{-8} \text{ mm}^2/\text{cycle}$  when the serviceability 12.5 million cycles were reached (after only 15 mm of radial propagation (see Figure 6.6)). Finally, in the curve corresponding to  $R=0.3$  (SPB.2F2) only the intermediate region was exhibited, showing that for this particular fatigue loading, the last region would have developed after more than 12.5 million cycles.

#### 6.3.4 Load-displacement hysteresis loops and stiffness degradation

The load-displacement hysteresis loops developed during the fatigue loading of SPA.1F are presented in Figure 6.9. The upper and lower parts of the loops corresponded respectively to the loading and unloading portions of the cycles. As can be observed, the loops exhibited a particular shape, referred to as “banana” shape in literature [45]. This shape became more accentuated as the crack propagated. The loops shifted towards the right as a result of the increase in the opening displacement. Furthermore, the area inside the loops (corresponding to the dissipated energy within a cycle) followed an increasing trend with the number of cycles, as can be observed for the two SPA panels in Figure 6.10 ( $N_f$  is the total number of cycles sustained in the experiment). Similar behavior was obtained for all the experiments.

The global stiffness of the panels at each cycle,  $K$ , was assumed as being the slope of the hysteresis loops as defined in Figure 6.9. The evolution of the global stiffness in all the experiments is presented in Figure 6.11. A sharp initial degradation of the stiffness was exhibited in all panels. After a progressive decrease in the degradation rate, a plateau was achieved in SPA.1F, SPA.2F and SPB.2F1 experiments whereas in SPB.2F2, although a progressive decrease was also exhibited, the plateau did not completely develop. Again, similar behavior was exhibited in both SPA panels. In SPB.1F, only a small reduction occurred in the degradation rate before failure.

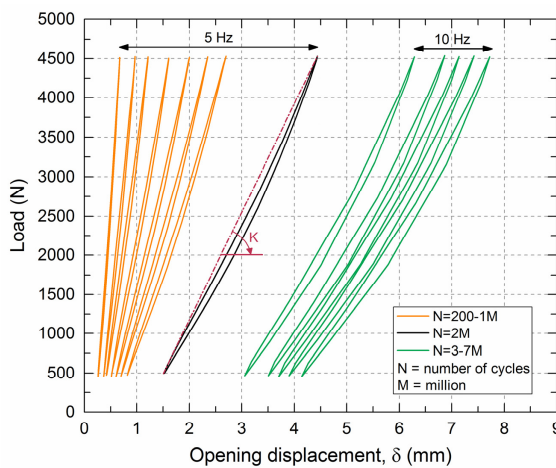


Figure 6.9 – Load-displacement hysteresis loops of SPA.1F panel

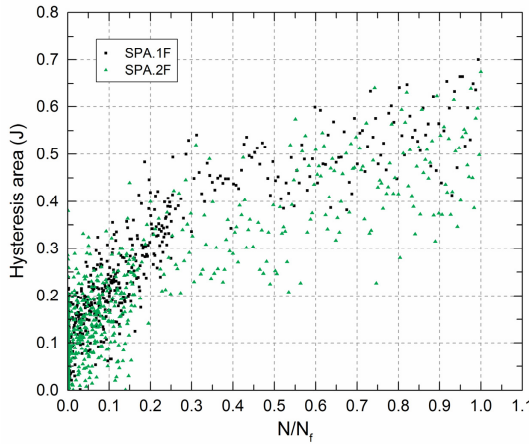


Figure 6.10 – Hysteresis area per cycle vs normalized number of cycles of SPA panels

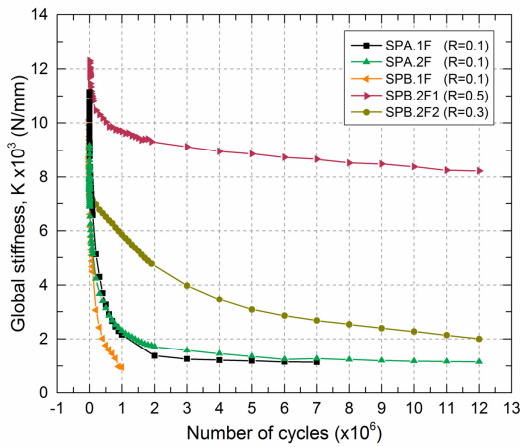


Figure 6.11 – Global stiffness vs number of cycles

In Figure 6.12, the crack growth rate is plotted against the global stiffness for all the experiments, showing a strong correlation between both parameters. The stabilization of the crack (i.e. no propagation) coincided with the stabilization of the global stiffness (i.e. no further degradation) for both SPA configuration experiments (once again showing comparable results) and for SPB.2F1, which showed the steepest curve. Neither the crack propagation nor the global stiffness stabilized however in SPB.1F and SPB.2F2 experiments.

The evolution of the global stiffness throughout all the experiments vs the total crack area is presented in Figure 6.13. As can be observed, almost overlapping curves were obtained for all the configurations and  $R$ -ratios, confirming that the selected layups of the face sheets had, as intended, exhibited a comparable bending stiffness (see Section 6.2.2).

### 6.3.5 Radial and circumferential strain distribution

The in-plane radial and circumferential strains in the top surface of the face sheet were extracted from the 3D DIC measurements recorded during the experiments as described in Section 6.2.3. The strain profiles corresponding to a radial path (starting from the pre-crack front) in the SPA.1F panel are shown in Figure 6.14. Three groups of profiles, corresponding to three different fatigue cycles, are presented: the black profiles, extracted at cycle 500,000; the orange profiles, extracted at cycle 1.0 million



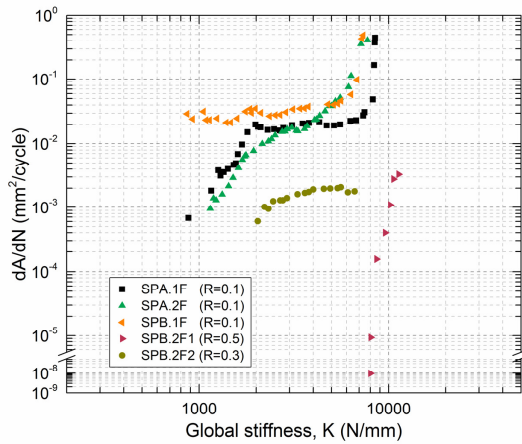


Figure 6.12 – Crack area growth rate vs global stiffness

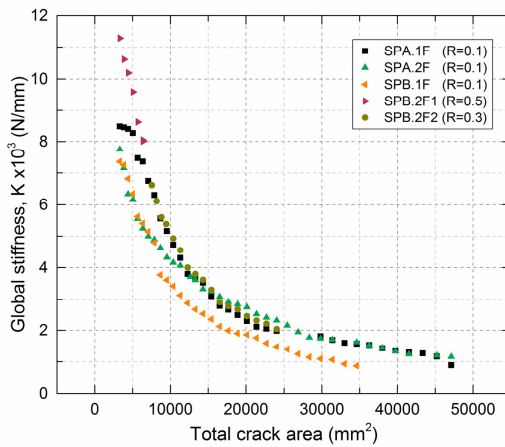


Figure 6.13 – Global stiffness vs total crack area

and the green profiles, extracted at cycle 1.5 million. The crack tip is indicated for each group of strain profiles (i.e. at a total radial crack length of 77.5, 95.0 and 105.0 mm respectively). The radial strain profiles were partially in compression and partially in tension while full tensile circumferential strain profiles were obtained. The typical compression state in the laminate in front of the crack tip ([46], i.e. in the un-cracked region) can be observed, mainly in the radial profiles.

### 6.3.6 Evolution of face sheet surface temperature

The distribution and magnitude of the surface temperature in four of the performed experiments, before the last fatigue cycles, are shown in Figure 6.15. The presented temperature scale ranges from 10°C to 42°C. The regions exhibiting higher temperatures (i.e. hotspots outside the measuring scale) are thus indicated in white. Due to the comparable fatigue behavior obtained in both SPA.1F and SPA.2F experiments, a similar evolution of the surface temperature was obtained. Thus, only one of two SPA experiments (i.e. SPA.2F) is shown in Figure 6.15. As can be observed, a clear hotspot (white color) was detected in the loading area for SPA.2F and SPB.1F due to the high internal friction generated owing to the concentrated damage in the region, which, ultimately, led to failure. Due to the absence of damage in the loading

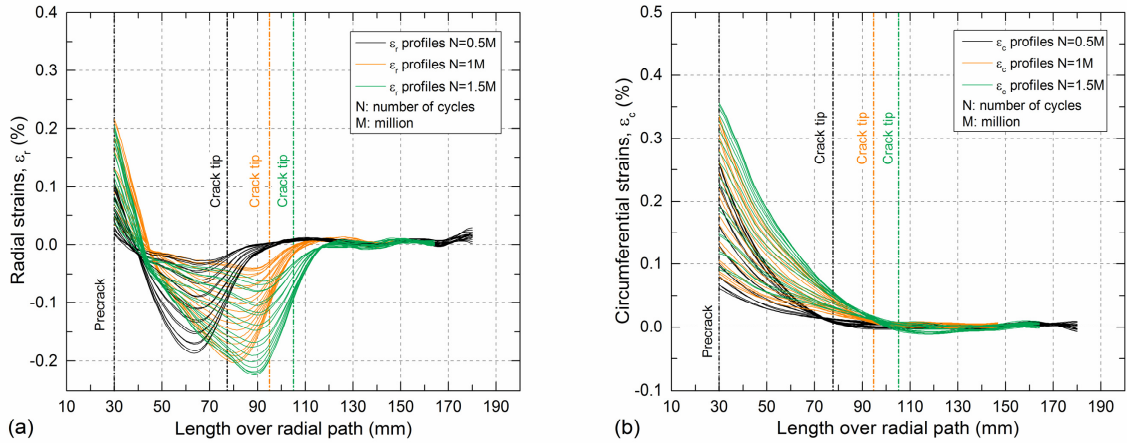


Figure 6.14 – Face sheet top surface in-plane strain distributions extracted from DIC; (a) in radial directions and (b) in circumferential direction for SPA.1F

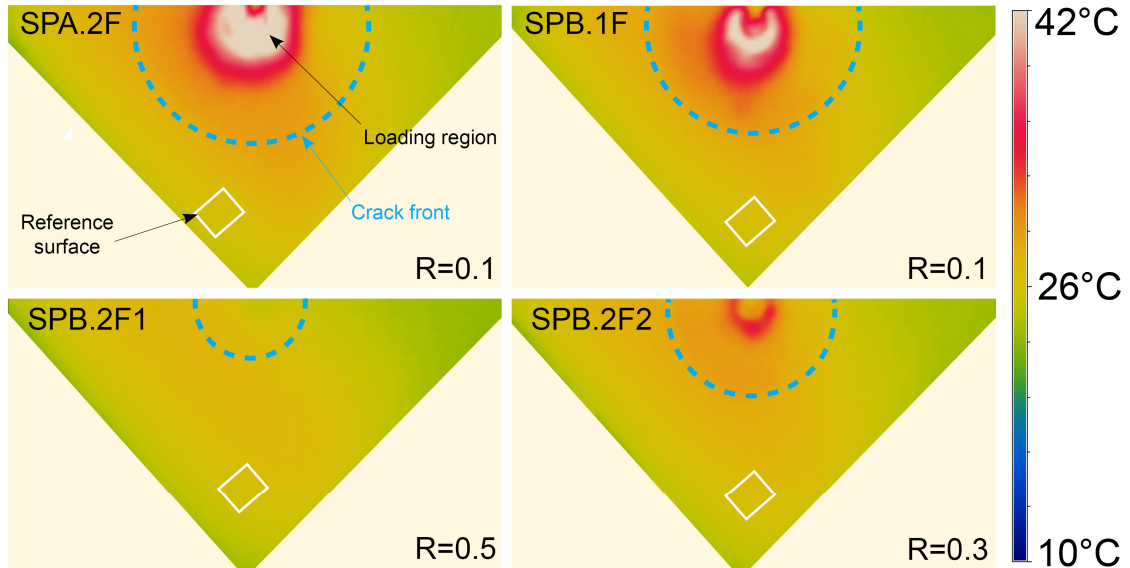


Figure 6.15 – Surface temperature before last fatigue cycles in four of performed experiments

region of SPB.2F1 ( $R=0.5$ ), no temperature increase occurred throughout the 12.5 million cycles. The intermediate loading case ( $R=0.3$ , SPB.2F2) already exhibited a temperature increase in the loading area after the serviceability 12.5 million cycles, which correlated with the already visible localized damage. The corresponding maximum temperatures registered in the loading region of the panels immediately before failure/end of the experiments are presented in Table 6.3. They remained well below the glass transition temperature of the laminate ( $66.3^\circ\text{C}$  onset value from DMA) and thus did not cause any significant material softening.

No relevant temperature increase at the crack front (compared to the reference surface) was registered in any of the experiments (see dashed lines in Figure 6.15). However, the temperature was measured on the surface of the face sheets and therefore, if a temperature increase occurred around the crack tip, for instance, as a result of the friction of the developing fiber-bridging, the generated temperature may have dissipated through the thickness of the laminate.

## 6.4 Discussion

### 6.4.1 Load vs displacement control in 1D and 2D fatigue experiments

Quasi-static investigations of 2D delamination in laminated plates [35] and 2D debonding in sandwich panels [37] have proved that continuously increasing loads are required to propagate an embedded 2D crack due to the natural increase of the length of the perimeter of the 2D crack (i.e. the crack front) and the resulting disproportional growth of the crack area. This 2D behavior is the opposite of the typical 1D behavior of beam-like fracture experiments where cracks propagate with a constant crack front length under decreasing loads. As a result of this difference, the experimental fatigue fracture behavior under load and displacement control modes in 1D crack propagation cases is different from that in 2D cases. A comparison of these cases is discussed in the following.

The schematic quasi-static load-displacement curves corresponding to 1D and 2D crack propagation are presented in Figure 6.16. These curves correspond to simplified fracture cases where after the critical load and opening displacement at which the crack is initiated (i.e.  $P_{cr}^0$  and  $\delta_{cr}^0$  in Figure 6.16) no relevant fracture process zone (FPZ) develops. The fatigue loading state after the propagation of a certain crack length “ $a$ ” and a certain crack area “ $A$ ” is evaluated considering both displacement and load control. Under displacement control, maintaining, for instance,  $\delta_{cr}^0$  as the maximum fatigue opening displacement ( $\delta_{max}$ ), the maximum fatigue load corresponding to a crack length “ $a$ ” ( $P_a$ ) or crack area “ $A$ ” ( $P_A$ ) is smaller than the quasi-static critical load corresponding to the same crack length ( $P_{cr}^a$  and  $P_{cr}^A$  respectively). Consequently, a stable fatigue propagation of the crack, eventually reaching a non-propagating state indicating the absence of fatigue damage, is achieved under displacement control in both 1D and 2D fracture experiments. However, this is not the case when fatigue experiments are performed under load control. If, following the same reasoning as in displacement control,  $P_{cr}^0$  is selected as the maximum fatigue load ( $P_{max}$ ), different results are obtained for 1D and 2D cases. In 1D cases, the selected  $P_{max}$  will always be greater, irrespective of the crack length, than the corresponding quasi-static critical load.

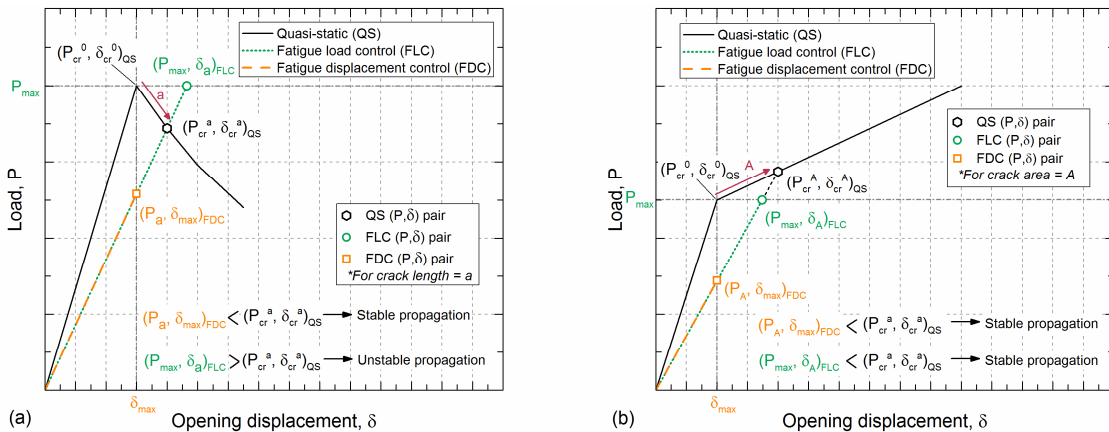


Figure 6.16 – Schematic comparison between load and displacement control in (a) 1D and (b) 2D fatigue fracture experiments

As can be observed in Figure 6.16(a), for the evaluated crack length “ $a$ ”,  $P_{max}$  is greater than  $P_{cr}^a$ . Therefore, an unstable crack propagation occurs under load control for 1D experiments if the static critical load is selected as the maximum fatigue load. To overcome this problem, in 1D fracture experiments under load control, a maximum fatigue load significantly smaller than the critical static load is typically selected, thus permitting an initial slow and stable propagation before the final rupture of the specimen (i.e. when the selected  $P_{max}$  reaches the corresponding  $P_{cr}^a$ ). In the 2D case (Figure 6.16(b)), and again selecting  $P_{cr}^0$  as the maximum fatigue load ( $P_{max}$ ), the quasi-static critical load corresponding to a crack area “ $A$ ” ( $P_{cr}^A$ ) is always greater than  $P_{max}$ . It can therefore be concluded that, owing to the continuously increasing load required to propagate a 2D crack, stable crack propagation can also be achieved under load control. This conclusion is corroborated by the 2D fatigue results presented in this investigation where, under load control, an initially fast crack propagation was registered followed by progressive stabilization.

As a result of the stable crack propagation always associated with displacement control in 1D fatigue experiments, they are easier to perform than those under load control. Thus, displacement control experiments are generally preferred in 1D fatigue investigations [33, 34]. As has been shown, in 2D crack propagation cases, both load and displacement control lead to a stable propagation of the crack and final crack arrest. However, as can be observed in Figure 6.16(b), the amount of crack propagation under displacement control may be considerably smaller than that under load control due to the more drastic reduction of load at the crack tip associated with displacement control. This reduction in the amount of propagated crack may lead to incomplete development of the three regions (see Section 6.3.3.) associated with crack propagation under fatigue. Consequently, load-controlled experiments may even be preferable for 2D crack propagation investigations. Further experimental work is required to fully confirm this statement.

#### 6.4.2 Effect of local damage in loading region

Throughout the experiments, the stiffness of the loading region of the panel face sheets was progressively reduced due to 1) the detachment of the reinforcement layers and 2) the local damage of the face sheet laminate. Any local stiffness reduction was however compensated by an increment in the already increasing opening displacement and thus did not affect the propagation of the investigated cracks. This was possible thanks to the load control conditions applied to all the experiments, which assured the continuous loading of the crack front.

For instance, as shown in Figure 6.5, in both SPA panels a jump in the displacement was exhibited after the initiation of the detachment of the reinforcement layers (indicated as “RD”, see Section 6.3.1) whereas the propagation of the crack continued. As the opening displacement increased, local damage progressively appeared in the loading region of the face sheet laminate, which reached failure after attaining the maximum displacement increment (i.e. around 3.7 mm for the SPA configuration

panels, see Section 6.3.1). Due to the more rapid detaching process occurring in SPA.1F (see the length of “RD” region), the mentioned maximum displacement increment (and thus failure) was reached ~4.5 million cycles earlier than in SPA.2F (see Table 6.3). In view of the fact that the crack propagation was already stabilized before failure in both panels, no fatigue fracture data was lost. This can also be concluded from Figure 6.8 where a sharp decrease of the crack growth rate was exhibited in both panels towards the end of the experiments.

Regarding the SPB.1F and SPB.2F2 experiments, the local stiffness reduction due to the detachment of the reinforcement layers was also compensated by the increased displacement. A jump was exhibited in the displacement curve of the SPB.1F experiment whereas, as a result of the slow progression of the detachment process, a smoother variation in the displacement curve was observed in the SPB.2F2 experiment (see Figure 6.7). In both cases, the propagation also continued until failure for SPB.1F and until the serviceability number of cycles for SPB.2F2.

The continuously decreasing trend of the global stiffness,  $K$  (extracted from the load-displacement hysteresis loops as described in Section 6.3.4), showed that a general softening of the panels occurred. Both crack propagation and  $K$  evolved similarly throughout the fatigue experiments (see Figures. 6.4, 6.6 and 6.11), eventually exhibiting a simultaneous stabilization. It can thus be concluded that the local progressive damage in the loading region did not affect the fracture behavior of the panels.

#### 6.4.3 *R*-ratio effects

The fracture behavior of the investigated sandwich panel configurations under quasi-static opening loads [37] showed that, compared to the SPA panels, the introduction of CFM plies at the face sheet/core interface enhanced the load-bearing performance and led to a significant crack arrest in the SPB panels. The dense fiber-bridging generated during crack propagation was the cause of the improved fracture behavior. However, this conclusion cannot be directly applied to the fatigue fracture behavior, where, as discussed in the following, the fiber-bridging effect under fatigue loads was highly dependent on the selected *R*-ratio.

The two SPA configuration experiments and SPB.1F experiment were performed under the same *R*-ratio (i.e.  $R=0.1$ ) and thus the obtained fatigue fracture behaviors are comparable. Based on the quasi-static behavior, a denser fiber-bridging was expected in the SPB configuration than in the SPA configuration, also resulting in a significant crack arrest and therefore steeper (again compared to SPA panels)  $dA/dN$  vs total crack area curves (Figure 6.8). However, due to the high fatigue amplitudes ( $\Delta P$ ) associated with low *R*-ratios such as  $R=0.1$ , the cyclic crack closure in the SPB.1F experiment crushed most of the fibers-bridging the crack faces and any contribution of the fiber-bridging to the fracture performance was consequently minimized. As a result, as can be observed in Figure 6.8, the SPB.1F panel exhibited a less steep  $dA/dN$ -total crack area curve than SPA panels which proved that, under  $R=0.1$  fatigue loading, the SPB

configuration did not result in a better fracture performance than the SPA configuration, as was the case under quasi-static loading conditions.

Comparing the results of the three SPB configuration experiments, the influence of the  $R$ -ratio can be clearly observed (Figure 6.8). As discussed above,  $R=0.1$  led to an almost complete destruction of the fiber-bridging and consequently, a rapid increase of the crack and opening displacement occurred within the first million cycles (see Figure 6.6). As a result, the third branch of the  $dA/dN$ -total crack area curve, corresponding to the stabilization of the crack (see Section 6.3.3), was lacking. Steeper  $dA/dN$ -total crack area curves were obtained for increasing  $R$ -ratios. Specifically, almost no crack propagation occurred under  $R=0.5$ , thus indicating a rapid crack arrest as a result of the dense non-destroyed fiber-bridging. As the experiment under  $R=0.3$  (SPB.2F2) was performed on the same panel as the SPB.2F1 experiment, the fiber-bridging generated during the latter was already present and thus the first branch of the  $dA/dN$ -total crack area curve was lacking and yet an intermediate slope between  $R=0.1$  and  $R=0.5$  was exhibited. Similar effects of the  $R$ -ratio on fiber-bridging were reported in [27] (1D-experiments).

#### 6.4.4 Load-displacement hysteresis loops and stretching-stiffening effect

The “banana” shape exhibited by the load-displacement hysteresis loops in all the performed experiments was caused by an increase of the cyclic stiffness ( $K^*$ ) within each cycle. The slopes corresponding to the initial and last stiffnesses ( $K_0^*$  and  $K_1^*$  respectively) are indicated in Figure 6.17(a) for the SPA.1F hysteresis loops corresponding to 0.6 and 3 million cycles. Additionally, the compliance (calculated as  $\delta/P$  within a cycle) vs fatigue load curves corresponding to the loading part of both cycles are presented in Figure 6.17(b). Typically, in 1D experiments, as a result of crack propagation, the compliance increases throughout the loading of the cycle [35]. However, as can be observed in Figure 6.17(b), for the investigated 2D experiments, the compliance initially increased up to a maximum and subsequently decreased, thereby indicating an initial softening followed by a stiffening within the same cycle. Similarly

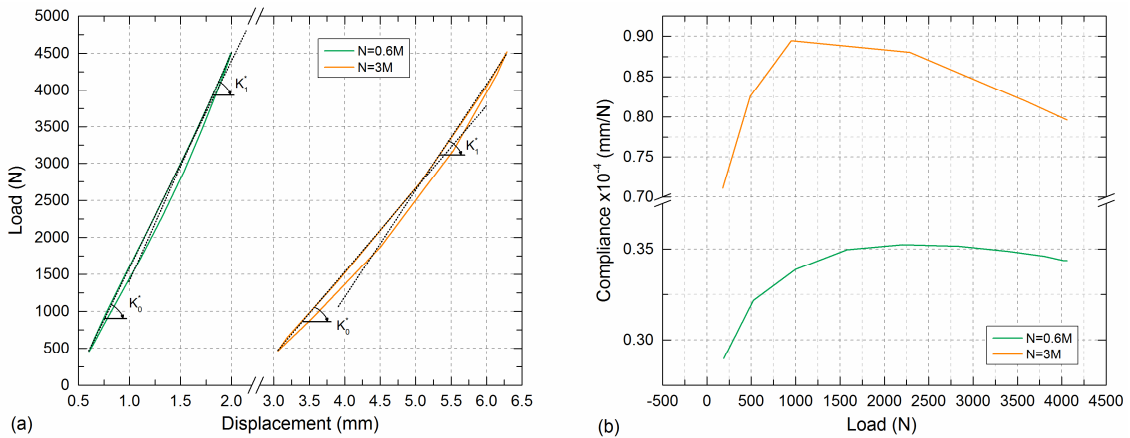


Figure 6.17 – (a) Load-displacement hysteresis loops and (b) loading part compliances vs load curves at 0.6 million cycles and 3 million cycles; results for SPA.1F panel

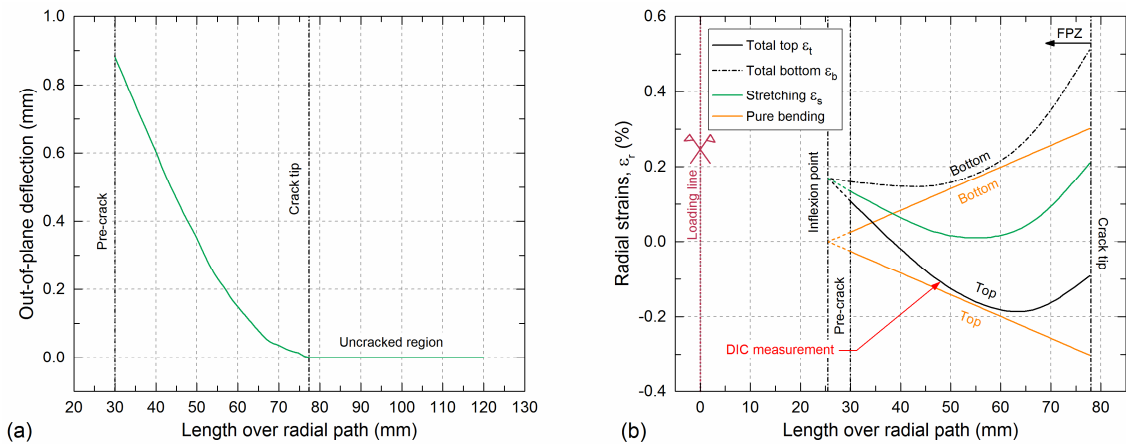


Figure 6.18 – Results obtained from face sheet top surface of panel SPA.1F at maximum deformation state at cycle 0.5M; (a) out-of-plane radial deflection profile; (b) radial strain profiles; all data derived from DIC

to both quasi-static 2D panel delamination and 2D sandwich debonding [35, 37], the stiffening was caused mainly by the in-plane stretching (in both the radial and circumferential directions), due to the geometrical constraints, in the opened part of the laminate. Within each of the load cycles the stiffening occurred only after a certain level of deformation and thus after a certain increase of the load (i.e. the softening prevailed at the beginning of each cycle). As a result of the crack propagation and opening displacement increase, the deformation of the face sheet (and thus the in-plane stretching strains and stresses) also increased. The ratio between the initial and last cyclic stiffnesses (i.e.  $K_I^*/K_0^*$ , see Figure 6.17) can be used to quantify the stiffening effect within each cycle. As expected, a smaller ratio was obtained at 0.6 million cycles (1.09, i.e. 9% increase) compared to 3 million cycles (1.28, i.e. 28% increase).

As mentioned in Section 6.3.4 and observed in Figure 6.10 for the SPA panels, the area inside the loops exhibited an increasing trend with number of cycles for all the studied cases. Four sources of energy dissipation contributed to this increase: 1) the energy released as a result of the propagation of the main crack; 2) the energy released due to the damage created in the loading region; 3) the thermal energy dissipation at the crack tip as a result of the friction created in the fiber-bridging zone and 4) the thermal energy dissipation as a result of the friction between the crack faces generated in the loading region. The contribution of each of the sources varied throughout the experiments. Initially, during the rapid increase of the crack area, the energy released due to the propagation of the crack prevailed (see the rapid increase in the hysteresis area in Figure 6.10). Subsequently, when the crack started to stabilize (i.e. approached the plateau) and the damage in the loading region initiated, the damage and thermal energy dissipation in the loading region (i.e. sources 2 and 4) constituted the main source until the end of the experiments. Since the hysteresis area started approaching a plateau in this phase however, this latter contribution must have been significantly smaller than the former.

In beam-like specimens, small hysteresis areas develop and thus the hysteresis of the cyclic load-displacement behavior is typically disregarded (i.e. a linear behavior is



assumed [47]). However, the length of the crack front increased throughout the propagation of an embedded 2D crack, resulting in a disproportional growth of the crack area [35, 37]. Consequently, considerably more energy (in terms of J, not J/m<sup>2</sup>) is dissipated during the propagation of a 2D crack, thus increasing the hysteresis.

#### 6.4.5 Derivation and evolution of in-plane stretching strains

If the face sheets of the investigated sandwich panels were under pure bending conditions, zero strain points corresponding to the change from compression to tension strains (such as those exhibited in the radial strain profiles presented in Figure 6.14(a)) would necessarily indicate the location of an inflection point. However, the out-of-plane deflection radial profiles of the top surface of the face sheets (extracted from the DIC measurements) did not reveal an inflexion point at the exhibited zero strain points, as can be observed for the SPA.1F panels (particularly at 0.5 million cycles) in Figure 6.18. This mismatch between inflection and zero strain points was attributed to the radial in-plane stretching strains which counteracted the bending compression strains and increased the bending tensile strains. The full tensile circumferential strains present in the top surface of the face sheet (see Figure 6.14(b)) were increased by the corresponding in-plane circumferential stretching strains. Similar results were obtained for the quasi-static sandwich panels [37].

Using both the measured radial top strains and the curvature derived from the deflection profile, the corresponding radial bottom strains and stretching strains were derived. The stretching strains were subtracted from the total top and bottom strains to obtain the “pure” bending strain profiles. All the profiles are shown in Figure 6.18(b)). A detailed description of this procedure can be found in [37]. The derived stretching values may not be accurate close to the fracture process zone (FPZ) since they are affected by the fiber-bridging. Further discussion regarding this effect can be found in [37]. As can be observed in the stretching strain profile, towards the extremes (i.e. loading region and crack tip) higher values were obtained as a result of the greater deformation exhibited in these regions. Linear “pure” bending strain profiles were also obtained, representing the linear behavior inherent to a punctual load.

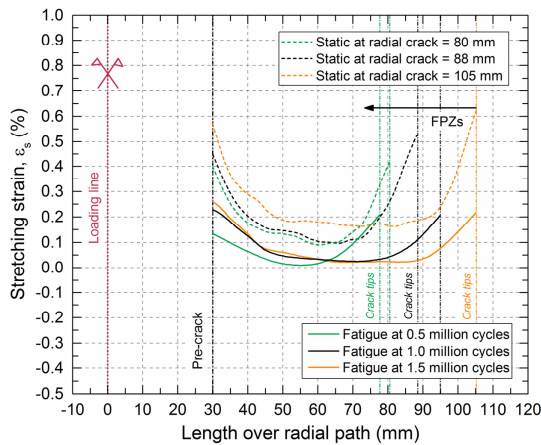


Figure 6.19 – Comparison of calculated radial stretching strains in fatigue SPA.1F and static SPA.2 [37] panels

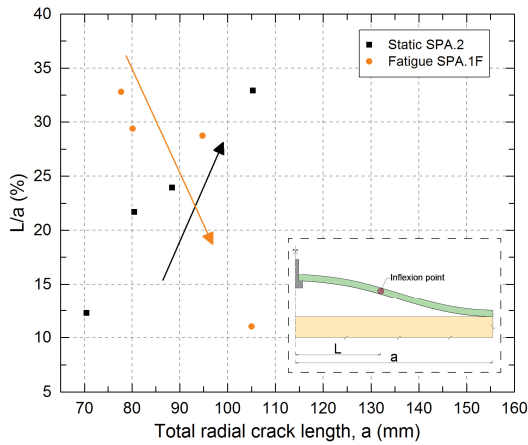


Figure 6.20 – Evolution of inflexion point with crack propagation in fatigue SPA.1F and static SPA.2 [37] panels

The radial stretching strain profiles corresponding to the other two cycles represented in Figure 6.14 (i.e. 1.0 and 1.5 million cycles) were likewise extracted and are shown, together with the profile at 0.5 million cycles, in Figure 6.19. As can be observed, a general increasing trend (mainly from 0.5 million to 1 million cycles) of the stretching strains occurred as the crack propagated and thus the face sheet deformed. This constitutes further confirmation of the increase of the stiffening effect obtained revealed in the load-displacement hysteresis loops and discussed in Section 6.4.4. For the sake of comparison, three radial stretching profiles corresponding to one of the SPA sandwich panels (SPA.2) quasi-statically investigated in [37] were added to Figure 6.19. The total crack lengths corresponding to the evaluated fatigue cycles were similar to those corresponding to the quasi-static profiles. For the same total radial crack lengths, the corresponding quasi-static load was always higher than the maximum fatigue load investigated here. Consequently, the fatigue stretching strains were smaller than the quasi-static stretching strains.

#### 6.4.6 Location and evolution of inflection points

The location of the inflection point was determined for different total radial crack lengths throughout the SPA.1F experiment. If the inflection point was located inside the DIC measuring area (i.e. from the pre-crack front onwards) it was already identified in the radial out-of-plane deflection profiles and if it was located outside the measuring area (i.e. in the pre-crack area) it could be identified by extending the pure bending linear profiles (see Figure 6.18(b)).

The evolution of the inflexion point location with respect to the total radial crack length (i.e.  $L/a$ ) for SPA.1F is presented in Figure 6.20. For the sake of comparison, results corresponding to the quasi-static SPA.2 panel are also shown. Opposite behaviors were obtained under quasi-static and fatigue loading, exhibiting increasing and decreasing trends of  $L/a$  values respectively. As discussed in [37], the propagation of the crack shifted the inflection point towards the exterior of the face sheet (i.e. increasing  $L/a$ ) while the local damage in the loading region shifted the inflection point towards the center of the face sheet (i.e. decreasing  $L/a$ ). The effective location of the

inflection point was thus the result of both opposing effects. In the quasi-static experiments, the propagation of the crack prevailed over the local damage of the loading region, shifting the inflection point towards the exterior of the face sheet. For the fatigue experiments on the other hand, the shift due to the local damage in the loading region prevailed over that of the propagation of the crack, moving the inflection point towards the center of the face sheet.

## 6.5 Conclusions

An experimental program designed to study the 2D fatigue face sheet debonding in GFRP/balsa sandwich panels with embedded cracks subjected to out-of-plane fatigue tensile loads was conducted. Two different face sheet configurations were investigated via a total of five experiments. One of the configurations (SPA) consisted of a pure woven fabric layup while in the other (SPB) layers of continuous filament mat were inserted above and below the woven plies. Circular pre-cracks were introduced at the face sheet/core interface. Experiments were performed under load control and under different  $R$ -ratios. The crack growth and opening displacement responses and the in-plane strain distributions of the face sheet were examined. Likewise, the  $R$ -ratio effects, developed load-displacement hysteresis loops and evolution of the global stiffness were analyzed. Furthermore, the differences between displacement-control and load-control fatigue loading in 1D and 2D fracture experiments were thoroughly discussed. The following conclusions were drawn:

1. Decreasing crack growth rates were obtained under load-control fatigue conditions exhibiting a threefold trend: 1) an initial rapid decrease, 2) a moderate decrease and 3) a final rapid decrease. The first and third stages corresponded, respectively, to the initial rapid propagation of the crack and final arrest of crack propagation. Depending on the experiment, full or partial development of the described stages was achieved.
2. The decreasing crack growth rates obtained in the 2D fatigue experiments under load control are in contrast with those of standard 1D beam-like fatigue experiments under load control, where increasing crack growth rates (up to failure) are exhibited (i.e. an unstable crack propagation and final rupture of the specimen occur). This particular 2D fracture fatigue behavior was attributed to the increasing load required to propagate a 2D crack due to the constant increase of the crack front length (i.e. the perimeter of the 2D crack). As a result, the quasi-static load required to maintain the propagation of a 2D crack will always be greater than any selected maximum fatigue load and thus a stable propagation and final arrest of a 2D crack can always be achieved under load control conditions.
3. The fracture efficiency of including plies prone to develop fiber-bridging at the face sheet/core interface was found to be strongly dependent on the type of loading (i.e. quasi-static or fatigue) and, particularly under fatigue, on the

considered  $R$ -ratio. Under quasi-static conditions, the introduction of such layers enhanced the fracture performance due to the dense fiber-bridging generated. However, due to the high fatigue amplitude associated with low  $R$ -ratios such as  $R=0.1$ , most of the fibers bridging the crack faces were broken, thus minimizing any fiber-bridging contribution and therefore not providing any improvement in terms of fatigue fracture performance. Increasing  $R$ -ratios however positively affected the fatigue performance due to the decrease in fiber-bridging crushing.

4. Due to the increasing length of the crack front throughout the propagation of an embedded 2D crack and the corresponding disproportional growth of the crack area, the amount of dissipated energy due to crack nucleation also increased as the crack propagated. As a result, the hysteresis area exhibited by the load-displacement loops considerably increased during the propagation of the crack. This behavior was the opposite of that of 1D beam-like specimens where the hysteresis of the cyclic load-displacement behavior is typically small and thus disregarded.
5. The load-displacement hysteresis loops exhibited an increase in the cyclic stiffness within each fatigue cycle. As in the quasi-static experiments, this stiffening was caused mainly by in-plane stretching stresses (developed as a result of the geometrical constraints). Based on the top surface face sheet in-plane strains extracted from the DIC measurements, the magnitude of the in-plane radial stretching strains was quantified showing an increasing trend of the in-plane stretching with increasing crack propagation. The magnitudes of load and displacement were smaller in the fatigue experiments than in the quasi-static experiments, resulting in a less deformed face sheet and thus smaller stretching strains.

## References

1. Hollaway, L. A review of the present and future utilization of FRP composites in civil infrastructure with reference to their important in-service properties. *Constr. Build. Mater.*, 2010; 24(12): 2419:2445.
2. Keller, T. Recent all-composite and hybrid fiber-reinforced polymer bridges and buildings. *Prog. Struct. Eng. Mater.*, 2001; 3(2): 132-140.
3. Uddin, N. *Developments in Fiber-Reinforced Polymer (FRP) Composites for Civil Engineering*. 1st ed. Woodhead Publishing; 2013.
4. Keller, T., Rothe, J., De Castro, J., Osei-Antwi, M. GFRP-Balsa Sandwich Bridge Deck: Concept, Design, and Experimental Validation. *J. Compos. Constr.*, 2013; 18(2): 04013043.
5. Osei-Antwi, M., De Castro, J., Vassilopoulos, A.P., Keller, T. Structural limits of FRP-balsa sandwich decks in bridge construction. *Composites: Part B*, 2014; 63: 77-84.
6. Osei-Antwi, M., De Castro, J., Vassilopoulos, A.P., Keller, T. FRP-Balsa Composite Sandwich Bridge Deck with Complex Core Assembly. *J. Compos. Constr.*, 2013; 17(6): 04013011.

7. Cantwell, W.J., Davies, P. A test technique for assessing core-skin adhesion in composite sandwich structures. *Journal of Material Science Letters*, 1994; 13: 203-205.
8. Ratcliffe, J.G., Reeder, J.R. Sizing a single cantilever beam specimen for characterizing facesheet-core peel debonding in sandwich structure. *Journal of Composite Materials*, 2011; 45(25): 2669-2684.
9. Saseendran, V., Berggreen, C., Krueger, R. Mode mixity analysis of face/core debonds in a single cantilever beam sandwich specimen. *J. Sandwich Structures and Materials*, 2018; 0(0): 1-31.
10. Farmand-Ashtiani, E., Cugnoni, J., Botsis, J. Monitoring and characterization of the interfacial fracture in sandwich composites with embedded multiplexed optical sensors. *Composite Structures*, 2013; 96: 476-483.
11. Cantwell, W.J., Scudamore, R., Ratcliffe, J., Davies, P. Interfacial fracture in sandwich laminates. *Comp. Sci. Tech.*, 1999; 54(14): 2079-2085.
12. Carlsson, L.A., Matteson, R.C., Aviles, F., Loup, D.C. Crack path in foam core DCB sandwich fracture specimens. *Compos. Sci. Technol.*, 2005; 65: 2612-21.
13. Li, X., Carlsson, L.A. The tilted sandwich debond (TSD) specimen for face/core interface fracture characterization. *J. Sandwich Structures and Materials*, 1999; 1: 60-75.
14. Li, X., Carlsson, L.A. Elastic foundation analysis of tilted sandwich debond (TSD) specimen. *J. Sandwich Structures and Materials*, 2000; 2: 3-32.
15. Ratcliffe, J., Cantwell, W.J. A new test geometry for characterizing skin-core adhesion in thin-skinned sandwich structures. *Journal of Material Science Letters*, 2000; 19: 1365-1367.
16. Ural, A., Zehnder, A.T., Ingrassia, A.R. Fracture mechanics approach to facesheet delamination in honeycomb: measurement of energy release rate of adhesive bond. *Eng Fract Mech*, 2003; 70: 93-103.
17. Shivakumar, K.N., Smith, S.A. in situ fracture toughness testing of core materials in sandwich panels. *Journal of Composite Materials*, 2004; 39(8): 655-668.
18. Berggreen, C., Simonsen, B.C., Borum, K.K. Experimental and numerical study of interface crack propagation in foam-cored sandwich beams. *Journal of Composite Materials*, 2007; 41(4): 493-520.
19. Stutz, S., Cugnoni, J., Botsis, J. Studies of mode I delamination in monotonic and fatigue loading using FBG wavelength multiplexing and numerical analysis. *Compos. Sci. Technol.*, 2011; 71: 443-449.
20. Berkowitz, K.C., Johnson, W. Fracture and fatigue tests and analysis of composite sandwich structure. *Journal of Composite Materials*, 2004; 39(16): 1417-1431.
21. Shafiq, B., Quispitupa, A. Fatigue characteristics of foam core sandwich composites. *International Journal of Fatigue*, 2006; 28(2): 96-102.
22. Shipsha, A., Burman, M., Zenkert, D. Interfacial fatigue crack growth in foam core sandwich structures. *Fatigue and Fracture of Engineering Materials and Structures*, 1999; 22: 123-131.
23. Manca, M., Berggreen, C., Carlsson, L.A. G-control fatigue testing for cyclic crack propagation in composite structures. *Eng. Frac. Mech.*, 2015; 149: 375-386.
24. Gillespie, J.W., Carlsson, L.A., Gawandi, A.A., Bogetti, T.A. Fatigue crack growth at the face sheet-core interface in a discontinuous ceramic-tile cored sandwich structure. *Composite Structures*, 2012; 94: 3186-3193.
25. Manca, M., Quispitupa, A., Berggreen, C., Carlsson, L.A. Face/core debond fatigue crack growth characterization using the sandwich mixed mode bending specimen. *Composites: Part A*, 2012; 43: 2120-2127.

26. Shahverdi, M., Vassilopoulos, A.P., Keller, T. Experimental investigation of R-ratio effects on fatigue crack growth of adhesively-bonded pultruded GFRP DCB joints under CA loading. *Composites Part A*, 2012; 43(10); 1689-1697.
27. Bak, B.L.V., Sarrado, C., Turon, A., Costa, J. Delamination under fatigue loads in composite laminates. A review of the observed phenomenology and computational methods. *Appl. Mech. Rev.*, 2014; 66: 060803-1-060803-24.
28. Rans, C., Alderliesten, R.C., Benedictus, R. Misinterpreting the results: how similitude can improve our understanding of fatigue delamination growth. *Compos. Sci. Technol.*, 2011; 124: 214-227.
29. Simon, I., Banks-Sills, L., Fourman, V. Mode I delamination propagation and R-ratio effect in woven composite DCB specimens for a multi-directional layup. *Inter. Journal of Fatigue*, 2017; 96: 237-251.
30. Pascoe, J.A., Alderliesten, R.C., Benedictus, R. Towards understanding fatigue disbond growth via cyclic strain energy. *Procedia Mater. Sci.*, 2014; 3: 610-615.
31. Brunner, A.J., Murphy, N., Pinter, G. Development of a standardized procedure for the characterization of interlaminar delamination propagation in advanced composites under fatigue mode I loading conditions. *Eng. Frac. Mech.*, 2009; 76: 2678-2689.
32. Campilho, R.D.S.G., da Silva, L.F.M. Mode I fatigue and fracture behavior of adhesively-bonded carbon fibre-reinforced polymer (CFRP) composite joints. *Fatigue and Fracture of Adhesively-bonded Composite Joints*: Ed. Vassilopoulos A.P. Woodhead Publishing; 2015.
33. Renart, J., Costa, J., Sarrado, C., Budhe, S., Turon, A., Rodríguez-Bellido, A. Mode I fatigue behavior and fracture of adhesively-bonded fibre-reinforced polymer (FRP) composite joints for structural repairs. *Fatigue and Fracture of Adhesively-bonded Composite Joints*: Ed. Vassilopoulos A.P. Woodhead Publishing; 2015.
34. Yoshida, K., Aoki, T. Beam on elastic foundation analysis of sandwich SCB specimen for debond fracture characterization. *Composite Structures*, 2018; 195: 83-92.
35. Cameselle-Molares A., Vassilopoulos A.P., Keller T. Experimental investigation of two-dimensional delamination in GFRP laminates. *Eng. Frac. Mech.*, 2018; 203: 152-171.
36. Cameselle-Molares A., Vassilopoulos A.P., Renart J., Turon A., Keller T. Numerical simulation of two-dimensional in-plane crack propagation in FRP laminates. *Comp. Struc.* 2018; 200: 396-407.
37. Cameselle-Molares A., Vassilopoulos A.P., Keller T. Two-dimensional quasi-static debonding in GFRP/balsa sandwich panels. *Comp. Struc.* 2019; 215:391-401.
38. Swiss Composite Product Catalogue. <<https://www.swiss-composite.ch/pdf/Produkteuebersicht.pdf>> (Accessed 16 October 2017).
39. Owen's Corning Reinforcements Composite Solutions Guide. <[http://www.ocvreinforcements.com/pdf/library/Composite\\_Solutions\\_Guide\\_100360\\_E\\_finalprintable.pdf](http://www.ocvreinforcements.com/pdf/library/Composite_Solutions_Guide_100360_E_finalprintable.pdf)> (Accessed 26 March 2018).
40. Sicomin SR8100 resin datasheet. <<http://www.sicomin.com/datasheets/product-pdf94.pdf>> (Accessed 12 November 2018).
41. EN 1991-2 Eurocode 1. Actions on structures – Part 2: Traffic loads on bridges.
42. Clarke, J.L. (ed.). *Structural design of polymer composites: Eurocomp design code and handbook*. London: E & FN Spon; 1996.
43. Correlated Solutions Inc. VIC 3D-v7 reference manual. Columbia, USA: Correlated Solutions.
44. ASTM E647-15e1: Standard Test Method for Measurement of Fatigue Crack Growth Rates, ASTM International, West Conshohocken, PA, 2015.

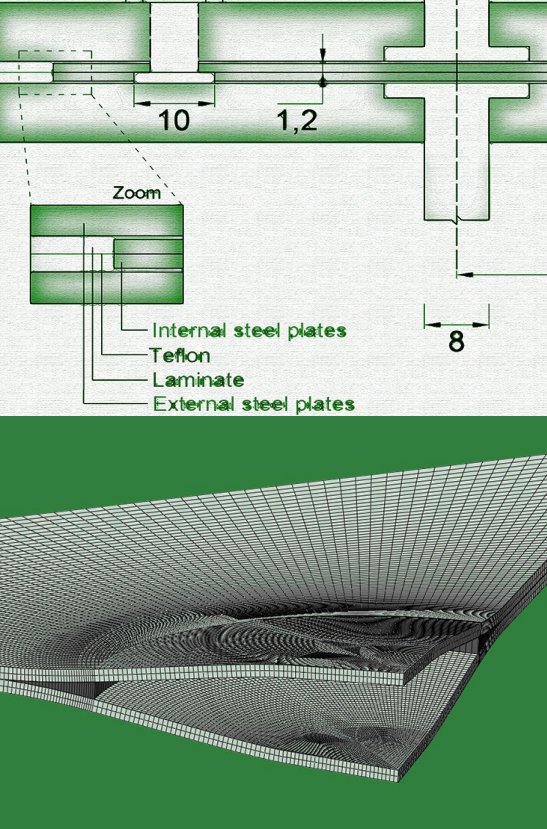
45. Vieille, B., Albouy, W. About the applicability of a simple model to predict the fatigue life and behavior of woven-ply thermoplastic laminates at  $T > T_g$ . *Composites Part B*, 2014; 61: 181-190.
46. Pappas, G., Botsis, J. Intralaminar fracture of unidirectional carbon/epoxy composite: experimental results and numerical analysis. *Int. J. Solids and Struc.*, 2016; 85-86: 114-124.
47. Pascoe, J.A., Alderliesten, R.C., Benedictus, R. On the relationship between disbond growth and the release of strain energy. *Eng. Fract. Mech.*, 2015; 133: 1-13.



---

**Contributions:** *Aida Cameselle Molares conceived, designed and performed the experimental campaign under the supervision of Prof. Thomas Keller and Dr. Anastasios Vassilopoulos. The analysis of the results was carried out by Aida Cameselle Molares in collaboration with Prof. Thomas Keller and Dr. Anastasios Vassilopoulos.*

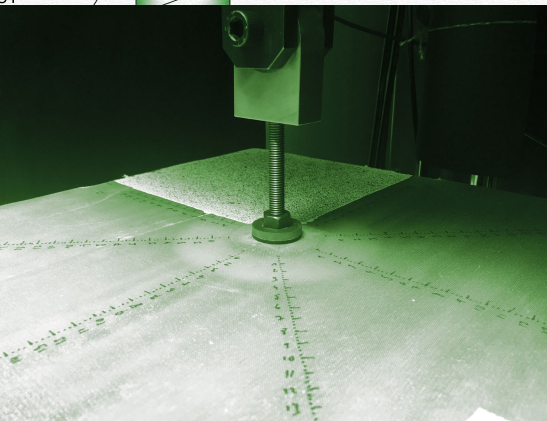
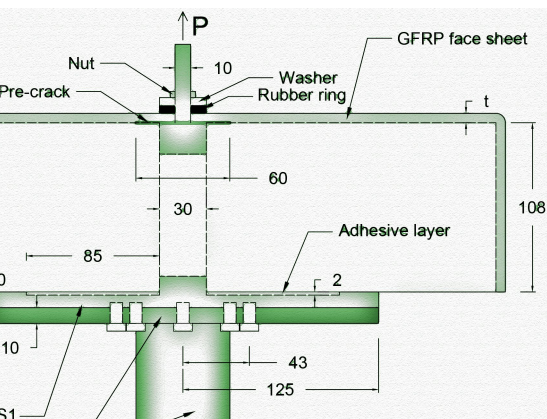




**Step 2:** performance of FE analyses using the same separation law in all directions. Different values of  $\alpha$  are used. At least three FE analyses with three different values of  $\alpha$  are performed.

**Step 3:** extraction of the numerical load-displacement curves (i.e. for each analysis) and calculation of the critical load  $P_{cr}$  from the last linear part of the curves.

**Step 4:** with the obtained  $\alpha - \bar{G}_{tot}$  results, determine the best fitting (a linear equation in the cases presented in the paper).



# Chapter 7

## Conclusions and future work

### 7.1 Conclusions

Two-dimensional (2D) crack growth in GFRP laminates and GFRP/balsa sandwich panels was experimentally investigated. Quasi-static and fatigue out-of-plane tensile loads were applied to open embedded circular pre-cracks introduced at the midplane of the laminated plates and the face sheet/core interface of the sandwich panels. New experimental designs and set-ups were developed within the framework of this investigation. Different 2D effects were identified based on experimental and numerical findings. Likewise, a 2D fracture characterization method was developed and validated. The main conclusions derived from this research are presented below.

#### 7.1.1 Two-dimensional effects on delamination and debonding fracture behavior

##### *Increasing loads*

Throughout the propagation of the embedded 2D crack in the GFRP laminated plates and GFRP/balsa sandwich panels, the length of the crack front (i.e. the perimeter of the crack) increased, resulting in a disproportionate growth of the crack area that forced the opening load to increase in order to maintain the propagation of the crack. This behavior is intrinsic to any embedded defect extending in all possible directions and is in contrast with that of standard beam-like experiments (1D) where the crack front length (i.e. crack width) remains constant during crack propagation, thus resulting in decreasing loads as the crack grows.

### ***Stretching and stress-stiffening effect***

The analysis of the exhibited quasi-static load-bearing and compliance behaviors demonstrated that a stiffening of the investigated laminated plates occurred during the 2D delamination. The boundary conditions, inherent to an embedded 2D crack propagating in a laminated plate, caused the development of in-plane stretching stresses in the opened part of the plates that were found to be the main cause of stiffening. This stress stiffening, together with the developed fiber-bridging (which also contributed to the overall stiffening), delayed the softening caused by the propagation of the crack. The minimum value of the compliance response was identified as the threshold between stiffening and softening predominance.

Similar stress-stiffening effects were observed in the quasi-static sandwich panels also due to the in-plane stretching that developed in the deformed face sheet as the 2D embedded disbond propagated. Increasing radial stretching strains with increasing crack propagation were measured in both of the investigated face sheet configurations.

This stress-stiffening effect was also reflected in the load-displacement hysteresis loops obtained from the fatigue experiments on sandwich panels that exhibited an increase in the cyclic stiffness within each fatigue cycle.

### ***Stretching-induced mode-mixity***

As a result of the in-plane stretching strains that developed in the opened part of the face sheets of the sandwich panels, shear fracture mode contributions were activated throughout the propagation of the disbonds. This stretching-induced mode-mixity constitutes an additional 2D effect in embedded cracks propagating under out-of-plane tensile loads which, depending on the face sheet layup, can trigger different crack propagation behaviors. Particularly for the face sheet configurations investigated here, the stretching-induced mode-mixity resulted in crack migration (from the face sheet/core interface to a parallel interface inside the face sheet) and nucleation of new interlaminar crack surfaces.

Throughout this research, this particular 2D effect was only observed in the 2D debonding of sandwich panels, where the stretching strains developed in the face sheet while the core did not deform, thereby activating the stretching-induced fracture modes. However, in the investigated 2D delamination cases, the crack always propagated in the midplane and therefore the laminates above and below the crack deformed equally thus developing similar stretching strains (i.e. no shear fracture modes arose). Eccentric defect propagation in laminated plates would also lead to stretching-induced shear fracture modes.

### ***Stable crack propagation under fatigue load control***

Due to the increasing load required to propagate a 2D crack, any selected maximum load value in load control fatigue experiments will always be, beyond a certain crack propagation area, smaller than the corresponding quasi-static load. Consequently, decreasing crack growth rates and thus stable crack propagation and final crack arrest

were obtained under load control in all the fatigue experiments performed on sandwich panels. These results are in contrast with those obtained in standard 1D beam-like fatigue experiments performed under load control where increasing crack growth rates are typically observed and unstable crack propagation until final failure of the specimens occurs. Considering that excessive crack arrest may occur under fatigue displacement control, load-controlled experiments may even be preferable for fatigue 2D crack propagation investigations.

#### ***Increasing fatigue hysteresis area***

As a result of the increasing crack front length of an embedded 2D crack and the corresponding disproportionate growth of the crack area, the amount of energy dissipated due to the nucleation of new crack surfaces increased as the crack propagated. This was reflected in the hysteresis area exhibited by the load-displacement loops obtained from the fatigue experiments on sandwich panels that increased considerably during the propagation of the crack. This behavior is once again in contrast with that of 1D fracture specimens where the hysteresis of the load-displacement loops is typically small and thus disregarded, thereby assuming a linear behavior.

#### **7.1.2 Influence of 2D effects on fiber-bridging development**

The numerical simulation of the 2D delamination behavior of the continuous filament mat (CFM) plates confirmed a 50% increase, compared to DCB specimens of the same fiber architecture, in the total strain energy release rate (SERR) required to propagate the crack. The increase in the developed fiber-bridging as a result of 1) the increase in the flexural stiffness (from beam to plate) and 2) the stress stiffening due to the in-plane stretching stresses, was found to be the cause of the SERR increase.

Furthermore, additional fiber-bridging was activated during the 2D debonding in sandwich panels as a result of the crack migration and the nucleation of new crack surfaces, both triggered by the stretching-induced shear fracture modes. As for the laminated plates, all the fiber-bridging was likewise enhanced by the increase in the flexural stiffness (from beam to panel) and the stress-stiffening effect.

Considering that none of these effects on fiber-bridging are present in standard 1D Mode-I dominated fracture experiments, the fracture properties derived from them would underestimate the actual fracture performance of an FRP structural member. Thus, taking into consideration stiffness-related effects in delamination and debonding involving fiber-bridging can lead to much more efficient damage-tolerant designs.

#### **7.1.3 Fiber architecture effects**

Depending on the fiber architecture of the laminated plates, different crack propagation patterns were exhibited. Concentric crack propagation (from the circular pre-crack) was obtained for the in-plane isotropic CFM plates while for the woven plates, the crack propagated more rapidly along the most reinforced directions (i.e. the stiffest) than along the least reinforced and thus least stiff directions. In the latter case, the

propagation patterns caused an uneven deformation of the opened part of the plates, leading to additional circumferential opening and thus crack propagation. As a result, both radial and circumferential fiber-bridging developed.

Two different face-sheet configurations were selected for the investigation of 2D debonding of the GFRP/balsa sandwich panels: a pure woven layup and a combination of woven plies and CFM layers. Although different stiffnesses existed depending on the propagation direction, a concentric crack propagation (from the circular pre-crack) occurred for both the investigated sandwich panel configurations. This was directly related to the outer boundary conditions which, unlike those in the laminated plates whose edges were completely free, did not allow any relative vertical movement of the edges of the face sheet (i.e. the face sheet was anchored to the lateral sides of the panels).

Comparing the quasi-static results obtained for the two investigated configurations, the fracture resistance was enhanced by introducing plies prone to fiber-bridging development (i.e. CFM plies) at the face sheet/core interface, improving the load-bearing performance and achieving significant crack arrest. However, under fatigue loading conditions, the fracture efficiency effect of including these plies was highly dependent of the  $R$ -ratio. Due to the high fatigue amplitude associated with low  $R$ -ratios, complete fiber-bridging crushing occurred under  $R=0.1$  while increasing  $R$ -ratios improved the fatigue performance as a result of a reduction in fiber-bridging crushing.

#### **7.1.4 Numerically-based method for 2D delamination fracture characterization**

A novel and simple numerically-based method, suitable for determining the mean total SERR involved in the Mode I-dominated 2D in-plane delamination of FRP laminated plates was established and validated. The method is based on the relationship between the slope of the load-displacement curves after full development of the fracture process zone (FPZ) and the total SERR involved in the 2D delamination process observed in previously investigated GFRP laminated plates. The above-mentioned slope corresponds to the overall fracture behavior and thus represents the mean total SERR involved in the 2D delamination, regardless of any local SERR variation along the crack front. The method allows the reduction of experimental and computational efforts.

The mean total SERR value obtained from the established method can be used in any 2D Mode I-dominated delamination damage-tolerant design where an estimation of the fracture load level is desired. In cases where an accurate prediction of crack propagation patterns is required or a shear fracture mode contribution would occur, the method would not be applicable.



## 7.2 Original contributions

The original contributions of this thesis with regard to existing knowledge on this research topic are the following:

1. New experimental designs and set-ups, suitable for the investigation of both 2D delamination and 2D debonding in FRP laminates and sandwich panels, have been developed. The designs were able to capture the relevant 2D effects that do not occur in 1D fracture experiments.
2. The quasi-static 2D in-plane delamination behavior in FRP laminates with embedded defects subjected to out-of-plane tensile loads has been experimentally and numerically investigated, providing a more realistic fracture approach compared to that of traditional fracture characterization methods.
3. The differences between 1D and 2D delamination behavior (i.e. 2D effects) have been identified based on the experimental and numerical results and their influence on the delamination fracture performance has been ascertained. The conclusions addressing the role of the 2D effects on the fracture mechanisms are highly relevant for achieving more efficient damage-tolerant designs.
4. A new numerically-based method able to 1) determine the mean total SERR driving Mode I-dominated 2D delamination in any FRP laminated structural member and 2) estimate the corresponding fracture load level was developed and validated. The proposed method is the only existing method addressing the 2D delamination fracture problem in an affordable way (i.e. without excessive experimental and numerical efforts).
5. The quasi-static and fatigue 2D in-plane debonding behavior in GFRP/balsa sandwich panels with embedded disbonds subjected to out-of-plane tensile loads has been experimentally investigated also providing a more realistic fracture approach.
6. Quasi-static debonding experiments permitted the identification of new 2D effects in addition to those already identified in the 2D delamination investigation. Based on the experimental results, the influence of the new 2D effects on quasi-static and fatigue debonding fracture performance was also addressed.
7. The influence of the inclusion of plies prone to develop fiber-bridging at the face sheet/core interface in FRP sandwich panels on the quasi-static and fatigue 2D debonding fracture performance was investigated and discussed. The results obtained are of significance for tailoring FRP sandwich face sheet/core interfaces that provide an improved debonding damage performance.

### 7.3 Recommendations for future work

Research topics offering prospects for further development of the present work are as follows.

#### 7.3.1 Quasi-static 2D crack growth under shear-dominated fracture modes

The present research has focused on the investigation of 2D crack growth under out-of-plane tensile loads which led to opening fracture modes in the investigated GFRP laminated plates and to both opening and shear fracture modes in the investigated GFRP/balsa sandwich panels. The shear modes in the latter were activated mainly due to the in-plane stretching strains that developed in the face sheet and not in the core (i.e. due to a 2D effect) and not as a result of the type of loading.

Considering that defects in real structures may grow under a combination of both opening and shear fracture modes as a result of different types of loading [1], the investigation of 2D delamination and debonding behavior under mixed-mode conditions (i.e. both shear and opening fracture modes) is essential for the continuation of the present line of research. In order to characterize 2D crack propagation behavior under mixed-mode, it is necessary to investigate it first under pure shear fracture modes and identify any additional 2D effects. The development of suitable new experimental set-ups (e.g. bending of laminated plates also presenting a circular pre-crack at the midplane) would be required along with numerical work to achieve 2D shear fracture characterization.

#### 7.3.2 Further validation of developed numerically-based method

The numerically-based method developed within the framework of this thesis to determine the mean total SERR involved in 2D delamination cases (Chapter 4) was validated for three different glass fiber architectures. Considering that the application of the method is valid for any Mode I-dominated delamination case under opening loads, additional experiments similar to those performed for laminated GFRP plates (Chapter 2) but varying the material (e.g. carbon fiber reinforcements), pre-crack shape (e.g. elliptical or irregular shapes) or boundary conditions (e.g. fixed contour), would provide valuable results for further validation of the method.

Furthermore, the mean total SERR value provided by application of the method can be used to predict the fracture load level in any other Mode I-dominated delamination occurring under any other type of loading. For instance, the buckling of the laminate above an interlaminar defect located at the midplane of a laminated structural member subjected to compression loads would lead to the propagation of the defect under Mode-I dominated conditions [2]. Conducting an experiment recreating such a scenario would provide a compression load-opening displacement response that could be subsequently compared with that obtained from an FE model. The numerical simulation would be performed by implementing the mean total SERR value obtained from the method in all propagation directions. A correct estimation of the experimental load level would provide a strong validation of the method.

### 7.3.3 Numerical investigation of 2D delamination considering local variation of total SERR

The in-plane delamination pattern of a 2D embedded crack, growing under Mode-I dominated fracture conditions in a FRP laminate, is determined by the initial shape of the defect and the stiffness in each propagation direction, which depends for instance on the laminate's fiber architecture and the boundary conditions (Chapter 4). The effect of the stiffness variation on the propagation pattern and fiber-bridging development was also discussed in Chapter 4 based on the crack pattern observed in the W50.50 plates. It was concluded that as a result of the uneven deformation of the opened part of the plates, additional circumferential opening and thus delamination occurred leading to both radial and circumferential fiber-bridging development. Therefore different degrees of fiber-bridging would occur along the crack front and different total SERR values would drive the delamination depending on the propagation direction.

In order to investigate the variation of fiber-bridging development along the crack front and thus the local variation of total SERR, an advanced numerical model considering different cohesive formulations along the different propagation directions should be developed. The results would provide a better understanding of Mode-I dominated delamination fracture behavior with complex fiber-bridging development. This numerical investigation could be performed based on the experimental and numerical results obtained from the W50.50 and W60.40 laminated plates.

### 7.3.4 Numerical investigation of quasi-static and fatigue 2D debonding in GFRP/balsa sandwich panels

The 2D debonding in GFRP/balsa sandwich panels was experimentally investigated under quasi-static and fatigue loading conditions (Chapters 5 and 6 respectively). As for the laminated plates, due to the 2D effects associated with the propagation of 2D embedded cracks under opening loads, traditional data reduction methods are not suitable for deriving the SERR involved in the fracture process. Thus, the numerical investigation of 2D debonding in the sandwich panels presented in this research is required to characterize the quasi-static and fatigue debonding behavior (e.g. fatigue crack growth curves).

The stretching-induced mode-mixity (2D effect) caused the nucleation of new crack surfaces and crack migration (Chapter 5). Thus, complex numerical models with different fracture interfaces and capable of simulating the corresponding migrations [3] have to be developed.

Furthermore, in order to compare the 2D debonding results to those from 1D fracture specimens, the level of mode-mixity at the 2D crack (determined from the developed FE models) should be adequately reproduced in 1D experiments using, for instance, double cantilever beam specimens loaded by uneven bending moments (DCB-UBM) or mixed-mode bending (MMB) specimens.

### 7.3.5 Investigation of fatigue 2D debonding under displacement control

The experimental program defined for the investigation of the 2D fatigue debonding behavior of GFRP/balsa sandwich panels (Chapter 6) was conducted exclusively under load control fatigue conditions. The experimental results showed a stable fatigue crack growth under load control as a result of the increasing loads required to maintain the propagation of a 2D crack whose crack front length continuously increases. Although stable propagation of the crack would also be achieved under displacement control, the propagated crack area is expected to be considerably lower than under load control.

Thus, conducting a new experimental fatigue program under displacement control on sandwich panels with the same configuration as those of the sandwich panels investigated under load control in this thesis (Chapter 6) would provide valuable data to determine whether load control fatigue experiments would be preferable for 2D crack propagation investigations.

### 7.3.6 Investigation of fatigue 2D debonding in sandwich panels with pure woven face sheet configuration under different $R$ -ratios

The experimental investigation of the SPB sandwich panel configuration (i.e. with a layup combining woven and continuous filament mat layers, see Chapter 6) was performed under different  $R$ -ratios and results showed a strong dependency between the selected  $R$ -ratio and fiber-bridging crushing (lower for higher  $R$ -ratios). However, only one  $R$ -ratio ( $R=0.1$ ) was considered for the investigation of the SPA configuration panels (i.e. with a pure woven ply layup face sheet, see Chapter 6). The fatigue investigation of the SPA configuration under the same additional  $R$ -ratios as those investigated for the SPB configuration (i.e.  $R=0.3$  and  $0.5$ ) would provide supplementary information to analyze the benefits of including plies prone to develop fiber-bridging at the face sheet/core interface in the debonding damage performance of sandwich panels. The conclusions would thus complement those derived from the quasi-static sandwich panel experiments (Chapter 5).

### 7.3.7 Establishment of fracture energy correction factors to include 2D effects

Based on the experimental and numerical delamination and debonding results presented and discussed in this thesis, three main different 2D effects, not present in 1D fracture experiments, have been identified: 1) increase in flexural stiffness (from beam to plate/panel); 2) stress stiffening caused by stretching of the opened part of the laminates and face sheets of the sandwiches and 3) stretching-induced mode-mixity (exclusive to sandwich panels). The first two 2D effects lead to an increase in fiber-bridging while the last can trigger, for instance, crack migration or nucleation of new crack surfaces. Any additional fiber-bridging activated due to any crack propagation behavior triggered by the stretching-induced mode-mixity is also magnified by the other 2D effects.

Experimental approaches involving 1D beam-like experiments have been widely used and standardized [4] for the characterization of FRP material fracture behavior

thanks to their simplicity and rapid execution. However, as shown in the present research and elsewhere [5], the fracture properties obtained from simple 1D fracture experiments may not be representative, particularly in large fiber-bridging scenarios, for damage-tolerant structural design.

In view of the complexity involved in performing more elaborate experiments (such as those developed in the framework of this thesis), an investigation oriented to the establishment of correction factors able to take into account the influence of the identified 2D effects on delamination and debonding fracture behavior would be extremely valuable. The correction factors could be applied to the fracture properties obtained from simple 1D beam-like experiments (e.g. double cantilever beam (DCB) for laminates and single cantilever beam (SCB) for sandwich panels) so that the resulting values would coincide with those derived from the 2D investigations. To accomplish this, the individual contribution of each 2D effect should be quantified and isolated, certainly requiring an exhaustive numerical investigation.

## References

1. Sridharan, S (ed). Delamination behavior of composites. 1<sup>st</sup> ed., Woodhead Publishing and CRC Press; 2018.
2. Nilsson, K.F., Asp, L.E., Alpman, J.E., Nystedt, L. Delamination buckling and growth for delaminations at different depths in a slender composite panel. *Int. J. of Solids and Struct.*, 2001; 38: 3039-3071.
3. Tay, T.E., Sun, X.S., Tan, V.B.C. Recent efforts toward modeling interactions of matrix cracks and delamination: an integrated XFEM-CE approach. *Advanced Comp. Mat.*, 2014; 23(5-6): 391-408.
4. ASTM 5828-13: Standard test method for mode I interlaminar fracture toughness for unidirectional fiber-reinforced polymer matrix composites, in *Annual book of ASTM standard: adhesive section 15.03*.
5. Pappas, G., Botsis, J. Intralaminar fracture of unidirectional carbon/epoxy composite: experimental results and numerical analysis. *Inter. J. Solids Struct.*, 2016; (85-86): 355-66.



# Appendices

**Appendix A | Vacuum infusion procedure for GFRP laminated plates**

**Appendix B | GFRP laminated plate experiments**

**Appendix C | Effect of stiffness variation on fiber-bridging development**

**Appendix D | Vacuum infusion procedure for GFRP/balsa sandwich panels**

**Appendix E | Quasi-static sandwich experiments**

**Appendix F | Fatigue sandwich experiments**





# Appendix A

## Vacuum infusion procedure for GFRP laminated plates

### A.1 Introduction

A detailed description of the vacuum infusion procedure followed during the fabrication of the glass fiber-reinforced polymer (GFRP) laminated plates (described in Chapter 2) is presented in this appendix. The equipment and material employed to perform the vacuum infusion process is also described.

The same general infusion method was used for all the laminated plates although small modifications were made depending on the resin-impregnation capacity of each type of reinforcement. A similar procedure was also applied in the fabrication of the laminates from which the DCB specimens (described in Chapter 3) were cut. All fabrications were carried out by the author at the EPFL Civil Engineering Institute (IIC) facilities.

### A.2 Vacuum infusion procedure

A schematic diagram of the vacuum infusion set-up used is shown in Figure A.1. This diagram is supplemented by a sequence of photos illustrating the actual infusion set-up (see Figure A.2). A list of the different steps adopted during the fabrication process is presented. The material and equipment described in the following is duly indicated in both figures.

1. *Preparation of the infusion substrate:* a polypropylene plate was selected as infusion substrate due to its epoxy-releasing properties. However, in order to assure the correct demolding of the laminate after infusion, three additional layers of release agent were applied.

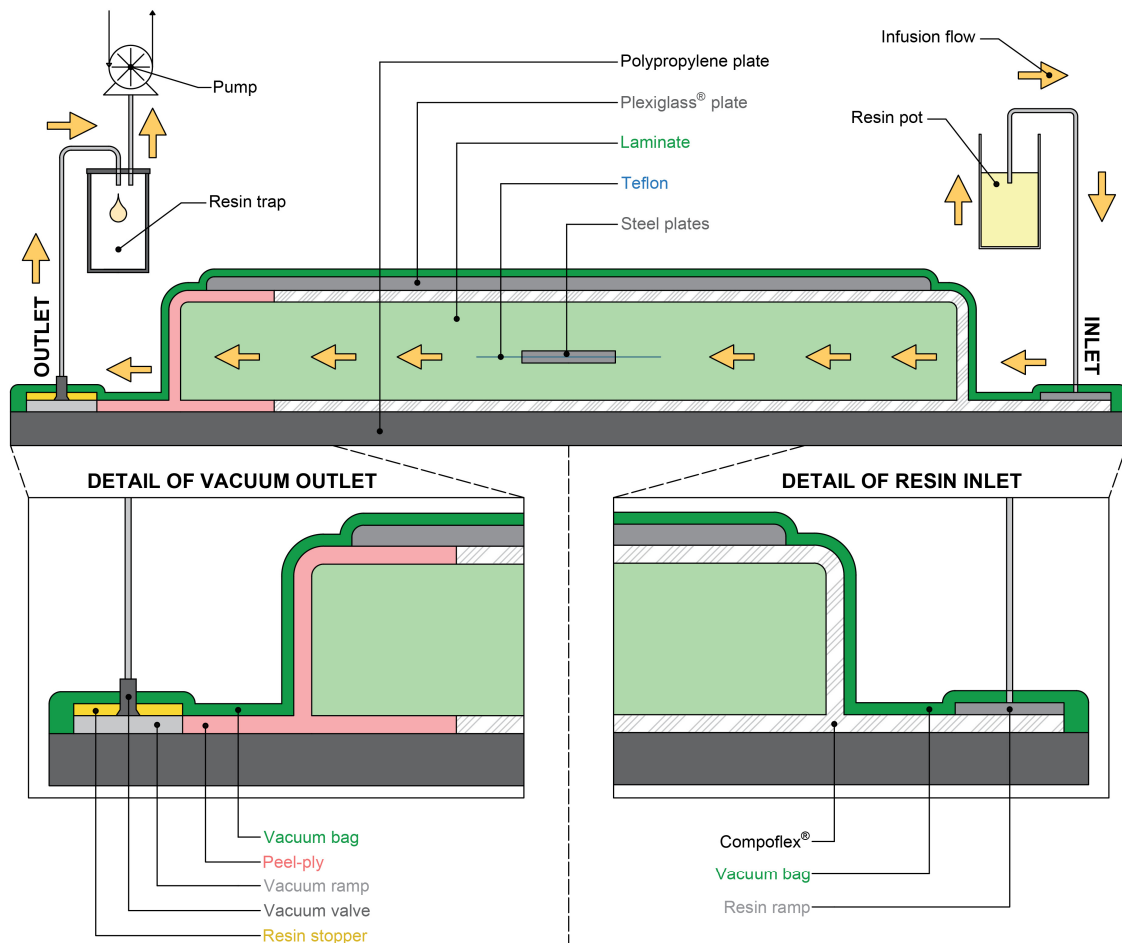


Figure A.1 – Vacuum infusion set-up for GFRP laminated plates (not to scale)

2. *Placement of the reinforcement layers up to the midplane:* the glass fiber-reinforcement layers were placed over the substrate and the borders fixed with tape.
3. *Placement of the steel inserts and Teflon film:* the steel inserts were placed at the center of the reinforcement layers and between them the Teflon film to introduce the pre-crack. In the case of the laminates for the DCB specimens, only the Teflon film was inserted in different locations depending on the selected cutting layout.
4. *Placement of the remaining reinforcement layers:* the remaining glass fiber-reinforcement layers (i.e. from the midplane to the top) were placed and also fixed with tape.
5. *Placement of Compoflex®:* an all-in-one peel-ply and flow-media mesh layer (Compoflex®) was placed over the reinforcement layers. Approximately the last five centimeters of reinforcement (in the infusion flow direction) towards the vacuum outlet should not be covered by this layer to avoid excessive suction of the resin when the infusion is complete. Likewise, the layer has to be of sufficient size for it to connect with the resin inlet location (see Figure A.1). The borders

were also fixed with tape. If the glass reinforcement presented a low resin-impregnation capacity (e.g. the multidirectional or woven reinforcements, see Chapter 2), an additional layer of Compoflex<sup>®</sup>, following the same protocol, was placed below the reinforcement. In the case of reinforcements with a high resin-impregnation capacity (i.e. continuous filament mat, see Chapter 2), the Compoflex<sup>®</sup> layer was only required to cover the reinforcement layers for the first 2-3 cm (in the infusion flow direction).

6. *Placement of a Plexiglass<sup>®</sup> plate:* a Plexiglass<sup>®</sup> plate was placed over the Compoflex<sup>®</sup> layer to assure a flat final surface. In the case of continuous filament mat (CFM) plates, the Plexiglass<sup>®</sup> plate was placed directly over the reinforcement layer. Irrespective of the type of reinforcement, three layers of release agent were applied to the surfaces and edges of the plate.
7. *Preparation of the resin inlet:* the resin inlet consisted of a resin ramp (i.e. an element capable of distributing the incoming resin homogeneously, see material sample in Figure A.3(a)) connected to an exterior plastic tube which was subsequently connected to the resin pot(s). A flat resin ramp formed by a permeable net was used (see Figure A.1 and A.2).
8. *Preparation of the vacuum outlet:* the vacuum outlet consisted of a resin stopper (i.e. a material capable of absorbing and blocking the outgoing resin, see material sample in Figure A.3(b)), a vacuum ramp (element capable of distributing the vacuum suction homogeneously, see material sample in A.3(c)), and a vacuum valve that connected (via a plastic tube) the vacuum ramp to the resin trap

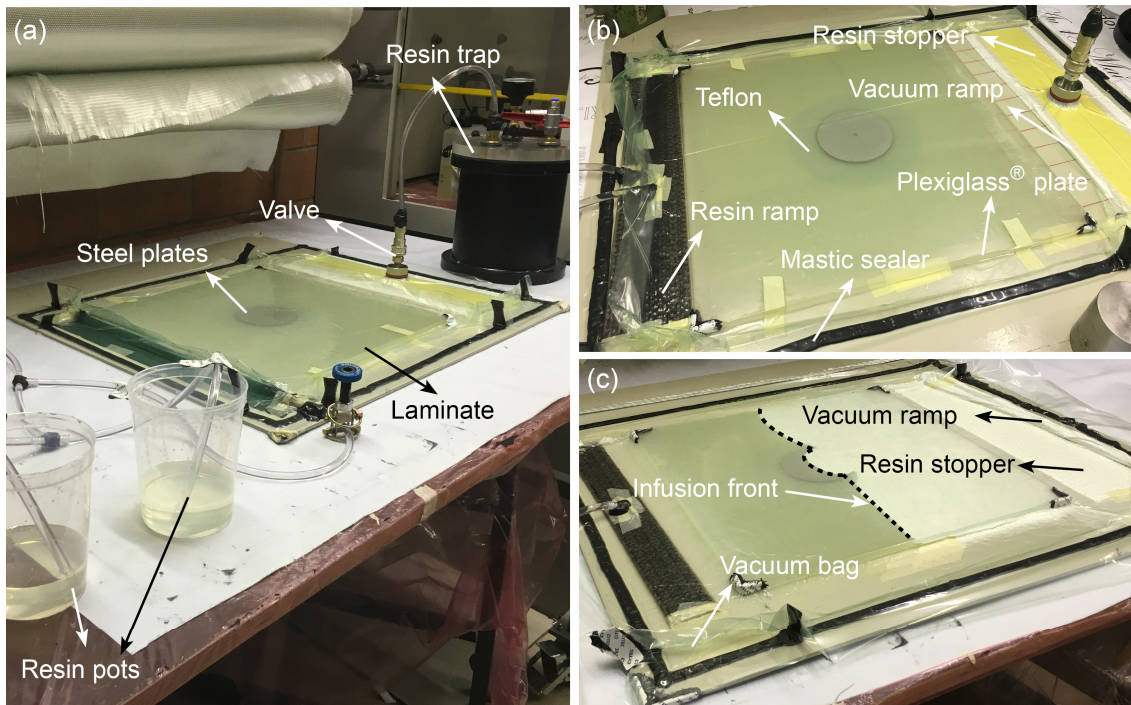


Figure A.2 – Vacuum infusion set-up; (a) general and (b) detailed views of infusion set-up (after resin infusion completion) and (c) detail of infusion front during resin infusion.

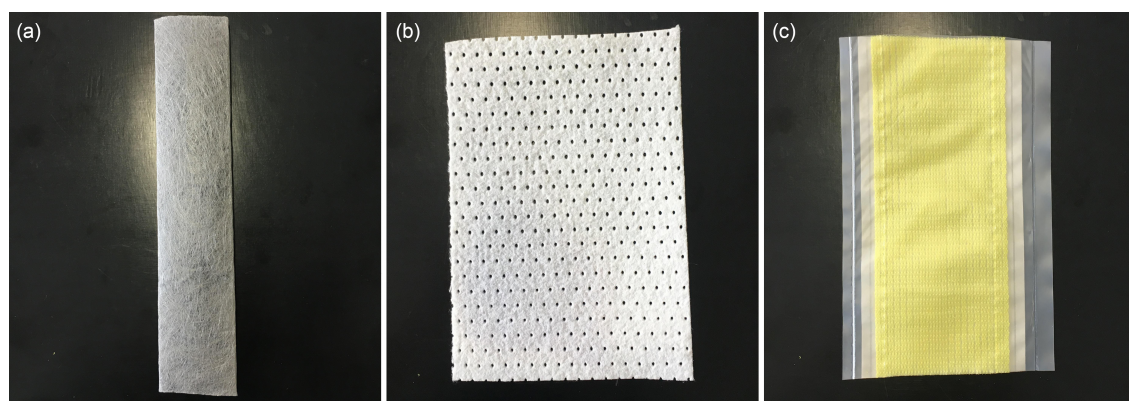


Figure A.3 – Vacuum infusion material samples; (a) resin ramp; (b) resin stopper and (c) vacuum ramp

and ultimately to the pump. The vacuum outlet was connected to the reinforcement layers by a peel-ply fabric (see Figures A.1 and A.2) and placed at least 40 mm from the border of the reinforcement layers to avoid any excessive suction of the resin. In some cases, as can be seen in Figure A.2(c), the vacuum ramp shown in Figure A.3(c) was substituted by a coated tube that performs a similar role.

9. *Placement of the vacuum bag and sealing:* a vacuum bag was placed over all the previously mentioned elements with holes to connect the resin inlet to the resin pot(s) and the vacuum outlet to the resin trap and vacuum ramp. The contours and holes were duly sealed with mastic tape intended for vacuum infusion application (see Figure A.2).
10. *Connection to the resin trap and the vacuum pump:* the plastic tube connected to the vacuum valve in the vacuum outlet was connected to a resin trap (i.e. an intermediate recipient where the potential resin that may pass through the vacuum outlet could be accumulated, thus preventing it from reaching and thus damaging the vacuum pump). A second plastic tube was used to connect the resin trap and the vacuum bag. A resin trap of 5-liter capacity and vacuum pump KNF-035 of 55-liter molding capacity and capable of achieving a 90% final vacuum, were used (see Figure A.1 and Figure A.2(a)).
11. *Starting of vacuum pump:* once everything was in place, the pump was turned on and the absence of air leaks verified. The tube of the resin inlet (not yet connected to the resin pot(s)) was clamped to close the system. The absence of air leaks was verified with a vacuum leak detector equipped with cable and headphones. A loud “beep” was heard if a leak existed.
12. *Resin and hardener blending and degassing:* the epoxy resin and hardener were mixed. Depending on the laminate, the total amount of resin was divided in two different pots to avoid excessive heating and thus a reduction of the pot life (see Figure A.2(a)). The resin was always degassed inside a vacuum bell (c.a. 940 mbar) to remove trapped air.

13. *Connection to the resin pot and infusion initiation:* the pot(s) were placed close to the resin inlet and the plastic tube(s) placed inside them. The clamp(s) blocking the resin inlet was opened and the infusion started. The speed of the incoming resin was regulated by adjusting the degree of the clamp opening.
14. *Monitoring of the infusion process:* a uniform resin infusion front (see Figure A.2(b)) was assured throughout the infusion process. The temperature of the resin in the pot(s) was constantly measured with an appropriate thermometer and when it reached ca 42°C (i.e. the level of hardening impeded the resin flow) the tube(s) was/were clamped again. The laminates were left under vacuum at room temperature for at least 16 hours.
15. *Demolding and post-curing:* when the laminate had hardened (after the 16 hours at room temperature) the vacuum bag and different infusion materials were removed. The resulting laminate was post-cured at 70°C for eight hours.

After post-curing, the laminated plates were prepared to assemble the loading system as described in detail in Chapter 2.





# Appendix B

## GFRP laminated plate experiments

### B.1 Introduction

Appendix B presents supplementary data and results from experiments conducted on the GFRP laminated plates described in Chapter 2.

The experimental program was conducted on a total of twelve GFRP laminated plates using six different types of glass-fiber reinforcements (i.e. four types of woven fabrics with different proportions of reinforcement in the warp/weft directions (W), a long continuous strand mat (CFM) and a multidirectional quadriaxial fabric (MD). Two laminated plates for each type of reinforcement were fabricated and experimentally investigated.

A digital image correlation system (DIC) was one of the crack measuring systems used to monitor the crack front, particularly along the east “E” direction. The changes from straight to curved in the out-of-plane deflection profiles (extracted from the 3D DIC analysis) were assumed as being the crack tip.

A selection of recorded DIC images showing the evolution of the crack front are presented for each laminated plate in Section B.2. Likewise, the out-of-plane deflection profiles and location of the crack tips are shown in Section B.3 for all the laminated plates except W80.20 and MD plates due to their respective lack of propagation before failure and irregular and unstable crack propagation (including crack migration).

## B.2 Crack front evolution

### CFM plates

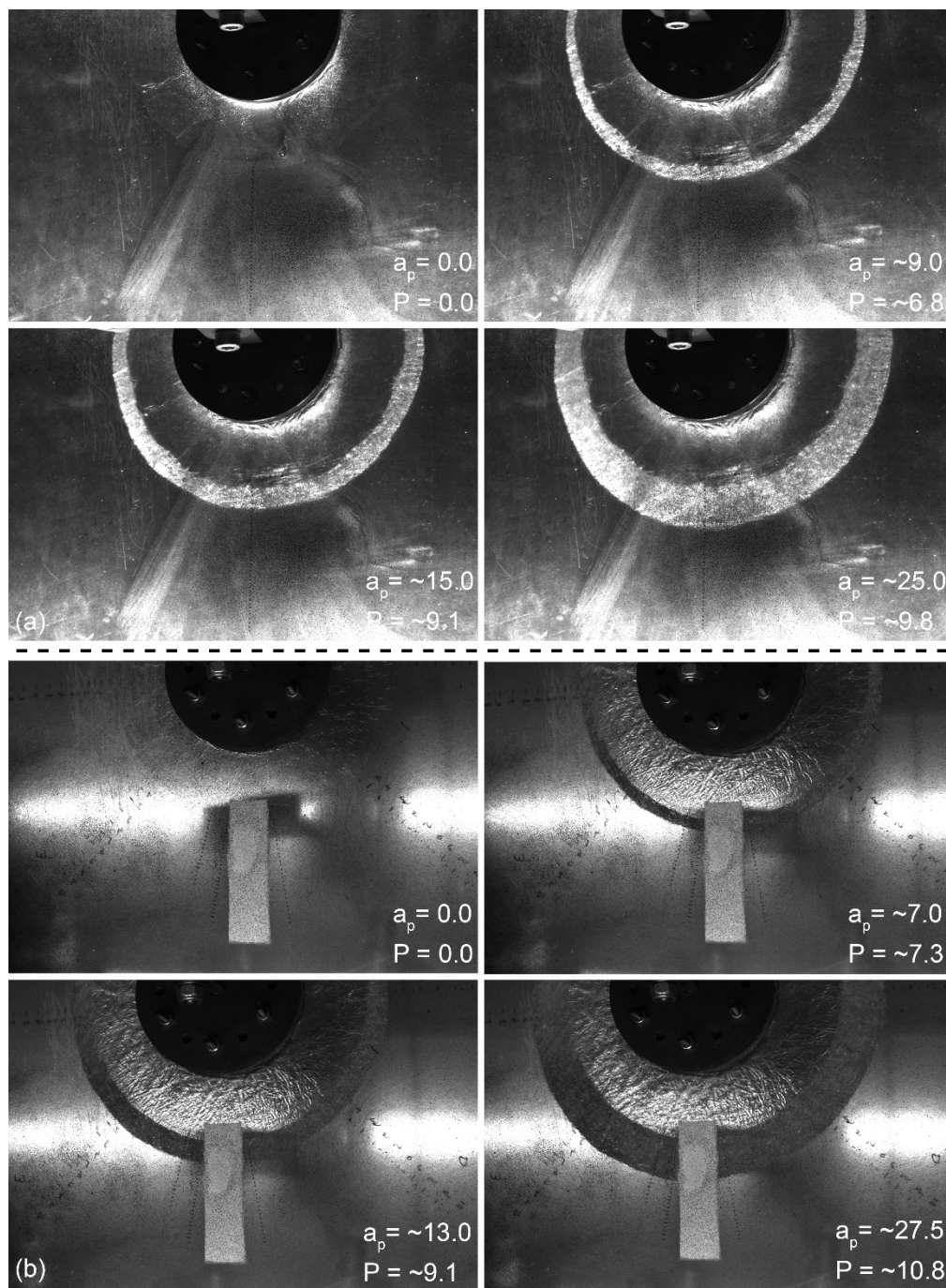


Figure B.1 – Sequence of crack fronts and load in (a) CFM.1 and (b) CFM.2 panels ( $a_p$  is total propagated radial crack length and  $P$  is corresponding load). Units in mm and kN

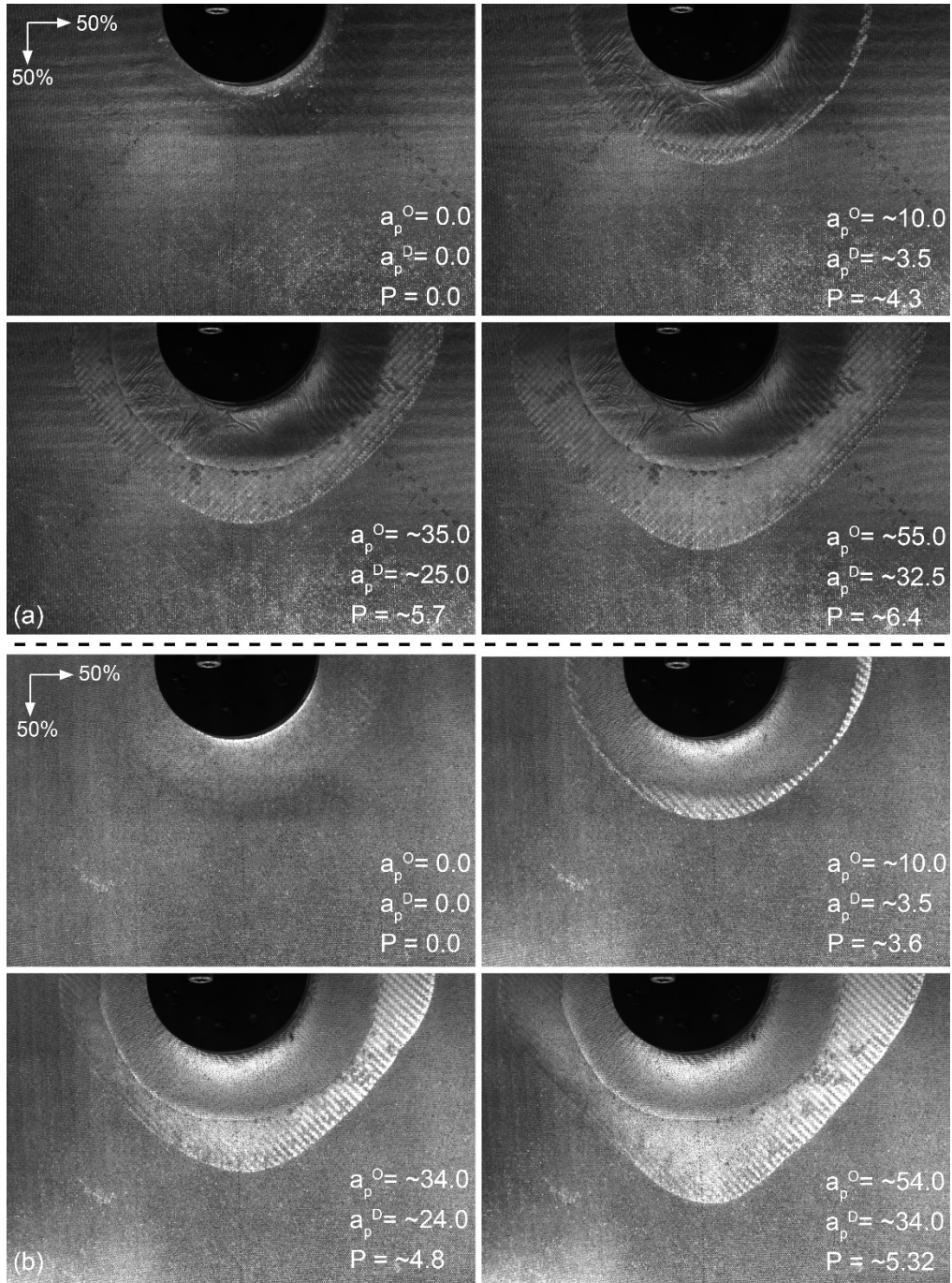
**W50.50 plates**

Figure B.2 – Sequence of crack fronts and load in (a) W50.50.1 and (b) W50.50.2 panels ( $a_p^O$  and  $a_p^D$  are total propagated radial crack lengths in orthogonal and diagonal directions respectively) and  $P$  is corresponding load). Units in mm and kN

### W60.40 plates

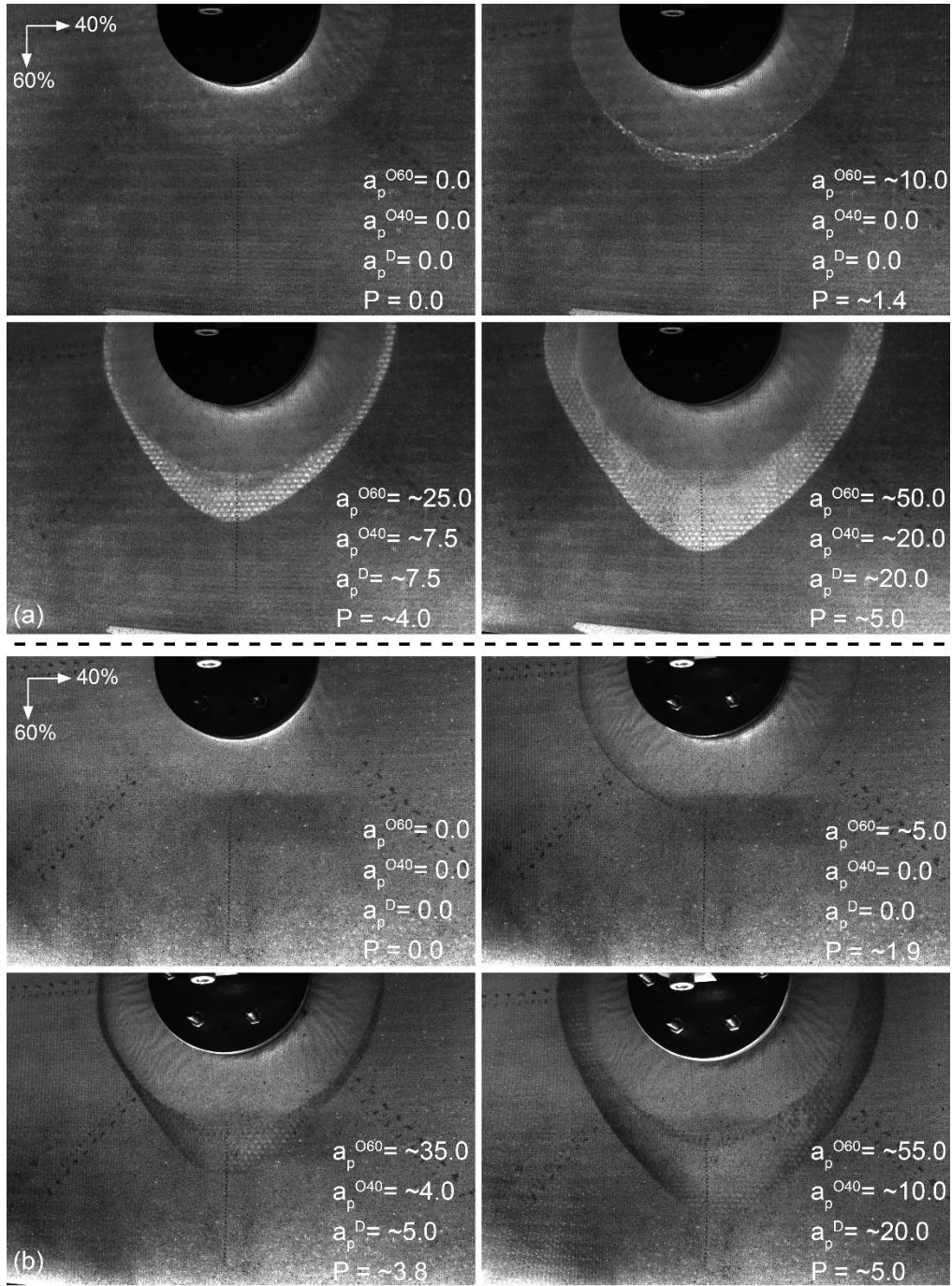


Figure B.3 – Sequence of crack fronts and load in (a) W60.40.1 and (b) W60.40.2 panels ( $a_p^{O60}$ ,  $a_p^{O40}$  and  $a_p^D$  are total propagated radial crack lengths in orthogonal (in 60 and 40 directions of reinforcements) and diagonal directions respectively) and  $P$  is corresponding load). Units in mm and kN

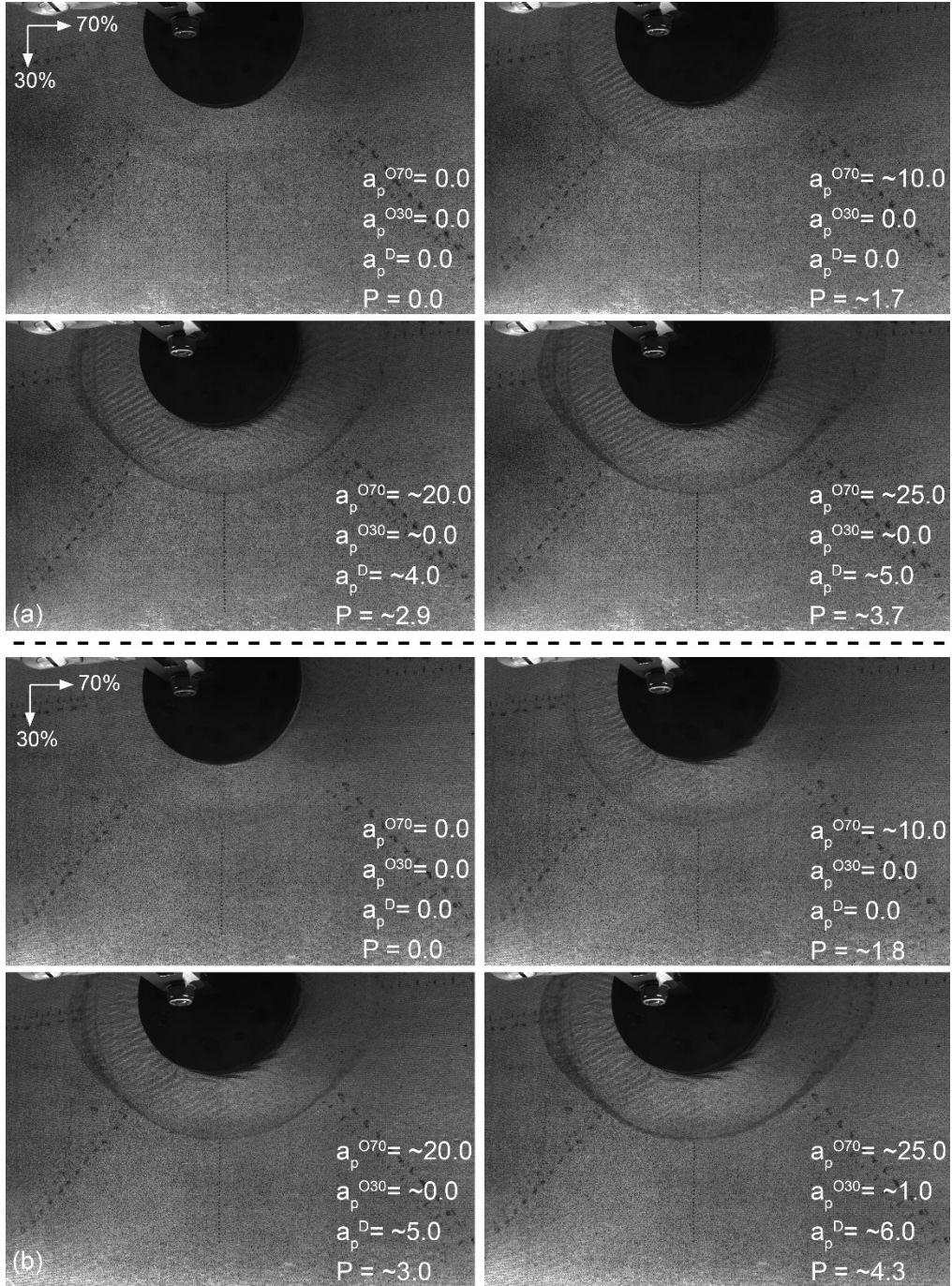
**W70.30 plates**

Figure B.4 – Sequence of crack fronts and load in (a) W70.30.1 and (b) W70.30.2 panels ( $a_p^{O70}$ ,  $a_p^{O30}$  and  $a_p^D$  are total propagated radial crack lengths in orthogonal (in 70 and 30 directions of reinforcements) and diagonal directions respectively) and  $P$  is corresponding load). Units in mm and kN



### W80.20 and MD plates

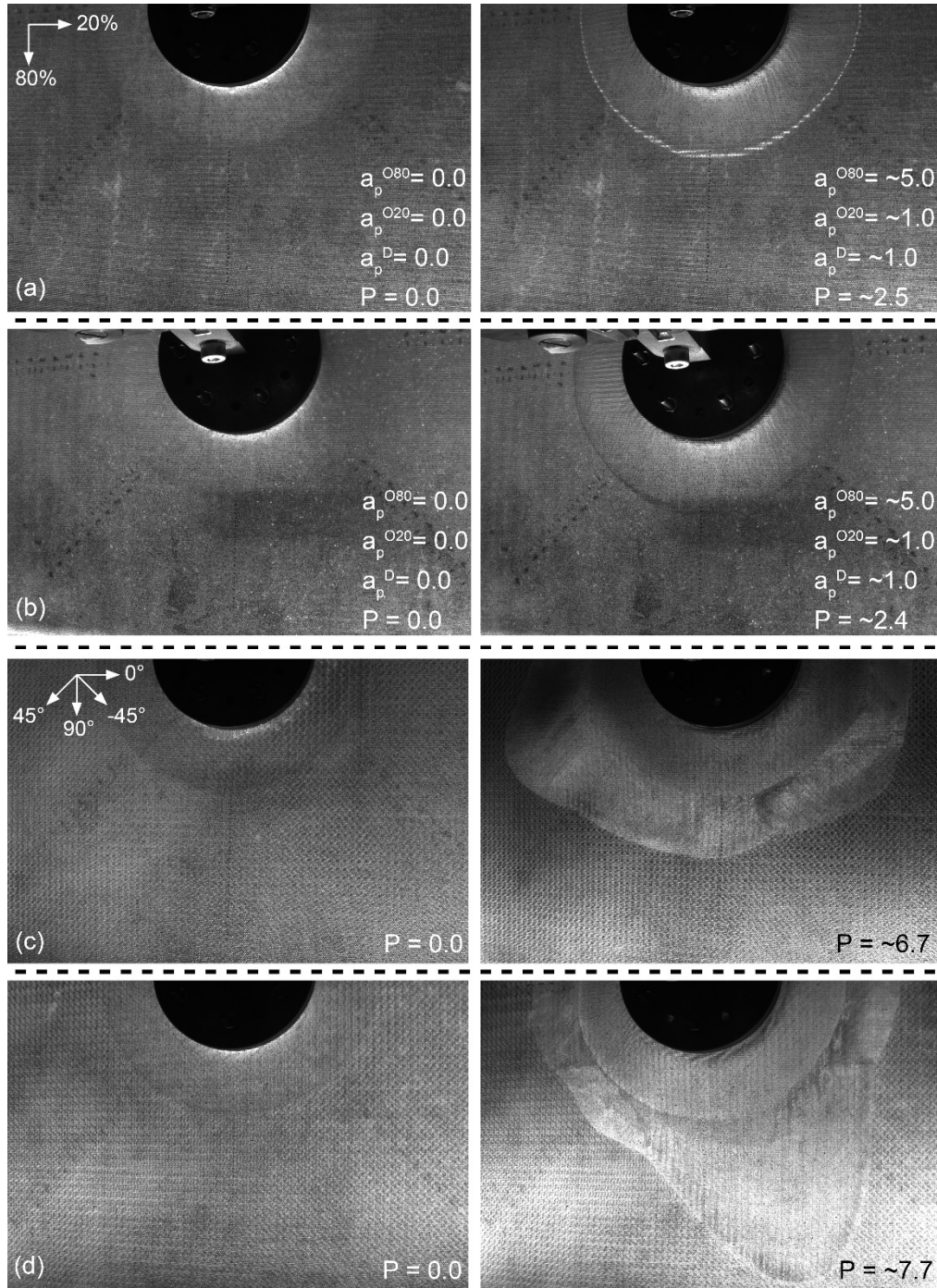


Figure B.5—Sequence of crack fronts and load in (a) W80.20.1, (b) W80.20.2, (c) MD.1 and (D) MD.2 panels ( $a_p^{080}$ ,  $a_p^{020}$  and  $a_p^D$  are total propagated radial crack lengths in orthogonal (in 60 and 40 directions of reinforcements) and diagonal directions respectively) and  $P$  is corresponding load). Units in mm and kN

### B.3 Out-of-plane deflection profiles

#### CFM plates

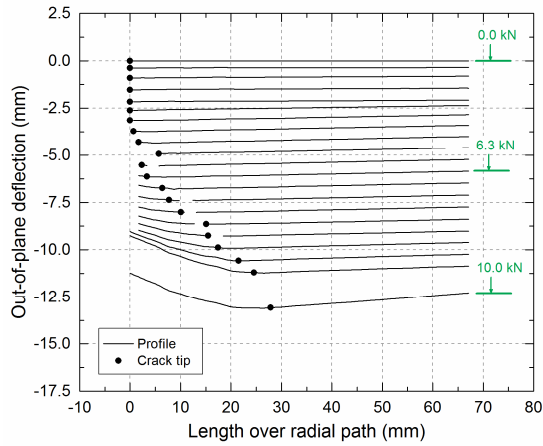


Figure B.6 – Evolution of out-of-plane deflection profiles and location of crack tip, CFM.1 plate

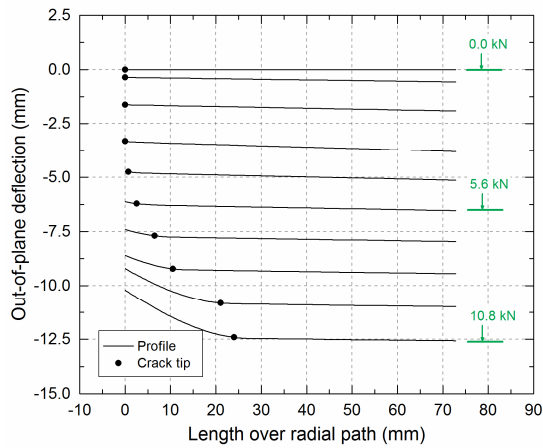


Figure B.7 – Evolution of out-of-plane deflection profiles and location of crack tip, CFM.2 plate



W50.50 plates

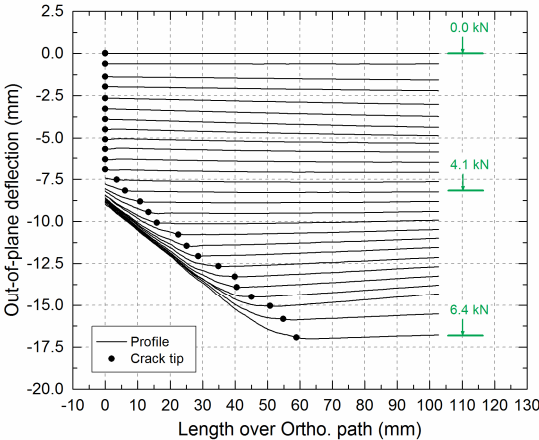


Figure B.8 – Evolution of out-of-plane deflection profiles and location of crack tip, W50.50.1 plate

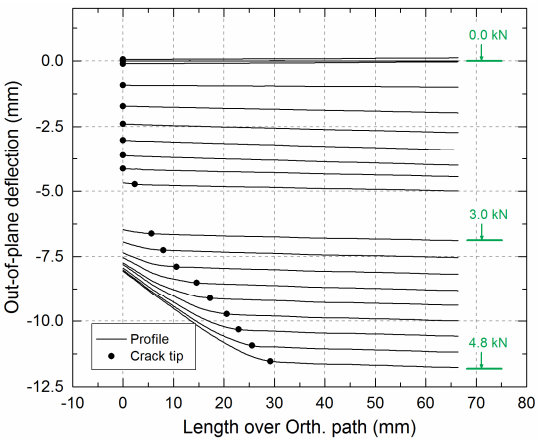


Figure B.9 – Evolution of out-of-plane deflection profiles and location of crack tip, W50.50.2 plate

### W60.40 plates

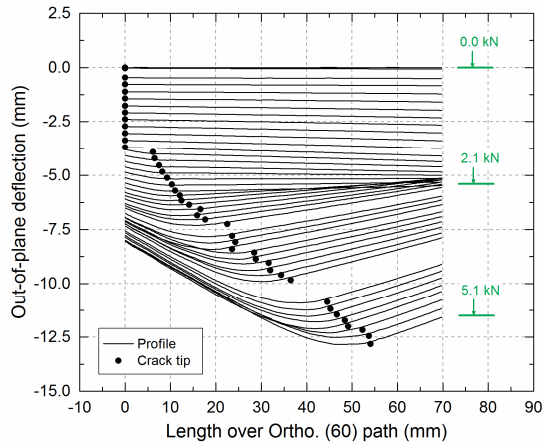


Figure B.10 – Evolution of out-of-plane deflection profiles and location of the crack tip, W60.40.1 plate

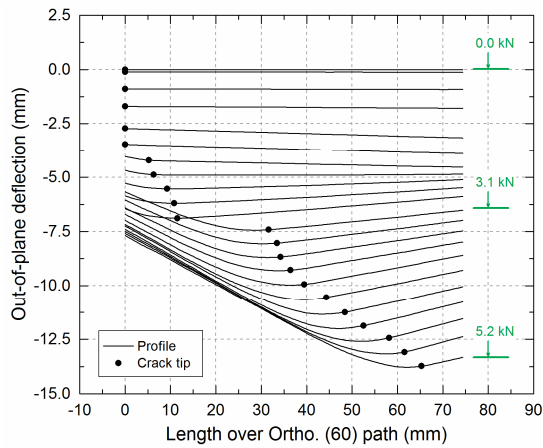


Figure B.11 – Evolution of out-of-plane deflection profiles and location of the crack tip, W60.40.2 plate (the observed jump at c.a. 7.5 mm of out-of-plane deflection corresponded to a jump in crack propagation, see also Figure 2.8)

W70.30 plates

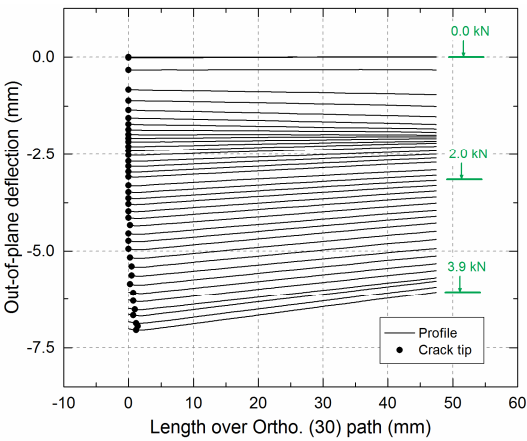


Figure B.12 – Evolution of out-of-plane deflection profiles and location of the crack tip, W70.30.1 plate

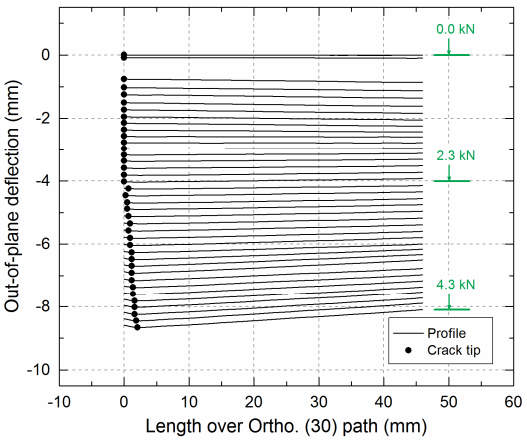


Figure B.13 – Evolution of out-of-plane deflection profiles and location of the crack tip, W70.30.2 plate

## Appendix C

# Effect of stiffness variation on fiber-bridging development

### C.1 Introduction

The propagation pattern of a 2D embedded crack growing under opening fracture mode in a composite laminate depends on the stiffness in each propagation direction, which may vary along the crack front as a result of, for instance, the laminate's fiber architecture or the boundary conditions. Particularly in cases where all the propagation directions have the same stiffness (e.g. the in-plane isotropic CFM plates investigated in this thesis), every point of the crack front would propagate similarly (i.e. a concentric crack propagation in CFM plates). However, in cases where different stiffnesses exist depending on the propagation direction (e.g. the woven (W) plates also investigated in this thesis), the crack would also propagate differently in each direction. The effect of this stiffness variation on the propagation pattern and thus on fiber-bridging development were presented and discussed in Chapter 4. Based on the crack pattern observed in W50.50 plates (i.e. the crack propagated more along the orthogonal directions (the stiffest) than along the diagonal directions (the least stiff)) and the consequent uneven deformation of the opened part of the plate, it was concluded that, due to the additional circumferential opening and thus crack propagation caused by the latter, the fiber-bridging developed both radially and circumferentially (see Figure 4.8 and 4.17). Therefore, a greater degree of fiber-bridging would correspond to higher total strain energy release rate (SERR) values.

By applying the numerically based method presented in Chapter 4, the  $\bar{G}_{tot}$  value driving the delamination in W50.50 plates was derived. The numerical load-displacement response using the obtained  $\bar{G}_{tot}$  in all directions was likewise discussed

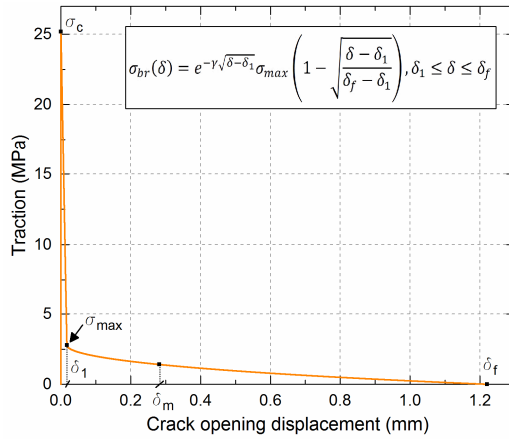


Figure C.1 – Optimized traction-separation law

in Chapter 4 showing fairly good agreement with the experimental results after the transition point (TP). As also indicated in Chapter 4, if a more accurate prediction of the load-displacement response before the TP and of the crack propagation pattern is required, a further optimization of the traction-separation law is required.

In this appendix a first optimization of the traction-separation law in W50.50 plates is presented and the corresponding numerically obtained fracture responses are discussed. The same finite element (FE) model as that developed for W50.50 plates in the investigation presented in Chapter 4 was used in this study. The same traction-separation law was used in all directions (i.e. without considering different values of the total SERR). The effect of this assumption is discussed and related to the previously mentioned circumferential fiber-bridging development and consequent total SERR variation along the crack front.

## C.2 Cohesive zone modeling

The traction-separation law used in this study is shown in Figure C.1. As can be observed, the same shape as that used in Chapter 3 was also adopted (i.e. a combination of linear and exponential softening) as it was proved to be the most suitable shape in fracture processes involving fiber-bridging development (see Chapter 3 and [1-5]). The first part corresponding to linear softening represented the initial damage growth and the second corresponding to exponential softening to the fiber-bridging development. The equation defining the bridging tractions is shown in Figure C.1. The areas under the first and second parts of the law equal the SERR involved in crack initiation ( $G_{tip}$ ) and fiber-bridging development ( $G_{br}$ ) respectively. The addition of these two SERR values equals the total area under the traction-separation law (i.e.  $G_{tot}=G_{tip} + G_{br}$ ). The formulation of this type of traction-separation law can be found in Chapter 3 and [5] and it was implemented in the finite element (FE) model via a user material subroutine (UMAT) [5, 6]. An iterative process to adjust the values of the traction-separation law was performed so that the numerical load-displacement (also before the TP) and crack

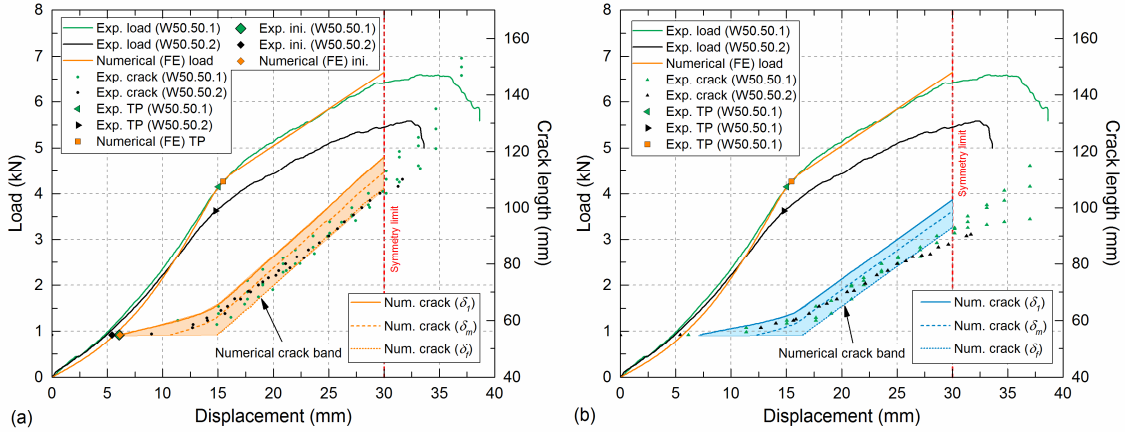


Figure C.2 – Comparison of experimental and numerical load vs opening displacement and total crack length curves in the orthogonal (a) and diagonal (b) directions of W50.50 plates

propagation responses were comparable to the experimental ones, presented in Figure C.2. A description of the adjustment process leading to the cohesive parameters shown in Figure C.1 is given in the following.

The maximum traction for damage initiation was assumed to be 30% of the tensile strength of the matrix (84 MPa, [7]), according to [8], resulting in a value of  $\sigma_c = 25.2$  MPa. The initial stiffness,  $K_0$ , was set to 100,000 MPa/mm [6, 8, 9]. The remaining parameters were iteratively determined considering an area under the curve (i.e.  $G_{tot}$ ) equal to the  $\bar{G}_{tot}$  obtained for the W50.50 plates in Chapter 4 (i.e. 1296.8 J/m<sup>2</sup>).

The area under the first part of the traction-separation law (i.e. between  $\delta=0$  and  $\delta_i$  in Figure C.1) corresponding to the SERR required for crack initiation (i.e.  $G_{tip}$ ) was adjusted so that the numerical initiation of the crack approached the two experimental measurements of crack initiation (see Figure C.2). The numerical initiation was considered as the point where the first cohesive element after the pre-crack reached a crack-opening displacement (COD) equal to  $\delta_i$  (see Figure C.1). Values of  $G_{tip}=240$  J/m<sup>2</sup> and  $\delta_i=0.017$  mm were obtained corresponding to a crack initiating at a load-displacement pair of 1.031 kN-6.113 mm, which was within the range of the experimental results (see Figure C.2). Consecutively, the parameters of the second part of the law were also adjusted by considering  $G_{br}=1056.8$  J/m<sup>2</sup> (i.e.  $G_{br} = \bar{G}_{tot} - G_{tip}$ ) and a value of  $\sigma_{max}$  between 2 and 3 MPa [10]. The values of  $\gamma$  (bridging traction decay ratio, see equation in Figure C.1 and  $\delta_f$  (COD at the end of the bridging zone) were finally fitted to  $\sigma_{max} = 2.79$  MPa,  $\gamma=0.10$  and  $\delta_f=1.22$  mm (see Figure C.1).

### C.3 Numerical results

#### C.3.1 Load-displacement and crack-displacement responses

The experimental and numerical load- and crack-displacement responses obtained using the previously described traction-separation law to model the fracture interface in all propagation directions are presented in Figure C.2. The crack-displacement curves were plotted for the main propagation directions (orthogonal at 0/90°, in Figure C.2(a)

and diagonal at  $\pm 45^\circ$ , in Figure C.2(b)). The numerical simulation was performed with a maximum displacement of 30 mm, this being the value of the experimental limit of symmetric propagation (see Chapter 2 and [11]). Further details regarding the FE model can be found in Chapter 4.

As can be observed, good agreement with the experimental load-displacement curve of W50.50.1 was obtained. As already mentioned in Chapter 4, the overestimation of the load level found for the W50.50.2 plates was attributed to the experimental scatter.

The experimental crack tip values shown in Figure C.2 corresponded to the whitening of the plates observed as the crack advanced. Due to the medium translucency exhibited by the W50.50 plates (see Chapter 2), identification of the visually observed crack tips with the COD corresponding to crack initiation (i.e. the beginning of the bridging zone,  $\text{COD}=\delta_i$ ) cannot be assured (as it was for the CFM plates, see Chapter 3). Therefore, and in order to cover all the ranges of COD during the evolution of the bridging zone (along which the visual measurements of the crack tip could have been taken), numerical crack bands for the orthogonal and diagonal directions are indicated in Figure C.2. The upper and lower boundaries of the band correspond respectively to the beginning ( $\delta_i$ ) and the end ( $\delta_f$ ) of the bridging part in the traction-separation law (see in Figure C.1). An additional curve corresponding to an intermediate COD value ( $\delta_m$ ) was also plotted. It can be observed that the experimental measurements of the crack tip were within the boundaries of the numerical bands.

### C.3.2 Compliance responses

The experimental and numerical crack area vs compliance (calculated as  $\delta/P$ ) curves are shown in Figure C.3. As can be observed, a good agreement with the experimental trend was obtained. As for the crack length vs opening displacement curves in Figure C.2, the numerical compliance band is also plotted. In this case, the upper and lower limits corresponded to CODs equal to  $\delta_f$  and  $\delta_i$  respectively. The intermediate curve corresponding

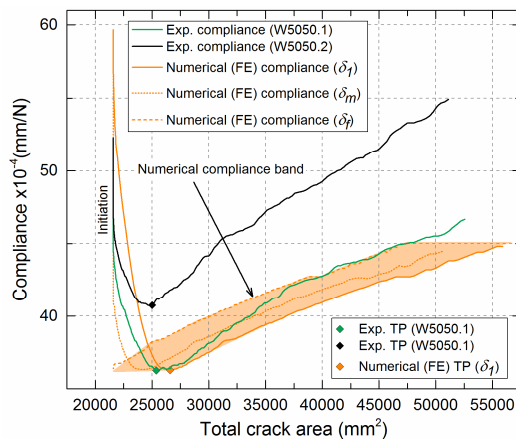


Figure C.3 – Comparison of numerical and experimental compliance vs total crack area curves of W50.50 laminates



to a COD of  $\delta_m$  (see Figure C.1) was also plotted. The numerical transition point (TP) was identified using the lower limit curve (i.e. that corresponding to  $\text{COD} = \delta_l$ ) showing good agreement with the experimental transition points (see Figure C.3). The transition points were likewise identified on the load-displacement curves in Figure C.2.

### C.3.3 R-curves

The numerical R-curves developed in the orthogonal ( $0/90^\circ$ ) and diagonal ( $\pm 45^\circ$ ) directions are shown in Figure C.4. Propagated crack length values (i.e. with the pre-crack length of 55 mm, see Chapter 2) corresponding to the upper limit of the numerical crack bands in both directions (Figure C.2) were used. In the zoom shown in Figure C.4(b), different values of propagated crack length were identified: 1) those corresponding to the full development of the fiber-bridging lengths in both directions, i.e. the initiation of the plateaus and 2) those corresponding to the numerical TP. The total crack area values at each of these points are likewise indicated. The full fiber-bridging length developed after 10.31 mm of crack propagation in the orthogonal directions (corresponding to a total crack area of 25830  $\text{mm}^2$ ) and after 9.72 mm of crack propagation in the diagonal directions (corresponding to a total crack area of 28427  $\text{mm}^2$ ). The total crack area at the numerical TP was 26580  $\text{mm}^2$  (see Figure C.3) and corresponded to 12.0 and 7.4 mm of propagated crack length in the orthogonal and diagonal directions respectively.

## 3. Discussion

One of the conclusions derived from Chapter 3 was that in the in-plane isotropic CFM plates the value of the total crack area at the TP coincided with the fully developed fiber-bridging area. Considering the results presented in the previous section, the same relationship may not be applicable to the W50.50 plates investigated here. The value of the total crack area at the TP was found to be greater than the total crack area at the full

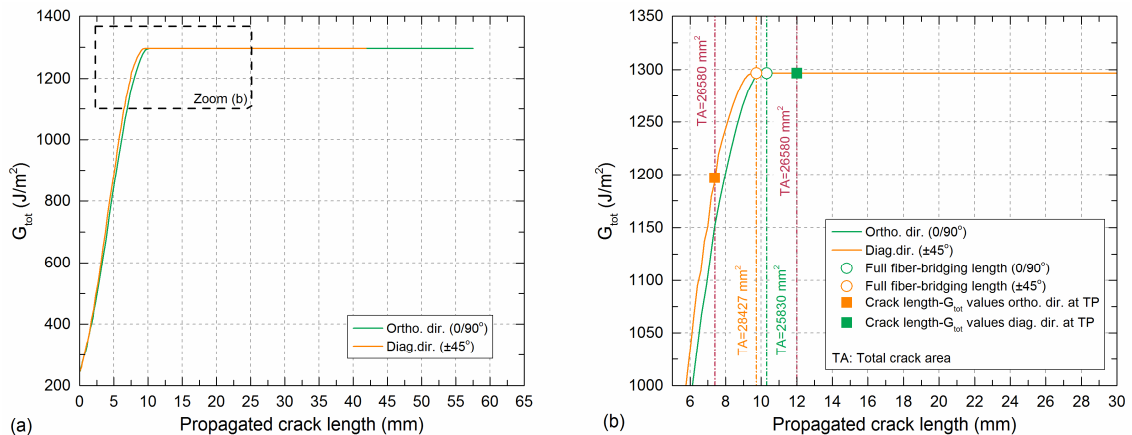


Figure C.4 – (a) Numerical R-curves in orthogonal and diagonal directions; (b) zoom of region indicated in (a)

development of the fiber-bridging length at  $0/90^\circ$  ( $26580 > 25830 \text{ mm}^2$ ) but smaller than that at  $\pm 45^\circ$  ( $26580 < 28427 \text{ mm}^2$ ), meaning that at the TP the full fiber-bridging area had not yet developed in all directions.

As mentioned in the introduction to this appendix and in Chapter 4, the uneven deformation of the opened part of the W50.50 plates caused an additional circumferential opening and propagation of the crack and therefore both radial and circumferential fiber-bridging developed (see Figure 4.8). Considering the observed crack propagation patterns (see Figure 4.3) and the opening profile of the crack (see Figure 4.17), the amount of circumferential fiber-bridging is expected to reach its maximum level in regions close to the orthogonal directions and minimum in the regions close to the diagonal directions. Consequently, the greatest total SERR values would be required towards the orthogonal directions and the smallest values towards the diagonal directions. However, because the total SERR used (in all directions) in this study was the mean total SERR value extracted from the application of the method presented in Chapter 4, the total SERR value was underestimated in the orthogonal directions and overestimated in the diagonal directions. If a total SERR greater than the mean total SERR is implemented in the orthogonal directions, the full development of the fiber-bridging would be delayed and thus occur at a greater total crack area value. Likewise, if a total SERR smaller than the mean total SERR is implemented in the diagonal directions, the full development of the fiber-bridging would be anticipated and thus occur at a smaller total crack area value. As a result, it could be expected that the full development of the fiber-bridging in all directions would coincide with the TP, as was concluded for the CFM plates. This anticipated behavior is presented schematically in Figure C.5. This result would further and numerically prove the existence of circumferential fiber-bridging 2D delamination cases where different stiffnesses apply depending on the propagation direction.

### 3. Conclusions

A first optimization of the traction-separation law defining the cohesive fracture behavior of W50.50 plates has been presented in this appendix and the effects of assuming the same mean total SERR in all directions have been discussed.

As proved in Chapter 4, the use of the mean total SERR (derived by applying the presented method) in all propagation directions sufficed to match the experimental load level. In this case, after optimization of the traction-separation law, the load-displacement curves compared well before and after the transition point (TP).

Based 1) on the correlation found in Chapter 3 for the CFM plates between the full fiber-bridging area and the TP and 2) on the numerical R-curves obtained in this study, it could be inferred that the use of the same mean total SERR underestimated and overestimated the local total SERR in the orthogonal and diagonal direction respectively. However, a more advanced numerical model introducing local variation of the total SERR (and thus of the traction-separation law) is required to prove this

inferred behavior. This would also constitute further proof of the existence of circumferential fiber-bridging in 2D delamination cases where different stiffnesses apply depending on the propagation direction.

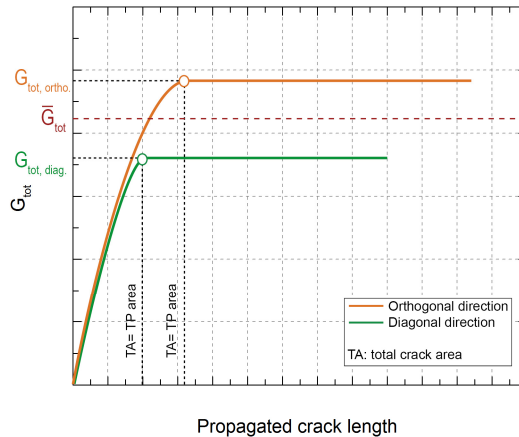


Figure C.5 – Schematic anticipated behavior with varying total SERR along crack front

## References

1. Pappas G, Canal L.P., Botsis J. Characterization of intralaminar mode I fracture of AS4/PPS composites using inverse identification and micromechanics. *Composites: Part A*, 2016; 91; 117-126.
2. Suo Z., Bao G., Fan B. Delamination R-curve phenomena due to damage. *J. Mech. Phys. Solids*, 1992; 40 (1): 1-16.
3. Manshadi B.D., Vassilopoulos A.P., Botsis J. A combined experimental/numerical study of the scaling effects on mode I delamination of GFRP. *Comp. Science and Tech.*, 2013; 83; 32-39.
4. Canal L.P., Alfano M., Botsis J. A multi-scale based cohesive zone model for the analysis of thickness scaling effect in fiber bridging. *Comp. Science and Tech.*, 2017; 139; 90-98.
5. Cameselle-Molares, A., Vassilopoulos, A.P., Renart, J., Turon, A., Keller, T. Numerical simulation of two-dimensional in-plane crack propagation in FRP laminates. *Composite Structures*, 2018; 200: 396-407.
6. Turon A., Camanho P.P., Costa J., Dávila C.G. A damage model for the simulation of delamination in advanced composites under variable-mode loading. *Mechanics of Materials*, 2006; 38(11): 1072–1089.
7. Sika datasheet product. <[https://deu.sika.com/dms/getdocument.get/dd4b783e-bfa5-32e3-a705-f9f548f6b326/Biresin\\_CR83\\_eng.pdf](https://deu.sika.com/dms/getdocument.get/dd4b783e-bfa5-32e3-a705-f9f548f6b326/Biresin_CR83_eng.pdf)> (Accessed 19 October 2017).
8. Camanho P.P., Dávila C.G., Ambur D.R. Numerical simulation of delamination growth in composite materials. NASA/TP-2001-211041. Hampton: NASA Langley Research Center; 2001.
9. Turon A., Camanho P.P., Costa J., Renart J. Accurate simulation of delamination growth under mixed-mode loading using cohesive elements: Definition of interlaminar strengths and elastic stiffness. *Composite Structures*, 2010; 92(8): 1857–1864.
10. Heidari-Rarani M., Shokrieh M.M., Camanho P.P. Finite element modeling of mode I delamination growth in laminated DCB specimens with R-curve effects. *Composites: Part B*; 2013; 45; 897-903.
11. Cameselle-Molares A., Vassilopoulos A.P., Keller T. Experimental investigation of two-dimensional delamination in GFRP laminates. *Eng. Frac. Mech.*, 2018; 203: 152-171.



## Appendix D

# Vacuum infusion procedure for GFRP/balsa sandwich panels

### D.1 Introduction

A detailed description of the vacuum infusion procedure followed during the fabrication of the GFRP/balsa sandwich panels is presented in this appendix.

All the investigated sandwich panels (described in Chapters 5 and 6) were fabricated following the same procedure. The material assembly and vacuum infusion process were carried out by Décision S.A (Ecublens, Switzerland).

### D.2 Fabrication procedure

A sequence of photos illustrating some of the material preparation steps carried out before the vacuum infusion process is shown in Figure D.1. A diagram of the vacuum infusion set-up is presented in Figure D.2 and supplemented by another sequence of photos illustrating the infusion set-up presented in Figure D.3. The following is a sequential list describing the different fabrication steps:

1. *Drilling of hole in balsa core*: a 30-mm-diameter hole for the subsequent insertion of the loading screw was drilled in the center of the balsa core (see Figure D.1(a)).
2. *Sealing of hole in balsa core*: to prevent any resin from entering the hole drilled in the balsa core during the infusion, the latter was duly sealed with a polyoxymethylene (POM) cylinder and mastic (see Figure D.1(b) and D.2).

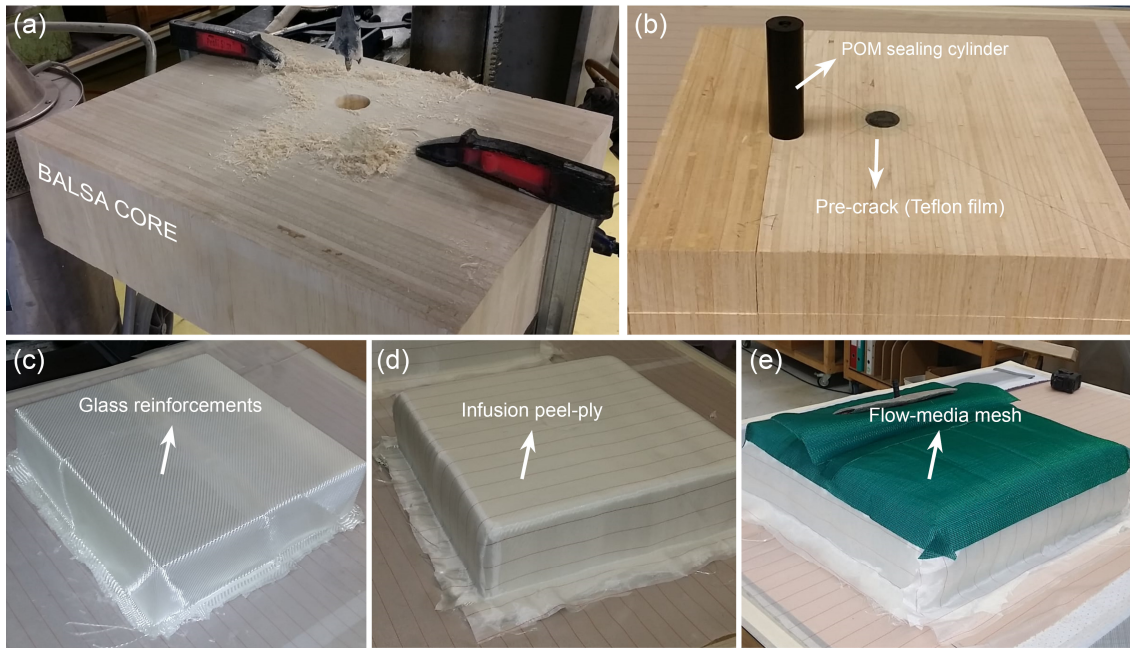


Figure D.1 – Sequence of material assembly for vacuum infusion; (a) perforation of hole in balsa wood, (b) introduction of POM sealer inside drilled hole and pre-crack placement and placement of (c) glass fiber-reinforcement layers, (d) infusion peel-ply and (e) flow media mesh.

3. *Preparation of the work table:* the infusion of the sandwich panels was carried out on a table covered with a peel-ply tissue that was easily detached once the vacuum infusion process was finished (see Figure D.1 and D.2).
4. *Placement of balsa core and Teflon film:* the balsa core with the hole already sealed was placed over the peel-ply tissue and the circular Teflon film used to introduce the pre-crack was placed in the center of the balsa core (i.e. over the sealed hole).
5. *Placement of reinforcement layers:* the different layers of reinforcement depending on the specimen configuration, including the additional circular woven reinforcement layers intended to reinforce the top of the loading region, were placed (see Figure D.1(c)).
6. *Placement of infusion peel-ply fabric and flow-media mesh:* an infusion peel-ply was placed over the reinforcement layers covering both the surface and sides of the sandwich panel. Subsequently, the flow-media mesh was placed over the peel-ply and in this case the surface of the sandwich panel was fully covered down to only approximately 3 cm along the sides (see Figure D.1(e)). Additionally, the flow-media mesh was folded at the center as part of the resin inlet described in the following.
7. *Preparation of resin inlet:* one resin inlet was created in the center of the panel (see Figures D.2 and D.3(a)). The resin ramp was placed over one of the sides of the folded flow-media mesh (see Figures D.2, D.3(a, c) and A.3(a)). A plastic tube (which was later connected to the resin deposit) was connected to the resin ramp.

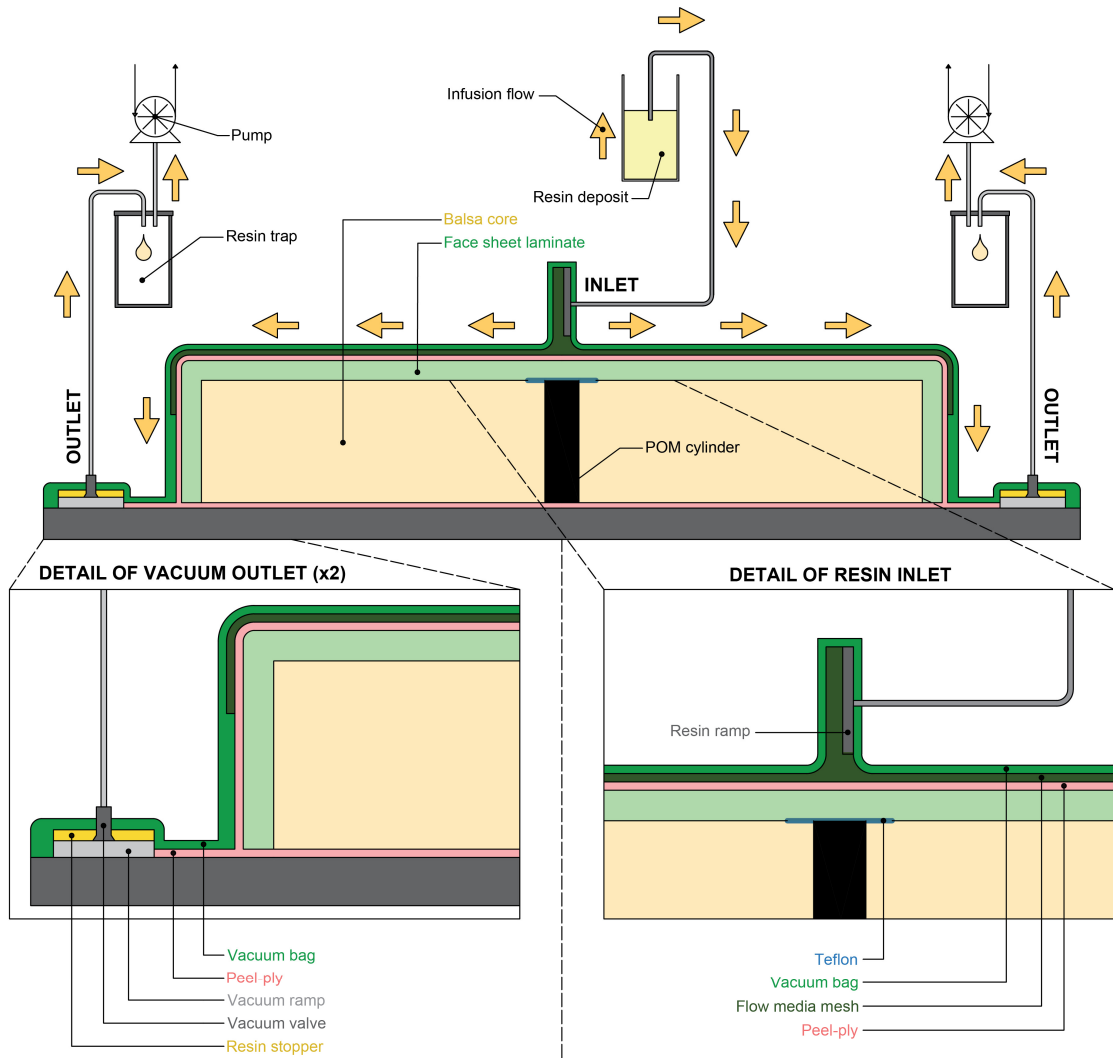


Figure D.2 – Vacuum infusion set-up for GFRP/balsa sandwich panels (not to scale)

8. *Preparation of the vacuum outlet:* two vacuum outlets were created, one on each side of the panel (see Figures D.2 and D.3(a)). The vacuum outlets consisted of a resin stopper (to absorb the outgoing resin, see also Figure A.3(b)), a vacuum ramp (to homogeneously distribute the vacuum, see also Figure A.3(c)), and a vacuum valve that connected (via a plastic tube) the vacuum outlet to the resin trap and the vacuum pump (see detail in Figure D.3(b)).
9. *Placement of the vacuum bag and sealing:* a vacuum bag was placed over all the previously mentioned elements. At the location of the resin inlet and vacuum outlet tubes, holes of approximately the size of the tubes were perforated in the vacuum bag. The contours and holes were duly sealed by means of mastic tape intended for vacuum infusion application (see Figures D.2 and D.3(a, c)).
10. *Connection to the resin trap and vacuum pump:* the plastic tubes from the vacuum outlets were connected to the resin trap (i.e. an intermediate deposit where any resin that may pass through the vacuum outlet could be accumulated,



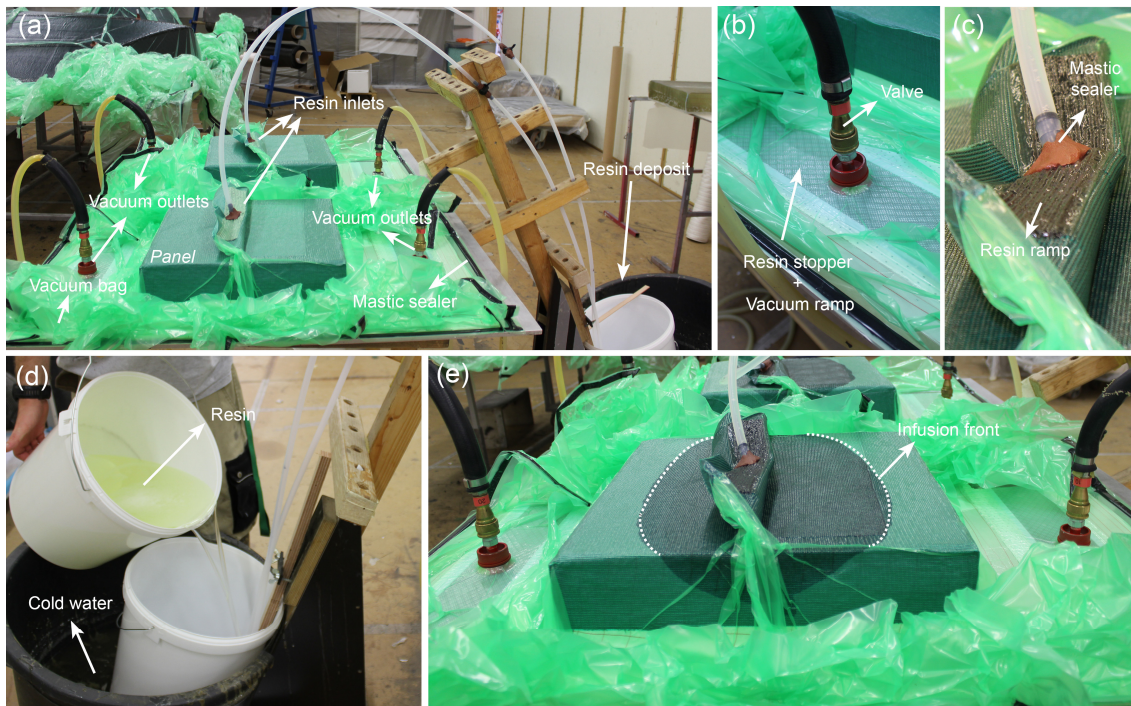


Figure D.3 – Vacuum infusion set-up; (a) general view of infusion set-up, (b) detail of vacuum outlet, (c) detail of resin inlet, (d) detail of resin deposit and (e) detail of infusion front during resin infusion.

therefore preventing it from reaching and thus damaging the pump (see Figure D.2).. A vacuum pump MILS EVISA of 150 m<sup>3</sup>/h capacity and capable of achieving a 95% final vacuum, were used.

11. *Starting of vacuum pump:* once everything was in place, the pump was turned on and the absence of air leaks verified. The tube from the resin inlet was closed by means of a resin-control valve.
12. *Resin and hardener blending and degassing:* the epoxy resin and hardener were mixed. The required amount of resin was mixed in the same resin recipient (see Figures D.2 and D.3(d)). To avoid excessive heating of the mixture, the resin recipient was placed inside a large bucket full of cold water. The water was periodically replaced throughout the infusion to maintain the temperature of the resin below 42°C until the total infusion of the panel was completed. The resin had been previously degassed in a vacuum bell (c.a. 950 mbar) to remove trapped air.
13. *Connection to the resin pot and infusion initiation:* the tube from the resin inlet was placed inside the resin deposit and the resin-control valve was opened to start the infusion. The speed of the resin income was regulated by adjusting the degree of opening of the resin-control valve.
14. *Monitoring the infusion process:* due to the single central resin inlet and the two-sided vacuum outlets, a symmetric infusion front was obtained (see Figure D.3(c)). The temperature of the resin deposit was monitored by means of an infrared thermometer and when it reached ca 42°C (i.e. the level of hardening

impeded the resin flow) the resin-control valve was closed again. The laminates were left under vacuum at room temperature for at least 12 hours.

15. *Post-curing and demolding*: still under vacuum, the panels were post-cured at 45°C for eight hours. Subsequently, they were demolded and the POM sealing cylinder was removed.

After post-curing, the sandwich panels were prepared for the assembly of the loading system as described in detail in Chapter 5.



# Appendix E

## Quasi-static debonding experiments

### E.1 Introduction

Appendix E presents supplementary data and results from the quasi-static experiments conducted on the GFRP/balsa sandwich panels described in Chapter 5.

The experimental program was conducted on two different configurations of GFRP/balsa sandwich panels: 1) the SPA configuration that consisted of 18 plies of woven reinforcement and 2) the SPB configuration that consisted of a symmetric layup combining nine plies of woven fabrics and two plies of continuous filament mat (CFM) above and below. Two sandwich panels of each configuration were fabricated and experimentally investigated.

One of the employed crack-front-monitoring systems was a digital camera placed above the sandwich panels. A selection of recorded images showing the evolution of the crack front is presented for each sandwich panel in Section E.2. The damage in the loading region can also be observed in the images.

A 3D digital image correlation (DIC) system (also located above the panels) was used to measure the out-of-plane deformation and in-plane strain distributions of the top surface of one quarter of the face sheets. The measured out-of-plane deflection and radial and circumferential strain profiles corresponding to a radial path (starting from the pre-crack front) are presented, for all the panels, in Section E.3.

## E.2 Crack front evolution

### SPA panels

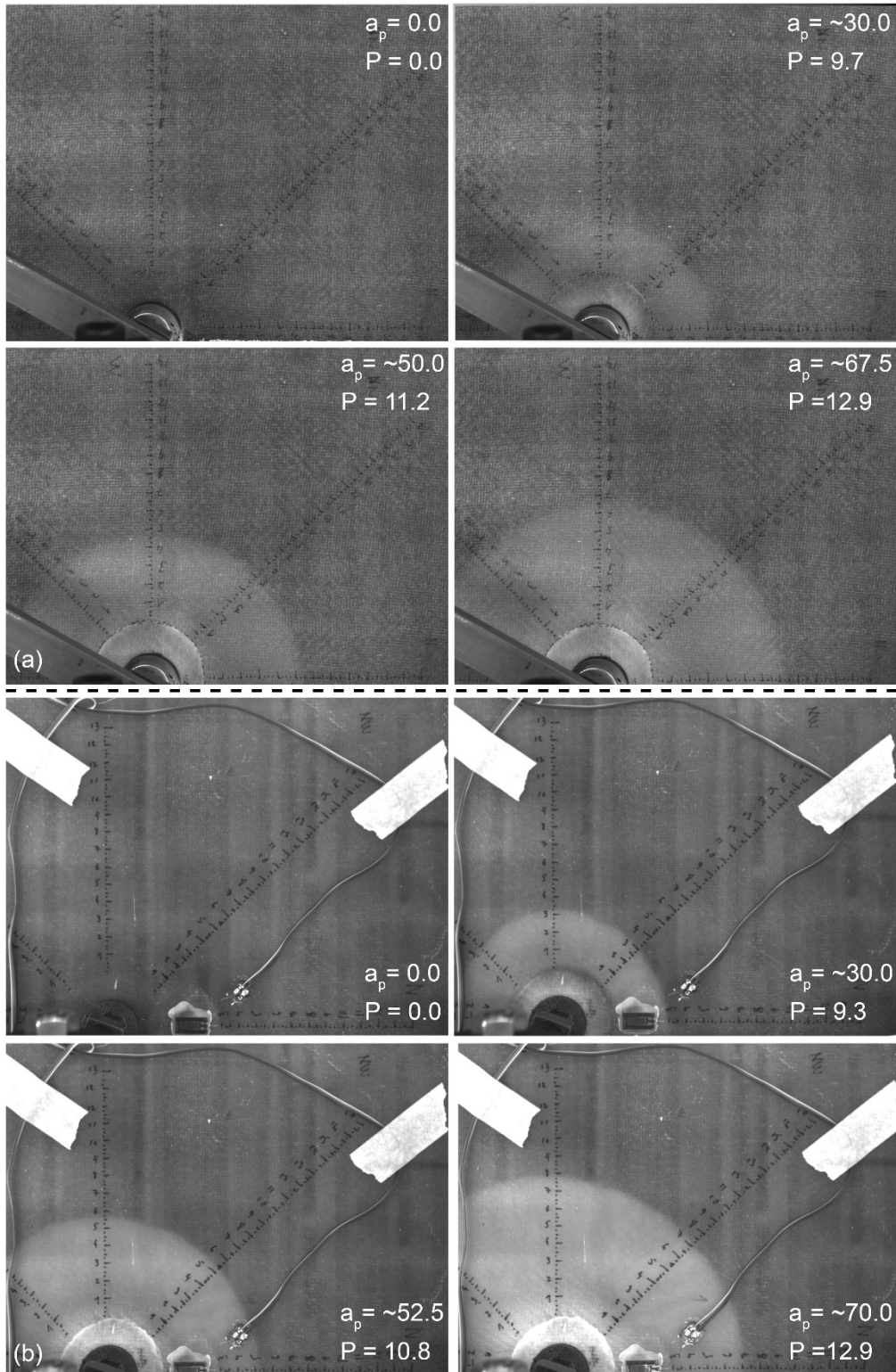


Figure E.1 – Sequence of crack fronts and load in (a) SPA.1 and (b) SPA.2 panels ( $a_p$  is total propagated radial crack length and  $P$  is corresponding load). Units in mm and kN



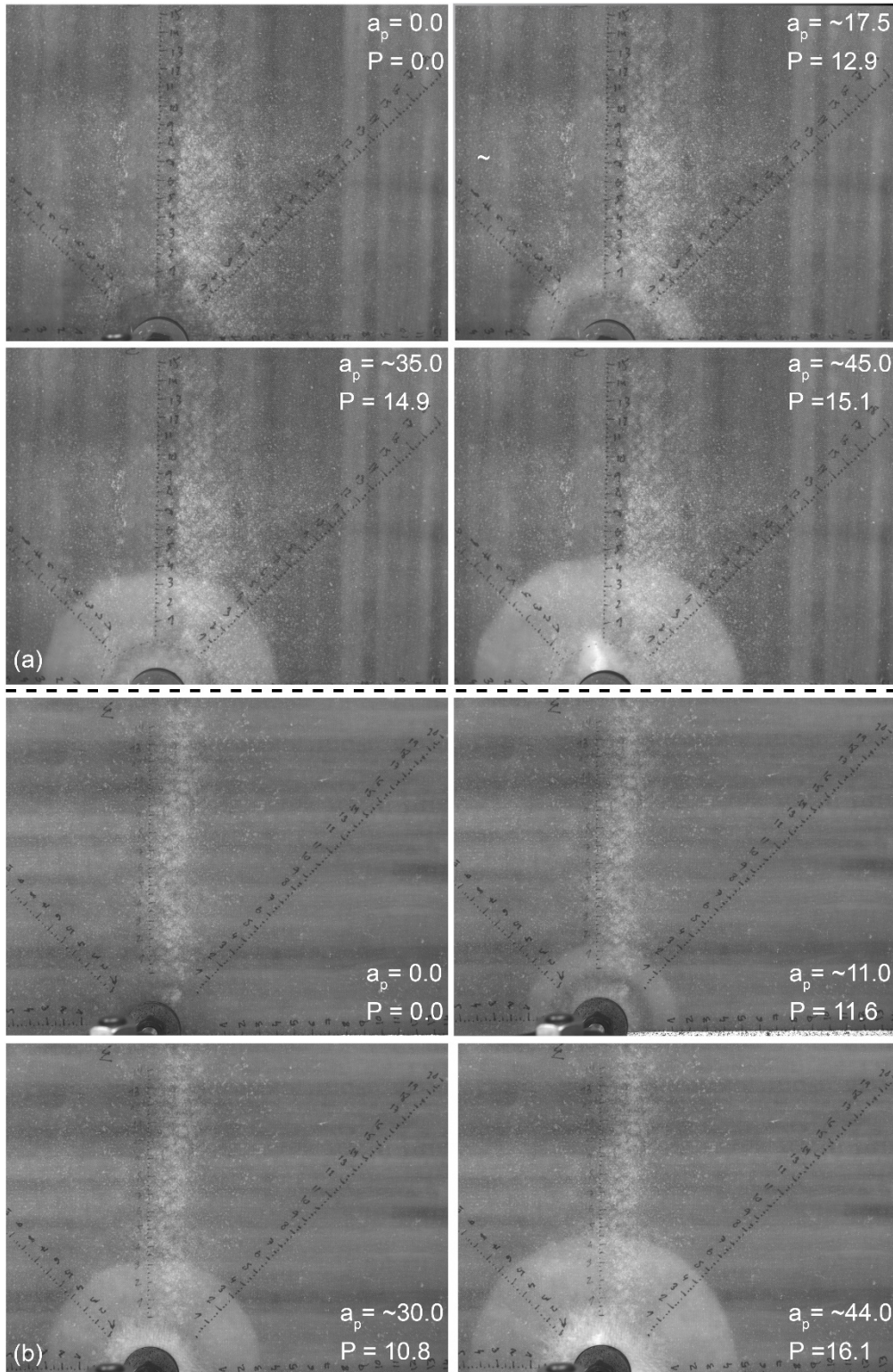
**SPB panels**

Figure E.2 – Sequence of crack fronts and load in (a) SPB.1 and (b) SPB.2 panels ( $a_p$  is total propagated radial crack length and  $P$  is corresponding load). Units in mm and kN

E.3 In-plane strain and out-of-plane deflection profiles

SPA panels

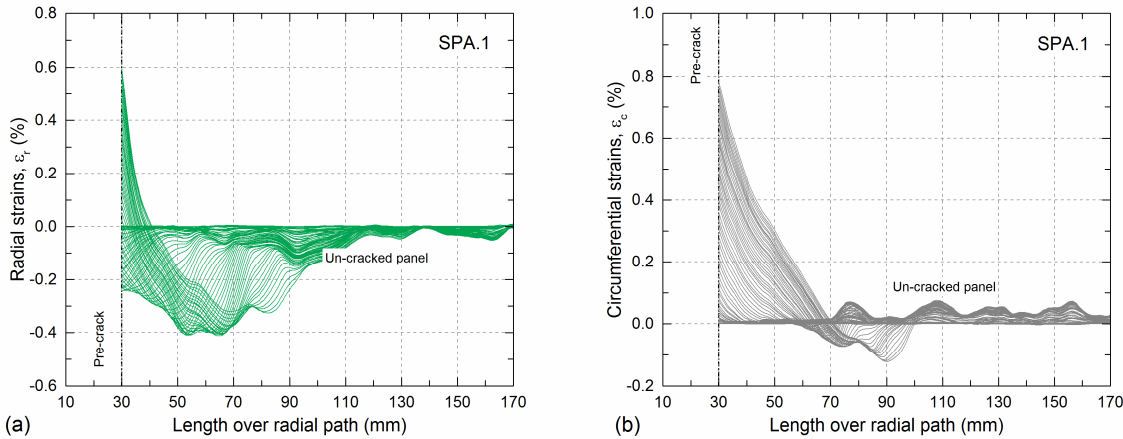


Figure E.3 – Face sheet top surface in-plane strain distributions, (a) radial direction and (b) circumferential direction, SPA.1 panel

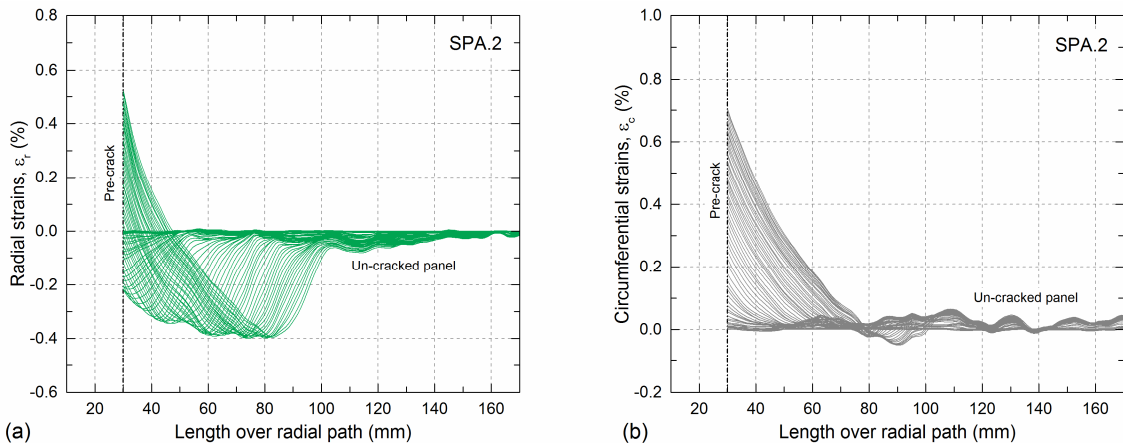


Figure E.4 – Face sheet top surface in-plane strain distributions, (a) radial direction and (b) circumferential direction, SPA.2 panel

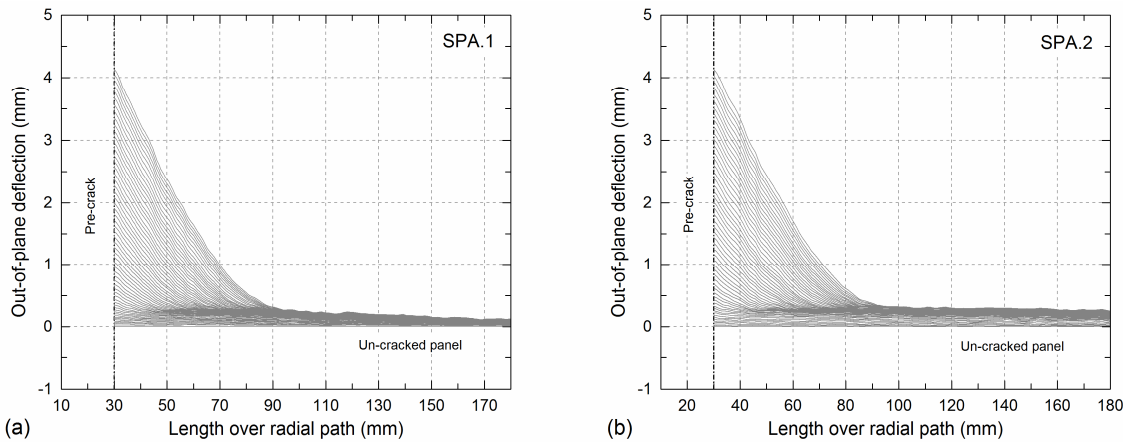


Figure E.5 – Out-of-plane radial deflection profile in (a) SPA.1 and (b) SPA.2 panels



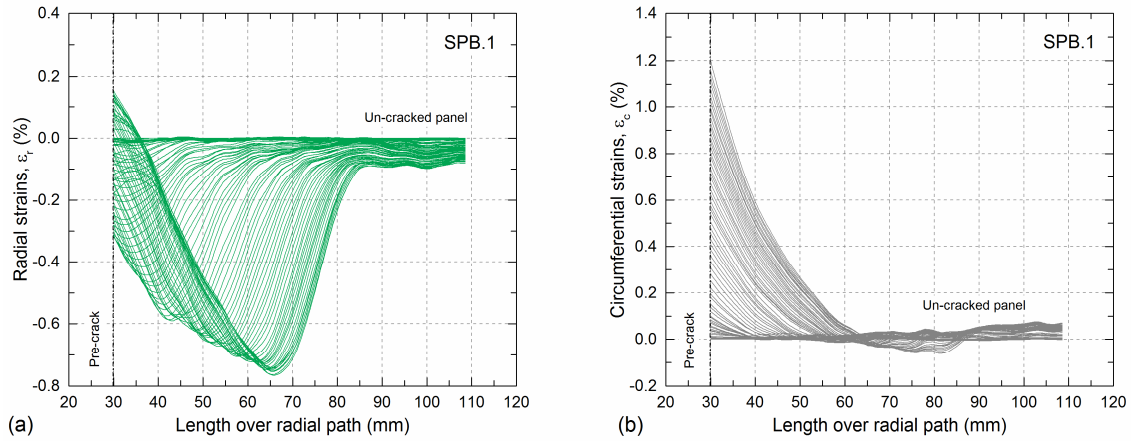
**SPB panels**

Figure E.6 – Face sheet top surface in-plane strain distributions, (a) radial direction and (b) circumferential direction, SPB.1 panel

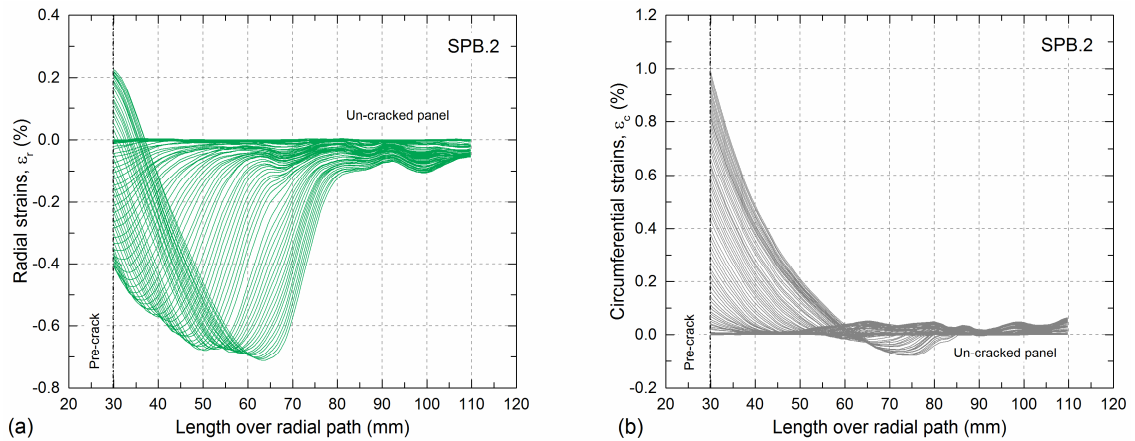


Figure E.7 – Face sheet top surface in-plane strain distributions, (a) radial direction and (b) circumferential direction, SPB.2 panel

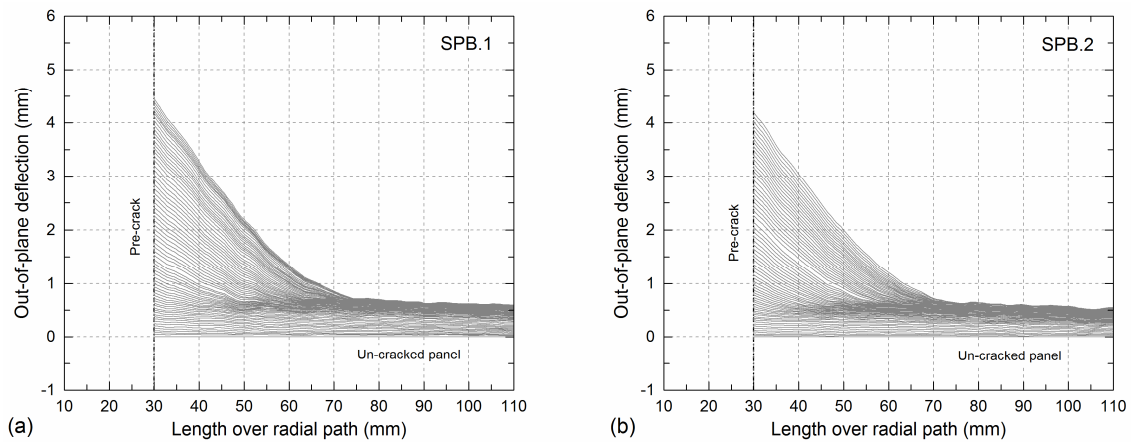


Figure E.8 – Out-of-plane radial deflection profile in (a) SPB.1 and (b) SPB.2 panels



# Appendix F

## Fatigue debonding experiments

### F.1 Introduction

Appendix F presents supplementary data and results from the fatigue experiments conducted on GFRP/balsa sandwich panels described in Chapter 6.

The experimental program was conducted on two different configurations of GFRP/balsa sandwich panels: 1) the SPA configuration that consisted of 18 plies of woven reinforcement and 2) the SPB configuration that consisted of a symmetric layup combining nine plies of woven fabrics and two plies of continuous filament mat (CFM) above and below. Two sandwich panels of each configuration were fabricated. Experiments under  $R$ -ratio of  $R=0.1$  were conducted on each of the two SPA panels (i.e. SPA.1F and SPA.2F) while three different  $R$ -ratios were investigated for the SPB panels:  $R=0.1$ , applied to one of the panels (SPB.1F) and  $R=0.5$  and  $0.3$ , applied consecutively to the second panel (designated SPB.2F1 and SPB.2F2 respectively).

One of the employed crack front monitoring systems was a digital camera placed above the sandwich panels. A selection of recorded images showing the evolution of the crack front is presented for each sandwich panel in Section F.2. The damage in the loading region can also be observed in the images.

A 3D digital image correlation (DIC) system (also located above the panels) was used to measure the out-of-plane deformation and in-plane strain distributions of the top surface of one quarter of the face sheets. The measured out-of-plane deflection and radial and circumferential strain profiles corresponding to a radial path (starting from the pre-crack front) are presented, for all the panels, in Section F.3. Negative values of

out-of-plane deflection were measured due to the location of the DIC cameras with respect to the loading jack of the experimental rig (i.e. the cameras were located above the sandwich panels and the load was applied by descending the bottom jack of the machine, and thus moving the face sheet surface away from the DIC cameras). Groups of profiles corresponding to representative fatigue cycles are shown in different colors (i.e. each group corresponds to one fatigue cycle). The DIC analysis performed on the images recorded for the SPA.2F panel revealed a projection error above the standard accepted limit for this type of analysis. It is believed that an excessive exposure time (not detected during calibration) caused a certain motion blur on the recorded images and thus an error in the measurements. As can be observed in Figure F.4, this error led to irregular strain profiles. Although, to a minor extent, irregular out-of-plane deflection profiles were also obtained (see Figure F.5(b)). The same trend as in SPA.1F was however found. A reduction in accuracy and thus more irregular profiles were also found in measurements after two million cycles due to the increase of the fatigue frequency from 5 to 10 Hz. This can be observed in Figures F.7, F.8, F.10 and F.11.

The measured load-displacement hysteresis loops are presented in Section F.4. The upper and lower parts of the loops corresponded respectively to the loading and unloading portions of the cycles. The “banana” shape described in Chapter 6 can be observed for all the experiments.

The hysteresis area of each of the load-displacement hysteresis loops vs normalized number of cycles is presented in Section F.5.

## F.2 Crack front evolution

### SPA panels

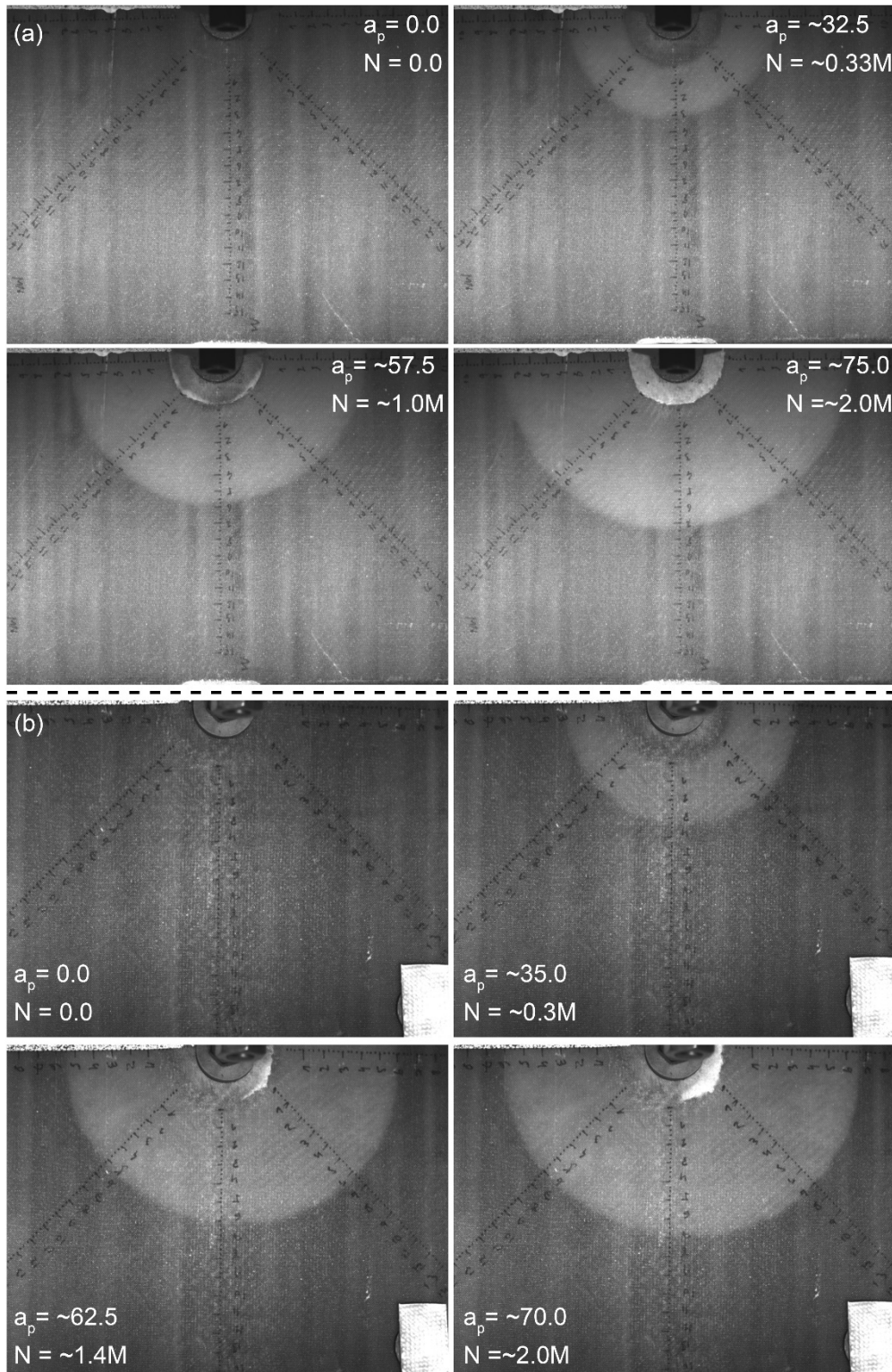


Figure F.1 – Sequence of crack fronts and load in (a) SPA.1F and (b) SPA.2F panels ( $a_p$  is total propagated radial crack length and  $N$  is corresponding number of cycles). Units in mm and millions (M) of cycles

### SPB panels

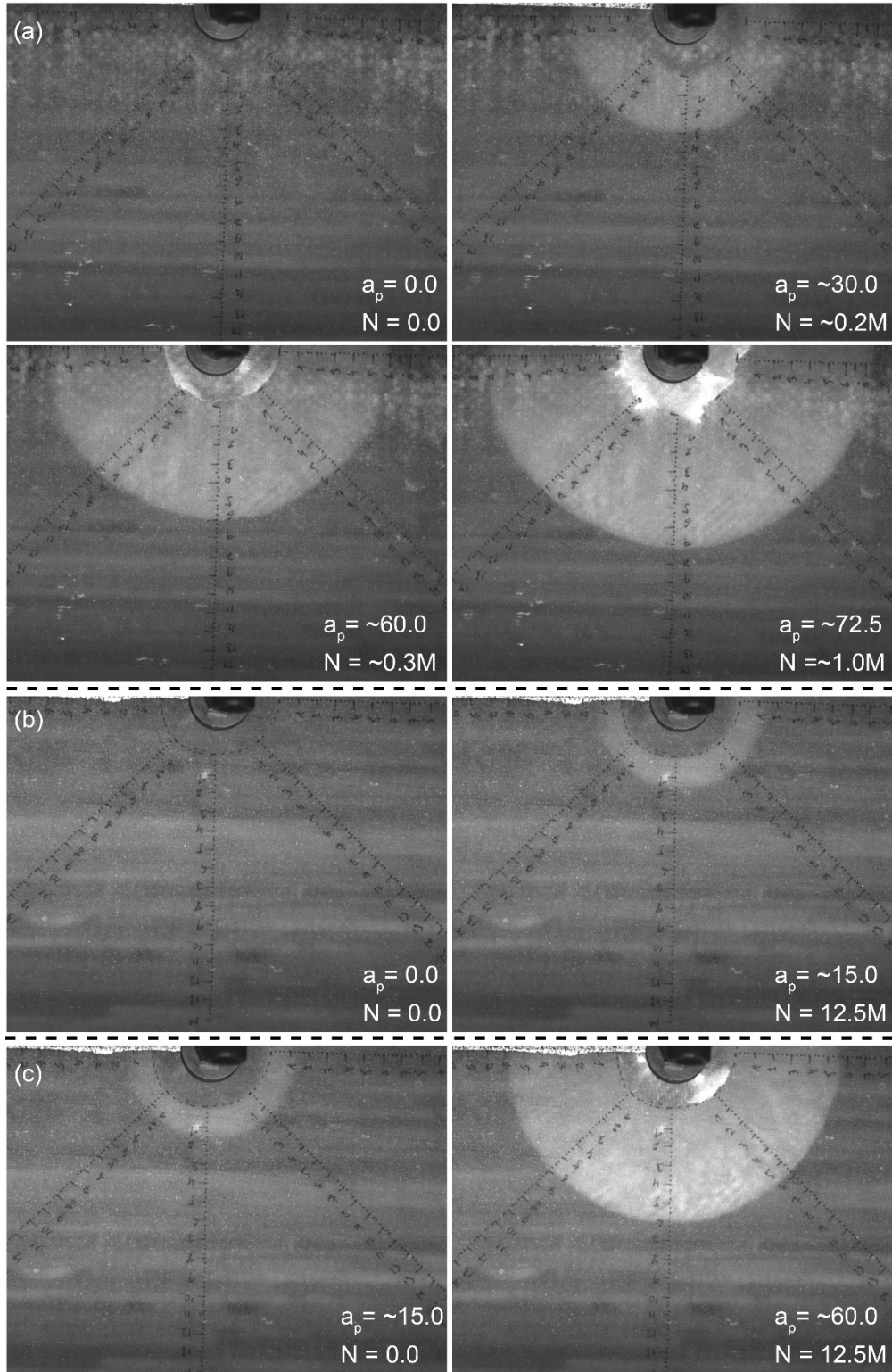


Figure F.2 – Sequence of crack fronts and load in (a) SPB.1F, (b) SPB.2F1 and (c) SPB.2F2 panels ( $a_p$  is total propagated radial crack length and  $N$  is corresponding number of cycles). Units in mm and millions (M) of cycles

### F.3 In-plane strain and out-of-plane deflection profiles

#### SPA panels

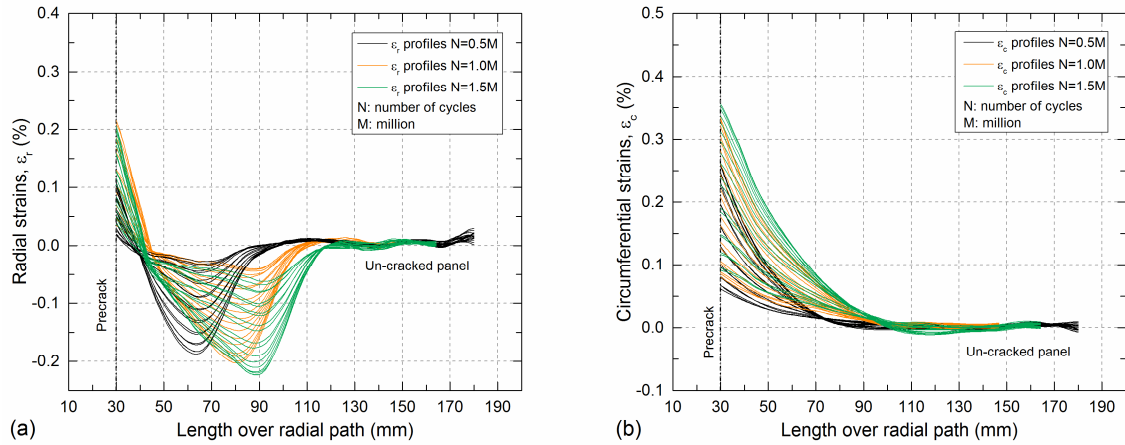


Figure F.3 – Face sheet top surface in-plane strain distributions, (a) radial direction and (b) circumferential direction, SPA.1F panel

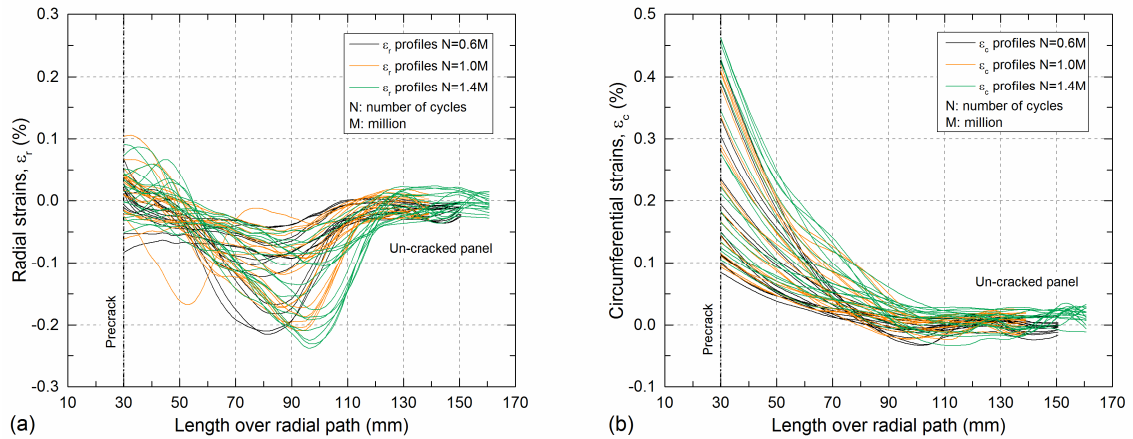


Figure F.4 – Face sheet top surface in-plane strain distributions, (a) radial direction and (b) circumferential direction, SPA.2F panel

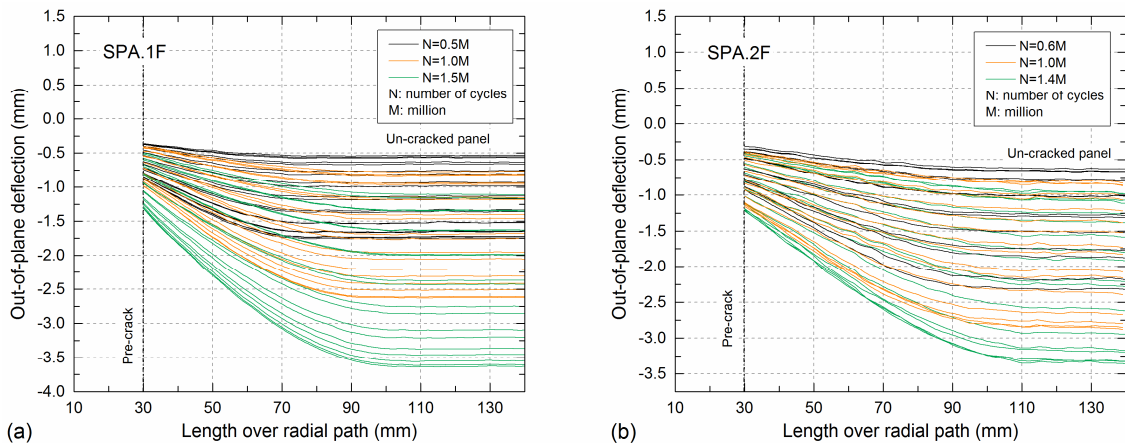


Figure F.5 – Out-of-plane radial deflection profile in (a) SPA.1F and (b) SPA.2F panels



## SPB panels

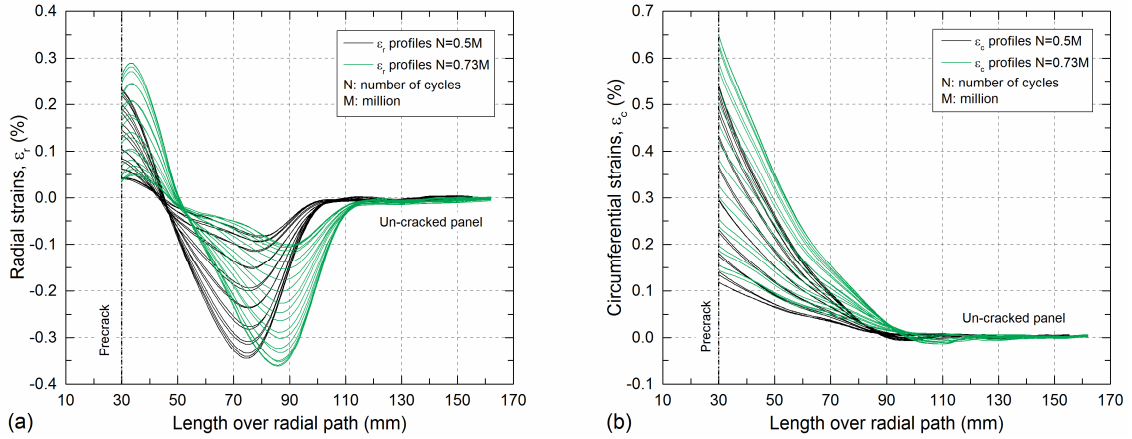


Figure F.6 – Face sheet top surface in-plane strain distributions, (a) radial direction and (b) circumferential direction, SPB.1F panel

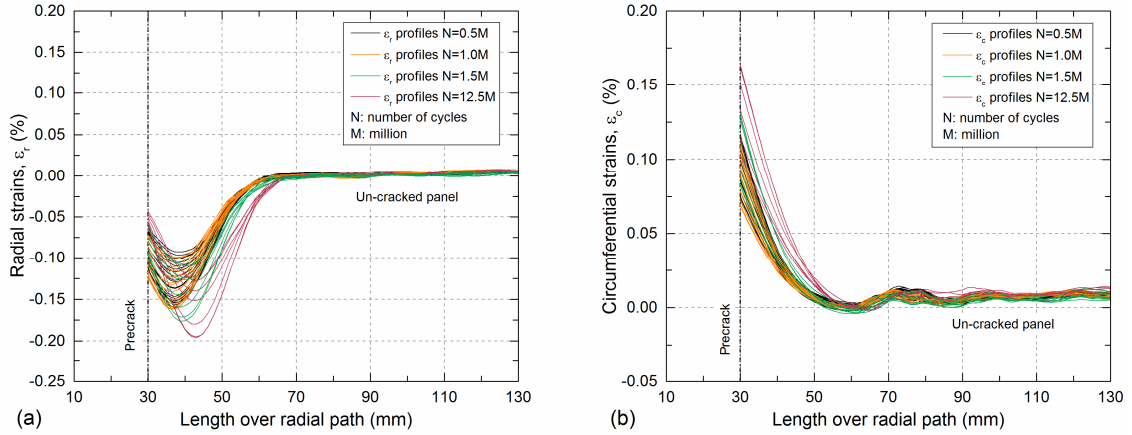


Figure F.7 – Face sheet top surface in-plane strain distributions, (a) radial direction and (b) circumferential direction, SPB.2F1 panel

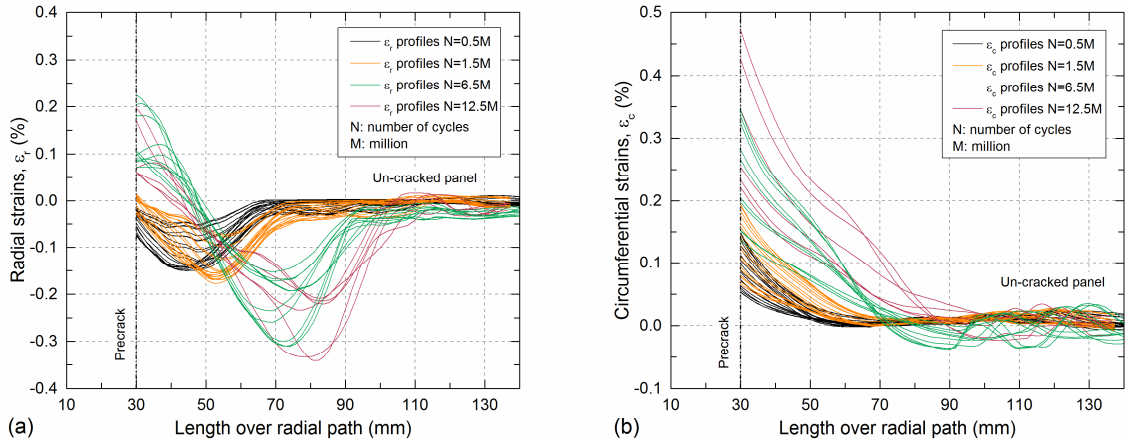


Figure F.8 – Face sheet top surface in-plane strain distributions, (a) radial direction and (b) circumferential direction, SPB.2F2 panel

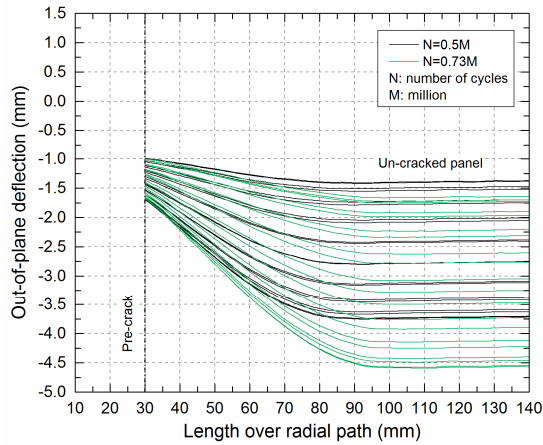


Figure F.9 – Out-of-plane radial deflection profile, SPB.1F

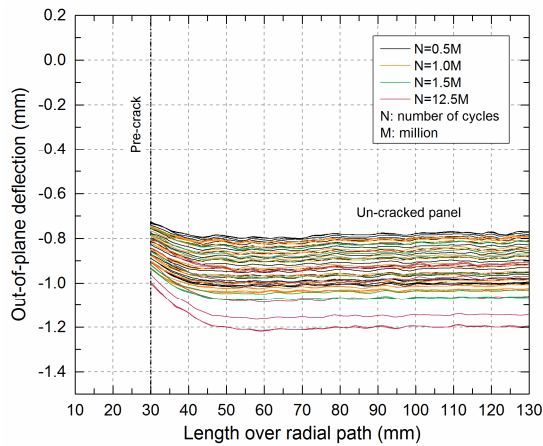


Figure F.10 – Out-of-plane radial deflection profile, SPB.2F1

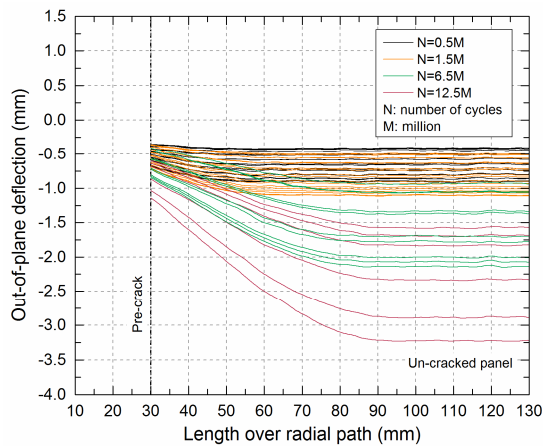


Figure F.11 – Out-of-plane radial deflection profile, SPB.2F2

F.4 Load-displacement hysteresis loops

SPA panels

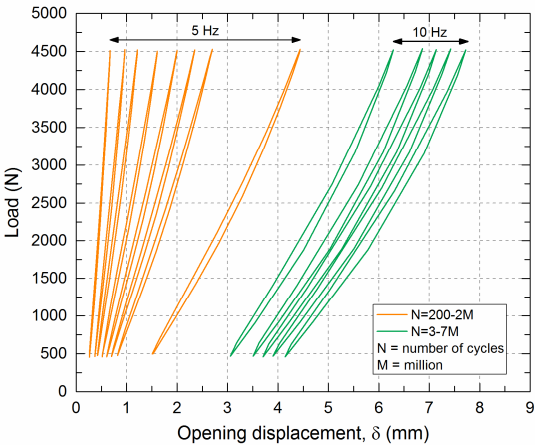


Figure F.12 – Load-displacement hysteresis loops, SPA.1F panel

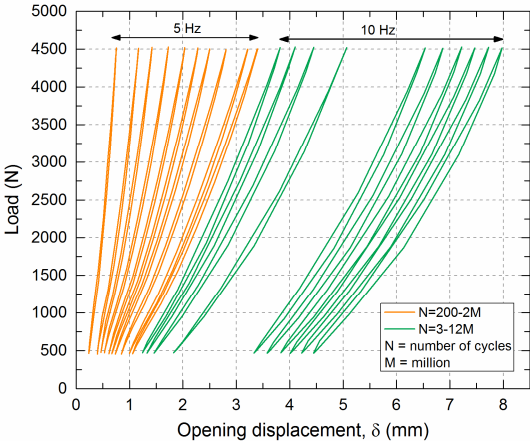


Figure F.13 – Load-displacement hysteresis loops, SPA.2F panel

## SPB panels

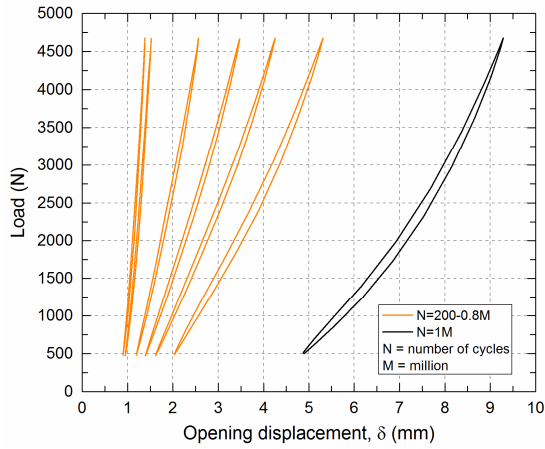


Figure F.14 – Load-displacement hysteresis loops, SPB.1F panel

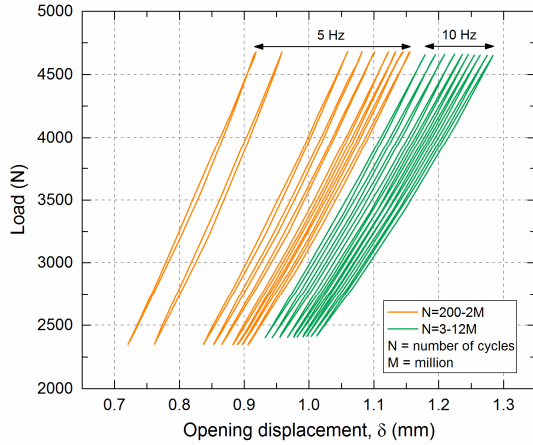


Figure F.15 – Load-displacement hysteresis loops, SP2.2F1 panel

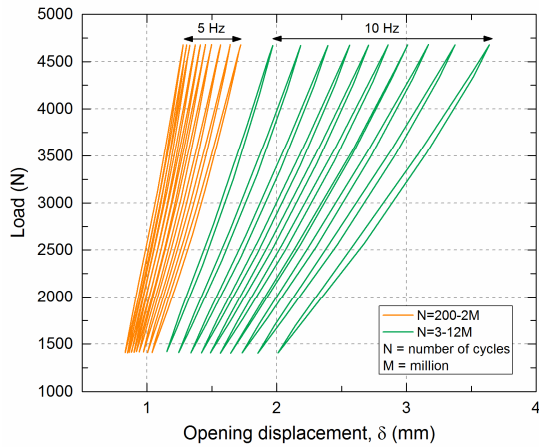


Figure F.16 – Load-displacement hysteresis loops, SPB.2F2 panel

## F.5 Hysteresis area per cycle vs normalized number of cycles

### SPA panels

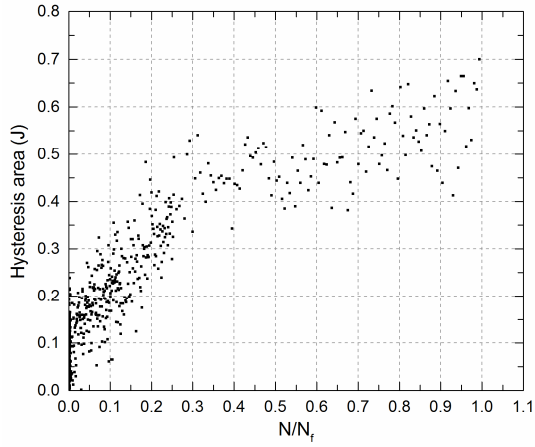


Figure F.17 – Hysteresis area per cycle vs normalized number of cycles, SPA.1F panel

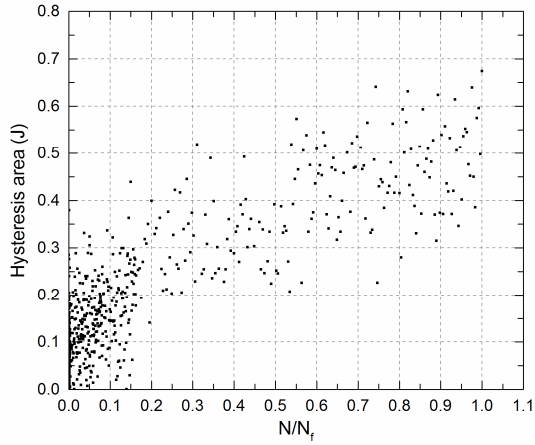


Figure F.18 – Hysteresis area per cycle vs normalized number of cycles, SPA.2F panel

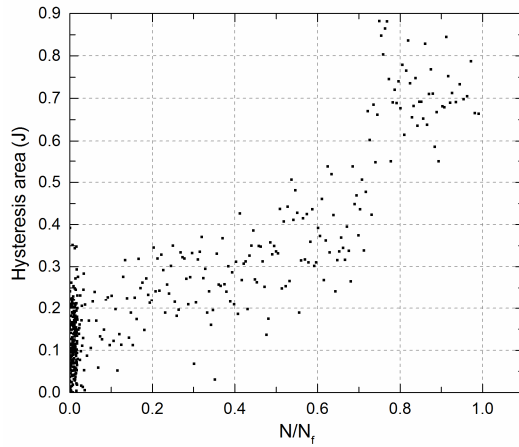
**SPB panels**

Figure F.19 – Hysteresis area per cycle vs normalized number of cycles, SPB.1F panel

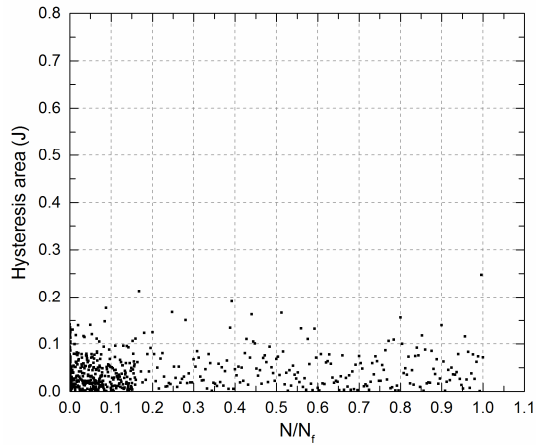


Figure F.20 – Hysteresis area per cycle vs normalized number of cycles, SPB.2F1 panel

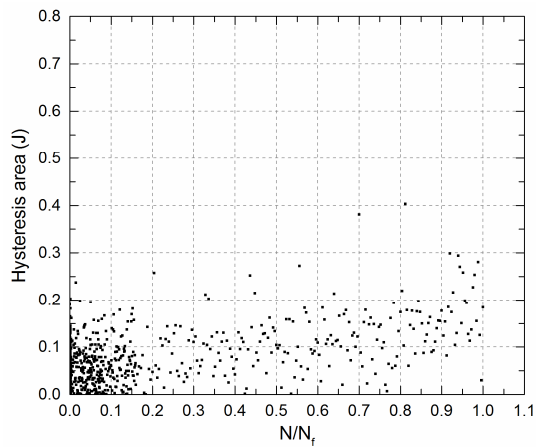


Figure F.21 – Hysteresis area per cycle vs normalized number of cycles, SPB.2F2 panel





# Curriculum Vitae

**AIDA CAMESELLE MOLARES**

✉ [aida.cameselle@gmail.com](mailto:aida.cameselle@gmail.com)

Birth date: April 22, 1990

Nationality: Spanish

Languages: Spanish, Galician, English and French

## EDUCATION

- 2015–2019      PhD candidate in Civil Engineering**  
Composite Construction Laboratory (CCLab), Prof. Thomas Keller  
Ecole Polytechnique Fédérale de Lausanne (EPFL), Lausanne, Switzerland  
*PhD Thesis:* Two-dimensional crack growth in FRP structures
- 2008–2014      Master (MSc) in Civil Engineering**  
Universidad de A Coruña (UDC), A Coruña, Spain  
*Final degree project:* Stress ribbon footbridge (43-m span)  
*Undergraduate research project:* Experimental investigation of bond behavior between GFRP and concrete

## ADDITIONAL EDUCATION

- 2018 (Spring)      Innosuisse-Swiss Innovation Agency Start-up Training: Business Concept**  
EPFL, Lausanne, Switzerland (14-week training program)

## WORK EXPERIENCE

- 2015–2019      Research and Teaching Assistant at CCLab-EPFL, Lausanne, Switzerland**  
Experimental and numerical (FEM) research on fracture in FRP structures  
Teaching assistant: “Structures et matériaux I/II” (Bachelor in Architecture)
- 2014–2015      Structural and Research Engineer in Structural Mechanics Group (GME), ETSICCP, A Coruña, Spain**  
Research and consulting on structural projects in collaboration with Airbus and Acciona-Windpower
- 2012 (Summer)      Trainee student, Enmacosa, A Coruña, Spain**  
Technical consulting on civil engineering projects

## PUBLICATIONS

- Journal papers**
- Cameselle-Molares A, Vassilopoulos A.P, Keller T. Two-dimensional fatigue debonding in GFRP/balsa sandwich panels. *Int J Fatigue* 2019; 125: 72-84.
- Cameselle-Molares A, Vassilopoulos A.P, Keller T. Two-dimensional quasi-static debonding in GFRP/balsa sandwich panels. *Compos Struct* 2019; 215: 391-401.
- Cameselle-Molares A, Renart J, Turon A, Vassilopoulos A.P, Keller T. Numerically-based method for fracture characterization of Mode I-dominated two-dimensional delamination in FRP laminates. *Compos Struct* 2019; 214: 143-152.

Cameselle-Molares A, Renart J, Turon A, Vassilopoulos A.P, Keller T. Numerical simulation of two-dimensional in-plane crack propagation in FRP laminates. *Compos Struct* 2018; 200: 396-407.

Cameselle-Molares A, Vassilopoulos A.P, Keller T. Experimental investigation of two-dimensional delamination in GFRP laminates. *Eng Fract Mech* 2018; 203: 152-171.

Cameselle-Molares A, Sarfaraz R, Shahverdi M, Keller T, Vassilopoulos A. P. Fracture mechanics-based progressive damage modelling of adhesively bonded fibre-reinforced polymer joints. *Fatigue and Fract Eng Mater Struct*, 2017; 40(12): 2183-2193.

#### Conference papers

Cameselle-Molares A, Vassilopoulos A. P, J. Renart, A. Turon, Keller T. 2D quasi-static delamination in GFRP laminates: numerical investigation. In: 12th International Conference on Sandwich Structures (ICSS). Lausanne, Switzerland, 19-22 August 2018.

Cameselle-Molares A, Vassilopoulos A. P, Keller T. 2D quasi-static delamination in GFRP laminates: experimental investigation. In: 12th International Conference on Sandwich Structures (ICSS). Lausanne, Switzerland, 19-22 August 2018.

Cameselle-Molares A, Vassilopoulos A. P, J. Renart, A. Turon, Keller T. Numerical simulation of two-dimensional crack propagation. In: 18th International Conference on Composite Materials. Athens, Greece, 24-28 June 2018.

Cameselle-Molares A, Vassilopoulos A. P, Keller T. Novel experimental design for two-dimensional delamination in fiber-reinforced polymer laminates. In: 18th International Conference on Experimental Mechanics (ICEM). Brussels, Belgium, 1-5 July 2018.

Cameselle-Molares A, Vassilopoulos A. P, Keller T. Two-dimensional delamination in GFRP laminates: experimental investigation. In: 9th International Conference on Fibre-Reinforced Polymer (FRP) Composites in Civil Engineering (CICE). Paris, France, 17-19 July 2018.

Cameselle-Molares A, Vassilopoulos A. P, Keller T. Experimental procedure and phenomenological analysis of 2D quasi-static crack propagation in GFRP laminates. In: 8th International Conference on Fracture of Polymers, Composites and Adhesives. Les Diablerets, Switzerland, 10-14 September 2017.

#### AWARDS AND SCHOLARSHIPS

- |             |   |
|-------------|---|
| <b>2017</b> | <b>Mobility Award, Doctoral School of Civil Engineering (EDCE), EPFL</b><br>Funding for three-month scientific visit to AMADE Group, Girona, Spain                                |
| <b>2014</b> | <b>“Puentes” Award for best Structural Final Degree Project</b><br>Award granted by the civil engineering company “Grupo Puentes” and the School of Civil Engineering of A Coruña |
| <b>2013</b> | <b>Collaboration Scholarship in University Departments, University of A Coruña</b><br>Award granted to students achieving high academic performance                               |
| <b>2008</b> | <b>Graduate Scholarship, Comunidad Autónoma (CA) de Galicia</b><br>First year funding for undergraduate studies, awarded to high-level students                                   |
| <b>2008</b> | <b>Award for Excellence in Academic Performance, University of A Coruña</b><br>Award granted to students with the best mark in the university entrance exam                       |
| <b>2008</b> | <b>Award for Excellence in Academic Performance, CA de Galicia</b><br>Award granted to students with the best mark in the university entrance exam                                |



